

## Abstract

# Quantum Optomechanics with Superfluid Helium

Alexey Shkarin

2018

The field of optomechanics deals with the interaction between light and mechanical objects. One of the goals in this field is to gain ability to coherently manipulate mechanical states with single-quantum precision and to interface these states with electromagnetic radiation without loss. Recent achievements enabled by this power include cooling of the mechanical oscillator to its quantum ground state, generating optical or mechanical squeezing, or entangling mechanical and optical degrees of freedom. To accomplish these goals, one generally aims to create a system with strong optomechanical coupling, while maintaining low optical and mechanical losses and low temperature. Superfluid helium is a liquid which is uniquely well-suited to meet these requirements.

In this work I describe the cavity optomechanics systems in which we couple infrared light to a standing acoustic wave in superfluid helium. With this system, we used light to coherently excite acoustic vibrations and manipulate their frequency and damping rate using the dynamic back-action effect. In addition, we measured thermal fluctuations of the mechanical mode corresponding to mean phonon number of five. These measurements had sufficient precision to reveal quantum signatures in the motion of the acoustic waves and in their interaction with light. Specifically, we observed the expected one-phonon difference between the Stokes and anti-Stokes mechanical sidebands, and indirectly measured the action of the optical shot noise on the mechanical object by investigating the correlations between these sidebands.

# Quantum Optomechanics with Superfluid Helium

A Dissertation  
Presented to the Faculty of the Graduate School  
of  
Yale University  
in Candidacy for the Degree of  
Doctor of Philosophy

by  
Alexey Shkarin

Dissertation Director: Jack Harris  
May 2018

Copyright © 2018 by Alexey Shkarin  
All rights reserved.

# Contents

<b>Content</b>	<b>iii</b>
<b>Acknowledgements</b>	<b>viii</b>
<b>List of Figures</b>	<b>ix</b>
<b>List of Tables</b>	<b>xi</b>
<b>List of Symbols</b>	<b>xii</b>
<b>List of Acronyms</b>	<b>xxi</b>
<b>1 Introduction</b>	<b>1</b>
<b>2 Canonical optomechanical system</b>	<b>3</b>
2.1 Single optical mode . . . . .	3
2.1.1 Closed system . . . . .	3
2.1.2 Open system . . . . .	3
2.1.3 Input fields statistics . . . . .	4
2.1.4 Solution for a driven damped optical mode . . . . .	5
2.2 Optomechanical coupling and its interpretations . . . . .	7
2.2.1 Canonical system and its Hamiltonian . . . . .	7
2.2.2 Interpretation of the optomechanical coupling . . . . .	9
2.3 Equations of motion and steady-state solution . . . . .	9
2.3.1 Equations of motion . . . . .	10
2.3.2 Linearization and steady state solution . . . . .	10
2.4 Position detection . . . . .	12
2.4.1 General expression . . . . .	12
2.4.2 Unresolved sideband limit . . . . .	13
2.5 Dynamical backaction . . . . .	13
2.5.1 Bare mechanical oscillator . . . . .	13
2.5.2 Optomechanical self-energy and modified mechanical susceptibility . . . . .	14
2.5.3 Optical spring and optomechanical damping . . . . .	15
2.5.4 Sideband cooling . . . . .	15
2.5.5 Optical spring in the unresolved sideband regime . . . . .	17
2.6 Undriven mechanical motion and RPSN . . . . .	18
2.6.1 Mechanical motion PSD . . . . .	18
2.6.2 Reflected light PSD . . . . .	20
2.7 Driven response measurements (OMIT/A) . . . . .	20
2.7.1 General treatment . . . . .	21
2.7.2 Resolved sideband limit . . . . .	22

<b>3</b>	<b>Overview and current progress</b>	<b>25</b>
3.1	Common implementations . . . . .	25
3.2	Linear quantum cavity optomechanics . . . . .	26
3.2.1	Overview . . . . .	27
3.2.2	Thermal cooperativity . . . . .	27
3.2.3	Cooperativity improvement possibilities . . . . .	29
<b>4</b>	<b>Superfluid helium and acoustic modes</b>	<b>31</b>
4.1	General superfluid helium properties . . . . .	31
4.2	Device principle . . . . .	32
4.3	Previous helium optomechanics work . . . . .	33
4.3.1	Spontaneous Brillouin scattering . . . . .	33
4.3.2	Superfluid helium optomechanics . . . . .	33
4.4	Wave equation and modes . . . . .	34
4.4.1	Wave equation . . . . .	34
4.4.2	Boundary conditions . . . . .	35
4.4.3	Stored energy . . . . .	35
4.5	Loss mechanisms . . . . .	36
4.5.1	Intrinsic loss . . . . .	36
4.5.2	Acoustic radiation loss . . . . .	37
4.6	Other excitations and non-ideality considerations . . . . .	37
4.7	Coupling mechanism . . . . .	38
4.7.1	Overlap integral . . . . .	38
4.7.2	Mode normalization . . . . .	39
4.7.3	Wavelength matching condition . . . . .	40
<b>5</b>	<b>Experimental setup overview</b>	<b>43</b>
5.1	Device description . . . . .	43
5.2	Measurement setup . . . . .	44
5.2.1	Light preparation . . . . .	44
5.2.2	Tones generation . . . . .	46
5.2.3	Detection . . . . .	47
5.2.4	Laser locking . . . . .	47
5.2.5	Auxiliary measurements . . . . .	48
<b>6</b>	<b>First generation device</b>	<b>50</b>
6.1	Initial optical characterization and filling . . . . .	50
6.1.1	Device parameters . . . . .	50
6.1.2	Empty cavity characterization . . . . .	50
6.1.3	Filled cavity characterization . . . . .	51
6.2	Driven response measurements . . . . .	52
6.2.1	Experimental procedure . . . . .	52
6.2.2	Acoustic cavity length and optical penetration depth . . . . .	53
6.2.3	Analysis of OMIT/A data . . . . .	55
6.2.4	Photothermal coupling . . . . .	55
6.2.5	Optomechanical coupling results . . . . .	57
6.3	Mechanical quality factor and heating . . . . .	58
6.3.1	Mechanical quality factor measurements . . . . .	58
6.3.2	Heating model . . . . .	60
6.3.3	Fitting the quality factor measurements . . . . .	64
6.3.4	Thermal relaxation time . . . . .	65

6.4	Performance and limitations . . . . .	66
<b>7</b>	<b>Undriven motion measurement theory</b>	<b>68</b>
7.1	Double control beam scheme . . . . .	68
7.1.1	Measurement schematic . . . . .	68
7.1.2	Equations of motion and linearization . . . . .	70
7.1.3	Solution, dynamical backaction and outgoing field . . . . .	71
7.2	Photocurrent PSDs and a cross-correlator . . . . .	72
7.2.1	Relating photocurrent to the outgoing field . . . . .	72
7.2.2	Correlator values and interpretation . . . . .	74
7.3	Photothermal coupling . . . . .	77
7.3.1	Quantum treatment of the photothermal coupling . . . . .	77
7.3.2	Effects of the photothermal coupling . . . . .	78
7.4	Summary . . . . .	80
<b>8</b>	<b>Second generation device</b>	<b>82</b>
8.1	Design improvements and device parameters . . . . .	82
8.2	OMIT measurements and the dynamical backaction . . . . .	84
8.3	Undriven motion measurement . . . . .	85
8.3.1	Measurement scheme . . . . .	86
8.3.2	Normalization scheme . . . . .	87
8.4	Thermal motion . . . . .	90
8.5	Quantum signatures . . . . .	92
<b>9</b>	<b>Conclusion and future directions</b>	<b>96</b>
9.1	Device performance . . . . .	96
9.1.1	Comparison to other superfluid helium optomechanics experiments . . . . .	97
9.2	Future directions . . . . .	98
9.2.1	Acoustic wave optomechanics . . . . .	98
9.2.2	Other superfluid helium excitations . . . . .	100
9.3	Summary and conclusions . . . . .	101
	<b>Appendices</b>	<b>103</b>
<b>A</b>	<b>Mathematical definitions</b>	<b>104</b>
A.1	Correlator and power spectral density . . . . .	104
A.1.1	Correlator . . . . .	104
A.1.2	Power spectral density . . . . .	104
A.1.3	Properties . . . . .	105
A.2	Fourier transform . . . . .	105
A.2.1	“Coherent” Fourier transform . . . . .	105
A.2.2	“Noise” Fourier transform . . . . .	106
A.2.3	Properties and conventions . . . . .	106
<b>B</b>	<b>Mode-related derivations</b>	<b>107</b>
B.1	Cavity frequency perturbation . . . . .	107
B.2	Cavity modes . . . . .	109
B.2.1	Gaussian beam . . . . .	109
B.2.2	Gaussian modes . . . . .	109
B.2.3	Resonance frequencies and free spectral range . . . . .	110
B.3	Transfer matrix formalism . . . . .	111

B.3.1	Definition	112
B.3.2	Common cases	112
B.3.3	Scattering matrix	113
B.3.4	Cavities	114
B.3.5	Perfect mirrors approximation	115
B.4	Distributed Bragg reflectors	116
B.4.1	Finite DBR	116
B.4.2	Infinite DBR approximation and penetration depth	117
B.5	One-dimensional propagation of acoustic waves	119
B.5.1	Wave equation	119
B.5.2	Energy density and energy flux	120
B.5.3	Boundary conditions	121
B.5.4	Transfer matrix description for sound	121
B.5.5	Interaction with a movable boundary	122
<b>C</b>	<b>General optics derivations</b>	<b>124</b>
C.1	Optical detection description	124
C.1.1	General photocurrent expression	124
C.1.2	Heterodyne measurements and photocurrent PSD	124
C.2	Laser noise	125
C.2.1	Definitions	125
C.2.2	Quadratic detection	126
C.2.3	Direct detection of a noisy laser	127
C.2.4	Effects of linear transformations	127
C.2.5	Power dependence	128
C.2.6	Delay line phase noise measurement	129
C.2.7	Cavity reflection	130
C.3	Phase modulation	130
C.3.1	General representation	131
C.3.2	Heterodyne detection	131
C.3.3	Non-linearity effects	134
C.3.4	IQ optical modulation	138
<b>D</b>	<b>Measurement setup details</b>	<b>141</b>
D.1	Tunable filter cavity setup	141
D.1.1	Setup schematic	141
D.1.2	Error signal	141
D.2	Locking and IQ modulator details	143
D.2.1	Obtaining error signal	143
D.2.2	Adjusting laser frequency	144
D.2.3	Calibrating and stabilizing IQM control voltages	145
D.3	Image rejection mixer circuit	146
D.4	Laser noise measurements	147
D.4.1	Direct detection	148
D.4.2	Phase noise measurements	149
D.5	EDFA noise calibration	151
D.6	VNA loop gain calibration	154
D.7	Phase modulator $V_\pi$ calibration	155
D.7.1	Optical spectroscopy approach	155
D.7.2	Carrier depletion approach	157
D.8	Incident and reflected power calibration	158

D.9 Sideband correlator angle calibration . . . . .	158
D.10 Additional calibrations . . . . .	162

<b>Bibliography</b>	<b>167</b>
---------------------	------------

# Acknowledgements

First and foremost, I would like to thank my advisor Jack Harris for all the mentoring and guidance he provided. I was very lucky to get into his group, where he assembled many interesting, friendly and knowledgeable people. I am grateful to him for good advice he gave me about designing and performing experiments, understanding their results, and learning how to present them. His office door was always open to discuss any problem, big or small, and he always took our concerns to heart and put an effort to help us with them.

The most indispensable person on the helium optomechanics project was, undoubtedly, Anna Kashkanova. She has been working on it from the day one, long before I joined, and has been the main driving force moving the project forward. It is really thanks to her that we were able to do any of the experiments described in this work.

Nathan Flowers-Jacobs is the postdoc with whom I worked during the first three years in the lab. He was the person who had the strongest influence on my understanding of physics and experiment design. Without his guidance and the effort that he put into earlier generations of the experiment, this work would not have been possible. I would also like to acknowledge Scott Hoch, who spent a lot of time working with me and teaching me about the membrane experiment. Besides, he's just a really fun person to talk to, and he made the first couple of years of my PhD much more enjoyable.

I would like to extend my gratitude to the people without whose assistance the experiment could not have been done: Vincent Bernardo and all of the Yale machine shop for the help with the device design and for its manufacturing; Sandy Tranquilli and Daphne Klemme for their administrative support; Dave DeMille, Hong Tang, Dan Prober and Rob Schoelkopf for letting us borrow their equipment; Jakob Reichel, Sebastien Garcia, Konstantin Ott, and Leander Hohmann for manufacturing the fiber mirrors. I would also like to thank my committee members: Michel Devoret, Steve Girvin, and R. Shankar, for reading my thesis and giving me many useful comments.

Another person who made a great contribution to the helium project is Lilian Childress. Even though I didn't get to work with her directly, I am thankful to her laying down the theoretical and practical foundations of the experiment. I also want to mention Charles Brown, whose assistance in running the experiment and taking data was very helpful at the later stages of the project. Finally, I want to wish the best of luck to Lucy Yu and Sean Frazier, the graduate students who are continuing and expanding our work.

Throughout my PhD there were many great people in lab who created a nice, positive and friendly atmosphere. Thank you Dave, Anthony, Glen, Donghun, Woody, Dustin, Ivana, Kale, and many others for your help and support, and for many relevant and irrelevant discussions during lunch or coffee time. And, of course, I'd like to thank my non-lab-related friends: Ryan, Hannah, Evan, Corey, Shannon, Jed. Hanging out with you really has brightened up my time in New Haven.

In conclusion, I want to thank my family. My parents, who, although unhappy about my decision to study far from home, were always supportive and understanding. And my wife, Anya, who's always been encouraging me during the doubtful times when nothing seemed to work; I'm really happy to have met you and to have you in my life!

# List of Figures

2.1	Example of an optical cavity response . . . . .	6
2.2	Schematic representation of the canonical optomechanical system . . . . .	7
2.3	Schematic of optical tones in the sideband cooling experiment . . . . .	16
2.4	Examples of an OMIT/A response . . . . .	23
4.1	Schematic of the superfluid helium filled device . . . . .	32
4.2	Schematic of optical and acoustic modes inside the cavity . . . . .	41
4.3	Normalized overlap integral as a function of the mirror reflection phase $\phi$ . . . . .	42
5.1	Detailed schematic of the first generation superfluid helium device . . . . .	43
5.2	Schematic of the measurement setup . . . . .	45
6.1	Frequency and linewidth comparison between an empty and a filled cavity . . . . .	51
6.2	OMIA tone schematic and a sweep example . . . . .	52
6.3	Optical and mechanical resonance frequencies over several FSR . . . . .	53
6.4	OMIA response dependence on the control beam power and detuning . . . . .	56
6.5	Calculated values of $g^{(0)}$ as a function of the reflection phase $\phi$ . . . . .	58
6.6	Mechanical quality factor $Q_m$ as a function of the mixing chamber temperature and the circulating laser power . . . . .	59
6.7	Thermal model of the device . . . . .	60
6.8	Mechanical quality factor $Q_m$ as a function of the calculated device temperature . . . . .	64
6.9	Amplitude and phase of the mechanical linewidth response as a function of the intracavity power modulation frequency . . . . .	65
6.10	Cooperativity and thermal cooperativity of the first generation device . . . . .	67
7.1	Schematic of the optical tones for different undriven motion measurements . . . . .	69
7.2	Illustration of mechanical sideband PSDs and cross-correlator . . . . .	76
8.1	Detailed schematic of the second generation superfluid helium device . . . . .	82
8.2	Comparison of mechanical linewidths between the two device generations . . . . .	83
8.3	Frequency comparison between optical resonances in an empty and a filled cavity, and between mechanical and optical resonances in the filled cavity . . . . .	84
8.4	Dynamical backaction measurement results . . . . .	85
8.5	Example of a PSD of an undriven motional sideband . . . . .	86
8.6	Thermal phonon occupation of the mechanical bath vs. MC temperature and calculated device temperature . . . . .	91
8.7	Change in the mechanical frequency and linewidth as a function of the circulating photon number and the MC temperature . . . . .	92
8.8	Example of the measured motional sideband PSDs and their cross-correlator . . . . .	93
8.9	Experimental quantum signatures for different device temperatures . . . . .	94
9.1	Experimental dependence of the MC temperature on the total incident optical power . . . . .	96

9.2	Cooperativity and thermal cooperativity of the second generation device . . . . .	97
9.3	Cooperativity and thermal cooperativity of the second generation device, including potential improvements . . . . .	98
B.1	Schematic of the transfer matrix description of wave propagation and material boundary . . . . .	111
B.2	Schematic of a distributed Bragg reflector (DBR) . . . . .	116
B.3	Schematic an acoustic wave interacting with a movable boundary . . . . .	122
C.1	Setup schematic and tone schematic for a heterodyne measurement using a phase modulator . . . . .	132
C.2	Comparison of detected beatnotes between the phase modulation and the single-sideband modulation . . . . .	133
C.3	Schematic of a DP-MZM . . . . .	139
D.1	Schematic of the TFCS . . . . .	142
D.2	Example of an error signal for the TFCS . . . . .	143
D.3	Example of an error signal in the experimental cavity lock setup . . . . .	144
D.4	Typical TFPC sweeps for the DP-MZM output . . . . .	145
D.5	Schematic of the IQM control voltage stabilization setup . . . . .	146
D.6	Schematics of MW SSB mixer circuits . . . . .	147
D.7	Result of the MW SSB mixer circuit characterization . . . . .	148
D.8	Schematics of the laser noise measurement setups . . . . .	148
D.9	Typical time dependence of the DC photodetector signal in the delay line laser noise measurement	150
D.10	Typical PSD of the photodetector signal in the delay line laser noise measurement . . . . .	151
D.11	Schematic of the EDFA calibration setup . . . . .	152
D.12	Results of the EDFA noise figure calibrations . . . . .	153
D.13	Results of the VNA loop gain calibration . . . . .	154
D.14	Results of the $V_\pi$ calibration using the optical spectroscopy approach . . . . .	156
D.15	Results of the $V_\pi$ calibration using the carrier depletion approach . . . . .	157
D.16	Schematic of the power calibration part of the setup . . . . .	158
D.17	Optical tone configuration for simultaneous measurements of both mechanical sidebands . . . . .	161

# List of Tables

- 8.1 Parameter comparison between the first and the second generation devices . . . . . 84
- 9.1 List of optical components in the main setup schematic and the filter cavity subsystem . . . . . 164
- 9.2 List of electronic components in the main setup schematic and the filter cavity subsystem . . . . . 165
- 9.3 List of electronic components in the mixer circuit and the IQM stabilization circuit . . . . . 166

# List of Symbols

Symbol	Meaning	Units
$\hat{a}$	Optical mode amplitude	1
$\bar{a}$	Steady state amplitude of the optical mode	1
$\hat{a}_{\text{in},i}$ $\hat{a}_{\text{out},i}$	Input / output optical field at a port $i$	$\text{s}^{-1/2}$
$a_{\text{in},i}^{(\text{dr})}$	Classical drive at a port $i$	$\text{s}^{-1/2}$
$\hat{a}_{\text{det}}$	Optical field incident on the photodetector	$\text{s}^{-1/2}$
$a_{\text{d}}$	Amplitude of the classical external optical drive	$\text{s}^{-1/2}$
$a_{\text{in}}$	Classical external optical drive	$\text{s}^{-1/2}$
$a_{\text{in},\ell}$ $a_{\text{in},\text{u}}$	Amplitude of the lower / upper control beam	$\text{s}^{-1/2}$
$\bar{a}_{\ell}$ $\bar{a}_{\text{u}}$	Steady state amplitude of the lower / upper control beam in the optical mode	1
$a_{\text{L}}$	Light wave amplitude (usually incident on a modulator)	$\text{s}^{-1/2}$
$a_{\text{L},0}$	Carrier amplitude	$\text{s}^{-1/2}$
$a_{\text{L},1}$	Sideband amplitude	$\text{s}^{-1/2}$
$a_{\text{OLO}}$	OLO amplitude	$\text{s}^{-1/2}$
$\bar{a}_{\text{out}}$	Steady state amplitude at the optical output	$\text{s}^{-1/2}$
$a_{\text{p}}$	Probe beam amplitude	$\text{s}^{-1/2}$
$\hat{a}_{\text{sig}}$	Optical field containing signal (not OLO)	$\text{s}^{-1/2}$
$\hat{b}$	Mechanical mode amplitude	1

$\bar{b}$	Steady state amplitude of the mechanical mode	1
$\mathbf{B}$	Magnetic B-field	T
$c$	Speed of light	m/s
$\hat{c}$	Fluctuations around the steady state of the mechanical mode	1
$c_{\text{He}}$	Speed of sound in superfluid helium	m/s
$C_{\hat{a},\hat{b}}(t, \tau)$	Correlator of arbitrary operators $\hat{a}$ and $\hat{b}$	$[\hat{a} \cdot \hat{b}]$
$C_{ii}(\tau)$	Photocurrent autocorrelator	A <sup>2</sup>
$C_{xx}(\tau)$ $C_{yy}(\tau)$	Autocorrelator of the classical amplitude / phase noise	1
$C_{xy}(\tau)$	Cross-correlator between the classical amplitude and phase noises	1
$\mathcal{C}$	Optomechanical cooperativity	1
$\mathcal{C}_{\text{th}}$	Optomechanical thermal cooperativity	1
$\hat{d}$	Fluctuations around the steady state of the optical mode	1
$\hat{d}_{\text{out}}$	Fluctuations around the steady state at the optical output	s <sup>-1/2</sup>
$\hat{d}_{\text{pt}}$	Contribution to optical mode fluctuations due to the photothermal loss channel noise	1
$\hat{d}_{\hat{z}}$	Contribution to optical mode fluctuations due to the mechanical motion	1
$\hat{d}_{\hat{\xi}}$	Contribution to optical mode fluctuations due to the vacuum noise	1
$\mathbf{D}$	Electric displacement field	C/m <sup>2</sup>
$e$	Electron's charge	C
$\mathbf{E}$	Electric field	V/m
$E_{\rightarrow}^{(i)}$ $E_{\leftarrow}^{(i)}$	Electric field in forward / backward propagation direction at a location $i$ ( $\ell$ for left, $r$ for right)	V/m
$E_{\text{He}}$	Young modulus of superfluid helium	Pa
$f_{\text{m}}^{(\text{rb})}$	Magnitude of the imaginary part of the mechanical sidebands cross-correlator normalized in phonons	1
$F$	Free spectral range	Hz

$F_{\text{eff}}$	Effective free spectral range	Hz
$F_{\text{eff}}^{(\text{ac})}$	Effective acoustic free spectral range	Hz
$F_{\text{eff}}^{(\text{opt})}$	Effective optical free spectral range	Hz
$\mathcal{F}$	Finesse	1
$\mathcal{F}_{\text{ac}}$	Acoustic finesse	1
$\hat{F}_{\text{RP}}$	Normalized radiation pressure force	$\text{s}^{-1}$
$\hat{F}_{\text{RPSN}}$	Normalized radiation pressure force noise	$\text{s}^{-1}$
$\hat{F}_{\text{OFSN}}$	Normalized optical force noise	$\text{s}^{-1}$
$\hat{F}_{\text{pt}}$	Normalized photothermal force	$\text{s}^{-1}$
$\hat{F}_{\text{th}}$	Normalized mechanical thermal force	$\text{s}^{-1}$
$g^{(0)}$	Single-photon optomechanical coupling rate	$\text{s}^{-1}$
$g_{\text{pt}}^{(0)}$	Single-photon photothermal optomechanical coupling rate	$\text{s}^{-1}$
$G$	Photodetector electron gain	C
$G_{\text{I}}$	Photodetector transimpedance amplifier voltage gain	V/A
$G_{\text{P}}$	Total photodetector voltage gain	V/W
$\hbar$	Reduced Plank's constant	J · s
$\mathbf{H}$	Magnetic H-field	A/m
$\hat{\mathcal{H}}_{\text{c}}$	Optical cavity Hamiltonian	J
$\hat{\mathcal{H}}_{\text{m}}$	Mechanical oscillator Hamiltonian	J
$\hat{\mathcal{H}}_{\text{om}}$	Optomechanical Hamiltonian	J
$i(t)$	Photocurrent	A
$i_{\text{r}} \quad i_{\text{b}}$	Photocurrent contributions from the red / blue mechanical sideband	A
$\hat{I}_{\text{out,pt}}$	Optical intensity dissipated into the photothermal loss channel	$\text{s}^{-1}$

$J_n(x)$	Bessel function of $n$ th order	1
$k_B$	Boltzmann's constant	J/K
$K_{\text{cav}}[\omega]$	Normalized cavity reflection transfer function	1
$L$	Optical cavity length	m
$L_{\text{eff}}^{(\text{ac})}$	Effective acoustic cavity length	m
$L_{\text{eff}}^{(\text{opt})}$	Effective optical cavity length	m
$\delta L$	Optical mirror penetration depth	m
$M$	Transfer matrix	1
$M^{(\text{b})}$	Material boundary transfer matrix	1
$M^{(\text{dl})}$	Dielectric thin layer transfer matrix	1
$M^{(\text{ds})}$	Dielectric slab transfer matrix	1
$M^{(\text{p})}$	Propagation transfer matrix	1
$\bar{n}_c$	Average intracavity photon number	1
$n_m^{(\text{rr})}$ $n_m^{(\text{bb})}$	Magnitude of red / blue mechanical sideband normalized in phonons	1
$n_m^{(\text{rb})}$	Magnitude of the real part of the mechanical sidebands cross-correlator normalized in phonons	1
$n_{\text{OFSN}}$	Effective bosonic occupation of the OFSN bath	1
$n_{\text{RPSN}}$	Effective bosonic occupation of the RPSN bath	1
$n_{\text{th}}(T, \omega)$	Thermal bosonic occupation corresponding to temperature $T$ and mode frequency $\omega$	1
$n_{\text{th,m}}$	Thermal bosonic occupation of the mechanical bath	1
$n_{\text{He}}^{(\text{r})}$	Refractive index of superfluid helium	1
$n_{\text{SiO}_2}^{(\text{r})}$ $n_{\text{Ta}_2\text{O}_5}^{(\text{r})}$	Refractive indices of $\text{SiO}_2$ and $\text{Ta}_2\text{O}_5$	1
$n_{\lambda/2}^{(\text{ac})}$	Number of half-wavelengths of acoustic mode inside a cavity	1
$n_{\lambda/2}^{(\text{opt})}$	Number of half-wavelengths of optical mode inside a cavity	1

$\Delta n_{\lambda/2}$	Wavelength mismatch between the acoustic and the optical mode	1
$p$	Local mechanical pressure	Pa
$P_{\text{con}}$	Control beam power	W
$P_{\text{d}}$	Optical drive power	W
$P_{\text{inc}}$	Incident optical power	W
$P_{\text{OLO}}$	OLO power	W
$P_{\text{refl}}$	Reflected optical power	W
$P_{\text{tot}}$	Total optical power incident on the photodetector	W
$Q_{\text{m}}$	Mechanical quality factor	1
$Q_{\text{m,eff}}$	Modified mechanical quality factor	1
$Q_{\text{m,int}}$	Internal mechanical quality factor	1
$Q_{\text{m,rad}}$	Radiative mechanical quality factor	1
$S_{\hat{a},\hat{b}}[\omega]$	Frequency-domain correlator of arbitrary operators $\hat{a}$ and $\hat{b}$	$[\hat{a} \cdot \hat{b}] / \text{Hz}$
$S_{\hat{a}^\dagger,\hat{a}}[\omega]$	PSD of an arbitrary operators $\hat{a}$	$[\hat{a}]^2 / \text{Hz}$
$S_{ii}[\omega]$	Photocurrent PSD	$\text{A}^2 / \text{Hz}$
$S_{ii}^{(\ell\ell)}[\omega]$	Measured photocurrent PSD of the lower / upper control beam sideband	$\text{A}^2 / \text{Hz}$
$S_{ii}^{(\text{uu})}[\omega]$		
$S_{ii}^{(\text{u}\ell)}[\omega]$	Measured cross-correlator between the lower and the upper control beam sidebands	$\text{A}^2 / \text{Hz}$
$S_{ii}^{(\text{rr})}[\omega]$	Photocurrent PSD of the red / blue sideband	$\text{A}^2 / \text{Hz}$
$S_{ii}^{(\text{bb})}[\omega]$		
$S_{ii}^{(\text{rb})}[\omega]$	Photocurrent cross-correlator between the red and the blue sideband	$\text{A}^2 / \text{Hz}$
$S_{\hat{F}^\dagger,\hat{F}}^{\text{OFSN}}[\omega]$	PSDs of the OFSN force	$\text{s}^{-1}$
$S_{\hat{F},\hat{F}^\dagger}^{\text{OFSN}}[\omega]$		
$S_{\hat{F},\hat{F}}^{\text{RPSN}}[\omega]$	PSD of the RPSN force	$\text{s}^{-1}$
$S_{\hat{F},\hat{F}^\dagger}^{\text{th}}[\omega]$	PSDs of the mechanical thermal force	$\text{s}^{-1}$
$S_{\hat{F}^\dagger,\hat{F}}^{\text{th}}[\omega]$		
$S_{\text{xx}}[\omega]$	PSD of the classical amplitude / phase noise	$\text{Hz}^{-1}$
$S_{\text{yy}}[\omega]$		

$S_{xy}[\omega]$	Frequency-domain correlator between the classical amplitude and phase noises	$\text{Hz}^{-1}$
$T_i$	Temperature of a bath at a port $i$	K
$T_{\text{cav}}$	Cavity temperature	K
$T_{\text{MC}}$	Mixing chamber temperature	K
$\mathbf{v}$	Local mechanical velocity	m/s
$V_{\text{mode}}$	Optical mode volume	$\text{m}^3$
$V_{\pi}$	$\pi$ -voltage of a phase modulator	V
$w_0$	Mode waist	m
$\hat{x}$	Displacement of the mechanical mode	m
$x^{\text{ZPF}}$	Amplitude of zero-point fluctuations of the mechanical mode	m
$\hat{z}$	Normalized displacement of the mechanical mode	1
$z_{\text{R}}$	Mode Rayleigh range	m
$\delta\hat{z}$	Fluctuation of the normalized displacement of the mechanical mode	1
$\mathcal{Z}$	Impedance (optical or acoustic)	$\Omega$ or $\frac{\text{kg}}{\text{m}^2 \cdot \text{s}}$
$\mathcal{Z}^{(\text{rel})}$	Relative impedance (optical or acoustic)	1
$\alpha_{\ell}, \alpha_{\text{u}}$	Normalized $\phi_{\text{mode}}$ drive amplitude corresponding to the lower / upper control beam	1
$\alpha_{\text{cal}}$	Normalized $\phi_{\text{mode}}$ drive amplitude corresponding to the calibration beam	$\text{s}^{-1}$
$\gamma_{\text{m}}$	Mechanical mode linewidth	$\text{s}^{-1}$
$\gamma_{\text{m,eff}}$	Modified mechanical mode linewidth	$\text{s}^{-1}$
$\delta\gamma_{\text{m,eff}}$	Mechanical mode linewidth modification (optomechanical damping)	$\text{s}^{-1}$
$\Gamma_{\text{meas}}$	Mechanical displacement measurement rate	$\text{s}^{-1}$
$\Gamma_{\text{meas},\ell}$ $\Gamma_{\text{meas},\text{u}}$	Mechanical displacement measurement rate of the lower / upper control beam	$\text{s}^{-1}$
$\delta(x)$	Dirac $\delta$ -function	$[x]^{-1}$

$\delta_{i,j}$	Kronecker $\delta$ -symbol	1
$\Delta$	Classical external drive detuning	$s^{-1}$
$\Delta_0$	Classical external drive detuning from the “bare” optical resonance frequency	$s^{-1}$
$\Delta_{\text{con}}$	Control beam detuning	$s^{-1}$
$\Delta_\ell$ $\Delta_u$	Lower / upper control beam detuning	$s^{-1}$
$\Delta_{\text{lock}}$	Lock beam detuning	$s^{-1}$
$\epsilon$	Permittivity	F/m
$\epsilon_0$	Vacuum permittivity	F/m
$\epsilon^{(r)}$	Relative permittivity	1
$\zeta$	Classical laser noise	1
$\zeta_x$ $\zeta_y$	Amplitude / phase quadrature of the classical laser noise	1
$\hat{\eta}$	Mechanical bath fluctuations	$s^{-1/2}$
$\eta_\ell$	Measurement efficiency contribution due to optical losses	1
$\eta_n$	Measurement efficiency contribution due to added optical noise	1
$\eta_r$	Measurement efficiency contribution due to residual sources	1
$\eta_t$	Total measurement quantum efficiency	1
$\eta_\kappa$	Measurement efficiency contribution due to imperfect external coupling of the optical cavity	1
$\lambda_0$	“Bare” optical cavity resonance wavelength	m
$\lambda_{\text{ac}}$	Acoustic wavelength	m
$\lambda_{\text{opt}}$	Optical wavelength	m
$\mu$	Permeability	H/m
$\mu_0$	Vacuum permeability	H/m
$\kappa$	Optical mode linewidth	$s^{-1}$

$\kappa_i$	Coupling rate at a port $i$	$\text{s}^{-1}$
$\kappa_{\text{int}}$ $\kappa_{\text{ext}}$	Internal and external loss rate of the optical mode	$\text{s}^{-1}$
$\kappa_{\text{pt}}$	Photothermal force channel loss rate	$\text{s}^{-1}$
$\nu_c$	Cavity frequency in MW domain (OLO-cavity detuning)	$\text{s}^{-1}$
$\nu_{\text{con}}$	Control MW tone frequency	$\text{s}^{-1}$
$\nu_{\text{con},\ell}$ $\nu_{\text{con},\text{u}}$	Lower / upper control MW tone frequency	$\text{s}^{-1}$
$\nu_{\text{lock}}$	Lock MW tone frequency	$\text{s}^{-1}$
$\nu_{\text{p}}$	Probe MW tone frequency	$\text{s}^{-1}$
$\hat{\xi}$	Total input vacuum noise	$\text{s}^{-1/2}$
$\hat{\xi}_i$	Input vacuum noise at a port $i$	$\text{s}^{-1/2}$
$\hat{\xi}_{\text{int}}$ $\hat{\xi}_{\text{ext}}$	Input vacuum noises for the internal / external loss channel	$\text{s}^{-1/2}$
$\hat{\xi}_{\text{pt}}$	Input vacuum noises for the photothermal loss channel	$\text{s}^{-1/2}$
$\rho$	Local mechanical density	$\text{kg}/\text{m}^3$
$\delta\rho$	Small fluctuations of local mechanical density	$\text{kg}/\text{m}^3$
$\rho_{\text{He}}$	Density of superfluid helium	$\text{kg}/\text{m}^3$
$\sigma$	Photodetector quantum efficiency	1
$\Sigma[\omega]$	Mechanical self-energy	$\text{s}^{-1}$
$\tau_{\text{d}}$	Time delay of a delay line	s
$\tau_{\text{pt}}$	Photothermal relaxation time	s
$\delta\phi$	Phase difference	rad
$\phi_v$	Velocity potential	$\text{m}^2/\text{s}$
$\Phi$	Heat load	W
$\chi_c[\omega]$	Cavity susceptibility	s

$\chi_{c,\text{rel}}[\omega]$	Normalized optical cavity susceptibility	1
$\chi_{\text{m}}[\omega]$	Mechanical susceptibility	s
$\chi_{\text{m,eff}}[\omega]$	Modified mechanical susceptibility	s
$\psi_{\text{G}}$	Gouy phase shift	rad
$\omega_{\text{c}}$	Optical cavity resonance frequency	$\text{s}^{-1}$
$\omega_{\text{c0}}$	“Bare” optical cavity resonance frequency	$\text{s}^{-1}$
$\omega_{\text{d}}$	Optical drive frequency	$\text{s}^{-1}$
$\omega_{\text{OLO}}$	OLO frequency	$\text{s}^{-1}$
$\omega_{\text{L}}$	Carrier frequency	$\text{s}^{-1}$
$\omega_{\text{m}}$	Mechanical resonance frequency	$\text{s}^{-1}$
$\omega_{\text{m,eff}}$	Modified mechanical resonance frequency	$\text{s}^{-1}$
$\delta\omega_{\text{m,eff}}$	Mechanical resonance frequency modification (optical spring)	$\text{s}^{-1}$
$\omega_{\text{r}} \quad \omega_{\text{b}}$	Frequency of the red / blue mechanical sideband	$\text{s}^{-1}$
$\Omega_{\text{p}}$	Detuning of the probe beam from the control beam	$\text{s}^{-1}$

# List of Acronyms

<b>Acronym</b>	<b>Meaning</b>
AM	Amplitude Modulator
ASE	Amplified Spontaneous Emission
AWG	Arbitrary Waveform Generator
BBS	Backward Brillouin Scattering
BN	Beatnote
DBR	Distributed Bragg Reflector
DP-MZM	Dual-Parallel Mach-Zehnder Modulator
EDFA	Erbium-Doped Fiber Amplifier
FFT	Fast Fourier Transform
FPGA	Field-Programmable Gate Array
FSR	Free Spectral Range
ID	Inner Diameter
IF	Intermediate Frequency
IQM	IQ Modulator
LFGL	Low Frequency Gain Limit
MC	Mixing Chamber
MIM	Membrane-in-the-middle
MW	Microwave
MWLO	Microwave Local Oscillator
MWPD	Microwave Power Detector
MWSW	Microwave Switch
NF	Noise Figure
OD	Outer Diameter
OFSN	Optical Force Shot Noise
OLO	Optical Local Oscillator
OMIT/A	Optomechanically Induced Transparency/Amplification
OSW	Optical Switch
PD	Photodetector
PDH	Pound-Drever-Hall
PI	Proportional-Integral
PM	Power Meter
PSD	Power Spectral Density

QND	Quantum Non-Demolition
RF	Radio Frequency
ROC	Radius Of Curvature
RPSN	Radiation Pressure Shot Noise
SA	Spectrum Analyzer
SBS	Stimulated Brillouin Scattering
SNR	Signal-to-Noise Ratio
SSB	Single Sideband
SSB-SC	Single Sideband Suppressed Carrier
TF	Tunable Filter
TFCS	Tunable Filter Cavity Setup
TFPC	Tunable Fabry-Perot Cavity
TL	Tunable Laser
VCO	Voltage Controller Oscillator
VDL	Variable Delay Line
VMWA	Variable Microwave Attenuator
VNA	Vector Network Analyzer
VOA	Variable Optical Attenuator
WGM	Whispering Gallery Mode
ZILI	Zurich Instrument Lock-In amplifier
ZPF	Zero-Point Fluctuations
$\phi$ M	Phase Modulator

# Chapter 1

## Introduction

As is evident from its name, optomechanics deals with coupling between optical (or, more generally, electromagnetic) and mechanical (i.e., associated with macroscopic motion) degrees of freedom. Taken at its face value, this is a very broad definition, as it includes any experiment in which light reflects off a potentially moving surface: interferometry, microscopy, or even just observing an indicator needle. This is why the term “optomechanics” is oftentimes restricted to the kind of experiments and systems where this interaction is *bidirectional*. Just as the mechanical position affects light (e.g., by changing its direction or phase), so does the light act on the mechanical object by exerting a force. In practice, such force can manifest in many ways: radiation pressure (which is the colloquial general name for this kind of force), electrostriction, optical tweezing (dipole forces), or just static Coulomb force. All these forces share the same important characteristics: they are unitary, in the sense that they arise from the same part of the Hamiltonian that describes the influence of the mechanical position on light (often referred to as the optomechanical interaction term). This means that the system evolution induced by these forces is, in principle, reversible and information-conserving. In contrast, another class of radiation-induced forces, so-called “photothermal” forces (which include temperature-related effects, such as thermal expansion or temperature-dependent refractive index), are inherently associated with some optical absorption and heating. Hence, these forces lead to loss of quantum coherence, and are less suitable for quantum operations.

There are many different reasons to be interested in optomechanics. The one that I will focus on most in this work involves quantum applications of optomechanics, where one can use light to manipulate or measure a state of a mechanical object with single-quantum precision. This ability gives rise to several important applications: transferring a quantum state between different systems by using the mechanical object as a bus; manipulating properties of light through its interaction with the mechanical object (e.g., generating optical quadrature squeezing); or creating non-classical mechanical states, which can be used, e.g., for testing different decoherence mechanisms (such as the ones arising from the gravitational interaction of mechanical objects).

Our system of choice for studying quantum optomechanics is superfluid helium, which for us has several attractive properties (low optical absorption, low temperature, low mechanical loss). The experimental efforts in this direction started in the Harris Lab about six years ago, and for the last 3.5 years I have been a part of this project. In that time, we have built two generations of superfluid helium optomechanics devices, performed some standard and less standard optomechanics experiments, and learned a great deal about the applicability and limitations of superfluid helium as an optomechanics medium. This thesis is my attempt to document these endeavors.

The thesis proceeds as follows:

- In Chapter 2 I describe the canonical optomechanical system and derive several standard optomechanics effects such as position detection, dynamical backaction and driven response measurements. This chapter mostly serves to establish the notation and to give an introduction to basic concepts, which are used and expanded upon in later chapters.
- Chapter 3 gives a brief overview of the field of optomechanics by describing the most common implementations of optomechanical systems and recapping recent achievements in quantum optomechanics.

It also introduces the thermal cooperativity, which is an important figure of merit in linear quantum optomechanics.

- Chapter 4 gives a description of superfluid helium, particularly in its relation to optomechanics. In this chapter I also provide expressions for some of its relevant properties, such as acoustic loss and optomechanical coupling.
- Next, in Chapter 5 I present our experimental schematic, including both the experimental device and the measurement setup.
- Chapter 6 shows the experimental results obtained with the first-generation experimental device, and describes limitations of its design.
- In Chapter 7 I take a brief intermission to give a theoretical description and an interpretation for the main measurements of this thesis: mechanical sideband asymmetry and the sideband cross-correlator.
- After that, in Chapter 8 I describe the improved version of the experimental device, and demonstrate the new measurements that we were able to perform with it: the dynamical backaction, and the undriven motion measurements (which is the focus of Chapter 7).
- Finally, in Chapter 9 I conclude by assessing the device performance and outlining some possible future improvements of this device and general potential directions in the superfluid helium optomechanics.

# Chapter 2

## Canonical optomechanical system

In this Chapter I will consider the theoretical description of a generic optomechanical system and derive several standard optomechanics effects. I will start by describing a single optical mode in input-output formalism (section 2.1). Then I will present the canonical optomechanical system and the optomechanical Hamiltonian arising from it (section 2.2). Using this Hamiltonian I will derive the Langevin-Heisenberg equations of motion (section 2.3), which are the starting point for describing many optomechanical experiments, including the ones described in later chapters. Finally, I will use this description to derive several standard effects in optomechanics theory including position detection (section 2.4), dynamical backaction (section 2.5), mechanical fluctuations and radiation pressure shot noise (section 2.6), and measurements of the driven mechanical response using the optomechanically induced transparency and amplification (OMIT/A) approach (section 2.7). These and many other effects are also described in a recent review [1].

### 2.1 Single optical mode

To introduce input-output theory, we start by considering a single optical mode without any mechanical elements. We derive a general form of Langevin-Heisenberg equation of motion for the mode's amplitude, and then solve this equation under the assumption of a single-tone external drive.

#### 2.1.1 Closed system

In order to establish notation, let us first consider a single optical mode with a frequency  $\omega_c$ . The Hamiltonian describing the internal dynamics of such system is that of a simple harmonic oscillator

$$\hat{\mathcal{H}}_c = \hbar\omega_c \left( \hat{a}^\dagger \hat{a} + \frac{1}{2} \right), \quad (2.1)$$

where  $\hat{a}$  is the annihilation operator of the mode, which obeys the standard bosonic commutation relation  $[\hat{a}, \hat{a}^\dagger] = 1$ . Using this Hamiltonian, we can derive the Heisenberg equation of motion for the time-dependent operator  $\hat{a}$ :

$$\dot{\hat{a}} = -\frac{i}{\hbar} [\hat{a}, \hat{\mathcal{H}}_c] = -i\omega_c \hat{a}. \quad (2.2)$$

#### 2.1.2 Open system

In order to describe damping as well as the outgoing fields, we are going to employ input-output theory[2]. It assumes a weak coupling of the system to a set of continuum Markovian baths through several ports. Each port  $i$  is described by its coupling rate  $\kappa_i$ , its input field  $\hat{a}_{\text{in},i}(t)$  and the corresponding output field  $\hat{a}_{\text{out},i}(t)$ . The input field determines the force exerted by the bath on the optical mode, while the output field describes how

the information about the optical mode leaks back into the bath. The input and output fields corresponding to the same port obey the commutation relations

$$\left[ \hat{a}_{\text{in},i}(t), \hat{a}_{\text{in},i}^\dagger(t') \right] = \left[ \hat{a}_{\text{out},i}(t), \hat{a}_{\text{out},i}^\dagger(t') \right] = \delta(t - t') \quad (2.3)$$

$$\left[ \hat{a}_{\text{in},i}(t), \hat{a}_{\text{in},i}(t') \right] = \left[ \hat{a}_{\text{out},i}(t), \hat{a}_{\text{out},i}(t') \right] = 0. \quad (2.4)$$

In addition, we assume that the baths coupled to different ports are completely independent, so the operators corresponding to different baths commute with each other:

$$\begin{aligned} \left[ \hat{a}_{\text{in},i}(t), \hat{a}_{\text{in},j}^\dagger(t') \right] &= \left[ \hat{a}_{\text{out},i}(t), \hat{a}_{\text{out},j}^\dagger(t') \right] \\ &= \left[ \hat{a}_{\text{in},i}(t), \hat{a}_{\text{in},i}(t') \right] = \left[ \hat{a}_{\text{out},i}(t), \hat{a}_{\text{out},i}(t') \right] = 0, \quad i \neq j. \end{aligned} \quad (2.5)$$

Coupling to these baths leads to two effects: it adds random forces (one per port) acting on the optical mode, and it induces damping (caused by the energy of the system leaking into the environment through the same ports). With that, the Heisenberg equation of motion (2.2) turns into a Langevin-Heisenberg equation

$$\dot{\hat{a}} = -\frac{i}{\hbar} \left[ \hat{a}, \hat{\mathcal{H}}_c \right] - \frac{\kappa}{2} \hat{a} + \sum_i \sqrt{\kappa_i} \hat{a}_{\text{in},i}, \quad (2.6)$$

where  $\kappa = \sum_i \kappa_i$  is the total damping of the optical mode. Substituting Hamiltonian (2.1) yields the equation

$$\dot{\hat{a}} = -\left( \frac{\kappa}{2} + i\omega_c \right) \hat{a} + \sum_i \sqrt{\kappa_i} \hat{a}_{\text{in},i}. \quad (2.7)$$

Finally, input-output theory provides an expression for the outgoing fields, which is a combination of the corresponding input fields and the optical mode escaping the cavity:

$$\hat{a}_{\text{out},i}(t) = \hat{a}_{\text{in},i}(t) - \sqrt{\kappa_i} \hat{a}(t). \quad (2.8)$$

### 2.1.3 Input fields statistics

To determine the system dynamics, we need to define the properties of the incoming fields. If there is no external drive (e.g., a laser or a microwave generator), then the incoming field is typically black-body radiation corresponding to the bath temperature  $T_i$ . In the Markovian approximation this leads to the bath operators' correlator

$$\left\langle \left( \hat{a}_{\text{in},i}(t) \right)^\dagger \hat{a}_{\text{in},j}(t') \right\rangle = n_{\text{th}}(T_i, \omega_c) \delta_{i,j} \delta(t - t'), \quad (2.9)$$

where  $n_{\text{th}}$  is the bosonic occupation number defined as

$$n_{\text{th}}(T, \omega) = \frac{1}{e^{\hbar\omega/(k_B T)} - 1}. \quad (2.10)$$

This approximation is valid for a high-Q resonator, where the dependence of  $n_{\text{th}}$  on frequency can be neglected. As far as higher-order correlations are concerned, the input radiation is assumed to be Gaussian and have zero mean ( $\langle \hat{a}_{\text{in},i}(t) \rangle = 0$ ), so all of the correlators can be expressed using Wick's theorem[3].

The optical modes considered in this work lie in the near-infrared (near-IR) part of the spectrum at frequencies of  $\sim 200$  THz. At such frequencies the occupation of a room temperature bath (with a characteristic frequency  $k_B T_{\text{room}}/\hbar \approx 2\pi \cdot 6$  THz) is extremely small, and so can be approximated to be zero. Thus, the external bath can be assumed to be in its ground state, so the incoming radiation will only have vacuum noise,

which we will denote as  $\hat{\xi}_i$  for  $i^{\text{th}}$  port. The statistical properties of this noise can be derived from expressions (2.3)-(2.5) and (2.9):

$$\left[ \hat{\xi}_i(t), \hat{\xi}_j^\dagger(t') \right] = \delta_{i,j} \delta(t-t') \quad (2.11)$$

$$\left\langle \hat{\xi}_i^\dagger(t) \hat{\xi}_j(t') \right\rangle = 0 \quad (2.12)$$

$$\begin{aligned} \left\langle \hat{\xi}_i(t) \hat{\xi}_j^\dagger(t') \right\rangle &= \left\langle \hat{\xi}_i^\dagger(t) \hat{\xi}_j(t') \right\rangle + \left[ \hat{\xi}_i(t), \hat{\xi}_j^\dagger(t') \right] \\ &= \delta_{i,j} \delta(t-t'). \end{aligned} \quad (2.13)$$

If a port is externally driven, then the incoming operator will have an additional part corresponding to the drive:

$$\hat{a}_{\text{in},i}(t) = a_{\text{in},i}^{(\text{dr})}(t) + \hat{\xi}_i. \quad (2.14)$$

Here  $a_{\text{in},i}^{(\text{dr})}(t)$  is the classical drive amplitude normalized by the photon flux, i.e.,  $\left| a_{\text{in},i}^{(\text{dr})}(t) \right|^2$  yields the incoming photon flux. For example, a single-tone drive of power  $P_d$  and frequency  $\omega_d$  will correspond to the amplitude of  $a_{\text{in}}^{(\text{dr})}(t) = \sqrt{\frac{P_d}{\hbar\omega_d}} e^{-i\omega_d t}$ .

### 2.1.4 Solution for a driven damped optical mode

As an instructive example, let us consider an optical mode  $\hat{a}$  with two ports. The first is the so-called ‘‘loss’’ or ‘‘internal’’ port with a coupling rate  $\kappa_{\text{int}}$  and an input  $\hat{a}_{\text{in,int}}$ ; it is not driven externally, so its input is simply a vacuum noise:  $\hat{a}_{\text{in,int}} = \hat{\xi}_{\text{int}}$ . The second port is called ‘‘input’’ or ‘‘external’’, and it has a coupling rate of  $\kappa_{\text{ext}} = \kappa - \kappa_{\text{int}}$  and an input operator  $\hat{a}_{\text{in,ext}}$ . We assume that this port experiences a classical drive  $a_{\text{in}}(t)$ , so its total input is  $\hat{a}_{\text{in,ext}}(t) = a_{\text{in}}(t) + \hat{\xi}_{\text{ext}}(t)$ .

With these two ports the generic equation of motion (2.7) transforms into

$$\dot{\hat{a}} = - \left( \frac{\kappa}{2} + i\omega_c \right) \hat{a} + \sqrt{\kappa_{\text{int}}} \hat{\xi}_{\text{int}} + \sqrt{\kappa_{\text{ext}}} \hat{\xi}_{\text{ext}} + \sqrt{\kappa_{\text{ext}}} a_{\text{in}}. \quad (2.15)$$

Next, to simplify the equation, let us move into a frame rotating at the frequency  $\omega_c$  by making a substitution  $\hat{a} \rightarrow \hat{a} e^{-i\omega_c t}$ . This results in the equation

$$\dot{\hat{a}} = - \frac{\kappa}{2} \hat{a} + \sqrt{\kappa_{\text{int}}} \hat{\xi}_{\text{int}} + \sqrt{\kappa_{\text{ext}}} \hat{\xi}_{\text{ext}} + \sqrt{\kappa_{\text{ext}}} a_{\text{in}} e^{i\omega_c t}. \quad (2.16)$$

To obtain this equation we have also made a transformation  $\hat{\xi}_{\text{int/ext}} \rightarrow \hat{\xi}_{\text{int/ext}} e^{-i\omega_c t}$ . However, this does not change the statistical properties of the noise (as its autocorrelator is non-zero only for zero time difference where the exponent is unity), so we can still treat these operators in the same way as before.

Let us assume that the drive is a single coherent tone with an amplitude  $a_d$  and a frequency  $\omega_d$ :  $a_{\text{in}}(t) = a_d e^{-i\omega_d t}$ . This turns the drive term in the equation of motion into  $\sqrt{\kappa_{\text{ext}}} a_d e^{-i\Delta t}$ , where  $\Delta = \omega_d - \omega_c$  is the drive detuning from the cavity resonance. Since the equation of motion is linear, we can separate the classical (driven) and the quantum (noise) parts of the intracavity field by looking for a solution in the form

$$\hat{a}(t) = \bar{a} e^{-i\Delta t} + \hat{d}(t), \quad (2.17)$$

where  $\bar{a}$  is a steady-state amplitude and  $\hat{d}(t)$  are fluctuations around it. Substituting this ansatz into the equation and separating the steady state and the fluctuation parts leaves us with two equations

$$-i\Delta \bar{a} = -\frac{\kappa}{2} \bar{a} + \sqrt{\kappa_{\text{ext}}} a_d \quad (2.18)$$

$$\dot{\hat{d}} = -\frac{\kappa}{2} \hat{d} + \sqrt{\kappa_{\text{int}}} \hat{\xi}_{\text{int}} + \sqrt{\kappa_{\text{ext}}} \hat{\xi}_{\text{ext}}. \quad (2.19)$$

The first equation results in the steady state amplitude  $\bar{a} = \chi_c[\Delta]\sqrt{\kappa_{\text{ext}}}a_d$ , where the cavity susceptibility  $\chi_c$  is defined as

$$\chi_c[\omega] = \frac{1}{\kappa/2 - i\omega}. \quad (2.20)$$

The magnitude and phase of the susceptibility are illustrated in Figure 2.1.

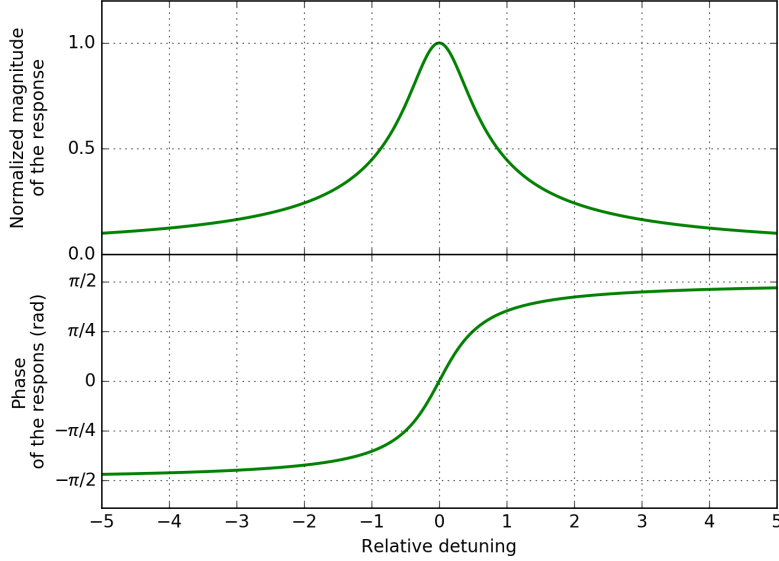


Figure 2.1: Relative magnitude of the cavity response  $|\chi_c[\Delta]/\chi_c[0]|$  (top) and the phase of the response  $\arg(\chi_c[\Delta])$  (bottom) as a function of detuning.

To solve the second equation, we can transform into the Fourier domain (for a discussion of the Fourier transform and its properties, see appendix A.2):

$$-i\omega\hat{d}[\omega] = -\frac{\kappa}{2}\hat{d}[\omega] + \sqrt{\kappa_{\text{int}}}\hat{\xi}_{\text{int}}[\omega] + \sqrt{\kappa_{\text{ext}}}\hat{\xi}_{\text{ext}}[\omega] \quad (2.21)$$

$$\hat{d}[\omega] = \chi_c[\omega] \left( \sqrt{\kappa_{\text{int}}}\hat{\xi}_{\text{int}}[\omega] + \sqrt{\kappa_{\text{ext}}}\hat{\xi}_{\text{ext}}[\omega] \right). \quad (2.22)$$

The statistical properties of the vacuum noise in the Fourier domain follow from its properties in the time domain (2.11)-(2.13) and our definition of the noise Fourier transform described in appendix section A.2:

$$\left[ \hat{\xi}_i[\omega], \hat{\xi}_j^\dagger[-\omega] \right] = \delta_{i,j} \quad (2.23)$$

$$\left\langle \hat{\xi}_i^\dagger[\omega] \hat{\xi}_j[-\omega] \right\rangle = 0 \quad (2.24)$$

$$\left\langle \hat{\xi}_i[\omega] \hat{\xi}_j^\dagger[-\omega] \right\rangle = \delta_{i,j}. \quad (2.25)$$

These lead to the following statistical properties of the intracavity vacuum noise:

$$\left[ \hat{d}[\omega], \hat{d}^\dagger[-\omega] \right] = \frac{\kappa}{(\kappa/2)^2 + \omega^2} \quad (2.26)$$

$$\left\langle \hat{d}^\dagger[\omega] \hat{d}[-\omega] \right\rangle = 0 \quad (2.27)$$

$$\left\langle \hat{d}[\omega] \hat{d}^\dagger[-\omega] \right\rangle = \frac{\kappa}{(\kappa/2)^2 + \omega^2}. \quad (2.28)$$

The equal-time commutator can be calculated (using the Wiener-Khinchin theorem similarly to equation (A.5) in appendix A.1.2) as

$$[\hat{d}(t), \hat{d}^\dagger(t)] = \int_{-\infty}^{+\infty} [\hat{d}[\omega], \hat{d}^\dagger[-\omega]] \frac{d\omega}{2\pi} = \int_{-\infty}^{+\infty} \frac{\kappa}{(\kappa/2)^2 + \omega^2} \frac{d\omega}{2\pi} = 1. \quad (2.29)$$

Thus, the intracavity field obeys the expected bosonic commutator relations (note that from (2.17)  $[\hat{a}, \hat{a}^\dagger] = [\hat{d}, \hat{d}^\dagger]$ , since the rest of  $\hat{a}$  is a classical amplitude).

The output field can be found using relation (2.8) and then decomposing into stationary and fluctuating parts similarly to expression (2.17). In the frame which is still rotating at  $\omega_c$  we can write

$$\hat{a}_{\text{out,ext}}(t) = \bar{a}_{\text{out}} e^{-i\Delta t} + \hat{d}_{\text{out}}(t) \quad (2.30)$$

$$\bar{a}_{\text{out}} = a_{\text{d}} - \sqrt{\kappa_{\text{ext}}} \bar{a} = a_{\text{d}} \left( 1 - \frac{\kappa_{\text{ext}}}{\frac{\kappa}{2} - i\omega} \right) \quad (2.31)$$

$$\begin{aligned} \hat{d}_{\text{out}}[\omega] &= \hat{\xi}_{\text{ext}}[\omega] - \sqrt{\kappa_{\text{ext}}} \hat{d}[\omega] \\ &= \left( 1 - \frac{\kappa_{\text{ext}}}{\frac{\kappa}{2} - i\omega} \right) \hat{\xi}_{\text{ext}}[\omega] - \frac{\sqrt{\kappa_{\text{ext}} \kappa_{\text{int}}}}{\frac{\kappa}{2} - i\omega} \hat{\xi}_{\text{int}}[\omega]. \end{aligned} \quad (2.32)$$

The statistics of the output noise is

$$[\hat{d}_{\text{out}}[\omega], \hat{d}_{\text{out}}^\dagger[-\omega]] = \left| 1 - \frac{\kappa_{\text{ext}}}{\frac{\kappa}{2} - i\omega} \right|^2 + \left| \frac{\sqrt{\kappa_{\text{ext}} \kappa_{\text{int}}}}{\frac{\kappa}{2} - i\omega} \right|^2 = 1 \quad (2.33)$$

$$\langle \hat{d}_{\text{out}}^\dagger[\omega] \hat{d}_{\text{out}}[-\omega] \rangle = 0 \quad (2.34)$$

$$\langle \hat{d}_{\text{out}}[-\omega] \hat{d}_{\text{out}}^\dagger[\omega] \rangle = 1. \quad (2.35)$$

The commutator expression (2.33) agrees with the expectation (2.3) for the output mode.

## 2.2 Optomechanical coupling and its interpretations

In this section we add a mechanical mode to produce the canonical optomechanical system, derive a Hamiltonian describing the optomechanical coupling, and discuss its interpretations.

### 2.2.1 Canonical system and its Hamiltonian

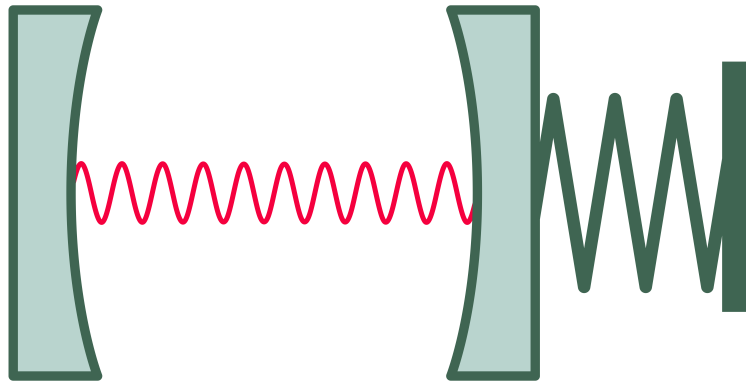


Figure 2.2: Schematic representation of the canonical optomechanical system.

The canonical optomechanical system is shown in Figure 2.2. It consists of two mirrors forming a Fabry-Perot cavity, with the output mirror being placed on a spring to create a mechanical oscillator. Let us denote the length of the cavity by  $L$  and let us consider the  $n^{\text{th}}$  cavity longitudinal mode, i.e., the mode with the wavelength  $\lambda_{c0} = L/(2n)$  (assuming perfect conductor boundary conditions, i.e., zero electric field at the mirror surfaces; for a more general treatment, see section B.2) and the corresponding frequency  $\omega_{c0} = 2\pi c/\lambda_{c0} = 4\pi nc/L$ . As in the previous section, the cavity mode is described by the Hamiltonian

$$\hat{\mathcal{H}}_c = \hbar\omega_{c0} \left( \hat{a}^\dagger \hat{a} + \frac{1}{2} \right). \quad (2.36)$$

Next, we need to introduce a mechanical Hamiltonian. Let us assume that the mechanical oscillator has mass  $m$  and spring constant  $k$ , such that its resonant frequency is  $\omega_m = \sqrt{k/m}$ . This results in a similar Hamiltonian

$$\hat{\mathcal{H}}_m = \hbar\omega_m \left( \hat{b}^\dagger \hat{b} + \frac{1}{2} \right), \quad (2.37)$$

where now  $\hat{b}$  is the annihilation operator of the mechanical oscillator. Its displacement can be expressed in terms of this annihilation operator as

$$\hat{x} = x_{\text{ZPF}} \left( \hat{b} + \hat{b}^\dagger \right) = x_{\text{ZPF}} \hat{z} \quad (2.38)$$

$$x_{\text{ZPF}} = \sqrt{\frac{\hbar}{2m\omega_m}}. \quad (2.39)$$

The zero-point fluctuation (ZPF) amplitude  $x_{\text{ZPF}}$  specifies the RMS mechanical displacement in the ground state: we can see that in the ground mechanical state

$$\langle \hat{x}^2 \rangle = x_{\text{ZPF}}^2 \langle \left( \hat{b} + \hat{b}^\dagger \right) \left( \hat{b} + \hat{b}^\dagger \right) \rangle = x_{\text{ZPF}}^2 \langle \hat{b} \hat{b}^\dagger \rangle = x_{\text{ZPF}}^2. \quad (2.40)$$

For brevity we have also introduced the dimensionless displacement operator

$$\hat{z} = \hat{b} + \hat{b}^\dagger = \frac{\hat{x}}{x_{\text{ZPF}}}, \quad (2.41)$$

which represents the mechanical position normalized by the ZPF amplitude.

Finally, we need to consider the fact that the cavity length (and, therefore, the optical resonance frequency) depends on the mechanical mode position:

$$\hat{\omega}_c(\hat{x}) = \frac{4\pi nc}{\hat{L}} = \frac{4\pi nc}{L + \hat{x}}, \quad (2.42)$$

In practice, the typical mechanical displacement  $\hat{x}$  is much smaller than the average cavity length  $L$ . Therefore, we can expand the optical frequency expression (2.42) to first order in  $\hat{x}$ :

$$\hat{\omega}_c \approx \omega_{c0} + \frac{\partial \omega_c}{\partial x} \hat{x} = \omega_{c0} + \frac{\partial \omega_c}{\partial x} x_{\text{ZPF}} \hat{z} = \omega_{c0} + g^{(0)} \hat{z}, \quad (2.43)$$

where  $\omega_{c0}$  is the optical resonance frequency for zero displacement and

$$g^{(0)} = \frac{\partial \omega_c}{\partial x} x_{\text{ZPF}}. \quad (2.44)$$

is the single-phonon optomechanical coupling. With this expansion the total Hamiltonian of the system becomes

$$\begin{aligned} \hat{\mathcal{H}} &= \hbar \left( \omega_{c0} + g^{(0)} \hat{z} \right) \left( \hat{a}^\dagger \hat{a} + \frac{1}{2} \right) + \hbar\omega_m \left( \hat{b}^\dagger \hat{b} + \frac{1}{2} \right) \\ &= \hbar\omega_{c0} \left( \hat{a}^\dagger \hat{a} + \frac{1}{2} \right) + \hbar\omega_m \left( \hat{b}^\dagger \hat{b} + \frac{1}{2} \right) + \hbar g^{(0)} \hat{z} \left( \hat{a}^\dagger \hat{a} + \frac{1}{2} \right) \\ &= \hat{\mathcal{H}}_c + \hat{\mathcal{H}}_m + \hat{\mathcal{H}}_{\text{om}}, \end{aligned} \quad (2.45)$$

where the optomechanical interaction Hamiltonian is

$$\hat{\mathcal{H}}_{\text{om}} = \hbar g^{(0)} \hat{z} \left( \hat{a}^\dagger \hat{a} + \frac{1}{2} \right). \quad (2.46)$$

The additional  $\frac{1}{2}$  term in this expression represents the Casimir force[4, 5], or, more precisely, the contribution to this force due to this particular optical mode. This effect is insignificant for the systems which are considered in this work, and to take it into account consistently we would need to consider all of the optical modes both inside and outside of the cavity (which, among other things, changes the sign of the force from repulsive to attractive). Thus, we will ignore this term for simplicity. Furthermore, we will also omit the  $\frac{1}{2}$  terms in the bare optical and mechanical parts, since all they contribute is a static shift to the Hamiltonian. These simplifications result in a slightly different Hamiltonian

$$\hat{\mathcal{H}} \approx \hbar \omega_{\text{c0}} \hat{a}^\dagger \hat{a} + \hbar \omega_{\text{m}} \hat{b}^\dagger \hat{b} + \hbar g^{(0)} \hat{z} \hat{a}^\dagger \hat{a}. \quad (2.47)$$

This Hamiltonian is universal, and it describes any optomechanical system which has one mechanical and one optical mode, and in which the optomechanical coupling is linear (i.e., expansion (2.43) is valid).

It is interesting to note that while in the canonical optomechanical system the definition of the mechanical displacement  $\hat{x}$  is very clear and natural, this is not the case for every optomechanical system. For example, in systems based on phononic defect cavities[6] the mechanical mode is described by a complicated displacement profile, so choosing how to quantify it with a single number is fairly subjective (in Ref. [6] the authors use the maximal point displacement); and in the case of the standing acoustic wave mode discussed in this thesis such displacement does not make much sense. This ambiguity also implies that values of the effective mass  $m$ , the effective spring constant  $k$ , and, correspondingly, the ZPF amplitude  $x_{\text{ZPF}}$  could be similarly poorly defined. Nevertheless, it turns out that the mechanical frequency  $\omega_{\text{m}}$  and the single-photon optomechanical coupling  $g^{(0)}$  are still model-independent and can be derived for any optomechanical system (e.g., see section 4.7 for the derivation in our system). Since these are the only mechanical system parameters entering the final Hamiltonian (2.47), the description presented in this section is universal, even though its derivation is not.

## 2.2.2 Interpretation of the optomechanical coupling

The optomechanical interaction Hamiltonian (2.46) can be understood in several different ways:

- (1) It can be interpreted in the way we just derived it, i.e., as a position-dependent resonant frequency of the optical cavity. To underscore this interpretation, we can write the interaction as  $\hat{\mathcal{H}}_{\text{om}} = \hbar \left( \frac{\partial \omega_{\text{c}}}{\partial x} \hat{x} \right) \hat{a}^\dagger \hat{a} = \hbar \delta \hat{\omega}_{\text{c}} \hat{a}^\dagger \hat{a}$  with  $\delta \hat{\omega}_{\text{c}} = \frac{\partial \omega_{\text{c}}}{\partial x} \hat{x}$ .
- (2) We can also write the Hamiltonian in a different form:  $\hat{\mathcal{H}}_{\text{om}} = \left( \hbar \frac{\partial \omega_{\text{c}}}{\partial x} \hat{a}^\dagger \hat{a} \right) \hat{x} = \hat{F} \hat{x}$ . This way it can be seen as a force acting on the mechanical resonator which is proportional to the energy stored in the optical mode. In the canonical optomechanical system this force is radiation pressure exerted by the light reflected off the movable mirror, but in different optomechanical systems it can have different origins (e.g., electrostatic force, or electrostriction).
- (3) Finally, by substituting  $\hat{z} = \hat{b} + \hat{b}^\dagger$  the interaction Hamiltonian can be written as  $\hat{\mathcal{H}}_{\text{om}} = \hbar g^{(0)} \left( \hat{b} \hat{a}^\dagger \hat{a} + \hat{b}^\dagger \hat{a}^\dagger \hat{a} \right)$ . This form suggests the interpretation of a three-wave mixing process where one photon (quantum of the optical mode excitation) is destroyed, one photon is created, and in the process one phonon (quantum of the mechanical mode excitation) is either created or destroyed.

## 2.3 Equations of motion and steady-state solution

Now we use the optomechanical Hamiltonian (2.47) to derive the equations of motion describing the optomechanical system, similar to the derivation of equation (2.16) from the Hamiltonian (2.1).

### 2.3.1 Equations of motion

As in section 2.1, equations of motion for the Heisenberg operators  $\hat{a}$  and  $\hat{b}$  can be derived using the input-output relation (2.6).

We consider the same two-port model for the optical mode as in the previous section. It leads to an equation of motion

$$\begin{aligned}\dot{\hat{a}} &= -\frac{i}{\hbar}[\hat{a}, \hat{\mathcal{H}}] + \sqrt{\kappa_{\text{int}}}\hat{\xi}_{\text{int}} + \sqrt{\kappa_{\text{ext}}}\hat{\xi}_{\text{ext}} + \sqrt{\kappa_{\text{ext}}}a_{\text{in}} \\ &= -\left(\frac{\kappa}{2} + i\omega_{c0}\right)\hat{a} - ig^{(0)}\hat{a}(\hat{b} + \hat{b}^\dagger) + \sqrt{\kappa_{\text{int}}}\hat{\xi}_{\text{int}} + \sqrt{\kappa_{\text{ext}}}\hat{\xi}_{\text{ext}} + \sqrt{\kappa_{\text{ext}}}a_{\text{in}}.\end{aligned}\quad (2.48)$$

We can again go into the frame rotating at  $\omega_{c0}$  to obtain

$$\dot{\hat{a}} = -\frac{\kappa}{2}\hat{a} - ig^{(0)}\hat{a}(\hat{b} + \hat{b}^\dagger) + \sqrt{\kappa_{\text{int}}}\hat{\xi}_{\text{int}} + \sqrt{\kappa_{\text{ext}}}\hat{\xi}_{\text{ext}} + \sqrt{\kappa_{\text{ext}}}a_{\text{in}}e^{+i\omega_{c0}t}.\quad (2.49)$$

A similar equation can be written for the mechanical mode as well. Since we are not going to consider any external mechanical drive or measurement channels, it is sufficient to introduce a single port to describe the intrinsic mechanical loss:

$$\begin{aligned}\dot{\hat{b}} &= -\frac{i}{\hbar}[\hat{b}, \hat{\mathcal{H}}] + \sqrt{\gamma_{\text{m}}}\hat{\eta} \\ &= -\left(\frac{\gamma_{\text{m}}}{2} + i\omega_{\text{m}}\right)\hat{b} - ig^{(0)}\hat{a}^\dagger\hat{a} + \sqrt{\gamma_{\text{m}}}\hat{\eta}.\end{aligned}\quad (2.50)$$

Here  $\gamma_{\text{m}}$  is the total mechanical damping and  $\hat{\eta}$  is the thermal noise force exerted by the bath. The statistics of this thermal force can be derived using equations (2.3) and (2.9) to be

$$\left[\hat{\eta}(t), \hat{\eta}^\dagger(t')\right] = \delta(t - t')\quad (2.51)$$

$$\left\langle \hat{\eta}^\dagger(t)\hat{\eta}(t') \right\rangle = n_{\text{th,m}}\delta(t - t')\quad (2.52)$$

$$\left\langle \hat{\eta}(t)\hat{\eta}^\dagger(t') \right\rangle = (n_{\text{th,m}} + 1)\delta(t - t')\quad (2.53)$$

in the time domain, and, correspondingly (similar to equations (2.23)-(2.25)),

$$\left[\hat{\eta}[\omega], \hat{\eta}^\dagger[-\omega]\right] = 1\quad (2.54)$$

$$\left\langle \hat{\eta}^\dagger[\omega]\hat{\eta}[-\omega] \right\rangle = n_{\text{th,m}}\quad (2.55)$$

$$\left\langle \hat{\eta}[\omega]\hat{\eta}^\dagger[-\omega] \right\rangle = n_{\text{th,m}} + 1\quad (2.56)$$

in the Fourier domain. The equilibrium mechanical bath occupation  $n_{\text{th,m}}$  is found from equation (2.10)

$$n_{\text{th,m}} = n_{\text{th}}(T, \omega_{\text{m}}) = \frac{1}{e^{\hbar\omega_{\text{m}}/(k_{\text{B}}T)} - 1} \approx \frac{k_{\text{B}}T}{\hbar\omega_{\text{m}}},\quad (2.57)$$

where the last approximation is done under the assumption of a relatively hot bath  $k_{\text{B}}T \gg \hbar\omega_{\text{m}}$ .

### 2.3.2 Linearization and steady state solution

The system of equations (2.49), (2.50) is non-linear, so it is extremely hard to solve in general. Therefore, we are going to obtain an approximate solution by linearizing these equations under the assumption of small optomechanical coupling:  $\left|g^{(0)}(\hat{b} + \hat{b}^\dagger)\right| \ll \kappa$ .<sup>a)</sup> Note that this condition is significantly stricter than simply

<sup>a)</sup>Strictly speaking, we only need to include the dynamical (oscillating) part of the mechanical displacement in  $\hat{b}$ . As shown later in this subsection, the static part can be absorbed in the optical drive detuning  $\Delta$ .

requiring  $g^{(0)} \ll \kappa$  (which holds well for all optomechanical experiments up to date), as it puts a limit on the maximal amplitude of the mechanical motion. In certain regimes, e.g., large mechanical oscillations caused by dynamic instability[7, 8], this condition is not satisfied, and different methods are required to solve the equations of motion. However, we will not consider these regimes in this work, so the linearization procedure will hold for all the experiments described here.

Before we linearize the equations of motion, we obtain the steady state solution by ignoring all the noise terms and assuming stationary optical and mechanical amplitudes. Thus, the intracavity field will become a classical variable  $a(t)$ , and, similarly, the mechanical mode will be described by a classical amplitude  $b(t)$ .

To make the solution more concrete, we specify the the optical drive to be a single tone with amplitude  $a_d$  and frequency  $\omega_d$ . The steady state equation then takes form

$$\dot{a} = -\frac{\kappa}{2}a - ig^{(0)}a(b + b^*) + \sqrt{\kappa_{\text{ext}}}a_d e^{-i\Delta_0 t} \quad (2.58)$$

$$\dot{b} = -\left(\frac{\gamma_m}{2} + i\omega_m\right)b - i|a|^2, \quad (2.59)$$

with  $\Delta_0 = \omega_d - \omega_{c0}$  being the drive detuning from the bare cavity resonant frequency. As before, we will look for a solution in the form  $a(t) = \bar{a}e^{-i\Delta_0 t}$  for the optical mode; for the mechanical mode we will simply assume a static displacement  $b(t) = \bar{b}$ . Depending on the parameters, this is not the only solution allowed by the system of equations above (see, e.g., [8]), but it is the most “stationary” one in the sense that both optical and mechanical displacements are simple oscillating functions (with the mechanical frequency being zero in this case). Substituting this ansatz into the equations, we arrive at

$$\bar{a} = \frac{\sqrt{\kappa_{\text{ext}}}a_d}{\frac{\kappa}{2} - i(\Delta_0 - g^{(0)}(\bar{b} + \bar{b}^*))} \quad (2.60)$$

$$\bar{b} = \frac{-ig^{(0)}|\bar{a}|^2}{i\omega_m + \frac{\gamma_m}{2}}. \quad (2.61)$$

In the second equation we can make an approximation  $\gamma_m \ll \omega_m$  (as this is the approximation required for the derivation of the equation (2.50) anyway), with which the amplitude  $\bar{b}$  becomes real. This leads to the final system of equations

$$\bar{a} = \frac{\sqrt{\kappa_{\text{ext}}}a_d}{\frac{\kappa}{2} - i(\Delta_0 - 2g^{(0)}\bar{b})} \quad (2.62)$$

$$\bar{b} = -\frac{g^{(0)}|\bar{a}|^2}{\omega_m}. \quad (2.63)$$

These equations could, in principle, have multiple solutions, which means that the optomechanical system could have several steady states (a situation known as static bistability[1, 9]). We will mostly ignore this aspect and assume that the system relaxes into one solution  $\bar{a}, \bar{b}$  (at least one solution always exists).

Next, we expand the equations of motion (2.49), (2.50) around this solution. In order to do so, let us look for a solution in the form  $\hat{a} = (\bar{a} + \hat{d})e^{-i\Delta_0 t}$  and  $\hat{b} = \bar{b} + \hat{c}$  (note that the expansion for  $\hat{a}$  is different from (2.17) as the perturbation is defined in the drive frame, not in the cavity frame; while the latter is more universal and is suitable for the case of more complicated optical drive, the former significantly simplifies expressions for the single-tone case). This expansion leads to the equations

$$\begin{aligned} \dot{\hat{d}} = & -\frac{\kappa}{2}\hat{d} - i\left(-\Delta_0 + 2g^{(0)}\bar{b}\right)\hat{d} - ig^{(0)}\left(\bar{a} + \hat{d}\right)\left(\hat{c} + \hat{c}^\dagger\right) \\ & + \sqrt{\kappa_{\text{int}}}\hat{\xi}_{\text{int}} + \sqrt{\kappa_{\text{ext}}}\hat{\xi}_{\text{ext}} \end{aligned} \quad (2.64)$$

$$\dot{\hat{c}} = -\left(\frac{\gamma_m}{2} + i\omega_m\right)\hat{c} - ig^{(0)}\left(\bar{a}\hat{d}^\dagger + \bar{a}^*\hat{d} + \hat{d}^\dagger\hat{d}\right) + \sqrt{\gamma_m}\hat{\eta}. \quad (2.65)$$

Now we linearize these equation by getting rid of the term  $-ig^{(0)}\hat{d}(\hat{c} + \hat{c}^\dagger)$  in the first equation and the term  $-ig^{(0)}\hat{d}^\dagger\hat{d}$  in the second equation, which both are small according to the linearization criterion. In addition, we

redefine the drive detuning by making a substitution  $\Delta = \Delta_0 - 2g^{(0)}\bar{b}$ . This merely means that we include the cavity frequency shift due to the static mechanical displacement  $\delta\omega_c = 2g^{(0)}\bar{b}$  into the definition of the detuning. The linearized equations now take form

$$\dot{\hat{d}} = -\left(\frac{\kappa}{2} - i\Delta\right)\hat{d} - ig^{(0)}\bar{a}\left(\hat{c} + \hat{c}^\dagger\right) + \sqrt{\kappa_{\text{int}}}\hat{\xi}_{\text{int}} + \sqrt{\kappa_{\text{ext}}}\hat{\xi}_{\text{ext}} \quad (2.66)$$

$$\dot{\hat{c}} = -\left(\frac{\gamma_{\text{m}}}{2} + i\omega_{\text{m}}\right)\hat{c} - ig^{(0)}\left(\bar{a}\hat{d}^\dagger + \bar{a}^*\hat{d}\right) + \sqrt{\gamma_{\text{m}}}\hat{\eta}. \quad (2.67)$$

As a final step, since both of the equations are linear, we can transform them into the Fourier domain:

$$\begin{aligned} -i\omega\hat{d}[\omega] &= -\left(\frac{\kappa}{2} - i\Delta\right)\hat{d}[\omega] - ig^{(0)}\bar{a}\left(\hat{c}[\omega] + \hat{c}^\dagger[\omega]\right) \\ &\quad + \sqrt{\kappa_{\text{int}}}\hat{\xi}_{\text{int}}[\omega] + \sqrt{\kappa_{\text{ext}}}\hat{\xi}_{\text{ext}}[\omega] \end{aligned} \quad (2.68)$$

$$-i\omega\hat{c}[\omega] = -\left(\frac{\gamma_{\text{m}}}{2} + i\omega_{\text{m}}\right)\hat{c}[\omega] - ig^{(0)}\left(\bar{a}\hat{d}^\dagger[\omega] + \bar{a}^*\hat{d}[\omega]\right) + \sqrt{\gamma_{\text{m}}}\hat{\eta}[\omega]. \quad (2.69)$$

These equations, together with the output field relation

$$\hat{d}_{\text{out}} = \hat{\xi}_{\text{ext}} - \sqrt{\kappa_{\text{ext}}}\hat{d} \quad (2.70)$$

describe a variety of optomechanical effects, and we will spend the remainder of this chapter exploring their consequences.

## 2.4 Position detection

One of the most direct consequences of the optomechanical interaction is imprinting of the mechanical motion on the complex amplitude of the intracavity and the output fields.

### 2.4.1 General expression

We start by deriving a general expression for this effect, for which we express the intracavity field  $\hat{d}[\omega]$  from equation (2.68):

$$\hat{d}[\omega] = \chi_{\text{c}}[\omega + \Delta] \left( -ig^{(0)}\bar{a}\delta\hat{z}[\omega] + \sqrt{\kappa_{\text{int}}}\hat{\xi}_{\text{int}}[\omega] + \sqrt{\kappa_{\text{ext}}}\hat{\xi}_{\text{ext}}[\omega] \right) \quad (2.71)$$

(similar to  $\hat{z}$  before we have defined  $\delta\hat{z} = \hat{c} + \hat{c}^\dagger$ , which is the mechanical fluctuations amplitude normalized by its zero-point fluctuations). The equation (2.70) lets us calculate the output field

$$\begin{aligned} \hat{d}_{\text{out}}[\omega] &= \left\{ \left( 1 - \frac{\kappa_{\text{ext}}}{\frac{\kappa}{2} - i(\omega + \Delta)} \right) \hat{\xi}_{\text{ext}}[\omega] - \frac{\sqrt{\kappa_{\text{ext}}\kappa_{\text{int}}}}{\frac{\kappa}{2} - i(\omega + \Delta)} \hat{\xi}_{\text{int}}[\omega] \right\} \\ &\quad - \sqrt{\kappa_{\text{ext}}}\chi_{\text{c}}[\omega + \Delta] \left( -ig^{(0)}\bar{a}\delta\hat{z}[\omega] \right). \end{aligned} \quad (2.72)$$

The first term depends only on the input noise and the bare cavity dynamics, and it is essentially the same as it was for the empty cavity (2.32), barring the different rotating frame frequency. As we have already shown in equations (2.33)-(2.35), the statistical properties of this term are the same as of the input vacuum noises (2.23)-(2.25). This means that we can denote it as another vacuum noise operator

$$\hat{\xi}_{\text{out}}[\omega] = \left( 1 - \frac{\kappa_{\text{ext}}}{\frac{\kappa}{2} - i(\omega + \Delta)} \right) \hat{\xi}_{\text{ext}}[\omega] - \frac{\sqrt{\kappa_{\text{ext}}\kappa_{\text{int}}}}{\frac{\kappa}{2} - i(\omega + \Delta)} \hat{\xi}_{\text{int}}[\omega], \quad (2.73)$$

which transforms (2.72) into

$$\hat{d}_{\text{out}}[\omega] = \hat{\xi}_{\text{out}}[\omega] + i\sqrt{\kappa_{\text{ext}}}\chi_{\text{c}}[\omega + \Delta]g^{(0)}\bar{a}\delta\hat{z}[\omega]. \quad (2.74)$$

The second term is proportional to the mechanical fluctuations amplitude  $\delta\hat{z}$ , and it is the term that provides readout of the mechanical displacement.

## 2.4.2 Unresolved sideband limit

It is interesting to consider the result above in the “unresolved sideband limit” (also known as “fast cavity limit”), in which the cavity response time  $1/\kappa$  is the fastest timescale in the problem, and in particular, faster than the mechanical period:  $\kappa \gg \omega_m$ . This means that the cavity susceptibility  $\chi_c[\omega + \Delta]$  can be treated as a frequency-independent constant, which transforms the mechanical displacement term in equation (2.71) into

$$\chi_c[\Delta] \left( -ig^{(0)} \bar{a} \delta \hat{z}[\omega] \right) \approx -i\bar{a} \frac{g^{(0)}}{\frac{\kappa}{2} - i\Delta} \delta \hat{z}[\omega]. \quad (2.75)$$

Interestingly, the same answer can be obtained by Taylor-expanding equation (2.60) for small mechanical fluctuations  $\delta \hat{b} \equiv \hat{c}$ :

$$\begin{aligned} \hat{a} &= \frac{\sqrt{\kappa_{\text{ext}}} a_d}{\frac{\kappa}{2} - i(\Delta_0 - g^{(0)}(\bar{b} + \hat{c} + \bar{b}^* + \hat{c}^\dagger))} = \frac{\sqrt{\kappa_{\text{ext}}} a_d}{\frac{\kappa}{2} - i(\Delta - g^{(0)} \delta \hat{z})} \\ &\approx \frac{\sqrt{\kappa_{\text{ext}}} a_d}{\frac{\kappa}{2} - i\Delta} \left( 1 - \frac{ig^{(0)} \delta \hat{z}}{\frac{\kappa}{2} - i\Delta} \right) = \bar{a} - i\bar{a} \frac{g^{(0)}}{\frac{\kappa}{2} - i\Delta} \delta \hat{z}. \end{aligned} \quad (2.76)$$

The first-order term agrees with the mechanical displacement term in the expression (2.75).

One potential problem with this derivation is that, strictly speaking, equation (2.60) was derived in the steady-state approximation, and is not applicable for the case of time-dependent  $\delta \hat{b}$ . However, the unresolved sideband limit ensures that the optical mode reacts quickly enough that it is essentially at the “steady state” even when  $\bar{b}$  changes, since this change is slow compared to the cavity response time.

## 2.5 Dynamical backaction

Now we consider the effects of light acting on the mechanical oscillator. We start by describing a single mechanical mode with no optomechanical interaction. After that, we include the optomechanical backaction and derive an expression for the optomechanical self-energy, which we then use to obtain magnitudes of the optical spring (change in the mechanical frequency) and the optomechanical damping (change in the mechanical linewidth). Finally, we present alternative interpretations of these effects: we explain the optomechanical damping as an imbalance between the Stokes process (which creates mechanical excitations) and anti-Stokes process (which annihilates them), and we demonstrate how the optical spring arises from the position-dependent radiation pressure force in the unresolved sideband limit.

### 2.5.1 Bare mechanical oscillator

First, let us first consider the mechanical equation of motion in the absence of optomechanical effects (e.g., by setting  $\bar{a} = 0$ ):

$$-i\omega \hat{c}[\omega] = -\left( \frac{\gamma_m}{2} + i\omega_m \right) \hat{c}[\omega] + \sqrt{\gamma_m} \hat{\eta}[\omega]. \quad (2.77)$$

Its solution can be expressed as

$$\hat{c}[\omega] = \chi_m[\omega] \sqrt{\gamma_m} \hat{\eta}[\omega], \quad (2.78)$$

where  $\chi_m[\omega] = (\gamma_m/2 - i(\omega - \omega_m))^{-1}$  is the mechanical susceptibility. This susceptibility describes a sharp complex Lorentzian peak of width  $\gamma_m$  centered at  $\omega_m \gg \gamma_m$ . Since the driving force noise has a frequency-independent spectrum (as can be seen from equations (2.54)-(2.56)), the power spectral density (PSD)  $S_{\hat{c}, \hat{c}^\dagger}$  of the mechanical annihilation operator will also be a Lorentzian centered around  $\omega_m$ :

$$\begin{aligned} S_{\hat{c}, \hat{c}^\dagger} &= \left\langle \hat{c}[\omega] \hat{c}^\dagger[-\omega] \right\rangle = \frac{\gamma_m}{\left( \frac{\gamma_m}{2} \right)^2 + (\omega - \omega_m)^2} \left\langle \hat{\eta}[\omega] \hat{\eta}^\dagger[-\omega] \right\rangle \\ &= \frac{\gamma_m}{\left( \frac{\gamma_m}{2} \right)^2 + (\omega - \omega_m)^2} (n_{\text{th},m} + 1). \end{aligned} \quad (2.79)$$

In contrast, the spectrum  $S_{\hat{c}^\dagger, \hat{c}}$  of the creation operator will be centered at  $-\omega_m$ :

$$S_{\hat{c}^\dagger, \hat{c}} = \left\langle \hat{c}^\dagger[\omega] \hat{c}[-\omega] \right\rangle = \frac{\gamma_m}{\left(\frac{\gamma_m}{2}\right)^2 + (\omega + \omega_m)^2} n_{\text{th}, m}. \quad (2.80)$$

## 2.5.2 Optomechanical self-energy and modified mechanical susceptibility

Now we go back to the full equations of motion which includes the optomechanical coupling. In order to solve the mechanical equation of motion, let us substitute the solution (2.71) for the optical field into the mechanical equation of motion (2.69). To simplify the notation, let us separate the solution (2.71) into two parts:

$$\hat{d}[\omega] = \hat{d}_z^\dagger[\omega] + \hat{d}_\xi[\omega] \quad (2.81)$$

$$\hat{d}_z^\dagger[\omega] = \chi_c[\omega + \Delta] \left( -ig^{(0)} \bar{a} \left( \hat{c}[\omega] + \hat{c}^\dagger[\omega] \right) \right) \quad (2.82)$$

$$\hat{d}_\xi[\omega] = \chi_c[\omega + \Delta] \left( \sqrt{\kappa_{\text{int}}} \hat{\xi}_{\text{int}}[\omega] + \sqrt{\kappa_{\text{ext}}} \hat{\xi}_{\text{ext}}[\omega] \right). \quad (2.83)$$

Substituting this into (2.69) yields

$$\begin{aligned} \left( \frac{\gamma_m}{2} - i(\omega - \omega_m) \right) \hat{c}[\omega] &= -ig^{(0)} \left( \bar{a} \hat{d}_z^\dagger[\omega] + \bar{a}^* \hat{d}_z[\omega] \right) - ig^{(0)} \left( \bar{a} \hat{d}_\xi^\dagger[\omega] + \bar{a}^* \hat{d}_\xi[\omega] \right) + \sqrt{\gamma_m} \hat{\eta}[\omega] \\ &= \left| \bar{a} g^{(0)} \right|^2 \left( \chi_c[\omega - \Delta] - \chi_c[\omega + \Delta] \right) \left( \hat{c}[\omega] + \hat{c}^\dagger[\omega] \right) \\ &\quad - ig^{(0)} \left( \bar{a} \hat{d}_\xi^\dagger[\omega] + \bar{a}^* \hat{d}_\xi[\omega] \right) + \sqrt{\gamma_m} \hat{\eta}[\omega] \\ &= -i\Sigma[\omega] \left( \hat{c}[\omega] + \hat{c}^\dagger[\omega] \right) - i\hat{F}_{\text{RPSN}}[\omega] + \hat{F}_{\text{th}}[\omega]. \end{aligned} \quad (2.84)$$

Here we have defined two stochastic forces acting on the mechanical oscillator: the thermal force

$$\hat{F}_{\text{th}}[\omega] \equiv \sqrt{\gamma_m} \hat{\eta}[\omega] \quad (2.85)$$

coming from the mechanical bath, and the radiation pressure shot noise (RPSN)

$$\hat{F}_{\text{RPSN}}[\omega] \equiv g^{(0)} \left( \bar{a} \hat{d}_\xi^\dagger[\omega] + \bar{a}^* \hat{d}_\xi[\omega] \right) \quad (2.86)$$

coming from the vacuum fluctuations of the optical field. The properties of these forces are explored in more detail in section 2.6. Additionally, we have introduced the optomechanical self-energy term

$$\Sigma[\omega] = -i \left| \bar{a} g^{(0)} \right|^2 \left( \chi_c[\omega + \Delta] - \chi_c[\omega - \Delta] \right). \quad (2.87)$$

Let us consider the self-energy term more closely. It represent an extra force acting on the mechanical oscillator, and is proportional to the displacement of the oscillator (hence the term ‘‘self-energy’’). In fact, this force consists of two components:  $-i\Sigma[\omega]\hat{c}[\omega]$  and  $-i\Sigma[\omega]\hat{c}^\dagger[\omega]$ . As equations (2.79) and (2.80) demonstrated, the first term is mostly non-zero around the mechanical frequency  $\omega_m$ , while the second term is only significant around  $-\omega_m$ . However, both of these forces are filtered by the same mechanical susceptibility  $\chi_m[\omega]$ , which is centered around the positive frequency  $+\omega_m$ . This means that the effect of the counter-rotating term  $-i\Sigma[\omega]\hat{c}^\dagger[\omega]$  is going to be significantly reduced (by a factor of  $\sim Q_m = \omega_m/\gamma_m$ ) compared to the other one, so we can neglect it entirely. After that, we can move the other term to the LHS, which results in the solution

$$\hat{c}[\omega] = \chi_{\text{m,eff}}[\omega] \left( -i\hat{F}_{\text{RPSN}}[\omega] + \hat{F}_{\text{th}}[\omega] \right) \quad (2.88)$$

$$\chi_{\text{m,eff}}[\omega] = \frac{1}{\frac{\gamma_m}{2} - i(\omega - \omega_m) + i\Sigma[\omega]}. \quad (2.89)$$

This solution is very similar to the bare mechanical oscillator (2.78), but it has two important differences. First, there is an additional stochastic force  $\hat{F}_{\text{RPSN}}$  acting on the mechanical object (the consequences of this force are considered in section 2.6). Second, the mechanical susceptibility is now modified by the self-energy term  $i\Sigma[\omega]$ .

### 2.5.3 Optical spring and optomechanical damping

While the expression (2.89) is fairly general (it only requires the linearized equations of motion (2.68), (2.69) and neglecting the counter-propagating term  $-i\Sigma[\omega]\hat{c}^\dagger[\omega]$ ), its intuitive meaning is easier to grasp with an additional assumption that the cavity susceptibility  $\chi_c[\omega]$  has weaker frequency dependence than the mechanical susceptibility  $\chi_{m,\text{eff}}$  (in other words, its width  $\kappa$  is much larger than the mechanical linewidth  $\gamma_m$ ). This assumption lets us replace  $\Sigma[\omega]$  by its value at the susceptibility peak  $\Sigma[\omega_m]$ . With that we can rewrite the mechanical susceptibility as

$$\chi_{m,\text{eff}}[\omega] \approx \frac{1}{\frac{\gamma_m - 2\text{Im}\{\Sigma[\omega_m]\}}{2} - i(\omega - (\text{Re}\{\Sigma[\omega_m]\} + \omega_m))}. \quad (2.90)$$

Thus, the self-energy leads to a modification of the mechanical frequency and damping, known as the optical spring effect and optomechanical damping (or anti-damping in the case of reduced mechanical linewidth). The new values of the mechanical parameters can be found as

$$\omega_{m,\text{eff}} = \omega_m + \text{Re}\{\Sigma[\omega_{m,\text{eff}}]\} \quad (2.91)$$

$$\gamma_{m,\text{eff}} = \gamma_m - 2\text{Im}\{\Sigma[\omega_{m,\text{eff}}]\}. \quad (2.92)$$

Note that in order for the definitions to be self-consistent, the value of  $\Sigma$  should be calculated at the modified frequency  $\omega_{m,\text{eff}}$ , which means that definition (2.91) is really a non-linear equation.

Finally, to make sure that the derivation is still consistent, we need to re-evaluate the assumptions that relied on the mechanical parameters. The first one concerned the counter-rotating terms  $\hat{c}^\dagger[\omega]$  and required a high mechanical quality factor  $Q_m = \omega_m/\gamma_m \gg 1$ ; now we have a potentially more strict requirement  $Q_{m,\text{eff}} = \omega_{m,\text{eff}}/\gamma_{m,\text{eff}} \gg 1$ . Second, the ‘‘broad cavity’’ assumption  $\kappa \gg \gamma_m$  should also be modified as  $\kappa \gg \gamma_{m,\text{eff}}$ . In the resolved sideband regime  $\omega_{m,\text{eff}} \gg \kappa$  this leads to an additional ‘‘weak optomechanical coupling’’ requirement  $|g^{(0)}\bar{a}| \ll \kappa$ . In the experiments considered in this work all of these assumptions hold, so we can safely use expressions (2.91), (2.92).

Let us reiterate the way we derived the optical spring and damping effect. First, we have calculated the effect that the mechanical motion has on the field amplitude, i.e., the  $\hat{d}_z$  part of the intracavity field. Second, we used  $\hat{d}_z$  to derive the radiation pressure force acting on the mechanical oscillator. Since this force is dependent on the mechanical position, it effectively results in a feedback loop mediated by the optomechanical interaction. It is this interpretation that resulted in the term ‘‘dynamical backaction’’: the mechanical motion gets imprinted on the cavity field, which then acts back on the mechanical object through the radiation pressure force.

### 2.5.4 Sideband cooling

Different interpretations of the dynamical backaction effects are possible. One particularly useful and intuitive interpretation of the optical damping comes from the rates of the Stokes and anti-Stokes processes mediated by the optomechanical interaction.

Let us start by examining the expression (2.82). It can be split into two parts:

$$\hat{d}_z[\omega] = \hat{d}_{\hat{c}}[\omega] + \hat{d}_{\hat{c}^\dagger}[\omega] \quad (2.93)$$

$$\hat{d}_{\hat{c}}[\omega] = -ig^{(0)}\bar{a}\chi_c[\omega + \Delta]\hat{c}[\omega] \quad (2.94)$$

$$\hat{d}_{\hat{c}^\dagger}[\omega] = -ig^{(0)}\bar{a}\chi_c[\omega + \Delta]\hat{c}^\dagger[\omega]. \quad (2.95)$$

The first (‘‘blue’’, or Stokes) part is proportional to  $\hat{c}$ , so it is centered around  $\omega = +\omega_{m,\text{eff}}$ . The second (‘‘red’’, or anti-Stokes) part involves  $\hat{c}^\dagger$ , so it is located at  $\omega = -\omega_{m,\text{eff}}$ . Both of these parts have relatively narrow width  $\gamma_{m,\text{eff}}$  and, therefore, can be seen as sharp sidebands around the main drive tone. Figure 2.3 is a rough schematic showing the drive tone and the sidebands.

The nature of these sidebands can be understood starting from the 3-wave mixing representation of the optomechanical Hamiltonian  $\hat{\mathcal{H}}_{\text{om}} = \hbar g^{(0)}(\hat{b}\hat{a}^\dagger\hat{a} + \hat{b}^\dagger\hat{a}^\dagger\hat{a})$ . If we perform the same linearization as for the

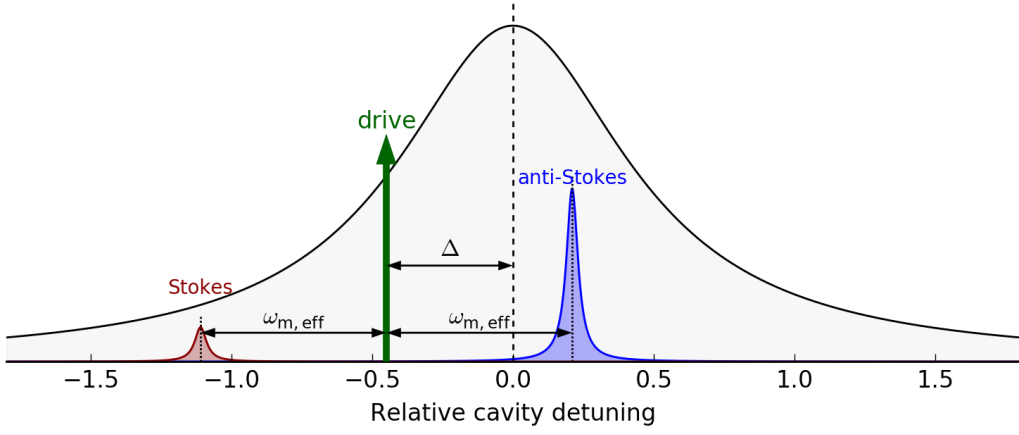


Figure 2.3: Schematic of optical tones and the mechanical sidebands experiencing cavity filtering in the sideband cooling experiment.

equations of motion before and focus on the leading-order (i.e., quadratic) terms, this Hamiltonian becomes

$$\hat{\mathcal{H}}_{\text{om}} = \hbar g^{(0)} \left( \bar{a} \hat{d}^\dagger \hat{c} + \bar{a} \hat{d} \hat{c}^\dagger + \text{h.c.} \right). \quad (2.96)$$

The first term leads to the part  $-ig^{(0)}\bar{a}\hat{c}$  in the equation of motion (2.68) and ultimately results in the blue sideband  $\hat{d}_{\hat{c}}$ . At the same time, it can be seen as describing a process in which a photon scatters from the strong classical drive into the blue sideband and removes one phonon along the way. Similarly, the second term gives rise to the the red sideband  $\hat{d}_{\hat{c}^\dagger}$ , and simultaneously it describes the process of scattering the photon into the red sideband and producing a phonon.

It is natural to assume that if one process creates phonons and the other annihilates them, then by altering their relative rates it is possible to cause net production or destruction of phonons, effectively altering the damping of the mechanical resonator.

To calculate the rates of these processes, consider the equations governing their amplitudes:

$$\dot{\hat{d}}_{\hat{A}} = -\left(\frac{\kappa}{2} - i\Delta\right) \hat{d}_{\hat{A}} - ig^{(0)}\bar{a}\hat{A}, \quad (2.97)$$

where  $\hat{A}$  is either  $\hat{c}$  or  $\hat{c}^\dagger$ .

The first term describes the cavity dynamics (including damping), while the second term corresponds to the drive (i.e., photon production). In the steady state these processes balance each other out, so the net rate of change of the sideband power is zero. However, we are only interested in the rate of the photon production process which is described by the second term. If we denote this term as  $\dot{\hat{d}}_{\hat{A}}^{(p)}$ , the photon production rate can be expressed as

$$\dot{\hat{n}}_{\hat{A}}^{(p)} = \hat{d}_{\hat{A}}^\dagger \dot{\hat{d}}_{\hat{A}}^{(p)} + \text{h.c.} = \hat{d}_{\hat{A}}^\dagger \left( -ig^{(0)}\bar{a}\hat{A} \right) + \text{h.c.} \quad (2.98)$$

To simplify this expression, we make the broad cavity approximation ( $\kappa \gg \gamma_{\text{m,eff}}$ ) in equations (2.94), (2.95), which allows us to rewrite them as

$$\hat{d}_{\hat{c}}[\omega] \approx -ig^{(0)}\bar{a}\chi_{\text{c}}[\omega_{\text{m,eff}} + \Delta]\hat{c}[\omega] \quad (2.99)$$

$$\hat{d}_{\hat{c}^\dagger}[\omega] \approx -ig^{(0)}\bar{a}\chi_{\text{c}}[-\omega_{\text{m,eff}} + \Delta]\hat{c}^\dagger[\omega]. \quad (2.100)$$

With these the rates become

$$\dot{\hat{n}}_{\hat{c}}^{(p)} = \left( ig^{(0)}\bar{a}^* (\chi_c[\omega_{m,\text{eff}} + \Delta])^* \hat{c}^\dagger \right) \left( -ig^{(0)}\bar{a}\hat{c} \right) + \text{h.c.} = r_{\hat{c}}\hat{c}^\dagger\hat{c} \quad (2.101)$$

$$\begin{aligned} r_{\hat{c}} &= 2 \left| g^{(0)}\bar{a} \right|^2 \text{Re} \{ \chi_c[\omega_{m,\text{eff}} + \Delta] \} \\ &= \kappa \left| g^{(0)}\bar{a} \right|^2 \left| \chi_c[\omega_{m,\text{eff}} + \Delta] \right|^2 \end{aligned} \quad (2.102)$$

$$\dot{\hat{n}}_{\hat{c}^\dagger}^{(p)} = \left( ig^{(0)}\bar{a}^* (\chi_c[-\omega_{m,\text{eff}} + \Delta])^* \hat{c} \right) \left( -ig^{(0)}\bar{a}\hat{c}^\dagger \right) + \text{h.c.} = r_{\hat{c}^\dagger}\hat{c}^\dagger\hat{c} \quad (2.103)$$

$$\begin{aligned} r_{\hat{c}^\dagger} &= 2 \left| g^{(0)}\bar{a} \right|^2 \text{Re} \{ \chi_c[-\omega_{m,\text{eff}} + \Delta] \} \\ &= \kappa \left| g^{(0)}\bar{a} \right|^2 \left| \chi_c[-\omega_{m,\text{eff}} + \Delta] \right|^2. \end{aligned} \quad (2.104)$$

Both process rates are proportional to the phonon number operator  $\hat{c}^\dagger\hat{c}$ , up to the commutator  $[\hat{c}, \hat{c}^\dagger] = 1$  in the second line (this additional term is related to such quantum optomechanical effects as radiation pressure shot noise and mechanical sideband asymmetry, and is discussed in section 2.6). This makes sense for a damping process, which is generally expressed as  $\dot{\hat{n}}_m^{(p)} = -\gamma\hat{n}_m^{(p)}$ . The additional damping rate can be obtained as the difference between the two rate prefactors  $r_{\hat{c},\hat{c}^\dagger}$  in front of the phonon number operator  $\hat{c}^\dagger\hat{c}$ :

$$\begin{aligned} \delta\gamma_{m,\text{eff}} &= r_{\hat{c}} - r_{\hat{c}^\dagger} = 2 \left| g^{(0)}\bar{a} \right|^2 \text{Re} \{ \chi_c[\omega_{m,\text{eff}} - \Delta] - \chi_c[\omega_{m,\text{eff}} + \Delta] \} \\ &= -2\text{Im} \{ \Sigma[\omega_{m,\text{eff}}] \}. \end{aligned} \quad (2.105)$$

This result agrees with the earlier expression (2.92).

### 2.5.5 Optical spring in the unresolved sideband regime

As a final exercise, we consider a simple way to interpret the optical spring effect in the unresolved sideband regime. As in subsection 2.4.2, we start by expressing the intracavity amplitude as a function of the instantaneous position  $\delta\hat{z}$ :

$$\hat{a} = \frac{\sqrt{\kappa_{\text{ext}}}a_d}{\frac{\kappa}{2} - i(\Delta - g^{(0)}\delta\hat{z})}. \quad (2.106)$$

From this amplitude we can find the intracavity power, which also depends on  $\delta\hat{z}$

$$\hat{a}^\dagger\hat{a} = \frac{\kappa_{\text{ext}}|a_d|^2}{\left(\frac{\kappa}{2}\right)^2 + (\Delta - g^{(0)}\delta\hat{z})^2}. \quad (2.107)$$

Finally, this power leads to a radiation pressure force

$$\hat{F}_{\text{RP}} = g^{(0)}\hat{a}^\dagger\hat{a} = g^{(0)}\frac{\kappa_{\text{ext}}|a_d|^2}{\left(\frac{\kappa}{2}\right)^2 + (\Delta - g^{(0)}\delta\hat{z})^2}, \quad (2.108)$$

which would enter the mechanical equation of motion (2.50) as

$$\dot{\hat{c}} = -\left(\frac{\gamma_m}{2} - i\omega_m\right)\hat{c} - i\hat{F}_{\text{RP}} + \sqrt{\gamma_m}\hat{\eta}. \quad (2.109)$$

Since this force is position-dependent, it contributes an effective spring constant

$$\begin{aligned} k_{\text{eff}} &= \left. \frac{\partial \hat{F}_{\text{RP}}}{\partial(\delta\hat{z})} \right|_{\delta\hat{z}=0} = \left( g^{(0)} \right)^2 \frac{\kappa_{\text{ext}}|a_d|^2}{\left(\frac{\kappa}{2}\right)^2 + \Delta^2} \frac{2\Delta}{\left(\frac{\kappa}{2}\right)^2 + \Delta^2} \\ &= \left| g^{(0)}\bar{a} \right|^2 \frac{2\Delta}{\left(\frac{\kappa}{2}\right)^2 + \Delta^2}, \end{aligned} \quad (2.110)$$

which lets us rewrite equation (2.109) as

$$\begin{aligned}\dot{\hat{c}} &= -\left(\frac{\gamma_m}{2} - i\omega_m\right)\hat{c} - ik_{\text{eff}}(\hat{c} + \hat{c}^\dagger) + \sqrt{\gamma_m}\hat{\eta} \\ &\approx -\left(\frac{\gamma_m}{2} - i(\omega_m + k_{\text{eff}})\right)\hat{c} + \sqrt{\gamma_m}\hat{\eta},\end{aligned}\quad (2.111)$$

where we neglected the static radiation pressure force and made the same rotating wave approximation  $\hat{c}^\dagger \approx 0$  as discussed in subsection 2.5.2. This equation can be compared to the expression (2.91) in the unresolved sideband limit:

$$\begin{aligned}\delta\omega_{m,\text{eff}} &\approx \text{Re}\{\Sigma[0]\} = \left|g^{(0)}\bar{a}\right|^2 \text{Im}\{\chi_c[\Delta] - \chi_c[-\Delta]\} \\ &= \left|g^{(0)}\bar{a}\right|^2 \frac{2\Delta}{\left(\frac{\kappa}{2}\right)^2 + \Delta^2}.\end{aligned}\quad (2.112)$$

As we can see, it yields the same result:  $k_{\text{eff}} = \delta\omega_{m,\text{eff}}$ .

## 2.6 Undriven mechanical motion and RPSN

In this section we consider the mechanical motion PSD excited by the mechanical thermal bath noise  $\hat{\eta}$ , and determine its signatures in the reflected light. We also briefly discuss interpretation of the asymmetry in the force noise spectrum and the mechanical displacement spectrum.

### 2.6.1 Mechanical motion PSD

We start by figuring out the PSD of the mechanical motion:

$$\begin{aligned}S_{\hat{z},\hat{z}}[\omega] &= \langle \hat{z}[\omega]\hat{z}[-\omega] \rangle = \langle (\hat{c}[\omega] + \hat{c}^\dagger[\omega])(\hat{c}[-\omega] + \hat{c}^\dagger[-\omega]) \rangle \\ &= S_{\hat{c}^\dagger,\hat{c}}[\omega] + S_{\hat{c},\hat{c}^\dagger}[\omega] + S_{\hat{c},\hat{c}}[\omega] + S_{\hat{c}^\dagger,\hat{c}^\dagger}[\omega].\end{aligned}\quad (2.113)$$

As mentioned in subsection 2.5.2,  $\hat{c}[\omega]$  is centered around  $+\omega_{m,\text{eff}}$  and has width  $\gamma_{m,\text{eff}} \ll \omega_{m,\text{eff}}$  (i.e., we work in the assumption of high-Q mechanical resonator). This means that the term  $S_{\hat{c},\hat{c}}[\omega] = \langle c[\omega]c[-\omega] \rangle \propto \chi_{m,\text{eff}}[\omega]\chi_{m,\text{eff}}[-\omega]$  will always be small, as for any frequency  $\omega$  at least one mechanical susceptibility term is far off-resonance. The same goes for  $S_{\hat{c}^\dagger,\hat{c}^\dagger}[\omega] = (S_{\hat{c},\hat{c}}[\omega])^*$ . Thus, we can simplify equation (2.113) as

$$S_{\hat{z},\hat{z}}[\omega] \approx S_{\hat{c}^\dagger,\hat{c}}[\omega] + S_{\hat{c},\hat{c}^\dagger}[\omega].\quad (2.114)$$

Similar to equations (2.79) and (2.80) in subsection 2.5.1, we can use equation (2.88) to derive:

$$S_{\hat{c}^\dagger,\hat{c}}[\omega] = |\chi_{m,\text{eff}}[-\omega]|^2 (S_{\hat{F},\hat{F}}^{\text{RPSN}}[\omega] + S_{\hat{F}^\dagger,\hat{F}}^{\text{th}}[\omega])\quad (2.115)$$

$$S_{\hat{c},\hat{c}^\dagger}[\omega] = |\chi_{m,\text{eff}}[+\omega]|^2 (S_{\hat{F},\hat{F}}^{\text{RPSN}}[\omega] + S_{\hat{F},\hat{F}^\dagger}^{\text{th}}[\omega]).\quad (2.116)$$

Note that, unlike in  $S_{\hat{c},\hat{c}}[\omega]$ , these terms involve  $\chi_{m,\text{eff}}$  only at one frequency.

The PSD of the thermal force is:

$$S_{\hat{F}^\dagger,\hat{F}}^{\text{th}}[\omega] \equiv \langle (\sqrt{\gamma_m}\hat{\eta}^\dagger[\omega])(\sqrt{\gamma_m}\hat{\eta}[-\omega]) \rangle = \gamma_m n_{\text{th},m}\quad (2.117)$$

$$S_{\hat{F},\hat{F}^\dagger}^{\text{th}}[\omega] \equiv \langle (\sqrt{\gamma_m}\hat{\eta}[\omega])(\sqrt{\gamma_m}\hat{\eta}^\dagger[-\omega]) \rangle = \gamma_m (n_{\text{th},m} + 1),\quad (2.118)$$

and the PSD of the radiation pressure is

$$\begin{aligned}S_{\hat{F},\hat{F}}^{\text{RPSN}}[\omega] &\equiv \langle \hat{F}_{\text{RPSN}}[\omega]\hat{F}_{\text{RPSN}}[-\omega] \rangle \\ &= \left(g^{(0)}\right)^2 |\bar{a}|^2 \langle \hat{d}_{\hat{\xi}}[\omega]\hat{d}_{\hat{\xi}}^\dagger[-\omega] \rangle \\ &= \left(g^{(0)}\right)^2 |\bar{a}|^2 \kappa |\chi_c[\omega + \Delta]|^2,\end{aligned}\quad (2.119)$$

where we have used

$$\begin{aligned} \langle \hat{d}_{\hat{\xi}}[\omega] \hat{d}_{\hat{\xi}}^\dagger[-\omega] \rangle &= |\chi_c[\omega + \Delta]|^2 \left( \kappa_{\text{int}} \langle \hat{\xi}_{\text{int}}[\omega] \hat{\xi}_{\text{int}}^\dagger[-\omega] \rangle + \kappa_{\text{ext}} \langle \hat{\xi}_{\text{ext}}[\omega] \hat{\xi}_{\text{ext}}^\dagger[-\omega] \rangle \right) \\ &= \kappa |\chi_c[\omega + \Delta]|^2. \end{aligned} \quad (2.120)$$

Since  $\hat{F}_{\text{RPSN}}$  is Hermitian, this is the only correlator that we need.

For the following discussion we note that

$$S_{\hat{F}, \hat{F}^\dagger}^{\text{th}}[\omega_{\text{m,eff}}] - S_{\hat{F}^\dagger, \hat{F}}^{\text{th}}[-\omega_{\text{m,eff}}] = \gamma_{\text{m}} \quad (2.121)$$

$$\begin{aligned} S_{\hat{F}, \hat{F}}^{\text{RPSN}}[\omega_{\text{m,eff}}] - S_{\hat{F}, \hat{F}}^{\text{RPSN}}[-\omega_{\text{m,eff}}] &= (g^{(0)})^2 |\bar{a}|^2 \kappa \left( |\chi_c[\omega_{\text{m,eff}} + \Delta]|^2 - |\chi_c[\omega_{\text{m,eff}} - \Delta]|^2 \right) \\ &= -2\text{Im}\Sigma[\omega_{\text{m,eff}}] \equiv \delta\gamma_{\text{m,eff}}, \end{aligned} \quad (2.122)$$

where  $\delta\gamma_{\text{m,eff}} \equiv \gamma_{\text{m,eff}} - \gamma_{\text{m}}$  is the damping rate induced by the dynamical backaction. This shows that the antisymmetric part of the force noise spectrum (with appropriate ordering for a non-Hermitian noise operator) is equal to the dissipation rate associated with this force: either the intrinsic loss  $\gamma_{\text{m}}$  for the environment mechanical noise  $\hat{\eta}$ , or the optomechanically induced damping  $\delta\gamma_{\text{m,eff}}$  for the radiation pressure shot noise. This is a well-known result from quantum noise theory[10], where the positive and the negative parts of the force spectrum are associated with the tendency of this force to respectively extract energy from or give energy to the system that it is acting on, so the difference between the two provides the net damping.

Another way to interpret equation (2.122) is to note that the positive and the negative frequency parts of the RPSN spectrum directly correspond to the Stokes and anti-Stokes photon production rate (per phonon) given by equations (2.102) and (2.104):

$$S_{\hat{F}, \hat{F}}^{\text{RPSN}}[\omega_{\text{m,eff}}] = \kappa \left| g^{(0)} \bar{a} \right|^2 |\chi_c[\omega_{\text{m,eff}} + \Delta]|^2 = r_{\hat{c}} \quad (2.123)$$

$$S_{\hat{F}, \hat{F}}^{\text{RPSN}}[-\omega_{\text{m,eff}}] = \kappa \left| g^{(0)} \bar{a} \right|^2 |\chi_c[-\omega_{\text{m,eff}} + \Delta]|^2 = r_{\hat{c}^\dagger}. \quad (2.124)$$

Hence, the antisymmetric part of the RPSN spectrum corresponds to the difference in the two rates, i.e., net damping rate (as shown by equation (2.105)).

When substituting force spectra into the equations for  $S_{\hat{c}^\dagger, \hat{c}}$  and  $S_{\hat{c}, \hat{c}^\dagger}$ , we can simplify them by assuming that  $\gamma_{\text{m,eff}} \ll \kappa$ , so the radiation pressure noise spectrum is approximately flat over the mechanical resonance. This lets us write

$$\begin{aligned} S_{\hat{c}^\dagger, \hat{c}}[\omega] &\approx |\chi_{\text{m,eff}}[-\omega]|^2 (S_{\hat{F}, \hat{F}}^{\text{RPSN}}[-\omega_{\text{m,eff}}] + S_{\hat{F}^\dagger, \hat{F}^\dagger}^{\text{th}}[-\omega_{\text{m,eff}}]) \\ &= |\chi_{\text{m,eff}}[-\omega]|^2 (n_{\text{RPSN}} \delta\gamma_{\text{m,eff}} + n_{\text{th,m}} \gamma_{\text{m}}) \end{aligned} \quad (2.125)$$

$$\begin{aligned} S_{\hat{c}, \hat{c}^\dagger}[\omega] &\approx |\chi_{\text{m,eff}}[\omega]|^2 (S_{\hat{F}, \hat{F}}^{\text{RPSN}}[\omega_{\text{m,eff}}] + S_{\hat{F}^\dagger, \hat{F}^\dagger}^{\text{th}}[\omega_{\text{m,eff}}]) \\ &= |\chi_{\text{m,eff}}[\omega]|^2 ((n_{\text{RPSN}} + 1) \delta\gamma_{\text{m,eff}} + (n_{\text{th,m}} + 1) \gamma_{\text{m}}), \end{aligned} \quad (2.126)$$

where we have defined the effective phonon occupation of the RPSN bath

$$n_{\text{RPSN}} = \frac{S_{\hat{F}, \hat{F}}^{\text{RPSN}}[-\omega_{\text{m,eff}}]}{\delta\gamma_{\text{m,eff}}} = \frac{S_{\hat{F}, \hat{F}}^{\text{RPSN}}[-\omega_{\text{m,eff}}]}{S_{\hat{F}, \hat{F}}^{\text{RPSN}}[\omega_{\text{m,eff}}] - S_{\hat{F}, \hat{F}}^{\text{RPSN}}[-\omega_{\text{m,eff}}]} \quad (2.127)$$

analogously to the thermal bath occupation  $n_{\text{th,m}}$ . To determine the final mean energy of the mechanical mode, we can find the expectation value of the phonon number operator by integrating its PSD:

$$\begin{aligned} n_{\text{m}} &= \langle \hat{c}^\dagger(t) \hat{c}(t) \rangle = \int_{-\infty}^{+\infty} S_{\hat{c}^\dagger \hat{c}}[\omega] \frac{d\omega}{2\pi} \\ &= \int_{-\infty}^{+\infty} \frac{n_{\text{RPSN}} \delta\gamma_{\text{m,eff}} + n_{\text{th,m}} \gamma_{\text{m}}}{\gamma_{\text{m,eff}}^2/4 + (\omega + \omega_{\text{m,eff}})^2} \frac{d\omega}{2\pi} = \frac{n_{\text{RPSN}} \delta\gamma_{\text{m,eff}} + n_{\text{th,m}} \gamma_{\text{m}}}{\gamma_{\text{m,eff}}}. \end{aligned} \quad (2.128)$$

This expression can be intuitively understood if we consider that the mechanical oscillator is coupled to two different baths (environment and radiation pressure force) at two different rates ( $\gamma_m$  and  $\delta\gamma_{m,\text{eff}}$  respectively). This implies that the final phonon occupation of the oscillator is a weighted average of the occupations of the two baths, with the weights being proportional to the coupling rates.

With this expression for  $n_m$  the mechanical PSDs simplify to

$$S_{\hat{c}^\dagger, \hat{c}}[\omega] = \frac{n_m \gamma_{m,\text{eff}}}{\gamma_{m,\text{eff}}^2/4 + (\omega + \omega_{m,\text{eff}})^2} \quad (2.129)$$

$$S_{\hat{c}, \hat{c}^\dagger}[\omega] = \frac{(n_m + 1)\gamma_{m,\text{eff}}}{\gamma_{m,\text{eff}}^2/4 + (\omega - \omega_{m,\text{eff}})^2}. \quad (2.130)$$

Note that the difference in the magnitude between the two PSDs (which can be traced to the asymmetry of the force noise spectra) is directly related to the equal-time commutator of the mechanical creation and annihilation operators:

$$\begin{aligned} [\hat{c}(t), \hat{c}^\dagger(t)] &= \langle [\hat{c}(t), \hat{c}^\dagger(t)] \rangle = \langle \hat{c}(t)\hat{c}^\dagger(t) \rangle - \langle \hat{c}^\dagger(t)\hat{c}(t) \rangle \\ &= (n_m + 1) - n_m = 1. \end{aligned} \quad (2.131)$$

## 2.6.2 Reflected light PSD

Now we can use relation (2.74) from section 2.4 to derive the PSD of the light leaving the cavity through the external port:

$$\begin{aligned} S_{\hat{d}_{\text{out}}^\dagger, \hat{d}_{\text{out}}}[\omega] &\equiv \langle \hat{d}_{\text{out}}^\dagger[\omega]\hat{d}_{\text{out}}[-\omega] \rangle \\ &= \kappa_{\text{ext}} \left(g^{(0)}\right)^2 |\bar{a}|^2 |\chi_c[-\omega + \Delta]|^2 (S_{\hat{c}^\dagger, \hat{c}}[\omega] + S_{\hat{c}, \hat{c}^\dagger}[\omega]) \\ &= \kappa_{\text{ext}} \left(g^{(0)}\right)^2 |\bar{a}|^2 |\chi_c[-\omega + \Delta]|^2 \times \\ &\quad \times \left( \frac{n_m \gamma_{m,\text{eff}}}{\gamma_{m,\text{eff}}^2/4 + (\omega + \omega_{m,\text{eff}})^2} + \frac{(n_m + 1)\gamma_{m,\text{eff}}}{\gamma_{m,\text{eff}}^2/4 + (\omega - \omega_{m,\text{eff}})^2} \right). \end{aligned} \quad (2.132)$$

We should keep in mind that the optical frame is rotating at the optical drive frequency  $\omega_d$  (subsection 2.3.2), which means that the frequency  $\omega$  above is also defined relative to the drive frequency. Because of the mechanical susceptibility terms, the PSD expression (2.132) has two sharp peaks at  $\omega = \pm\omega_{m,\text{eff}}$  and is zero everywhere else. This implies that in the stationary frame these peaks manifest as sidebands on the control beam, which are located at  $\omega = \omega_d \pm \omega_{m,\text{eff}}$ . These sidebands are precisely the Stokes and anti-Stokes sidebands discussed in subsection 2.5.4, and the perceived difference of one phonon in their magnitude is oftentimes referred to as ‘‘sideband asymmetry’’.

In the presented derivation the origin of the sideband asymmetry can be tracked to the difference between the positive and the negative parts of the mechanical spectrum (equations (2.129) and (2.130)), which describes the fundamental asymmetry between the rate of absorption (Stokes process) or emission (anti-Stokes process) of energy by the mechanical oscillator. It is worth noting that an alternative interpretation exists [11, 12, 13], in which this asymmetry can be attributed to the correlations between the mechanical motion and the vacuum noise background arising from the RPSN acting on the mechanical oscillator.

## 2.7 Driven response measurements (OMIT/A)

The last effect to consider in this section is the driven measurement of the mechanical response. In this kind of measurement the optical mode is used both to coherently drive the mechanical oscillator and to interrogate its motion. I will first present a general treatment, and then examine the results in the resolved sideband limit  $\omega_{m,\text{eff}} \gg \kappa$ .

### 2.7.1 General treatment

The technique we are going to consider is called optomechanically induced transparency or amplification (OMIT/A)[14, 15] and it relies on sending two optical tones into the cavity. The stronger tone, called the “control” is analogous to the drive tone that we have been considering so far. The other, weaker, tone is called the “probe”, and it is added to drive the mechanical oscillator (in combination with the control tone). When both tones excite the optical cavity, they produce intensity oscillations at a frequency equal to their frequency difference, which in turn results in an oscillating radiation pressure force. If the frequency of this force is close enough to the mechanical resonance, it can efficiently drive the mechanical oscillator. This driven motion imprints sidebands on the beams, and because it is induced by the beating between the beams, one of the control beam sidebands ends up being at the same frequency as the probe beam. This modifies the probe beam’s amplitude, which can be detected after it leaves the cavity.

To describe this measurement, we first need to modify the equations of motion (2.68), (2.69). Since the measurement scheme is coherent, we are going to ignore the noise terms proportional to  $\hat{\xi}$  or  $\hat{\eta}$ . Instead, we include the additional probe tone  $a_{p,\text{in}}(t) = a_p e^{-i\Omega_p t}$ , where  $a_p \ll a_d$  is the probe amplitude and  $\Omega_p$  is its detuning from the control beam (i.e., its frequency in the control beam frame). We will treat the probe as a perturbation, so it will be included into the equation for  $\hat{d}$  and not into the steady state amplitude  $\bar{a}$ . All of these changes transform equations of motion (2.68), (2.69) into

$$\dot{\hat{d}} = -\left(\frac{\kappa}{2} - i\Delta\right)\hat{d} - ig^{(0)}\bar{a}\left(\hat{c} + \hat{c}^\dagger\right) + \sqrt{\kappa_{\text{ext}}}a_p e^{-i\Omega_p t} \quad (2.133)$$

$$\dot{\hat{c}} = -\left(\frac{\gamma_m}{2} + i\omega_m\right)\hat{c} - ig^{(0)}\left(\bar{a}\hat{d}^\dagger + \bar{a}^*\hat{d}\right). \quad (2.134)$$

At this point the equations are purely classical; nevertheless, we will keep the operator notation for consistency.

As before, we want to Fourier transform these equations. Since we are dealing with coherent signals, we will use a “coherent” Fourier transform (see appendix A.2):

$$\left(\frac{\kappa}{2} - i(\omega + \Delta)\right)\hat{d}[\omega] = -ig^{(0)}\bar{a}\left(\hat{c}[\omega] + \hat{c}^\dagger[\omega]\right) + \sqrt{\kappa_{\text{ext}}}a_p\delta(\omega - \Omega_p) \quad (2.135)$$

$$\left(\frac{\gamma_m}{2} - i(\omega - \omega_m)\right)\hat{c}[\omega] = -ig^{(0)}\left(\bar{a}\hat{d}^\dagger[\omega] + \bar{a}^*\hat{d}[\omega]\right). \quad (2.136)$$

The next step is to again substitute the expression for  $\hat{d}[\omega]$  into the equation for  $\hat{c}[\omega]$ . The terms involving  $\hat{c}[\omega]$  and  $\hat{c}^\dagger[\omega]$  will result in exactly the same modification of the mechanical susceptibility as before in section 2.5, which leaves us with

$$\begin{aligned} (\chi_{m,\text{eff}}[\omega])^{-1}\hat{c}[\omega] &= -ig^{(0)}\sqrt{\kappa_{\text{ext}}}\left(\bar{a}\chi_c[\omega - \Delta]a_p^*\delta(\omega + \Omega_p)\right. \\ &\quad \left.+ \bar{a}^*\chi_c[\omega + \Delta]a_p\delta(\omega - \Omega_p)\right). \end{aligned} \quad (2.137)$$

The solution can be written as a sum of two  $\delta$ -functions corresponding to the frequencies  $\pm\Omega_p$ :

$$\hat{c}[\omega] = c_+\sqrt{\kappa_{\text{ext}}}a_p\delta(\omega - \Omega_p) + c_-\sqrt{\kappa_{\text{ext}}}a_p^*\delta(\omega + \Omega_p) \quad (2.138)$$

$$c_+ = -i\chi_{m,\text{eff}}[\Omega_p]g^{(0)}\bar{a}^*\chi_c[\Delta + \Omega_p] \quad (2.139)$$

$$c_- = -i\chi_{m,\text{eff}}[-\Omega_p]g^{(0)}\bar{a}\left(\chi_c[\Delta + \Omega_p]\right)^*. \quad (2.140)$$

Usually only one of these terms will be close to the mechanical resonance frequency, depending on the sign of  $\Omega_p$ . However, to keep the discussion general we need to preserve both terms. Substituting them back into the

equation for  $\hat{d}$ , we obtain

$$\begin{aligned}\hat{d}[\omega] &= \chi_c[\omega + \Delta] \sqrt{\kappa_{\text{ext}}} \left( \left( 1 - ig^{(0)} \bar{a} (c_+ + c_-^*) \right) a_p \delta(\omega - \Omega_p) - ig^{(0)} \bar{a} (c_+^* + c_-) a_p^* \delta(\omega + \Omega_p) \right) \\ &= \chi_c[\omega + \Delta] \sqrt{\kappa_{\text{ext}}} (a_+ a_p \delta(\omega - \Omega_p) + a_- a_p^* \delta(\omega + \Omega_p))\end{aligned}\quad (2.141)$$

$$\begin{aligned}a_+ &= 1 - ig^{(0)} \bar{a} (c_+ + c_-^*) \\ &= 1 - \left| g^{(0)} \bar{a} \right|^2 \chi_c[\Delta + \Omega_p] (\chi_{\text{m,eff}}[\Omega_p] - (\chi_{\text{m,eff}}[-\Omega_p])^*)\end{aligned}\quad (2.142)$$

$$\begin{aligned}a_- &= -ig^{(0)} \bar{a} (c_+^* + c_-) \\ &= - \left( g^{(0)} \bar{a} \right)^2 (\chi_c[\Delta + \Omega_p])^* (\chi_{\text{m,eff}}[-\Omega_p] - (\chi_{\text{m,eff}}[\Omega_p])^*).\end{aligned}\quad (2.143)$$

The amplitude of the probe tone inside the cavity is now modified by the factor  $a_+$ , which can be treated as a change in the effective cavity susceptibility for the probe beam:

$$\chi_{\text{c,eff}}[\Omega_p] = \chi_c[\Delta + \Omega_p] \left( 1 - \left| g^{(0)} \bar{a} \right|^2 \chi_c[\Delta + \Omega_p] (\chi_{\text{m,eff}}[\Omega_p] - (\chi_{\text{m,eff}}[-\Omega_p])^*) \right).\quad (2.144)$$

This change manifests as a sharp feature which is proportional to the effective mechanical susceptibility. Hence, it can be used to extract the effective mechanical frequency and linewidth. The magnitude of the feature can be described in terms of its amplitude relative to the background  $a_{\text{rel}}$ :

$$\begin{aligned}\chi_{\text{c,eff}}[\Omega_p] &= \chi_c[\Delta + \Omega_p] \left( 1 + a_{\text{rel,+}} \frac{\gamma_{\text{m,eff}}/2}{\gamma_{\text{m,eff}}/2 - i(\Omega_p - \omega_{\text{m,eff}})} \right. \\ &\quad \left. + a_{\text{rel,-}} \frac{\gamma_{\text{m,eff}}/2}{\gamma_{\text{m,eff}}/2 + i(\Omega_p + \omega_{\text{m,eff}})} \right)\end{aligned}\quad (2.145)$$

$$a_{\text{rel,+}} = - \frac{2 \left| g^{(0)} \bar{a} \right|^2}{\gamma_{\text{m,eff}}} \chi_c[\Delta + \omega_{\text{m,eff}}]\quad (2.146)$$

$$a_{\text{rel,-}} = \frac{2 \left| g^{(0)} \bar{a} \right|^2}{\gamma_{\text{m,eff}}} \chi_c[\Delta - \omega_{\text{m,eff}}]\quad (2.147)$$

Finally, from this effective susceptibility we can also find the amplitude of the probe beam reflection:

$$a_{\text{p,out}} = a_p - \kappa_{\text{ext}} \chi_{\text{c,eff}}[\Omega_p].\quad (2.148)$$

## 2.7.2 Resolved sideband limit

The results of the OMIT/A experiment are easier to understand in the resolved sideband limit  $\omega_{\text{m,eff}} \gg \kappa$ . First, we will consider the situation in which the control beam is detuned to the red side of the cavity  $\Delta = -\omega_{\text{m,eff}}$ , and the probe beam detuning is close to the mechanical resonance:  $\Omega_p = \omega_{\text{m,eff}} + \delta\omega$  with  $\delta\omega \sim \gamma_{\text{m,eff}}$ . In this regime the optomechanical damping becomes

$$\delta\gamma_{\text{m,eff}} = -2\text{Im} \{ \Sigma[\omega_{\text{m,eff}}] \} \approx \frac{4 \left| \bar{a} g^{(0)} \right|^2}{\kappa},\quad (2.149)$$

where we have neglected the off-resonant term  $\chi_c[\Delta - \omega_{\text{m,eff}}] = \chi_c[-2\omega_{\text{m,eff}}]$  in  $\Sigma[\omega_{\text{m,eff}}]$ . In the same approximation the mechanical frequency stays unchanged  $\omega_{\text{m,eff}} \approx \omega_{\text{m}}$ .

In calculating the effective probe beam susceptibility we can neglect the term  $\chi_{\text{m,eff}}[-\Omega_p] \approx \chi_{\text{m,eff}}[-2\omega_{\text{m}}]$ , as it is very far off resonance. This leaves us with

$$\begin{aligned}\chi_{\text{c,eff}}[\omega_{\text{m}} + \delta\omega] &\approx \chi_c[\delta\omega] \left( 1 - \frac{2 \left| g^{(0)} \bar{a} \right|^2}{\kappa} \chi_{\text{m,eff}}[\omega_{\text{m}} + \delta\omega] \right) \\ &= \chi_c[\delta\omega] \left( 1 - \frac{\delta\gamma_{\text{m,eff}}/2}{\gamma_{\text{m,eff}}/2 - i\delta\omega} \right)\end{aligned}\quad (2.150)$$

(inside the parentheses we have approximated  $\chi_c[\Delta + \Omega_p] = \chi_c[\delta\omega] \approx \chi_c[0] = 2/\kappa$ , as it multiplies  $\chi_{m,\text{eff}}[\omega_m + \delta\omega]$  which is only significant for  $\delta\omega \lesssim \gamma_{m,\text{eff}} \ll \kappa$ ). Right at the mechanical resonance this turns into

$$\chi_{c,\text{eff}}[\omega_m] = \chi_c[0] \frac{1}{1 + \delta\gamma_{m,\text{eff}}/\gamma_m} = \chi_c[0] \frac{1}{1 + \mathcal{C}}, \quad (2.151)$$

where  $\mathcal{C}$  is the optomechanical cooperativity defined as

$$\mathcal{C} = \frac{4 |\bar{a}g^{(0)}|^2}{\kappa\gamma} = \frac{\delta\gamma_{m,\text{eff}}}{\gamma_m} \quad (2.152)$$

(the second equality holds only in the case of the resolved sideband limit and red-detuned control beam  $\Delta = -\omega_m$ ). The peak susceptibility goes down by a factor of  $1 + \mathcal{C}$ , which in many systems can be much larger than one. Thus, even if the optomechanical coupling is much smaller than the cavity linewidth ( $|\bar{a}g^{(0)}| \ll \kappa$ ), it can still significantly modify the effective cavity susceptibility.

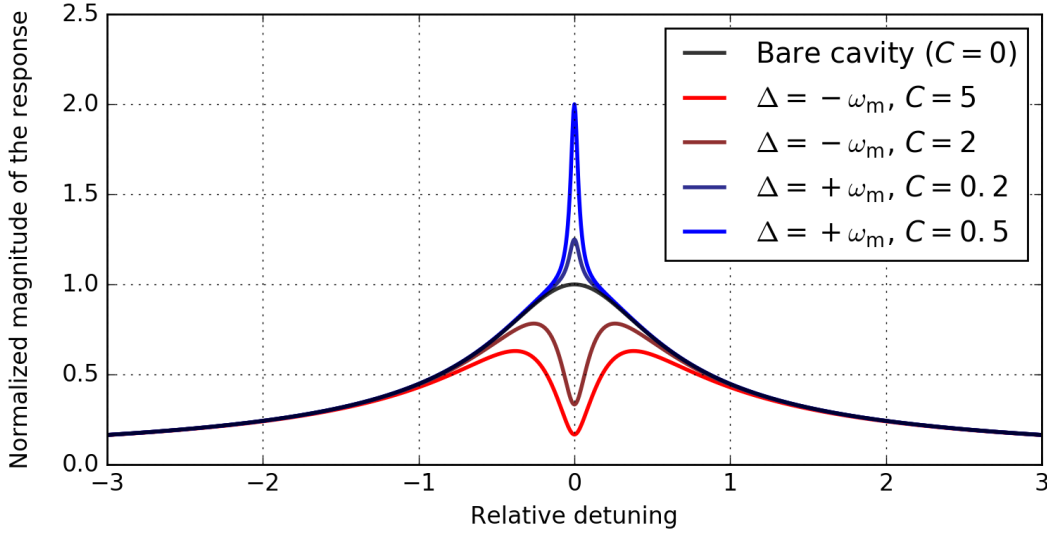


Figure 2.4: Examples of an OMIT/A response. The figure plots the magnitude of the effective probe beam response  $|\chi_{c,\text{eff}}[\Omega_p]|$  as a function of its cavity detuning  $\delta\omega$  for different control beam detunings  $\Delta$  and values of the cooperativity  $\mathcal{C}$ . Red lines denote the OMIT configuration when the control beam detuning is negative ( $\Delta = -\omega_m$ ), while blue lines correspond to the OMIA configuration ( $\Delta = +\omega_m$ ). The black line is the unperturbed cavity response  $\chi_c[\Omega_p]$ , which corresponds to  $\mathcal{C} = 0$ .

The OMIA experiment is fairly similar, except the signs on the probe and control beams detunings are flipped:  $\Delta = +\omega_m$  and  $\Omega_p = -\omega_{m,\text{eff}} - \delta\omega$ . This leads to optomechanical anti-damping (reduced linewidth)

$$\delta\gamma_{m,\text{eff}} \approx -\frac{4 |\bar{a}g^{(0)}|^2}{\kappa}, \quad (2.153)$$

and the effective susceptibility

$$\begin{aligned} \chi_{c,\text{eff}}[-\omega_m - \delta\omega] &\approx \chi_c[-\delta\omega] \left( 1 + \frac{2 |g^{(0)}\bar{a}|^2}{\kappa} (\chi_{m,\text{eff}}[\omega_m + \delta\omega])^* \right) \\ &= \chi_c[\delta\omega] \left( 1 - \frac{\delta\gamma_{m,\text{eff}}/2}{\gamma_{m,\text{eff}}/2 + i\delta\omega} \right). \end{aligned} \quad (2.154)$$

On resonance it is equal to

$$\chi_{c,\text{eff}}[-\omega_m] = \chi_c[0] \frac{1}{1 + \delta\gamma_{m,\text{eff}}/\gamma_m} = \chi_c[0] \frac{1}{1 - \mathcal{C}}. \quad (2.155)$$

The response is now larger by a factor of  $1/(1 - \mathcal{C})$ , which means that the probe beam is amplified[16, 15] in a narrow frequency band corresponding to the mechanical linewidth  $\gamma_{m,\text{eff}}$ ; hence the term “optomechanically induced amplification”.

Note that this treatment of OMIA is only valid for  $\mathcal{C} < 1$ . For  $\mathcal{C} > 1$  the effective linewidth becomes negative, which means that the optomechanical anti-damping overcomes the intrinsic mechanical damping. This leads to large mechanical oscillations (which can be thought of as a runaway process in a system with a positive feedback loop), whose amplitude is limited by higher-order non-linearities of the optomechanical interaction[7, 8], which are not included in the above treatment.

Figure 2.4 illustrates results (2.150) and (2.154) for several different values of the cooperativity  $\mathcal{C}$ . Note how the OMIT/A feature becomes broader for the OMIT configuration and narrower for the OMIA configuration; this reflects the impact of optical damping or anti-damping caused by the optomechanical interaction.

# Chapter 3

## Overview and current progress

### 3.1 Common implementations

Over the years there have been many realizations of optomechanical systems[1], covering the electromagnetic frequency range from microwave ( $\sim 5$  GHz) to optical ( $\sim 500$  THz), mechanical frequencies from Hz to GHz, masses from kg-scale mirrors to just  $\sim 100$  levitated atoms, and length-scales from meter- and even kilometer-long interferometers to  $\mu\text{m}$ -size optomechanical crystals or  $\sim 50$  nm-gap capacitors. In this section I will cover the most common implementations of optomechanical systems.

One of the first cavity optomechanics realizations was explored theoretically[17] and then implemented experimentally[18] by Braginsky *et al.*, where they considered the effects of optomechanical damping (section 2.5). The system was a microwave cavity with a movable wall suspended on a thin quartz fiber, which turned it into a high-Q pendulum. In the optical domain the first optomechanics experiment was reported in Ref. [9], where the radiation pressure induced static bistability (see section 2.3) was observed. There the optical system was a Fabry-Perot cavity, and the mechanical oscillator was one of its mirrors, which was likewise suspended by a string to form a pendulum. Shortly after, the static bistability was also observed in a microwave (MW) setting[19].

Since then many conceptually different realizations have arisen. Still, many modern systems continue implementing this general concept of a movable end-mirror. The sizes of these mirrors range from several kilogram LIGO mirrors[20, 21] to gram-scale suspended mirrors[22, 23] to sub-nanogram mirrors placed on the end of a cantilever[24, 25] or on a trampoline[26]. In addition, some experiments focus on the internal vibrational modes of the mirrors[27, 28], rather than their center-of-mass motion.

Similar to the vibrational mirror modes, other experiments also focus on internal mechanical degrees of freedom of a rigid optical resonator, which are often ignored due to their high frequency and stiffness. Some of the most notable systems of this kind are microtoroid resonators[29], where the optical mode is a whispering gallery mode (WGM) confined inside a microtoroid (with a diameter of  $\sim 100 \mu\text{m}$ ), and the mechanical modes are vibrational modes of this toroid. These systems were the first to demonstrate dynamical bistability[30, 7] and OMIT[14], and among the first to employ optomechanical cooling[31]. Conceptually similar are microsphere[32] and microdisk[33] devices.

A different approach is to use a fixed Fabry-Perot cavity and embed a separate mechanical element inside it, which lets one separate the optical and the mechanical subsystems and optimize them separately. One of the most successful implementations of this idea, the so-called membrane-in-the-middle (MIM) setup, was first demonstrated in the Harris Lab[34, 35]. There the mechanical element was a thin (50 nm) high-stress dielectric  $\text{Si}_3\text{N}_4$  membrane placed in the center of a high-finesse optical cavity. One of the advantages of such setup is the tunability of the form of the optomechanical coupling [36, 37], which allows one to switch from the standard linear coupling to the quadratic coupling, in which the cavity resonance frequency depends quadratically on the mechanical displacement (unlike the canonical optomechanical system, in which this dependence is linear). Another interesting feature of the MIM setup is the presence of multiple nearly-degenerate mechanical modes coupled to the same optical mode. This shared optical mode can mediate interactions between the mechanical

modes[38] and lead to non-trivial multimode behavior, e.g., topological energy transfer[39]. In addition, it has been shown that these membranes perform well even when coated with superconducting materials like Al[40, 41] or Nb[42]; this makes them a great candidate for a common mechanical element shared between optical and MW resonators, which can be used for information transfer between the two domains[42]. Finally, their relatively large size leads to very low mechanical loss: Q-factors above  $4 \cdot 10^7$ [43] and as high as  $10^8$ [44, 45] have been reported.

The mechanical element inside the cavity does not have to be a membrane. Other possibilities include nanorods[46], or levitated objects such as silica nanoparticles[47] or clouds of cold atoms [48]. The latter systems offer very strong optomechanical coupling, as they have extremely small mass (they consist only of  $10^2 \dots 10^5$  atoms) and, consequently, large ZPF amplitude. It is no surprise that many of the quantum optomechanics effects were first demonstrated in the cold atom systems (as discussed in the next section). Similarly, a Fabry-Perot cavity can be replaced with a different optical resonator, for example, a WGM in a microtoroid with the mechanical element being an evanescently coupled nanobeam[49].

Another class of systems use the advantages of modern micro- and nano-fabrication techniques and focus on miniaturization to achieve large optomechanical coupling and scalability. Some of the most notable systems of this kind are optomechanical crystals[6], in which both optical and mechanical modes are confined inside an artificial defect embedded into a combined photonic/phononic crystal. Due to the extremely small mode volume (only several  $\mu\text{m}^3$ ), they demonstrate large optomechanical coupling and high mechanical frequencies. As shown in section 3.2, this has allowed these systems to feature prominently in the quantum optomechanics field.

Another common approach to creating an optomechanical system is to use a MW resonator for the optical part, but instead of a cavity realize it as a lumped element *LC*-circuit. The optomechanical coupling in such a system is usually realized by making the mechanical motion modulate the gap in a vacuum-gap capacitor, which is embedded either directly in the *LC*-circuit[50, 51], or in a two-level system coupled to the *LC*-resonator[52]. Similarly to the optomechanical crystals, these systems concentrate EM energy in a very small volume, which helps them demonstrate a large optomechanical coupling compared to, e.g., MW MIM cavities[41].

Another set of optomechanical systems is built on the concept of stimulated Brillouin scattering[53, 54] (SBS), which is closely related to the work done in this thesis. SBS is a process of photon-phonon scattering similar to the Stokes and anti-Stokes scattering discussed in subsection 2.5.4, but it happens in a continuous medium (usually a 1D waveguide), so in addition to energy it also conserves momentum. Depending on the direction of the scattered photon SBS is usually separated into “forward” and “backward”, with the latter generating higher momentum and higher frequency phonons. Both of these processes have been demonstrated in experiments[55, 56, 57, 58], which usually involve WGM mechanical and optical modes in a toroid, disk, or sphere resonator. An interesting feature of these systems is the chirality of the optomechanical interaction, which can lead to non-reciprocal OMIT[59] and phonon transport[60]. This type of system has also been employed for demonstration of optomechanics with fluids[61].

## 3.2 Linear quantum cavity optomechanics

Now I want to present an overview of linear quantum cavity optomechanics. The name itself reflects that these experiments deal with quantum optomechanics, i.e., optomechanical effects which depend on or reveal the quantum nature of light or the mechanical oscillator. The typical sign of this is the ability to measure or manipulate the mechanical object with a single-quantum resolution (e.g., energy resolution of  $\sim \hbar\omega_m$  or position resolution of  $\sim x_{\text{ZPF}}$ ). At the same time, these experiments are still described by the linearized EOMs (2.66), (2.67), which means that the consideration is usually limited to Gaussian quantum states (coherent or squeezed states).<sup>a)</sup> This is to be contrasted with non-linear quantum optomechanics, which arises, for example, in the strong single-photon coupling regime  $g^{(0)} \gtrsim \kappa$ , or in the presence of a strong (single-phonon scale) intrinsic

---

<sup>a)</sup>It is still possible to generate non-Gaussian mechanical states in these systems using either non-Gaussian input optical states[62, 63], or non-linear detection mechanisms[64]. Nevertheless, the system dynamics in those cases is still linear, and non-Gaussianity arises either from the external source, or from the measurement and post-selection process.

mechanical non-linearity.

### 3.2.1 Overview

The quantum nature of the interaction of light with mechanical motion and RPSN was first explored by Einstein in his 1909 paper [65]. There he discussed the existence of a radiation pressure force noise which is not explained by classical radiation theory, but can be interpreted as the shot noise of momentum transfers from individual photons. More recently, RPSN was examined in the context of precision interferometry for gravitational wave detection[66], where it was interpreted as a source of noise which ultimately imposes the Heisenberg uncertainty relation on the position measurement precision[67, 68]. Its direct experimental observation in a cavity optomechanics setting was first performed in an atomic cloud system[48, 69], followed by the MIM system[70].

Later it was recognized that RPSN can serve as a resource, because the mechanical fluctuations it induces are correlated with the driving field intensity (these correlations were also used as a less direct signature of RPSN in Ref. [70]). These correlations were theoretically shown to generate ponderomotive quadrature squeezing of light inside the cavity[71, 72], improve the displacement sensitivity[73], or to provide a way for quantum non-demolition (QND) measurement of the light intensity [74, 75]. The ponderomotive squeezing scheme has since been realized in atomic clouds[76], optomechanical crystals[77], and MIM systems[78]. The latter system has also demonstrated improved position measurement sensitivity due to the non-classical correlations between the mechanical motion and the vacuum noise background[79].

Another quantum optomechanics signature related to the RPSN[11, 12] is the sideband asymmetry, that is, the difference in the magnitude between the Stokes and anti-Stokes mechanical sidebands (discussed in section 2.6). Its first direct observation in a cavity optomechanics system was performed in the optomechanical crystal defect setup[64, 80], which was followed by the atomic cloud systems[81], electromechanical systems with Al membrane capacitors[12] and optical MIM setups[82, 83]. Because these experiments rely on measuring the perceived energy difference of only one mechanical quantum, they benefit from starting at as low average mechanical phonon occupation  $n_m$  as possible. Since most of the systems start with a large thermal occupation of the mechanical mode, even when cryogenically pre-cooled (e.g., in Ref. [82] the starting phonon bath occupation is  $\gtrsim 10^4$  at the temperature of 0.4 K), additional sideband cooling (as described in subsection 2.5.4) is usually performed.

Finally, the fact that the optomechanical interaction is unitary (i.e., information preserving) allows one to use it for transferring quantum states between the optical and the mechanical objects, or for generating entanglement between them. The transfer methods have been successfully used to store[84] and re-shape[85] microwave pulses, as well as to perform continuous frequency conversion within the optical[86] or the microwave[87] domains, as well as between the two domains[42], all with only a few quanta of added noise. As far as entanglement is considered, schemes have been proposed to generate both steady-state continuous variable entanglement[88, 89, 90, 91], and an EPR-style entanglement using a pulsed technique[92]. The latter method has been implemented in microwave electromechanics[93] and in the optomechanical crystal defect[64] setting; in the latter experiment single-photon counters were also used to generate non-classical correlations between the optical and the mechanical systems, and potentially create non-Gaussian mechanical states.

### 3.2.2 Thermal cooperativity

The majority of the measurements mentioned above crucially rely on one figure of merit: the thermal cooperativity  $\mathcal{C}_{\text{th}}$ , defined as the ratio of the regular optomechanical cooperativity  $\mathcal{C}$  (defined in equation (2.152)) to the phonon occupation of the mechanical bath  $n_{\text{th},m}$ :

$$\mathcal{C}_{\text{th}} = \frac{\mathcal{C}}{n_{\text{th},m}} = \frac{4|\bar{a}g^{(0)}|^2}{\kappa\gamma_m n_{\text{th},m}}, \quad (3.1)$$

Here  $\bar{a}$  is the intracavity amplitude of the control tone,  $g^{(0)}$  is the single-photon optomechanical coupling, and  $\kappa$  and  $\gamma_m$  are the decay rates of the optical and the mechanical modes respectively. There are several ways of interpreting this quantity which are useful for different experiments. Here we will consider three interpretations:

- (1) First, let us examine the sideband cooling experiments. As equation (2.152) shows, in the resolved sideband limit and for the optimal control beam detuning  $\Delta = -\omega_m$  the magnitude of optomechanical damping is

$$\delta\gamma_{m,\text{eff}} = \frac{4|\bar{a}g^{(0)}|^2}{\kappa} = \mathcal{C}\gamma_m. \quad (3.2)$$

This means that the optical mode is cooled by a factor of  $\gamma_{m,\text{eff}}/\gamma_m \approx \mathcal{C}$ , where for simplicity we assume  $\mathcal{C} \gg 1$ . Hence, the mechanical phonon occupation is (equation (2.128))

$$\begin{aligned} n_m &= \frac{n_{\text{RPSN}}\delta\gamma_{m,\text{eff}} + n_{\text{th},m}\gamma_m}{\gamma_{m,\text{eff}}} = \frac{\mathcal{C}n_{\text{RPSN}} + n_{\text{th},m}}{\mathcal{C} + 1} \\ &\approx n_{\text{RPSN}} + \frac{n_{\text{th},m}}{\mathcal{C}} = n_{\text{RPSN}} + \frac{1}{\mathcal{C}_{\text{th}}}. \end{aligned} \quad (3.3)$$

As can be shown from equation (2.127), in the situation that we consider here ( $\Delta = -\omega_m$ ,  $\omega_m \gg \kappa$ ) the heating due to RPSN is negligible:  $n_{\text{RPSN}} \approx (\kappa/4\omega_m)^2 \ll 1$ , so the final phonon occupation can be written as

$$n_m \approx \frac{1}{\mathcal{C}_{\text{th}}}. \quad (3.4)$$

Thus,  $\mathcal{C}_{\text{th}}$  directly determines whether it is possible to cool the mechanical mode close to its vibrational ground state (i.e., achieve  $n_m < 1$ ).

- (2) Now consider a different kind of experiment, the detection of the RPSN. For simplicity, we assume an unresolved sideband limit  $\kappa \gg \omega_m$  and a resonant control beam  $\Delta = 0$ . In this regime the PSD of the RPSN (2.119) can be approximated as

$$S_{\hat{F},\hat{F}}^{\text{RPSN}}[\omega_m] = \left| \bar{a}g^{(0)} \right|^2 \kappa |\chi_c[\omega_m]|^2 \approx \left| \bar{a}g^{(0)} \right|^2 \kappa |\chi_c[0]|^2 = \frac{4|\bar{a}g^{(0)}|^2}{\kappa}. \quad (3.5)$$

To estimate the quality of this measurement, we need to compare this spectrum to the only other mechanical force in the system, the thermal noise. Their ratio can be determined as

$$\frac{S_{\hat{F},\hat{F}}^{\text{RPSN}}[\omega_m]}{S_{\hat{F}^\dagger,\hat{F}}^{\text{th}}[\omega_m]} = \frac{4|\bar{a}g^{(0)}|^2/\kappa}{\gamma_m n_{\text{th},m}} = \mathcal{C}_{\text{th}}. \quad (3.6)$$

Therefore, the thermal cooperativity can be thought of as the ratio of the optomechanical interaction effects (in this case, RPSN) to the thermal bath effects (thermal drive force). This means that if we want to manipulate the mechanical state with quantum precision (which requires the optomechanical effects to be stronger than the thermal decoherence effects) we need  $\mathcal{C}_{\text{th}} \gtrsim 1$ .

- (3) Finally, let us discuss experiments which rely on information transfer between the optical and the mechanical mode, for example, quantum state transfer, wavelength conversion, entanglement, or precision position measurement. To characterize the measurement efficiency, we can examine a simple measurement of the mechanical position. Let us again assume a single resonant measurement beam in the unresolved sideband regime. As shown in equation (2.76), the intracavity amplitude can be written as

$$\hat{a} = \bar{a} \left( 1 - i \frac{2g^{(0)}}{\kappa} \delta\hat{z} \right), \quad (3.7)$$

The modification due to the mechanical displacement  $\delta\hat{z}$  is imaginary (i.e., out of phase with the measurement drive), so we can interpret it as a small phase shift  $\delta\hat{\phi} = (2g^{(0)}/\kappa)\delta\hat{z}$ .

Now let us imagine that we want to detect this phase shift in the reflected light. Due to the discrete nature of light and the random photon arrival times, this measurement will have a statistical error [10]  $\delta\phi_e = 1/\sqrt{N}$ , where  $N$  is the total number of detected photons. This error would correspond to an uncertainty in the position measurement  $\delta z_e = (\delta\hat{z}/\delta\hat{\phi})\delta\phi_e = \kappa/(2g^{(0)}\sqrt{N})$ . Given the measurement time  $\tau$ , the total number of photons leaking out of the cavity is (using equation (2.31))

$$N = |\bar{a}_{\text{out}}|^2 \tau = |\bar{a}\sqrt{\kappa_{\text{ext}}}|^2 \tau = |\bar{a}|^2 \kappa_{\text{ext}} \tau. \quad (3.8)$$

Note that we only consider photons which interacted with the cavity, since these are the only ones bearing the phase shift  $\delta\hat{\phi}$  (we neglect the promptly reflected light, which can be in principle filtered out). Thus, the total uncertainty in the position measurement is

$$(\delta z_e)^2 = \frac{\kappa^2}{4(g^{(0)})^2 N} = \frac{\kappa}{\kappa_{\text{ext}}} \frac{\kappa}{4|\bar{a}g^{(0)}|^2 \tau} = \frac{1}{\eta_\kappa \Gamma_{\text{meas}} \tau}, \quad (3.9)$$

where we have introduced the measurement rate

$$\Gamma_{\text{meas}} = \frac{4|\bar{a}g^{(0)}|^2}{\kappa} \quad (3.10)$$

and the input coupling quantum efficiency

$$\eta_\kappa = \frac{\kappa_{\text{ext}}}{\kappa} \leq 1. \quad (3.11)$$

Equation (3.9) states that in order to measure  $\hat{z}$  with ZPF precision (which is roughly the precision required to distinguish two different quantum states), one needs to be measuring for a time  $\tau_0 = 1/(\Gamma_{\text{meas}}\eta_\kappa)$ ; for a perfect quantum efficiency  $\eta_\kappa = 1$  this simply turns into  $\tau_0 = 1/\Gamma_{\text{meas}}$ . Thus, we can interpret  $\Gamma_{\text{meas}}$  as the measurement rate, i.e., the rate with which we acquire the information about the quantum state of the mechanical oscillator. A more rigorous definition of the measurement rate and the derivation of equation (3.10) is given in Ref. [10]. In different experiments this rate can be interpreted as the entanglement rate [92, 93] or the information transfer rate [42, 92].

In order to assess the final measurement efficiency, we compare this rate to the thermal decoherence rate of the mechanical mode, which is the rate at which the information about the mechanical state gets corrupted by the environment. We can estimate it as the rate at which the mechanical system, initially in the ground state, acquires one phonon of energy, thus changing its quantum state. The total thermalization rate of the mechanical oscillator is  $\gamma_m$ , so it acquires  $\sim n_{\text{th},m}$  phonons in a time  $1/\gamma_m$ ; thus, to acquire one phonon it takes time  $(1/\gamma_m)/n_{\text{th},m} \equiv 1/\Gamma_{\text{th}}$ , where  $\Gamma_{\text{th}} \equiv \gamma_m n_{\text{th},m}$  is the desired thermal decoherence rate.

If we take the ratio of the two rates, we once again obtain

$$\frac{\Gamma_{\text{meas}}}{\Gamma_{\text{th}}} = \frac{4|\bar{a}g^{(0)}|^2/\kappa}{\gamma_m n_{\text{th},m}} = \mathcal{C}_{\text{th}}. \quad (3.12)$$

This provides another interpretation of the thermal cooperativity, as the ratio of the measurement and decoherence rates. To measure the mechanical state with quantum precision, we need the measurement rate to be higher (ideally, much higher) than the decoherence rate, which requires  $\mathcal{C}_{\text{th}} > 1$ . This requirement is a close analogue of the one derived from equation (3.6), where we were considering the state manipulation rates, not the measurement/decoherence rates.

### 3.2.3 Cooperativity improvement possibilities

All of this goes to show that the optomechanical cooperativity is, probably, the most important figure of merit in linear quantum optomechanics applications. To see what is required to improve it, we can examine equation (3.1):

- First, we need large optomechanical coupling  $g^{(0)}$ . Since it can be thought of as an optical resonant frequency shift due to a mechanical displacement of one ZPF, it can be improved by having large ZPF amplitude or large frequency shift per mechanical displacement. Thus, it benefits from having small and light mechanical object (which results in larger ZPF amplitude), small optical mode volume (which leads to better concentration of the optical power, and to larger fractional effects of the mechanical displacement), large mode overlap between the optical and the mechanical subsystems (so that most of the mechanical displacement works towards changing the optical mode frequency), and large interaction of the mechanical system material with light (e.g., large dielectric index of refraction). This is one of the most difficult conditions to satisfy, since sometimes these requirements are contradictory: for example, large mode overlap and large interaction effects usually require a larger mechanical object, while to have large ZPF amplitude we want it to be as small as possible.
- Second, we benefit from low optical loss  $\kappa$ . This means that in addition to having a low-loss empty optical cavity (which, for example, for Fabry-Perot cavities implies high-reflectivity mirrors with low surface roughness) the mechanical object itself should not introduce additional optical loss, e.g., due to absorption or scattering.
- Similarly, we need low mechanical loss  $\gamma_m$ , which requires both low intrinsic loss inside the material, and low clamping/radiation loss due to the confinement of the mechanical mode.
- In addition to low loss, the mechanical object also should have low bath phonon occupation  $n_{\text{th,m}}$ . Typically it requires cryogenic cooling of a system, and the majority of the experiments discussed in subsection 3.2.1 use it to lower the mechanical bath temperatures to values ranging from  $\sim 10$  K down to  $\sim 10$  mK.
- Finally, the thermal cooperativity benefits from having large circulating photon number  $|\bar{a}|^2$ . Oftentimes this value has technical limitations, for example, the maximum output laser power or the amount of classical optical noise. However, in cryogenic experiments it is usually restricted by the optical heating of the mechanical object, which acts against the previous requirement of low mechanical bath occupation. Thus, to support large circulating optical power, the optomechanical system should have low optical absorption and heating, and it should be well-thermalized to the cold environment.

Optomechanical systems based on superfluid helium seem to be well-suited to satisfy many of these criteria. The discussion of superfluid helium properties and their contribution to the requirements above is presented in the next Chapter.

# Chapter 4

## Superfluid helium and acoustic modes

In this Chapter I discuss superfluid helium properties, previous research on its interactions with light, and the general description of our optomechanical device.

I start by reviewing properties of the superfluid helium and how they affect its applications in optomechanics (section 4.1). Then I briefly describe the principles behind our optomechanical device (section 4.2) and review other experiments investigating the interaction of superfluid helium with EM radiation (section 4.3). After that I go into more details about the device and discuss the equations describing the acoustic modes (section 4.4), deduce limits on the mechanical quality factor (section 4.5), and derive the optomechanical coupling (section 4.7).

### 4.1 General superfluid helium properties

Compared to usual liquids, superfluid  $^4\text{He}$  has many extreme and unique properties. Among all liquids, it has one of the lowest densities  $\rho_{\text{He}} = 145 \text{ kg/m}^3$  (second only to liquid hydrogen with the density of  $71 \text{ kg/m}^3$  and liquid  $^3\text{He}$  with the density of  $82 \text{ kg/m}^3$ ) and the lowest speed of sound  $c_{\text{He}} = 238 \text{ m/s}$ [94]. It is a superfluid, which means that it has zero viscosity. Being a quantum fluid with non-trivial thermodynamic properties, it also offers unique kinds of excitations, such as quantized vortices[95, 96, 97], and second and third sound[96, 98]. Together with liquid  $^3\text{He}$  it is the only cryogenic fluid, in that it does not solidify under its own vapor pressure at arbitrarily low temperatures. This is of great importance for observing quantum behavior of helium itself, or of other systems embedded in it. These unique characteristics have already been exploited by using superfluid helium as a host for a variety of systems, such as individual electrons on the helium surface[99, 100, 101] or in bulk[102, 103]; helium excimers[104, 105]; ions, molecules, and atomic clusters[106, 107, 108].

Helium has additional advantages in optomechanics applications. Since we are aiming to perform quantum optomechanics experiments, let us consider superfluid helium (specifically, the acoustic waves in helium) in the context of optimizing the thermal cooperativity (subsection 3.2.3):

- Helium has low density and low effective mass, which contributes to having high ZPF amplitude and hence large optomechanical coupling. Furthermore, as a liquid it can fill an optical resonator and form acoustic modes which have the same shape as the optical modes. This creates a near-perfect overlap between the optical and the acoustic modes.

The downside of superfluid helium is its very low polarizability: its refractive index  $n_{\text{He}}^{(\text{r})} \approx 1.028$ [94] is only slightly higher than vacuum. This means that the optical frequency shift for a given relative helium density change is fairly small (a quantitative discussion of the coupling mechanism is given in section 4.7).

- Since helium stays liquid at arbitrary low temperatures, eventually all of its impurities except for  $^3\text{He}$  solidify and stick to container wall (“freeze out”). Hence, isotopically pure  $^4\text{He}$  (experiments have demonstrated  $^3\text{He}/^4\text{He}$  ratio of  $< 2 \cdot 10^{-10}$ , and possibly  $< 10^{-12}$ [109]) can be an extremely clean and homogeneous material. Combined with the lack of defects and a large electronic bandgap of  $> 18 \text{ eV}$ [110, 111], it results in helium having very low absorption or scattering of light, which leads to low optical loss.

- The absence of viscosity results in a very low sound attenuation, which contributes to high mechanical quality factor. Intrinsic Q-factors of  $10^8$  have been observed in Ref. [112], which is comparable to the state-of-the-art in solid state systems.
- As helium is a cryogenic liquid, it has intrinsically low bath temperature. It also has large thermal conductivity[113] (for an insulator) thanks to its low speed of sound, which makes it easier to thermalize to the cold environment.
- Finally the combination of the low intrinsic absorption and the large thermal conductivity of the superfluid helium contributes to better optical power handling.

This list shows that the density waves in helium should be well suited for optomechanics applications. Looking further, the ability of helium to host a variety of subsystems might make it useful for hybrid optomechanical devices, where a hosted subsystem interacts with acoustic waves, which are subsequently interfaced with light through the optomechanical interaction.

Nevertheless, superfluid helium still has some disadvantages. The most important one is its low index of refraction, which significantly affects the optomechanical coupling. A more technical problem is that it wets almost any material (the only relatively common exception is cesium), leading to the formation of a thin (several tens of nm) superfluid film, called the Rollin film[113, 114], which covers every surface. Since it has no viscosity, this film can support large flow, which makes superfluid helium notoriously hard to contain. Finally, since helium only becomes superfluid below the transition temperature of  $T_\lambda = 2.2$  K and its internal mechanical loss is strongly temperature-dependent (as described in subsection 4.5.1), it naturally requires cryogenic technology.

## 4.2 Device principle

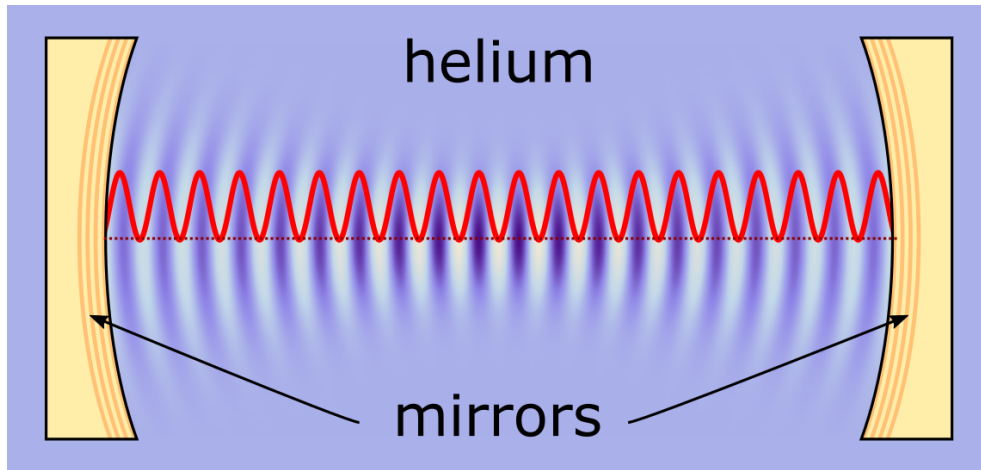


Figure 4.1: Schematic of the superfluid helium filled device. Blue color variations denote the standing acoustic wave, with darker regions corresponding to higher helium density; red line shows the intensity profile of the standing optical wave inside the cavity.

The basis of our device is a Fabry-Perot cavity filled with superfluid helium, as shown in Figure 4.1. This cavity supports optical modes as well as sound modes co-existing in the volume between the mirrors. Both types of modes obey the wave equation (albeit with different propagation velocities) and have the same boundaries, so they have similar mode structures.

The mode type that we are interested in are the Gaussian modes (described in appendix B.2), which closely correspond to the typical picture of standing 1D plane waves, with the mirror curvature providing transverse confinement. The optical modes are confined in the longitudinal direction by the high reflectivity dielectric coating at the mirror surfaces (section B.4), and typically have high finesse (i.e., the average number of photon

round-trips inside the cavity before decaying) of  $\gtrsim 10^4$ . The sound modes are confined by the acoustic impedance mismatch at the hard glass boundaries, which provides a finesse of  $\sim 100$ , as described in subsection 4.5.2. The optomechanical coupling arises due to the density-dependent dielectric constant of superfluid helium, and it is derived in section 4.7.

A more detailed device description is given in section 5.1 and in Ref. [115]. In addition, Ref. [116] gives the description of other kinds of acoustic modes in helium which are coupled to the optical modes in our device. Compared to the Gaussian modes described above, these modes have several disadvantages for our applications: their optomechanical coupling has a considerable photothermal component, they have lower frequencies (10 kHz  $\div$  10 MHz), they are less localized, and their frequencies are highly geometry-dependent. This is why I do not consider these modes in the thesis.

## 4.3 Previous helium optomechanics work

### 4.3.1 Spontaneous Brillouin scattering

Laser light has been used for a long time as an instrument to study acoustic waves[117, 118, 119, 120] and other mechanical excitations in superfluid helium, including rotons[121, 122], second sound[120, 123, 124], isotopic concentration variations[118], surface waves[125], and entropy fluctuations[119]. These studies were performed in the context of spontaneous light scattering: a strong laser beam was incident on the experimental helium cell, and then the scattered light (usually around  $90^\circ$  scattering angle) was collected to measure its intensity and spectrum. For acoustic wave studies, which are most relevant to the work in this thesis, the scattering process is spontaneous Brillouin scattering.

While this method utilizes the same kind of Brillouin interaction as does our work, it is different in several aspects. First, and most important, it is performed in free space without any kind of optical or acoustic resonators. This does not allow one to control the modes of the scattered light and acoustic waves (i.e., scattering happens equally into many different spatial modes), meaning that it is harder to make the interaction coherent and achieve good control and readout efficiency. Second (although related), the scattered light modes are different from the incident light mode; this is in contrast with the canonical optomechanical system, where there is only one optical mode containing both the drive and the scattered (Stokes and anti-Stokes) sidebands. Finally, the scattering experiments were done at a relatively high temperature ( $> 1$  K), where the internal loss of acoustic waves is fairly high: for 320 MHz sound used in our experiment the quality factor at 1 K is only  $\sim 100$  (see subsection 4.5.1). Our experiment is performed in a dilution refrigerator at much lower temperatures, so the mechanical quality factor is much higher (up to 100,000 at low optical powers).

### 4.3.2 Superfluid helium optomechanics

Recently several other cavity optomechanics experiments with superfluid helium have emerged. While they are qualitatively different from the schematic described in section 4.2, all of them use some kind of excitations in the superfluid helium as a mechanical resonator coupled to an EM mode via an optomechanical interaction.

The first reported experiment (and conceptually the closest to ours), is described in Ref. [126]. There the optical mode is a MW mode confined inside a superconducting cavity, and the mechanical mode is an acoustic density wave of helium filling this cavity. The optomechanical interaction arises for the same reasons as in our system (section 4.7), although it is harder to describe in terms of Brillouin scattering, since the optical and acoustic modes do not have a clear plane wave-like structure. This experiment demonstrated very high acoustic quality factors (its upgraded version[112] showed  $Q > 10^8$ ), but due to the very large mode volume, the optomechanical interaction was very small. While it was large enough to measure mechanical motion driven by a piezoelectric element, it was not sufficient to induce any radiation pressure effects.

The second experiment[127] employed a WGM microtoroid resonator to contain the optical mode, while the mechanical mode was third sound[96, 98, 128] (surface acoustic waves on a thin superfluid Rollin film) confined on the top of the toroid. The optomechanical coupling was predominantly photothermal, mediated by a fountain effect[96, 129, 130]. This experiment demonstrated optomechanical coupling strong enough to observe radiation

pressure effects such as optical spring and optomechanical damping. However, due to its photothermal nature it is not well-suited for observation of quantum optomechanics effects.

In the last experiment[131, 132] the mechanical oscillator is a fourth-sound Helmholtz resonator[133]. Its motion was detected via a parallel-plate capacitor, which is sensitive to changes in helium density due to the change in its dielectric constant (similar to Ref. [126] and our work). At the same time, electrostatic forces inside the capacitor were used to drive the acoustic mode by applying an oscillating voltage to the capacitor plates at the mechanical mode frequency. A major difference of this experiment from Ref. [126], apart from a different kind of mechanical mode, is that there is no electromagnetic mode present, and both drive and readout were performed using external devices (an arbitrary waveform generator and a lock-in amplifier). Nevertheless, one could imagine placing such device in a resonant  $LC$ -circuit to produce a more standard optomechanical device, similar to Ref. [50].

## 4.4 Wave equation and modes

In this section I consider the acoustic modes of superfluid helium. Most of the derivation in this section and section 4.7 is described more generally in Ref. [134].

### 4.4.1 Wave equation

First, we need to derive the equations obeyed by the superfluid helium. One of them is a standard continuity equation following directly from the conservation of mass:

$$\frac{\partial \rho}{\partial t} = -\nabla \cdot (\rho \mathbf{v}). \quad (4.1)$$

Here  $\rho$  is the local helium density and  $\mathbf{v}$  is the local velocity. The second equation describes the fluid dynamics, and it corresponds to a local Newton equation. Under the ideal fluid (i.e., no friction) assumption it is written as

$$\rho \frac{d\mathbf{v}}{dt} = \rho \frac{\partial \mathbf{v}}{\partial t} + \rho (\mathbf{v} \cdot \nabla) \mathbf{v} = -\nabla p, \quad (4.2)$$

where  $p$  is the local pressure. Note the difference between the partial time derivative  $\partial \mathbf{v} / \partial t$ , which corresponds to a fixed coordinate system (i.e., it describes change of the fluid velocity at a given fixed point), and the full time derivative  $d\mathbf{v} / dt$ , which corresponds to a coordinate system moving with the fluid (i.e., this derivative describes change in the velocity of a given fluid element). To simplify equation (4.2), we restrict ourselves to the case of “slow” subsonic fluid flows  $v \ll c_{\text{He}}$ . We can estimate the first term in the LHS of equation (4.2) as  $|\frac{\partial \mathbf{v}}{\partial t}| \sim \omega_m v$ , while the second term is only  $|(\mathbf{v} \cdot \nabla) \mathbf{v}| \sim \omega_m v (v / c_{\text{He}}) \ll \omega_m v$ . Thus, we can drop the second term and obtain

$$\rho \frac{\partial \mathbf{v}}{\partial t} = -\nabla p. \quad (4.3)$$

Finally, we need an equation which determines the local pressure. We will treat helium as a simple compressible fluid, for which this equation is

$$p = E_{\text{He}} \frac{\delta \rho}{\rho_{\text{He}}}, \quad (4.4)$$

where  $\delta \rho = \rho - \rho_{\text{He}}$  are the density fluctuations and  $E_{\text{He}} = c_{\text{He}}^2 \rho_{\text{He}}$  is the helium Young’s modulus.

Next, we can linearize the equations (4.1) and (4.3) under the assumption of small density variations. To do that, we substitute  $\rho = \rho_{\text{He}} + \delta \rho$  with  $|\delta \rho| \ll \rho_{\text{He}}$  and only keep the first-order terms in  $\delta \rho$  and  $\mathbf{v}$  (since from the continuity equation  $v / c_{\text{He}} \sim \delta \rho / \rho_{\text{He}}$ ):

$$\frac{\partial(\delta \rho)}{\partial t} = -\rho_{\text{He}} \nabla \cdot \mathbf{v} \quad (4.5)$$

$$\rho_{\text{He}} \frac{\partial \mathbf{v}}{\partial t} = -\nabla p. \quad (4.6)$$

Finally, since we are looking for oscillating wave-like excitations, we can assume that the velocity field is irrotational  $\nabla \times \mathbf{v} = 0$ , that is, there are no vortices in the liquid. This implies that we can define a velocity potential  $\phi_v$  such that  $\mathbf{v} = \nabla\phi_v$ . In terms of this potential equations (4.5) and (4.6) become

$$\frac{\partial(\delta\rho)}{\partial t} = -\rho_{\text{He}}\nabla^2\phi_v \quad (4.7)$$

$$\rho_{\text{He}}\frac{\partial\phi_v}{\partial t} = -p = -E_{\text{He}}\frac{\delta\rho}{\rho_{\text{He}}}. \quad (4.8)$$

Combining the two equations, we obtain the wave equation for the velocity potential

$$\nabla^2\phi_v - \frac{1}{c_{\text{He}}^2}\frac{\partial^2\phi_v}{\partial t^2} = 0. \quad (4.9)$$

Since we are looking for an oscillating solution, we assume  $\phi_v(\mathbf{r}, t) = \phi_v(\mathbf{r})e^{-i\omega_m t}$  for some frequency  $\omega_m$  (keeping in mind that the actual velocity potential is the real part of this expression). This results in

$$\nabla^2\phi_v + k_m^2\phi_v = 0, \quad (4.10)$$

where  $k_m = \omega_m/c_{\text{He}}$  is the mode wave-vector. The corresponding density profile can be obtained from equation (4.8):

$$\frac{\delta\rho}{\rho_{\text{He}}} = i\frac{\omega_m}{c_{\text{He}}^2}\phi_v. \quad (4.11)$$

The density is quarter of a period out of phase compared to the velocity, but its spatial profile is the same as  $\phi_v$ .

#### 4.4.2 Boundary conditions

The sound modes that we consider obey hard wall boundary conditions, which correspond to zero normal velocity. In terms of the velocity potential they are expressed as

$$\frac{\partial\phi_v}{\partial n} = 0, \quad (4.12)$$

where  $\frac{\partial\phi_v}{\partial n} = (\nabla\phi_v) \cdot \hat{\mathbf{n}}$  is the normal derivative of the velocity potential.

#### 4.4.3 Stored energy

Similar to appendix B.5.2, the energy consists of the kinetic and the potential part. The kinetic energy density is

$$u_{s,K} = \frac{\rho_{\text{He}}}{2}\mathbf{v}^2 = \frac{\rho_{\text{He}}}{2}(\nabla\phi_v)^2, \quad (4.13)$$

while the potential energy density is

$$u_{s,P} = \frac{p^2}{2E_{\text{He}}} = \frac{1}{2E_{\text{He}}}\left(\rho_{\text{He}}\frac{\partial\phi_v}{\partial t}\right)^2 = \frac{\rho_{\text{He}}}{2c_{\text{He}}^2}\left(\frac{\partial\phi_v}{\partial t}\right)^2. \quad (4.14)$$

For a mode with a frequency  $\omega_m$  and a spatial profile  $\phi_v(\mathbf{r})$  the total energy is

$$U_s = \int(u_{s,K} + u_{s,P})dV = \frac{\rho_{\text{He}}}{2}\int(\nabla\phi_v)^2dV + \frac{\rho_{\text{He}}}{2c_{\text{He}}^2}\int\left(\frac{\partial\phi_v}{\partial t}\right)^2dV. \quad (4.15)$$

The first integral can be done by parts using the boundary condition (4.12):

$$\int (\nabla \phi_v)^2 dV = \oint_{\partial V} \phi_v \frac{\partial \phi_v}{\partial n} dS - \int \phi_v \nabla^2 \phi_v dV = \frac{\omega_m^2}{c_{\text{He}}^2} \int \phi_v^2 dV. \quad (4.16)$$

The total energy then becomes

$$\begin{aligned} U_s &= \frac{\rho_{\text{He}} \omega_m^2}{2c_{\text{He}}^2} \int \left( \phi_v^2 + \frac{1}{\omega_m^2} \left( \frac{\partial \phi_v}{\partial t} \right)^2 \right) dV \\ &= \frac{\rho_{\text{He}} \omega_m^2}{2c_{\text{He}}^2} \int \left( (\text{Re} \{ \phi_v(\mathbf{r}) e^{i\omega_m t} \})^2 + (\text{Im} \{ \phi_v(\mathbf{r}) e^{i\omega_m t} \})^2 \right) dV \\ &= \frac{\rho_{\text{He}} \omega_m^2}{2c_{\text{He}}^2} \int |\phi_v(\mathbf{r})|^2 dV. \end{aligned} \quad (4.17)$$

The energy can also be rewritten in terms of the relative density change  $\delta\rho/\rho_{\text{He}}$  as

$$U_s = \frac{E_{\text{He}}}{2} \int \left| \frac{\delta\rho(\mathbf{r})}{\rho_{\text{He}}} \right|^2 dV. \quad (4.18)$$

## 4.5 Loss mechanisms

### 4.5.1 Intrinsic loss

For  $T < 600$  mK the main internal loss mechanism for acoustic waves in superfluid helium is the three-phonon process[135, 136, 137]. It can be described by an amplitude attenuation coefficient  $\alpha_{3\text{pp}}$

$$\alpha_{3\text{pp}}(\omega_m) = \frac{\pi^2 k_{\text{B}}^4 (u+1)^2}{30 \hbar^3 \rho_{\text{He}} c_{\text{He}}^6} \omega_m T^4 \left( \arctan(\omega_m \tau) - \arctan\left(\frac{3}{2} \gamma \bar{p}^2 \omega_m \tau\right) \right). \quad (4.19)$$

Here  $\omega_m$  is the acoustic wave frequency,  $T$  is the temperature,  $u = 2.84$  is the Grüneisen constant[138],  $\tau = \xi T^{-5}$  is the thermal phonon lifetime, where  $\xi = 1.11 \times 10^{-7} \text{ s} \cdot \text{K}^5$ [139] and  $\bar{p} = 3k_{\text{B}}T/c_{\text{He}}$  is the average thermal phonon momentum. Finally,  $\gamma$  is the coefficient for the cubic term in the phonon dispersion, which is expressed as  $\gamma = -\frac{1}{6c_{\text{He}}} \frac{d^3\epsilon}{dp^3}$ , where  $\epsilon$  and  $p$  are phonon energy and momentum respectively. It has been measured to be  $\gamma = -8 \times 10^{47} \text{ kg}^{-2} \text{ m}^{-2} \text{ s}^2$ [138].

The internal quality factor of an acoustic mode can be calculated from the attenuation length as

$$Q_{\text{m,int}} = \frac{\omega_m}{2c_{\text{He}} \alpha_{3\text{pp}}}. \quad (4.20)$$

For the relevant acoustic mode frequency  $\omega_m \approx 2\pi \times 300$  MHz and temperature  $T < 0.5$  K both arctan arguments in equation (4.19) are  $\gg 1$ , leading to the simple relationship

$$Q_{\text{m,int}} = \frac{\chi}{T^4}, \quad (4.21)$$

where

$$\chi = \frac{15 \hbar^3 \rho_{\text{He}} c_{\text{He}}^5}{\pi^3 k_{\text{B}}^4 (u+1)^2} \approx 118 \text{ K}^4. \quad (4.22)$$

## 4.5.2 Acoustic radiation loss

Another source of loss is the acoustic radiation of the standing sound wave into the confining mirrors. Like in the optical cavity, this loss can be calculated from the reflection coefficient of the mirrors, and described in terms of the acoustic cavity finesse. The reflection coefficient can be obtained from the acoustic impedance mismatch  $\mathcal{Z}^{(\text{rel})}$  using equation (B.115):

$$R^{(\text{b})} = |r^{(\text{b})}|^2 = \left| \frac{\mathcal{Z}^{(\text{rel})} - 1}{\mathcal{Z}^{(\text{rel})} + 1} \right|^2. \quad (4.23)$$

If we assume that the mirrors are made of silica with density  $\rho_{\text{SiO}_2} = 2.2 \cdot 10^3 \text{ kg/m}^3$  and speed of sound  $c_{\text{SiO}_2} = 6 \cdot 10^3 \text{ m/s}$ [140], the impedance mismatch becomes  $\mathcal{Z}^{(\text{rel})} = (\rho_{\text{SiO}_2} c_{\text{SiO}_2}) / (\rho_{\text{He}} c_{\text{He}}) \approx 380$ , and the reflection coefficient is  $R^{(\text{b})} \approx 99.0\%$ . This results in the acoustic finesse of (using equation (B.65))

$$\mathcal{F}_{\text{ac}} = \frac{\pi}{1 - R^{(\text{b})}} \approx 300. \quad (4.24)$$

For a typical acoustic frequency of  $\omega_{\text{m}} = 300 \text{ MHz}$  and cavity length of  $L = 80 \text{ }\mu\text{m}$  this leads to the quality factor

$$Q_{\text{m,rad}} = n\mathcal{F}_{\text{ac}} = \frac{\omega_{\text{m}}}{2\pi F} \mathcal{F}_{\text{ac}} = \frac{2\omega_{\text{m}}L}{2\pi c_{\text{He}}} \mathcal{F}_{\text{ac}} \approx 6 \cdot 10^4. \quad (4.25)$$

This simple calculation can be extended in two aspects. First, we should take into account the optical DBR layer structure by employing the full transfer matrix formalism described in the subsection B.5.4. Second, due to the difference in the sound velocities the acoustic wavelength in glass is about 30 times larger than in helium, so the sound in glass no longer obeys the paraxial approximation (the transverse mode size is no longer much larger than the wavelength). This means that the 1D plane-wave approximation is no longer applicable, and a full numerical simulation should be performed. Both of these complications are discussed in Ref. [141].

## 4.6 Other excitations and non-ideality considerations

It is evident from the discussion above, that the model of superfluid helium that we assume in our work is fairly simple: an ideal liquid with irrotational flow and simple linear loss due to a three-phonon process. However, superfluid helium is known to have complicated behavior with many different kinds of excitations, as described in section 4.1. In this section I want to try and justify our approximations.

It is well known[135, 136, 142] that below about 0.5 K the only excitations in helium are elementary phonons, as other elementary excitations have higher characteristic energies (roton energies are about 9 K), and therefore are rare enough to not affect phonon behavior. It can also be understood in terms of the two-fluid model[142, 143, 144] as rapid disappearance of the normal component: the relative normal density is  $\rho_{\text{n}}/\rho \approx 10^{-5}$  at 0.5 K[94], and it decreases as  $T^5$  at lower temperatures. Similarly, when considering sound attenuation, only three-phonon processes are taken into account, while phonon-roton interactions and higher-order (5-phonon) processes can be ignored [136].

On the other hand, light absorption in the mirror coating can generate substantial heat flux in helium directly next to the mirror surface, which can raise its temperature up to 1 – 2 K. As mentioned in section 8.4 and discussed in Ref. [141], this can drastically affect the mechanical mode dissipation and effective temperature. However, in that scenario the heated helium layer extends only by  $< 1 \text{ }\mu\text{m}$  from the mirror surface, and bulk of the helium inside the cavity is still at a temperature lower than 0.5 K.

Another important assumption that we made about helium is zero circulation, i.e., absence of vortices or turbulence. We mainly justify this by noting that in our experimental device there are no moving components which would normally generate vortices or turbulent flow. Furthermore, filling of the cavity (see section 5.1) is performed very slowly and at low ( $< 1 \text{ K}$ , and typically  $< 200 \text{ mK}$ ) temperature via superfluid Rollin film[114]. Hence, the cavity never contains bulk helium at a temperature above  $\lambda$ -point, or even any noticeable normal

fluid fraction in the superfluid state. It seems reasonable to assume that the residual vortices density for this case is at most as large as for helium samples which were carefully pumped through the  $\lambda$ -point. Estimates given in Ref. [145] suggest that in our geometry the surface vortex density is on the order of  $2 \cdot 10^3 \text{ mm}^{-2}$ , which results in  $\sim 500$  vortices inside the cavity (i.e., between the fiber mirrors, as described in section 5.1), leading to at most a couple of vortices penetrating acoustic or optical modes.

As far as impurity-type excitations are concerned, most of those are either specifically added impurities (such as molecules or ions[107], or electrons[100]), or require excitation or ionization of helium atoms (electron bubbles, and helium excimers). Such processes require high-energy (deep UV) photons, high power ultra-short laser pulses[105], electrical discharge[103, 146], or charged particles bombardment[147]; none of these sources are explicitly present in our system.

Finally, we need to consider the possibility of light-induced excitations on top the thermal distribution. As mentioned above, we do consider light absorption in cavity mirrors and associated heating effects. However, light scattering in helium itself is fairly small (as discussed in section 6.1.3, our experimental lower bound on the light attenuation length in helium is 15 m). This is in part due to low photon momentum, which means that the resulting excitations are either long-wavelength phonons (indeed, as discussed in the following section, this is one way to interpret the optomechanical coupling in our system), or at least pairs or higher-momentum excitations, such as rotons. The first kind of scattering is expected to be negligible, as even for our experimental phonon mode (which is optimized to have the maximum scattering efficiency) the light interaction effects are relatively small compared to the thermal population. The second kind of process, being higher-order, should be even less important (Ref. [121] suggest that for 488 nm light at  $\sim 1$  K this process is  $10^3$  times weaker, and the total light attenuation length is on the order of  $10^5 \dots 10^6$  m). Finally, non-elementary excitations (e.g., second sound), are, again, suppressed due to low helium temperature, which ensures that the phonons are almost non-interacting: the phonon mean-free path at 0.5 K is  $\approx 1$  mm[148] and goes down as  $T^{-4.3}$ , compared to the characteristic size of the device  $a \approx 100 \mu\text{m}$ .

This concludes my theoretical justification for treating low-temperature superfluid helium as a fairly ideal liquid. Ultimately, the most convincing argument is, probably, the fact we were not able to clearly observe any signatures (such as Stokes scattering peaks) of non-acoustic excitations in our experiments, nor did we need to employ them to explain our experimental results (light and sound attenuation, heat conductivity, or optomechanical coupling).

## 4.7 Coupling mechanism

### 4.7.1 Overlap integral

The origin of the optomechanical coupling is in the fact that the helium index of refraction depends on its change in density, so that it is affected by the acoustic mode. To derive this dependence, we start with the Clausius-Mossotti relation for the dielectric constant[149]

$$\frac{\epsilon^{(r)} - 1}{\epsilon^{(r)} + 2} = \frac{\alpha N}{3\epsilon_0}. \quad (4.26)$$

Here  $\epsilon^{(r)}$  is the relative dielectric constant,  $\alpha$  is the atomic polarizability and  $N$  is the atomic number density. By considering small perturbations of  $\epsilon^{(r)}$  and  $N$ , we arrive at

$$\frac{\delta\epsilon^{(r)}}{\epsilon^{(r)} - 1} - \frac{\delta\epsilon^{(r)}}{\epsilon^{(r)} + 2} = \frac{\delta N}{N} = \frac{\delta\rho}{\rho_0}, \quad (4.27)$$

where  $\delta\epsilon^{(r)}$  and  $\delta N$  are the perturbations of  $\epsilon^{(r)}$  and  $N$  respectively, and  $\rho_0$  is the equilibrium material density.

For superfluid helium  $\epsilon^{(r)} = \epsilon_{\text{He}}^{(r)} = 1.057$ [94],<sup>a)</sup> so the term with  $\epsilon^{(r)} - 1$  in the denominator dominates, and

---

<sup>a)</sup>Strictly speaking, this value for  $\epsilon_{\text{He}}^{(r)}$  is obtained in the low frequency (MW and RF) regime. However, the electronic bandgap of helium  $\omega_{\text{bg,He}} \approx 2\pi \cdot 4$  PHz is much larger than the NIR laser frequency used in this experiment  $\omega_{\text{L}} \approx 2\pi \cdot 200$  THz, which ensures that the optical polarizability  $\alpha$  is still within  $(\omega_{\text{L}}/\omega_{\text{bg,He}})^2 \approx 0.2\%$  of its low frequency value[150].

we can neglect the other term. This leads to

$$\delta\epsilon^{(\mathbf{r})} \approx (\epsilon_{\text{He}}^{(\mathbf{r})} - 1) \frac{\delta\rho}{\rho_{\text{He}}}. \quad (4.28)$$

As described in appendix B.1, perturbations in the dielectric constant can lead to changes in the resonant frequency of an optical mode. Let us assume the density change profile  $\delta\rho(\mathbf{r})$  and the optical intensity profile  $I(\mathbf{r}) \equiv |\mathbf{E}_0(\mathbf{r})|^2$ , where  $\mathbf{E}_0(\mathbf{r})$  is the electric field of the optical mode. Then equations (4.28) and (B.15) yield the relative change in the optical resonant frequency

$$\delta\omega_c = -\omega_c \frac{\int_V (\delta\epsilon^{(\mathbf{r})}(\mathbf{r})/2\epsilon_{\text{He}}^{(\mathbf{r})}) I(\mathbf{r}) dV}{\int_V I(\mathbf{r}) dV} = -\omega_c \frac{(\epsilon_{\text{He}}^{(\mathbf{r})} - 1)}{2\epsilon_{\text{He}}^{(\mathbf{r})}} \frac{\int_V (\delta\rho(\mathbf{r})/\rho_{\text{He}}) I(\mathbf{r}) dV}{\int_V I(\mathbf{r}) dV}. \quad (4.29)$$

### 4.7.2 Mode normalization

In order to derive the value of the single-photon optomechanical coupling  $g^{(0)}$  from equation (4.29), we need to correctly normalize the density fluctuations  $\delta\rho$ . To do this, we are going to use the value of the stored mechanical energy.

Let us recall the derivation of the single-photon optomechanical coupling presented in section 2.2. First, we considered only the mechanical system, which has frequency  $\omega_m$  and is described by the Hamiltonian (equation (2.37))  $\hat{\mathcal{H}}_m = \hbar\omega_m(\hat{b}^\dagger\hat{b} + 1/2)$ , where  $\hat{b}$  is the mechanical annihilation operator. Then, we normalized the mechanical displacement  $\hat{x}$  in terms of its creation and annihilation operators  $\hat{b}^\dagger$  and  $\hat{b}$  (equation (2.38)):  $\hat{x} = x_{\text{ZPF}}(\hat{b} + \hat{b}^\dagger)$ , where  $x_{\text{ZPF}}$  is the proportionality coefficient. Finally, we calculated the detuning of the optical cavity due to the mechanical displacement of  $x_{\text{ZPF}}$  and thus obtained  $g^{(0)}$  as the proportionality coefficient between the cavity detuning and the normalized displacement  $\hat{z} = \hat{b} + \hat{b}^\dagger$  (equation (2.43)):  $\delta\omega_c = g^{(0)}\hat{z}$ .

Now let us consider a large coherent state of the oscillator with some amplitude  $b_0 \gg 1$ , which we can assume WLOG to be real and positive. This lets us approximate the time-dependent annihilation operator  $\hat{b}(t)$  by a classical value  $b(t) = b_0 e^{-i\omega_m t}$ , where the time dependence comes from the Hamiltonian above. This results in the mechanical energy

$$U_m \approx \hbar\omega_m |b(t)|^2 = \hbar\omega_m b_0^2, \quad (4.30)$$

and the normalized mechanical displacement

$$z(t) = b(t) + b^*(t) = 2b_0 \cos(\omega_m t). \quad (4.31)$$

The amplitude of the mechanical motion is therefore  $z_0 = 2b_0$ , and the corresponding cavity detuning is

$$\delta\omega_c = g^{(0)} z_0 = 2g^{(0)} b_0. \quad (4.32)$$

Now we can find the optomechanical coupling  $g^{(0)}$  for the helium acoustic mode by reversing this procedure. Let us assume that the acoustic mode has a density profile  $\delta\rho$  with an arbitrary non-normalized amplitude. From equation (4.18) we can calculate the acoustic energy  $U_m$  stored in this mode, from which we can extract the corresponding amplitude of the coherent state  $b_0$  using equation (4.30):

$$b_0 = \sqrt{\frac{U_m}{\hbar\omega_m}}. \quad (4.33)$$

At the same time, we can calculate the cavity detuning  $\delta\omega_c$  from equation (4.29). Finally, we can combine these two expressions and equation (4.32) to extract the optomechanical coupling:

$$g^{(0)} = \frac{\delta\omega_c}{2b_0} = \delta\omega_c \sqrt{\frac{\hbar\omega}{4U_m}}. \quad (4.34)$$

If we explicitly substitute expressions (4.18) and (4.29) into (4.34), we will end up with the generic expression for the optomechanical coupling

$$g^{(0)} = \omega_c \frac{(\epsilon_{\text{He}}^{(r)} - 1)}{2\epsilon_{\text{He}}^{(r)}} \sqrt{\frac{\hbar\omega_m}{2E_{\text{He}}}} \frac{|\int_V \delta\rho \cdot IdV|}{(\int_V IdV) \sqrt{\int (\delta\rho)^2 dV}}. \quad (4.35)$$

The normalization integrals in the denominator ensure that the value of  $g^{(0)}$  does not depend on the magnitudes of the intensity profile  $I$  and the density profile  $\delta\rho$ .

To estimate the magnitude of  $g^{(0)}$ , we can rewrite it as

$$g^{(0)} = \omega_c \frac{(\epsilon_{\text{He}}^{(r)} - 1)}{2\epsilon_{\text{He}}^{(r)}} \sqrt{\frac{\hbar\omega_m}{2V_{\text{mode}}E_{\text{He}}}} a_{\text{ovl}}, \quad (4.36)$$

where

$$V_{\text{mode}} = \frac{(\int IdV)^2}{\int I^2 dV} \quad (4.37)$$

$$a_{\text{ovl}} = \frac{|\int_V \delta\rho \cdot IdV|}{\sqrt{(\int_V I^2 dV) \int (\delta\rho)^2 dV}}. \quad (4.38)$$

We can associate  $V_{\text{mode}}$  with the effective volume of the optical mode, and recognize  $0 \leq a_{\text{ovl}} \leq 1$  as the effective mode overlap (the limits come from the Cauchy-Schwartz inequality). If we assume the typical frequencies in our experiment  $\omega_c = 2\pi \cdot 200$  THz,  $\omega_m = 2\pi \cdot 300$  MHz, the mode volume of  $V_{\text{mode}} = 100 \mu\text{m} \times 10 \mu\text{m} \times 10 \mu\text{m} = 10^{-14} \text{m}^3$  and the perfect mode overlap ( $a_{\text{ovl}} = 1$ ), we get  $g^{(0)} \approx 2\pi \cdot 6$  kHz.

### 4.7.3 Wavelength matching condition

The fact that the optomechanical coupling is proportional to the overlap integral  $\int \delta\rho(\mathbf{r})I(\mathbf{r})dV$  places a strong restriction on which mechanical modes couple to a given optical mode. To understand this, let us start with a simplified 1D case, where the wave equation solutions are sine waves. For simplicity, we can assume perfect boundary conditions: for the optical mode this means a node of the amplitude at the boundary, while for the mechanical mode it implies a density maximum (as mentioned in subsection 4.4.2). Then the mode profiles can be expressed as

$$E(x) \propto \sin\left(\pi n_{\lambda/2}^{(\text{opt})} x\right) \quad (4.39)$$

$$I(x) \propto |E(x)|^2 = \sin^2\left(\pi n_{\lambda/2}^{(\text{opt})} x\right) \quad (4.40)$$

$$\delta\rho(x) \propto \cos\left(\pi n_{\lambda/2}^{(\text{ac})} x\right), \quad (4.41)$$

where  $0 \leq x \leq 1$  is the normalized position along the cavity, and  $n_{\lambda/2}^{(\text{opt})}$ ,  $n_{\lambda/2}^{(\text{ac})}$  are the numbers of half-wavelengths inside the cavity for the optical and the acoustic mode respectively. An example of an optical mode with  $n_{\lambda/2}^{(\text{opt})} = 3$  and two acoustic modes with  $n_{\lambda/2}^{(\text{ac})} = 6, 8$  is shown in Figure 4.2.

The overlap integral can be calculated as

$$\begin{aligned} \int_0^1 \delta\rho(x)I(x)dx &\propto \int_0^1 \sin^2\left(\pi n_{\lambda/2}^{(\text{opt})} x\right) \cos\left(\pi n_{\lambda/2}^{(\text{ac})} x\right) dx \\ &= \frac{1}{2} \int_0^1 \left(1 - \cos\left(2\pi n_{\lambda/2}^{(\text{opt})} x\right)\right) \cos\left(\pi n_{\lambda/2}^{(\text{ac})} x\right) dx \\ &= \frac{1}{4} \int_0^1 \left(2 \cos\left(\pi n_{\lambda/2}^{(\text{ac})} x\right) + \cos\left(\pi \left(n_{\lambda/2}^{(\text{ac})} + 2n_{\lambda/2}^{(\text{opt})}\right) x\right)\right. \\ &\quad \left.+ \cos\left(\pi \left(n_{\lambda/2}^{(\text{ac})} - 2n_{\lambda/2}^{(\text{opt})}\right) x\right)\right) dx. \end{aligned} \quad (4.42)$$

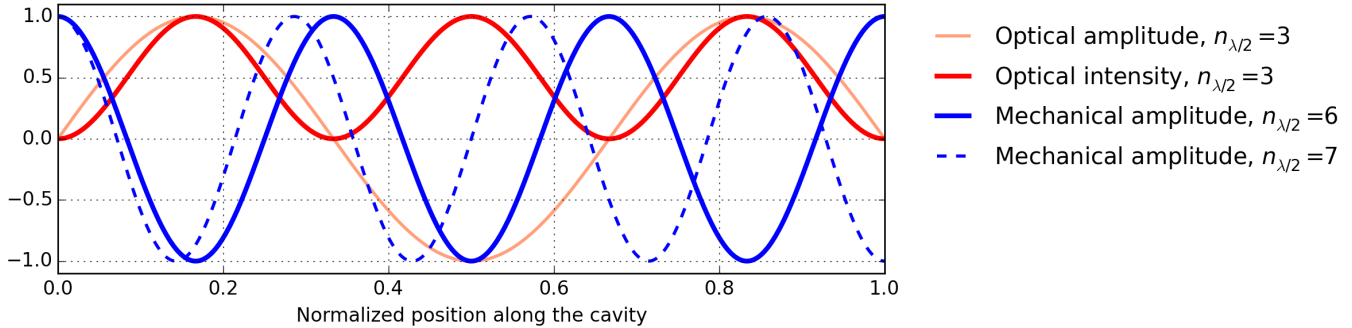


Figure 4.2: Amplitude and intensity for optical and acoustic modes as a function of position along the cavity. Red color corresponds to the optical mode, blue color correspond to acoustic modes.  $n_{\lambda/2}$  denotes the number of half-wavelengths inside the cavity for a given mode.

Since both  $n_{\lambda/2}^{(\text{ac})}$  and  $n_{\lambda/2}^{(\text{opt})}$  are positive integers, the first two terms cancel, and the overlap integral is non-zero only for  $n_{\lambda/2}^{(\text{ac})} = 2n_{\lambda/2}^{(\text{opt})}$ , or, in other words, when the acoustic wavelength is half of the optical wavelength. This can also be seen from Figure 4.2. The mode described by the solid blue line has a maximally negative displacement for every optical intensity maximum, so their overlap is non-zero. On the other hand, the dashed blue line mode is mismatched, and the overlap in the right half of the cavity cancels the overlap in the left half.

The matching condition can also be interpreted in terms of the backward Brillouin scattering (BBS) process. Consider a 1D waveguide (e.g., an optical fiber) which can support both mechanical and acoustic modes. The Brillouin scattering in this medium is a three-wave process in which a photon absorbs or produces a phonon and scatters in a different direction; for simplicity, let us focus on a production process. Since the medium is translationally invariant, this scattering process should obey momentum conservation:  $\mathbf{p}_{\text{in}} = \mathbf{p}_{\text{out}} + \mathbf{q}_{\text{phon}}$ , where  $\mathbf{p}_{\text{in}}$  and  $\mathbf{p}_{\text{out}}$  are correspondingly the momenta of the incident and scattered photons, and  $\mathbf{q}_{\text{phon}}$  is the momentum of the produced phonon. At the same time, the energy is also conserved, which can be expressed as  $\omega_{\text{in}} = \omega_{\text{out}} + \omega_{\text{phon}}$ , where  $\omega_{\text{in}}$ ,  $\omega_{\text{out}}$  and  $\omega_{\text{phon}}$  are the corresponding photon and phonon frequencies. Because the phonon frequency is much smaller than the photon frequency, we can approximate it as  $\omega_{\text{in}} \approx \omega_{\text{out}}$ , so that  $|\mathbf{p}_{\text{in}}| \approx |\mathbf{p}_{\text{out}}|$ . In the backwards scattering  $\mathbf{p}_{\text{in}}$  and  $\mathbf{p}_{\text{out}}$  have opposite direction (i.e., the scattered photon is traveling backwards), which results in  $\mathbf{q}_{\text{phon}} = \mathbf{p}_{\text{in}} - \mathbf{p}_{\text{out}} \approx 2\mathbf{p}_{\text{in}}$  and, consequently  $\lambda_{\text{phon}} = 2\pi/|\mathbf{q}_{\text{phon}}| = \pi/|\mathbf{p}_{\text{in}}| = \lambda_{\text{in}}/2$ , where  $\lambda_{\text{in}}$  is the wavelength of the incident (and, consequently, scattered) light and  $\lambda_{\text{phon}}$  is the sound wavelength.

Coming back to cavity systems, the confining mirrors turn forward-propagating photons into backward-propagating photons and vice versa, meaning that the incident and the scattered photons belong to the same optical mode. Otherwise, the reasoning outlined above still holds, so we can write the wavelength matching condition as  $\lambda_{\text{ac}} = \lambda_{\text{opt}}/2$ , where  $\lambda_{\text{opt}}$  and  $\lambda_{\text{ac}}$  are wavelengths of the optical and the acoustic standing wave respectively. As we can see, this condition exactly corresponds to  $n_{\lambda/2}^{(\text{ac})} = 2n_{\lambda/2}^{(\text{opt})}$  obtained earlier.

The precise requirement of the wavelength matching disappears if the acoustic and optical modes have different boundary conditions. This can happen because the optical mode is confined by an extended DBR structure (see appendix B.4) which can have complicated boundary conditions, while the acoustic confinement happens right at the helium/glass interface. To describe this situation, we can introduce an arbitrary reflection phase of the optical mode  $\phi$  at the boundary (same concept is used in appendix B.2.2); as an example, a perfect mirror corresponds to  $\phi = \pi$ . This changes the shape of the optical mode to

$$E(x) \propto \cos\left(\left(\pi n_{\lambda/2}^{(\text{opt})} - \phi\right)x + \phi/2\right), \quad (4.43)$$

where  $n_{\lambda/2}^{(\text{opt})}$  is still an integer, even though it does not anymore correspond to the number of half-wavelengths inside the cavity. To make this expression look more like equation (4.39), we can redefine  $\phi \rightarrow \pi + \phi$  (now  $\phi = 0$

describes an ideal mirror) and  $n_{\lambda/2}^{(\text{opt})} \rightarrow n_{\lambda/2}^{(\text{opt})} + 1$  to get

$$E(x) \propto \sin \left( \left( \pi n_{\lambda/2}^{(\text{opt})} - \phi \right) x + \phi/2 \right). \quad (4.44)$$

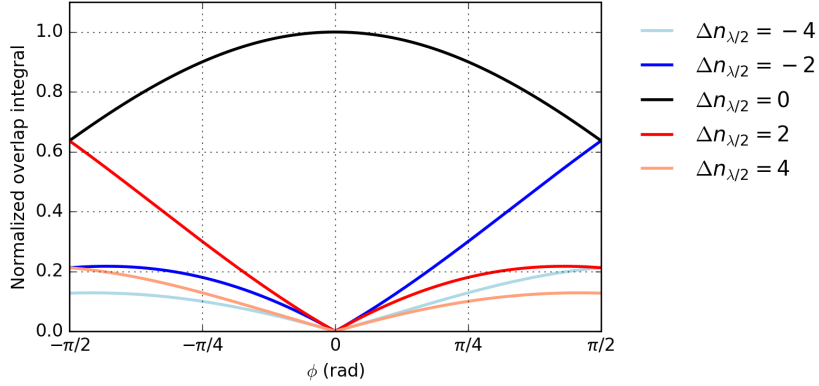


Figure 4.3: Normalized overlap integral as a function of the mirror reflection phase  $\phi$  for different mode mismatch values  $\Delta n_{\lambda/2}$ .

The overlap integral now becomes (after canceling the term which is exactly zero)

$$\begin{aligned} & \int_0^1 \delta\rho(x)I(x)dx \\ & \propto \int_0^1 \left[ \cos \left( \left( \pi n_{\lambda/2}^{(\text{ac})} + 2\pi n_{\lambda/2}^{(\text{opt})} - 2\phi \right) x + \phi \right) + \cos \left( \left( \pi n_{\lambda/2}^{(\text{ac})} - 2\pi n_{\lambda/2}^{(\text{opt})} + 2\phi \right) x - \phi \right) \right] dx \\ & = \begin{cases} 0, & n_{\lambda/2}^{(\text{ac})} \text{ is odd} \\ -2 \sin(\phi) \left( \frac{1}{\pi n_{\lambda/2}^{(\text{ac})} + 2\pi n_{\lambda/2}^{(\text{opt})} + 2\phi} + \frac{1}{\pi n_{\lambda/2}^{(\text{ac})} - 2\pi n_{\lambda/2}^{(\text{opt})} + 2\phi} \right), & n_{\lambda/2}^{(\text{ac})} \text{ is even.} \end{cases} \end{aligned} \quad (4.45)$$

If the cavity is long, i.e.,  $n_{\lambda/2}^{(\text{ac})}, n_{\lambda/2}^{(\text{opt})} \gg 1$ , we can neglect the first term and get

$$\int_0^1 \delta\rho(x)I(x)dx \propto \frac{\sin(\phi)}{\pi \Delta n_{\lambda/2} + 2\phi}, \quad (4.46)$$

where  $\Delta n_{\lambda/2} = n_{\lambda/2}^{(\text{ac})} - 2n_{\lambda/2}^{(\text{opt})}$  and we only consider even  $n_{\lambda/2}^{(\text{ac})}$ . It is evident that unless  $\phi = 0$ , the overlap integral is non-zero for  $\Delta n_{\lambda/2} \neq 0$ , that is, the matching condition is no longer perfect. This seemingly contradicts the Brillouin picture of scattering, where the matching requirement was derived without taking any kind of boundary conditions into account. However, since the cavity is finite, the translation symmetry is broken, and the momentum conservation is satisfied only within some precision  $\Delta p \approx 2\pi/L$ , where  $L$  is the cavity length. This precision corresponds to  $\Delta n_{\lambda/2} = 1$ , which is the characteristic scale of the matching condition (4.46).

Figure 4.3 demonstrates how the matching condition changes for  $\phi \neq 0$ . Since the coupling to the mismatched modes grows as  $\phi$  deviates further from zero, the magnitude of their coupling (or inability to observe these modes for a given signal-to-noise ratio) can place constraints on  $\phi$ .

The results are qualitatively the same when 3D Gaussian modes are considered, though analytic calculations quickly become intractable. Instead, the mode shapes are found from the known system parameters (cavity length, mirror radii of curvature, optical and acoustic frequencies) using the approach described in appendix B.2, and the integrals in equation (4.35) are carried out numerically. Numerical results for particular system geometries are given in sections 6.2.5 and 8.2.

# Chapter 5

## Experimental setup overview

### 5.1 Device description

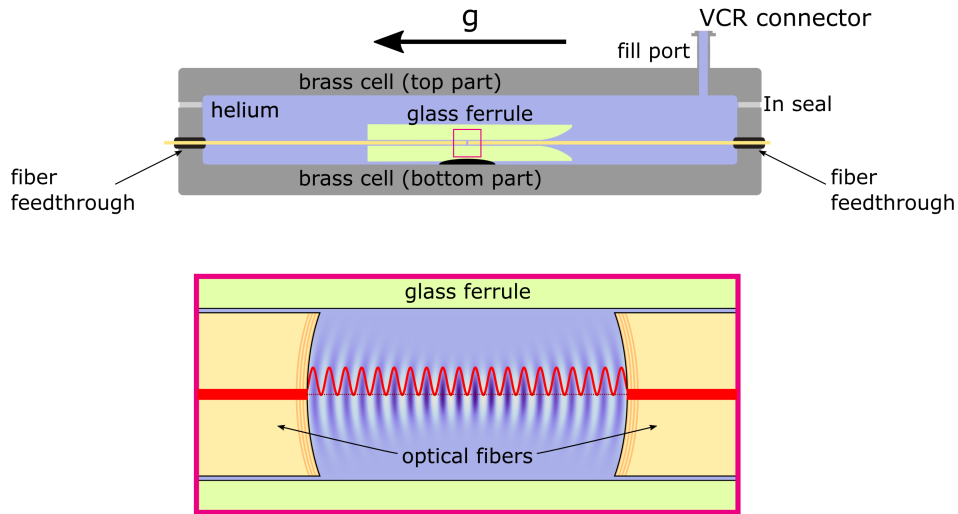


Figure 5.1: Top: Overall schematic of the device cell. The black arrow on top shows the direction of gravity. Bottom: Zoom-in of the cavity region denoted by the magenta rectangle in the top figure. Blue color variations denote the standing acoustic wave, with darker regions corresponding to higher helium density; red line shows the intensity profile of the standing optical wave inside the cavity.

A generic schematic of the main part of the device is shown in the top part of Figure 5.1. The schematic shown here is of the first generation device, in which the cavity is formed inside a single alignment ferrule. The differences of in second generation device are highlighted in section 8.1.

The cavity is formed in the space between the two fibers, whose ends are laser-machined[151] to form convex surfaces with radius of curvature (ROC) between  $200\ \mu\text{m}$  and  $500\ \mu\text{m}$ . The ends are subsequently coated with a high-reflectivity (0.9999 to 0.99999) dielectric DBR mirror coating (section B.4). The fibers are aligned inside a glass ferrule whose inner diameter (ID) is only several  $\mu\text{m}$  larger than the fibers outer diameter (OD). This creates a fairly precise and stable alignment, which can withstand thermal contractions. The ferrule is glued inside the brass cell with a cryogenically-compatible epoxy (Stycast 2850). The fibers are inserted into the cell though long narrow fiber feedthroughs, which are afterwards filled with the epoxy to ensure that they are superfluid helium tight; these feedthroughs are the two points which fix the cavity length. After the ferrule and the fibers are glued inside the cell, it is joined together with a top part using an indium seal, which is known to be very reliable in cryogenic environments. The top part has a helium fill port with a VCR connector for

controlled supplying of helium gas into the cell. After assembly, the device is mounted to the mixing chamber (MC) plate of the dilution refrigerator, which can be cooled down to  $\sim 10$  mK.

The helium fill port is connected to the room-temperature experimental gas handling system (expGHS) through a long stainless steel capillary with OD of 1.5 mm and ID of 0.5 mm. To minimize the heat load, the capillary is heat-sunk at every stage of the dilution refrigerator: 4K plate (4.2 K), 1K plate ( $\sim 1.5$  K), still plate ( $\sim 500$  mK), intermediate cold plate ( $\sim 150$  mK) and MC (down to 10 mK). Heat-sinking at the MC is done by an in-line sintered heat exchanger: a small ( $\sim 2$  cm<sup>3</sup>) chamber filled with sintered silver, which has a porous structure and, therefore, very large surface area ( $\gtrsim 1$  m<sup>2</sup>). This ensures good thermal contact between helium inside the device and the mixing chamber. All other heat sinks are copper bobbins which have capillaries wrapped around them and attached with silver solder.

The expGHS has several calibrated volumes, which allow us to send measured doses of helium gas into the device after it is cooled down. The most commonly used dose has a volume of 13.4 cm<sup>3</sup>, which at a typical pressure of 1.1 atm corresponds to about 0.02 cm<sup>3</sup> of liquid helium condensed inside the device. On the way to the device helium gas passes through a liquid nitrogen trap, which filters out most of the impurities. Additionally, the expGHS has a pressure relief, which is an evacuated vacuum chamber with the volume of 2 liters; it is continuously connected to the capillary going to the device. The relief is large enough to accommodate all of the helium in the system (expGHS and the device combined) at room temperature and pressure below 1 atm. This ensures that the device and the helium delivery lines will not get over-pressurized if the device temperature goes above helium boiling point and all of the liquid helium inside the device evaporates.

As far as the optical part of the device is concerned, the light is sent into and collected from the cavity using the same optical fibers which form the cavity. On the way from the device to the room temperature components the fibers pass through a heat-sink mounted on the 4K plate, which is designed to reduce the thermal load induced by the fibers. The heat-sink is a massive copper block with a channel in the middle, inside which the fibers are epoxied. Since the fibers are thin, and the glass thermal conductivity is fairly small at cryogenic temperatures[113], a single stage of heat-sinking is enough to avoid excessive device heating. After the heat-sink, the fibers travel along a clear-shot tube and through the room temperature vacuum feedthroughs towards the rest of the optical setup.

The bottom part of Figure 5.1b shows a zoomed-in view of the device cavity region. It demonstrates the optical mode intensity (red line) and acoustic mode density modulation (shades of blue) inside the cavity volume in between the two fiber faces. The modes shown satisfy the wavelength matching condition (subsection 4.7.3). However, their wavelengths are intentionally exaggerated for clarity: in the actual device the cavity is about 100 mechanical wavelengths long.

## 5.2 Measurement setup

The measurement setup schematic is shown in Figure 5.2. It can be generally divided into several regions, which are denoted by different color backgrounds in the schematic: light generation and preparation (green), tone generation (blue), detection (brown), cavity lock (purple), and auxiliary measurements and calibration (yellow). Every part is described in more detail below.

### 5.2.1 Light preparation

The light is generated by a tunable fiber-coupled diode laser (TL), whose wavelength (in vacuum) can be tuned between 1440 nm and 1590 nm (in most experiments it is tuned close to 1550 nm, as this is the design wavelength of the mirror coating). The output power is typically kept constant at about 20 mW to improve stability of the laser and the following components (TF, IQM and  $\phi$ M). The the experimental laser power is adjusted using the variable optical attenuator (VOA).

After that, the laser passes through the tunable filter cavity setup (TFCS) to filter out the classical noise. This setup involves several optical and electrical components which are not shown here for simplicity; its detailed description is given in appendix D.1. Due to the presence of the optical circulator at the input of this setup, it



also effectively serves as an optical isolator. This eliminates light reflection back into the laser output, which improves the laser stability and noise characteristics.

Next, the lasers pass through the optical IQ modulator (IQM) and phase modulator ( $\phi$ M), which are described in the corresponding subsections. After that, the light goes through the polarization controller (PCnt) and the VOA, both of which are computer-controlled. The PCnt is used to adjust the polarization to one of the cavity polarization eigenmodes, while the VOA is used to set the final laser power.

Finally, the light is sent into the experimental cavity through an optical circulator, and its reflection is sent onto the detection part of the setup.

### 5.2.2 Tones generation

All of the necessary optical signals (controls, probe, locking, calibration) are generated in the  $\phi$ M from a single laser tone (a detailed description of the phase modulator operation is presented in appendix C.3). Each optical tone is created with a single microwave tone going into the  $\phi$ M, with the transmitted carrier serving as the optical local oscillator (OLO) for the heterodyne detection. Thus, this kind of generation can be thought of as a direct mapping of the microwave domain signal onto the optical domain, while the heterodyne detection transforms the signal back onto the microwave domain; since the OLO is the  $\phi$ M carrier, the detected MW beatnotes end up being coherent and phase-locked with the corresponding MW generation signals. This allows for great setup flexibility (as adding another optical signal corresponds to simply sending an extra microwave tone into the  $\phi$ M) and high degree of coherence between different optical signals, which is limited only by the quality of external clock acquisition in the microwave generators.

In the electrical part of the setup, the main drive tones are generated by separate MW components and are then combined together in the main  $4 \times 1$  combiner. The combined drive gets amplified, and an optional calibration low-frequency tone is added using a direction coupler (the purpose of this tone is explained in appendix D.9). After that, the drive is sent through another directional coupler, where a small part of it is split off into the spectrum analyzer (SA) for monitoring and calibration of the  $\phi$ M drive, while the main output is sent into the  $\phi$ M. The procedure for calibrating the  $\phi$ M drive strength is described in appendix D.7.

Below is the list of the microwave drives:

- (a) First control drive (“control 1”), which corresponds to the lower frequency control beam. It is created using a single microwave generator (MWG 2), and its typical frequency is 1790 MHz. The tone is sent through a low-pass filter to reduce the noise added into the  $\phi$ M at the frequencies corresponding to the mechanical sideband (around 2110 MHz). This ensures that no classical laser noise is added in the  $\phi$ M.
- (b) Probe drive (“probe”), which is used in the OMIT/A measurements, and to obtain optical cavity sweeps. It is provided by the vector network analyzer (VNA) output, and typically lies between 1900 MHz and 2300 MHz. The VNA output is attenuated by about 20 dB (not shown) to reduce the classical microwave noise.
- (c) Second control tone (“control 2”), corresponding to the upper frequency control beam. It is generated by combining the microwave local oscillator (MWLO), which is provided by a microwave generator (MWG 1), with the output of the Zurich Instruments UHF Lock-In amplifier (ZILI) in the up-mixer circuit (described in appendix D.3). Similarly to the first control tone, this tone is also filtered to reduce its noise. However, since its frequency is higher than the mechanical sidebands, a high-pass filter is used. The typical frequency of this tone is 2430 MHz.
- (d) Lock tone (“lock”), which is used to determine the detuning of the OLO from the experimental cavity resonance. Its frequency is usually 2100 MHz, which is close to the OLO-cavity detuning (so that the optical locking beam lies near the cavity resonance). Like the “control 2” drive, it is generated by combining the MWLO with a ZILI output in a second up-mixer circuit. Similar to the probe drive, this tone is also attenuated to reduce the noise.

- (e) Phase calibration tone (“ $\phi_{cal}$ ”) used in the sideband correlation measurements. It adds a low frequency ( $\sim 320$  MHz) drive into the phase modulator, which is used to generate second-order sidebands on the control beams for phase calibration; a more detailed description of the calibration procedure is given in appendix D.9. This is the only microwave tone added not in the main combiner, due to its frequency being very different from the rest of the tones.

### 5.2.3 Detection

The light reflected from the cavity passes through the optical circulator and into the erbium-doped fiber amplifier (EDFA). The EDFA boosts the laser power by about a factor of 10 to 20, depending on its input power. Without it, the noise in the system is heavily dominated by the microwave amplifier noise on the output of the photodiode (PD), which significantly reduces the measurement SNR. The output of the EDFA contains the amplified optical signal together with the amplified spontaneous emission (ASE), which acts as a very broadband noise background with a bandwidth of about 20 nm. For low ( $\lesssim 10 \mu\text{W}$ ) optical power at the EDFA input most of its output power is contained in the ASE, which adds a lot of extra noise to the photocurrent. To reduce the ASE, the laser passes through a tunable filter (TF) with a bandwidth of about 0.6 nm (80 GHz), which is narrow enough to get rid of most of the ASE, but wide enough to not significantly affect the measurement signal.<sup>a)</sup> The procedure for calibrating the noise figure for the EDFA+TF system is described in appendix D.5.

The amplified and filtered optical signal subsequently lands on the photodiode and gets converted into a photocurrent, which goes through a high-pass filter (to get rid of the DC component) and a chain of MW amplifiers. It then gets split in a  $1 \times 3$  splitter into three branches:

- (a) One part goes to the input of the VNA, thus completing the driven optical measurement loop. As mentioned in the previous section, the generation and detection processes happen coherently, meaning that the VNA input is phase-coherent with its output. This allows one to obtain both amplitude and phase information from the VNA sweeps. For the calibration procedure of the measurement loop gain, see appendix D.6.
- (b) Another part gets mixed down with the same MWLO as used in the up-mixing procedure, and the IF signal is sent into the ZILI. This signal is used both for coherent detection of the locking beam beatnote (described in subsection 5.2.4), and for obtaining the PSD of the optical signal around the cavity resonance frequency. When measuring the undriven motion of the mechanical oscillator, this part of the optical spectrum contains the mechanical sidebands. Hence, the data obtained with ZILI is used to measure the PSD of the underdriven mechanical motion (section 8.4).

Care needs to be taken to ensure that the measured signals are phase-coherent. The locking beatnote signal is automatically coherent with the corresponding ZILI output, since the up-mixing and down-mixing is performed with the same MWLO, and the  $\text{MW} \Rightarrow \text{optical} \Rightarrow \text{MW}$  process is already coherent. However, the sideband correlation measurements require that the two control beams are also coherent. This is achieved by synchronizing the MWG 1, MWG 2 and ZILI internal clocks to the same 10 MHz clock signal generated by a commercial Rb clock.

- (c) Finally, part of the signal is directed towards the SA, where it is used to gain a broad-range coarse record of the reflection spectrum, mainly for debugging purposes.

### 5.2.4 Laser locking

Generally, the locking can be separated into 3 stages: obtaining the error signal, generating the feedback signal, and applying the feedback to correct for the error.

---

<sup>a)</sup>One should distinguish the photocurrent noise coming from the ASE beating with the OLO, and the noise coming from beating of the ASE with itself (which is the noise which exists even if there is no OLO). The first kind of noise comes from the ASE right at the signal frequency, and it directly corresponds to the SNR of the optical signal; thus, it cannot be reduced with simple filtering, which affects the signal and the noise to the same extent. The second kind of noise, however, comes from the full ASE bandwidth, and can be made smaller if the ASE bandwidth is reduced while its PSD is kept the same.

- (a) The error signal is obtained from the locking beam beatnote. First, both quadratures of the beatnote are detected in the ZILI, converted into voltage signals, and sent into the FPGA. In the FPGA the 2D beatnote signal is rotated, shifted and transformed into radial coordinates; the phase coordinate is then interpreted as the error signal. For more detail on obtaining the error signal, see appendix D.2.1.
- (b) The feedback signal is generated from the error signal using a proportional-integral (PI) controller with low frequency gain limit (LFGL), which is implemented digitally in the FPGA. More specifically, the feedback signal is a sum of the error signal plus the same signal passed through a single pole low-pass filter. The bandwidth of the filter and the gains of both signals are adjusted to optimize the lock quality.
- (c) Finally, to complete the loop, the feedback signal has to be converted into the laser frequency detuning. To adjust the laser frequency, we use an optical IQ modulator (IQM) working in the single sideband suppressed carrier (SSB-SC) regime. This means that the output of the modulator contains only one tone, which is a sideband whose frequency is either sum or difference (depending on the modulator settings) of the input optical frequency and microwave frequency. Hence, the modulator can be thought of as an optical frequency shifter, where the laser frequency is shifted by the microwave signal frequency. A more detailed description of the IQM is given in appendix D.2.2.

In the measurement setup the I and Q signals are created from a single microwave drive using a  $90^\circ$  hybrid. The microwave drive is generated by a voltage controlled oscillator (VCO), whose frequency tuning port is driven by the feedback signal. As a result, the optical frequency is controlled by the feedback voltage generated by the FPGA, providing the way to complete the feedback loop.

Compared to other feedback approaches (e.g., in which the error signal is sent to the laser piezo, cavity piezo, or acousto-optical modulators) this method has several advantages. First, unlike cavity or laser piezos, it does not impose any additional requirements on the hardware (in our setup neither the laser nor the cavity have piezo tuning). Second, it has a very large bandwidth (short reaction time), which in practice is only limited by the VCO reaction time and can be on MHz scale. Lastly, compared to acousto-optical modulators (AOMs) it has a fairly large range: it is limited by the combination of the VCO tuning range, the  $90^\circ$  hybrid and the IQM bandwidth, but can still span about 1 GHz (compared to  $\sim 10$  MHz for regular AOMs). The disadvantages of this approach are the relative complexity of the setup, large insertion loss (the total insertion loss of the shifter, including the SSB-SC efficiency, is about 10 dB), the need for fine tuning of the IQM bias voltages to achieve complete suppression of the carrier and the other sideband (see appendix D.2.3), and dependence of the laser power on the magnitude of the shift, which requires an additional feedback loop to stabilize (also described in appendix D.2.3).

### 5.2.5 Auxiliary measurements

There are several auxiliary measurements performed during the main experiment:

- (a) The “monitor” tap (Mtap), which is a 90:10 optical combiner after the VOA. Its 90% output is directed into the device, and the 10% (tap) output is used for analysis. Depending on the configuration of the optical switch (OSW), the tap output can either land directly on the photodetector (PD), or pass through a tunable Fabry-Perot cavity (TFPC) first. The first mode is used to monitor the power incident on the device during the experiment. In the second mode the TFPC length is modulated by a triangle wave, and its transmission is recorded as a function of time (i.e., effectively as a function of TFPC resonant frequency). This mode lets us analyze the light spectrum with the resolution of roughly the TFPC linewidth, which is  $\sim 200$  MHz. We use this kind of measurement when calibrating the phase modulator efficiency (appendix D.7) or adjusting the IQM control voltages (appendix D.2.3); examples of TFPC sweeps for the latter measurement are shown in Figure D.4.
- (b) The “reflection” tap (Rtap), which, like the Mtap, is a 90:10 combiner located right before the EDFA. The tap output of this combiner is used to monitor the power reflected off the experimental cavity; since the dependence of the EDFA output power on its input power is highly non-linear, this provides a much

easier and more reliable way to measure the reflection. In addition, this tap is used during the calibration of the EDFA noise figure (appendix D.5).

- (c) The “calibration” tap (Ctap) between the circulator and the experimental device. This tap is used in absolute calibration of the monitor and reflection taps as well as losses in the optical components. The calibration procedure is described in the appendix section D.8.
- (d) The SA used to monitor the coarse ( $\sim 1$  MHz resolution) spectrum of MW signals in the setup. The MW switch (MWSW) on its input allows it to measure either the spectrum of the  $\phi$ M drive, or the spectrum of the photocurrent. The  $\phi$ M spectrum is used to calibrate and later monitor the relative powers of all the tones generated by the  $\phi$ M (see appendix D.7.1). The photodiode spectrum is used for general setup debugging to make sure that there are no unaccounted optical tones.

# Chapter 6

## First generation device

In this Chapter I consider the experimental results obtained with our first generation optomechanical device. I start by presenting the device parameters (subsection 6.1.1) and our initial optical measurements (subsections 6.1.2 and 6.1.3). Then I describe the way we characterized the mechanical modes (section 6.2.1) and the information that it provides about the cavity (subsection 6.2.2) and about the coupling mechanism (subsections 6.2.3 to 6.2.5). After that I discuss in more detail the mechanical loss mechanism and the heating model which determines its dependence on the optical power (section 6.3). Finally, I briefly evaluate the device performance for quantum optomechanics applications (section 6.4).

Most of the results described here, as well as the device description given in section 5.1, are presented in Ref. [115].

### 6.1 Initial optical characterization and filling

#### 6.1.1 Device parameters

The schematic of the device is as described in section 5.1. The two fiber mirrors have radii of curvature (ROC)  $r_1 = 409 \mu\text{m}$  and  $r_2 = 282 \mu\text{m}$ , and their respective designed transmissions are  $T_1 = 103 \cdot 10^{-6}$  and  $T_2 = 10 \cdot 10^{-6}$ , which means that the maximum expected finesse is  $\mathcal{F} = \frac{2\pi}{T_1+T_2} \approx 55,000$ . Both fibers' OD is  $125 \pm 0.7 \mu\text{m}$  and the alignment ferule ID is  $133 \pm 5 \mu\text{m}$ . The cavity length at room temperature is  $\sim 130 \mu\text{m}$ , which contracts to  $\sim 70 \mu\text{m}$  when cooled down to the base temperature of 20 mK.

#### 6.1.2 Empty cavity characterization

When the cavity is cold, we use the frequencies of its fundamental resonances to precisely determine its effective length. To find these resonance frequencies, we use the optical frequency shifter (IQM) to repeatedly sweep the laser frequency over a small range ( $\sim 0.5 \text{ GHz}$ ), while also increasing the frequency of the tunable laser (TL) in  $\sim 0.2 \text{ GHz}$  steps. At the same time, we monitor the reflected power to determine when the laser frequency gets close to the cavity resonance. When the laser frequency is swept around the cavity resonance frequency, we expect to see a Lorentzian dip in reflection with the shape (relative to the background) given by (see equation (C.46)):

$$P_{\text{refl}}[\Delta] \propto |K_{\text{cav}}[\Delta]|^2 = \left| 1 - \frac{2\eta_\kappa}{1 - 2i\Delta/\kappa} \right|^2 = 1 - \frac{4\eta_\kappa(1 - \eta_\kappa)}{1 - 4(\Delta/\kappa)^2}, \quad (6.1)$$

where  $\kappa$  is the cavity linewidth and  $\eta_\kappa = \kappa_{\text{ext}}/\kappa$  is its relative input coupling. The magnitude of the cavity response (i.e., the value of  $\eta_\kappa$ ) helps us verify that we are observing a fundamental TEM00 cavity mode[152], and not a higher-order transverse mode (for which the response is significantly reduced).

After finding several resonance frequencies  $\omega_n$ , we use the differences between the consecutive frequencies  $\Delta\omega_n = \omega_{n+1} - \omega_n$  to determine the cavity's effective free spectral range (FSR)  $F_{\text{eff}}^{(\text{opt})} = \langle \Delta\omega_n \rangle / (2\pi)$  (where

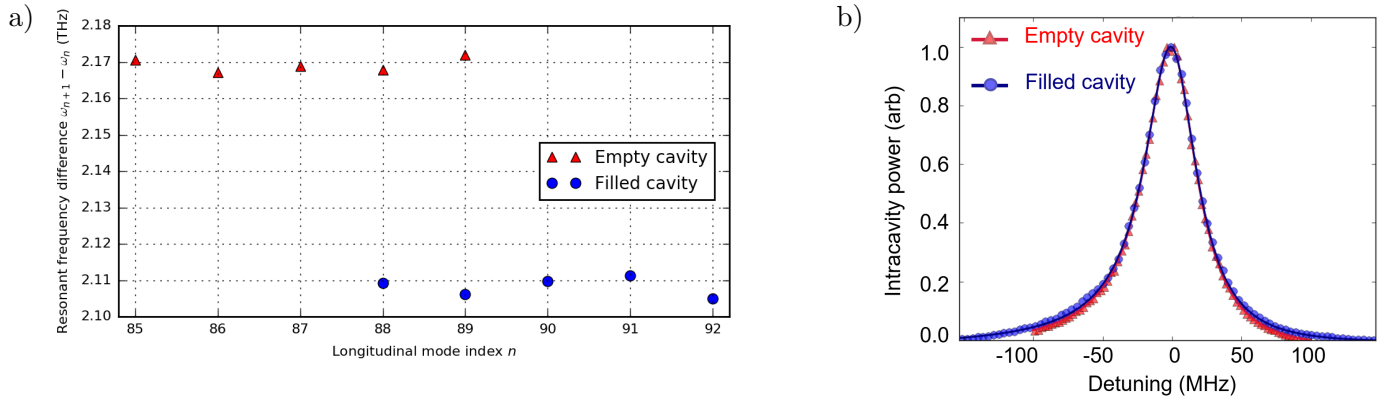


Figure 6.1: a) Frequency difference between consecutive resonances  $\Delta\omega_n$  for different resonance indices measured for empty cavity (red) and for the same cavity filled with superfluid helium (blue). The longitudinal index  $n$  corresponds to the number of nodes of the standing optical wave inside the cavity, and is formally defined in equation (B.32).

b) Optical cavity response for an empty cavity (red) and for a filled cavity (blue). Solid lines show fits to the expected Lorentzian profile.

averaging is taken over several resonances), and from that extract the effective cavity length  $L_{\text{eff}}^{(\text{opt})} = c/(2F_{\text{eff}}^{(\text{opt})})$  (see appendix B.2.3). Red markers in Figure 6.1a show the measured frequency difference. From this data, the cavity FSR is  $F_{\text{eff}}^{(\text{opt})} = 2.169 \pm 0.001$  THz (the error is the statistical uncertainty), which corresponds to an effective length of  $L_{\text{eff}}^{(\text{opt})} = 69.12 \pm 0.04$   $\mu\text{m}$ .

The optical linewidth is measured by locking the laser to the cavity resonance and performing a cavity response sweep using the VNA, as described in appendix subsection C.3.2. The responses are then fit to the expected Lorentzian lineshape, and the linewidth is extracted as a fit parameter. The red plot in Figure 6.1b shows one such response sweep along with the fit. The extracted optical linewidth is  $46.1 \pm 0.1$  MHz, corresponding to a finesse  $\mathcal{F} \approx 47,000$ . Overall, the linewidth shows a significant variation between different resonances, ranging from 46 MHz to 53 MHz. We attribute this variation to a combination of linewidth-dependent DBR reflectivity and geometrical imperfections, e.g., slight cavity misalignment or deviations in mirror surface profile. Such imperfections can cause the fundamental TEM00 mode to hybridize with higher-order transverse modes [152] (which usually have higher loss), and through that can affect its linewidth.

### 6.1.3 Filled cavity characterization

The cavity is filled with helium by slowly adding measured doses of helium gas using the experimental gas handling system (expGHS), as described in section 5.1 (for a detailed modeling of the filling process, see Ref. [116]). Once enough helium is added, the cavity get rapidly filled (since the cavity length is smaller than the typical helium level change for one dose, it goes from empty to filled almost immediately), and we observe a jump in the cavity resonance frequencies. The jump happens because the refractive index of the medium inside the cavity changes from 1 (vacuum) to  $n_{\text{He}}^{(\text{r})} = 1.0282$ [94] (helium). We characterize this change by repeating the measurement of the effective cavity length, and the results are shown with blue dots in Figure 6.1a. Note that red and the blue dots cover the same frequency range, but due to different effective FSRs they correspond to different longitudinal numbers, hence the shift along the horizontal axis. The new extracted FSR is  $F_{\text{eff}}^{(\text{opt})} = 2.109 \pm 0.002$  THz, yielding the length of  $L_{\text{eff}}^{(\text{opt})} = 71.07 \pm 0.06$  THz. This constitutes an increase in  $L_{\text{eff}}^{(\text{opt})}$  by a factor of  $1.0282 \pm 0.0011$ , which is consistent with the helium index of refraction.

At the same time, the optical linewidth does not demonstrate a consistent change. As an example, Figure 6.1b shows the response of the filled cavity (blue dots) plotted on top of the empty cavity response (red dots). The linewidth of this mode of the filled cavity is  $46.3 \pm 0.1$  MHz, which is well within its natural variability between different resonances. If we make a conservative estimate that the linewidth change introduced by

helium is less than  $\kappa = 2\pi \cdot 3$  MHz (half of the linewidth spread for the empty cavity), we obtain a lower bound on the optical attenuation length inside helium of  $c/\kappa \approx 15$  m. This is consistent with the calculated helium Rayleigh scattering length of 200 m for optical wavelength  $\lambda_{\text{opt}} = 78$  nm at  $T = 0.1$  K [153] (the same expression yields  $\sim 10^7$  m scattering length for  $\lambda_{\text{opt}} = 1550$  nm and  $T = 1$  K).

## 6.2 Driven response measurements

### 6.2.1 Experimental procedure

To characterize the mechanical mode, we perform driven mechanical response measurements. Specifically, we employ the optomechanically induced transparency and amplification (OMIT/A) technique, described in section 2.7. To recap: the technique requires injecting two beams in the cavity: a strong control beam and a weak probe beam. The beating between the two beams creates an oscillating force driving the mechanical mode, which modifies the reflection of the probe beam. The mechanical response can be obtained by observing this change in the reflection.

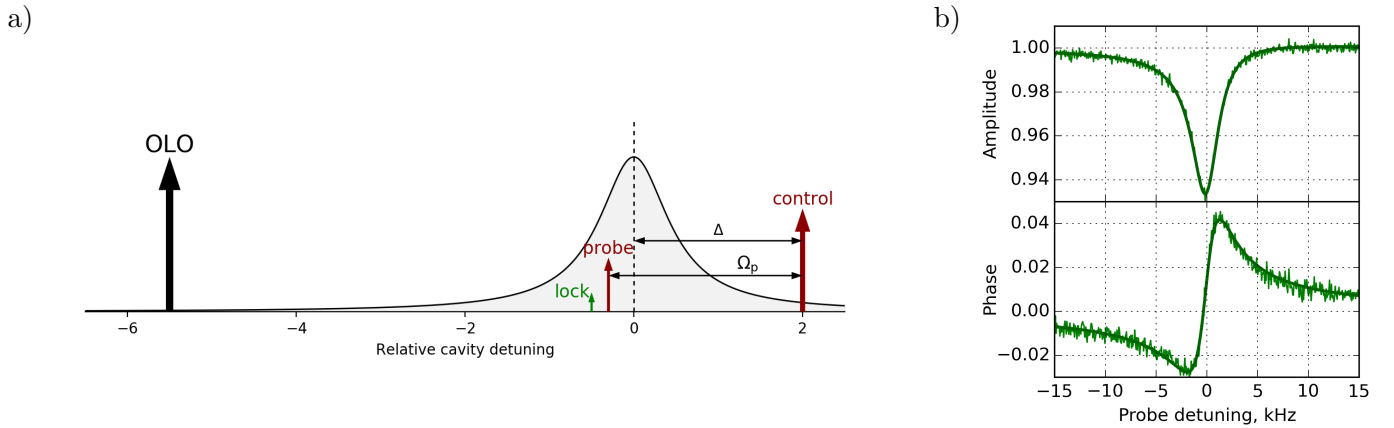


Figure 6.2: a) Optical tone configuration for the OMIA measurement. The horizontal axis is scaled in units of optical cavity linewidths. Tones detunings are not to scale (except for the locking beam).

b) Amplitude (top) and phase (bottom) of a single NA sweep  $a_{\text{p,out}}[\omega]$  as described in the text. The horizontal axis is shifted to have zero at the mechanical resonance frequency, and the data is normalized to have  $a_{\text{p,out}} = 1$  far from the mechanical resonance. Solid lines show the fit to the complex Lorentzian function (6.2).

The optical beams configuration for the OMIA measurement (which has a positive control beam detuning) is shown in Figure 6.2a. As described in section 5.2 and Figure 5.2, both control and probe beams are created in the phase modulator ( $\phi\text{M}$ ) using two microwave tones, with the carrier serving as the OLO. The MW drive corresponding to the control beam is created by a microwave generator MWG 2; the probe beam drive is generated by the NA, which is also used to read its response by measuring the beating between the probe beam and the OLO, as described in subsection 5.2.2 and appendix C.3.2. In addition, there is always a locking beam present to lock the OLO detuning from the cavity (see subsection 5.2.4 for the description). The measurement goes as follows:

- (a) Lock the laser and the experimental cavity; in most measurements the cavity resonance is detuned by  $\nu_c = 2\pi \cdot 2100$  MHz from the OLO.
- (b) Configure the MWG 2 to output a constant microwave tone at a frequency  $\nu_{\text{con}}$  and some fixed power. The power  $P_{\text{con}}$  in the corresponding optical control beam can be extracted knowing the total laser power, the microwave tone power, and the  $\phi\text{M}$  calibration (section D.7).

- (c) Perform an NA sweep in a narrow band (usually,  $\pm 100$  kHz) around  $\nu_p = \nu_{\text{con}} \pm \omega_m$ , where  $\omega_m$  is the mechanical resonance frequency. Typically, the sign is chosen to have the probe beam closer to the cavity resonance, which implies having  $\nu_p$  close to the OLO-resonance detuning  $\nu_c$ .

An example of one such sweep is shown in Figure 6.2b. It is fit to a complex Lorentzian on a complex background:

$$a_{\text{p,out}}[\omega] = a_{\text{bg}} \left( 1 + a_{\text{rel}} \frac{(\gamma_m/2)}{\gamma_m/2 - i(\omega - \omega_m)} \right), \quad (6.2)$$

from which we extract the mechanical frequency  $\omega_m$ , linewidth  $\gamma_m$  and the relative mechanical resonance amplitude  $a_{\text{rel}}$ .

## 6.2.2 Acoustic cavity length and optical penetration depth

First, we perform the OMIA measurements for different optical resonances (different optical longitudinal indices). As discussed in subsection 4.7.3, the optomechanical coupling is dependent on the mode-matching condition  $n_{\lambda/2}^{(\text{ac})} = 2n_{\lambda/2}^{(\text{opt})}$ , where  $n_{\lambda/2}$  is the number of half-wavelengths of a given mode (either acoustic or optical) inside the cavity, i.e., the longitudinal mode index  $n$  mentioned above. Therefore, we expect different optical modes to couple to different acoustic modes. This is indeed what we observe: for each optical mode we can detect only a single mechanical mode, and these detectable mechanical modes vary for different optical modes. Figure 6.3 demonstrates the optical mode frequencies and the corresponding coupled mechanical mode frequencies for several different optical resonances.

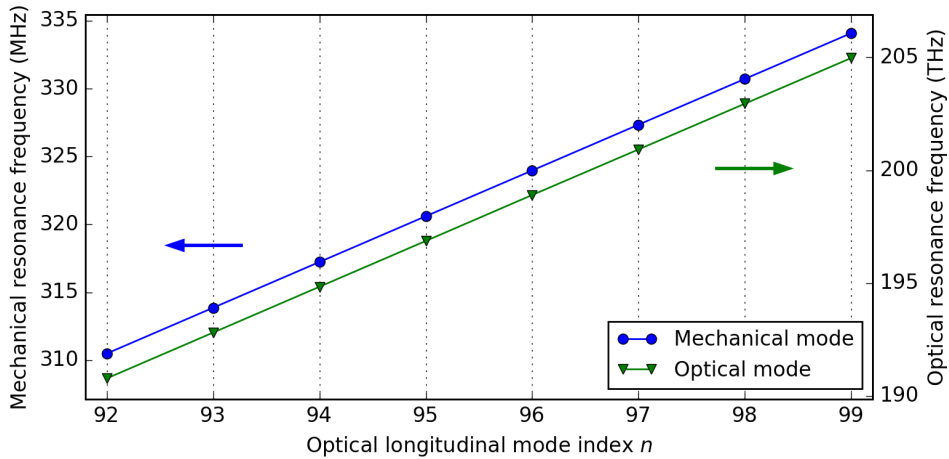


Figure 6.3: Mechanical (blue) and optical (green) resonance frequencies as a function of optical longitudinal mode index. Note that the plots have different vertical axes scale. The vertical axes are rescaled for the data to have the same slope, and shifted for clarity.

From this data we extract the acoustic FSR  $F_{\text{eff}}^{(\text{ac})} = (1/2)\langle\Delta\omega_n\rangle/(2\pi)$  (where  $\Delta\omega_n$  is the difference in mechanical frequencies corresponding to neighboring optical modes), from which we obtain the effective acoustic cavity length  $L_{\text{eff}}^{(\text{ac})} = c_{\text{He}}/F_{\text{eff}}^{(\text{ac})}$ . Note the extra factor of 2 in the expression for  $F_{\text{eff}}^{(\text{ac})}$ : since the acoustic mode number  $n_{\lambda/2}^{(\text{ac})}$  is twice the optical mode number  $n_{\lambda/2}^{(\text{opt})}$ , the mode index difference between the consecutive acoustic modes is 2 (i.e., their frequencies are different by  $2F_{\text{eff}}^{(\text{ac})}$ ). The obtained acoustic FSR is  $F_{\text{eff}}^{(\text{ac})} = 1.685 \pm 0.001$  MHz, and the corresponding cavity length is  $L_{\text{eff}}^{(\text{ac})} = 70.68 \pm 0.02$   $\mu\text{m}$ . Knowing this effective cavity length and the ROCs of the mirrors we can use equation (B.32) to predict the acoustic resonant frequencies in addition to the FSR. In doing that, we assume the geometric cavity length (which determines the Gouy phase shift from equation (B.30)) to be equal to the effective acoustic cavity length, and we set the mirror reflection

phases to be zero, which corresponds to the zero-velocity boundary condition (equation (4.12)). The predicted acoustic frequencies match the observed ones remarkably well, with a discrepancy of about 1% of the acoustic FSR (about 20 kHz).

At the same time, the optical modes yield a different effective cavity length: their FSR is  $F_{\text{eff}}^{(\text{opt})} = 2.090 \pm 0.002$  THz which corresponds to  $L_{\text{eff}}^{(\text{opt})} = 71.72 \pm 0.08 \mu\text{m}^{\text{a}}$ . The difference between the two extracted cavity lengths  $\Delta L_{\text{eff}} = L_{\text{eff}}^{(\text{opt})} - L_{\text{eff}}^{(\text{ac})} = 1.04 \pm 0.08 \mu\text{m}$  can be attributed to the finite penetration depth of the optical mode, as described in subsection B.2.3. Since the optical mode is confined by a DBR structure, it has a non-trivial reflection phase resulting in a non-zero penetration depth; on the other hand, the acoustic mode is almost entirely confined by the helium/fiber interface, and its effective cavity length should be very nearly equal to the geometric cavity length. To estimate the optical penetration depth, we can use the expression (B.93) from section B.4. The DBR mirror coating of our fiber mirrors is composed of layers of  $\text{Ta}_2\text{O}_5$  and  $\text{SiO}_2$  (with a  $\text{Ta}_2\text{O}_5$  outer layer), whose refractive indices are  $n_{\text{Ta}_2\text{O}_5}^{(\text{r})} = 2.05$  and  $n_{\text{SiO}_2}^{(\text{r})} = 1.47$ . Assuming the designed DBR wavelength  $\lambda_0 = 1.55 \mu\text{m}$ , we get the penetration depth of

$$\delta L = \frac{\lambda_0}{4} \frac{n_{\text{He}}^{(\text{r})}}{n_{\text{Ta}_2\text{O}_5}^{(\text{r})}} \frac{n_{\text{SiO}_2}^{(\text{r})}}{(n_{\text{Ta}_2\text{O}_5}^{(\text{r})} - n_{\text{SiO}_2}^{(\text{r})})} = 0.49 \mu\text{m}. \quad (6.3)$$

This is in a good agreement with the experimental result of  $\delta L = \Delta L_{\text{eff}}/2 = 0.52 \pm 0.04 \mu\text{m}$ .

There is another way to obtain the optical penetration depth by comparing the optical resonance data for the filled and the empty cavity. Recall the resonance condition for the  $n^{\text{th}}$  mode of an empty cavity (equation (B.32)):

$$\omega_n = 2\pi F \left( n + \frac{\Delta\psi_{\text{G}}}{\pi} - \frac{\phi(\omega_n)}{\pi} \right), \quad (6.4)$$

where  $\Delta\psi_{\text{G}}$  is Gouy phase shift for the Gaussian mode,  $\phi(\omega)$  is the frequency-dependent reflection phase of the mirror and  $F = c/(2L)$  is the ‘‘geometric’’ cavity FSR, in the sense that it involves the geometric cavity length  $L$ . The filled cavity condition looks almost the same, with the only differences being a rescaled FSR  $F' = F/n_{\text{He}}^{(\text{r})}$  and a potentially different reflection phase  $\phi'(\omega_n)$ :

$$\omega'_n = 2\pi \frac{F}{n_{\text{He}}^{(\text{r})}} \left( n + \frac{\Delta\psi_{\text{G}}}{\pi} - \frac{\phi'(\omega_n)}{\pi} \right). \quad (6.5)$$

We can combine these two expressions to get

$$\begin{aligned} \frac{1}{2F} \left( n_{\text{He}}^{(\text{r})} \omega'_n - \omega_n \right) &= \phi(\omega_n) - \phi'(\omega'_n) = (\phi(\omega_n) - \phi(\omega'_n)) - (\phi'(\omega'_n) - \phi(\omega'_n)) \\ &\approx \frac{\partial\phi}{\partial\omega} (\omega_n - \omega'_n) - (\phi'(\omega'_n) - \phi(\omega'_n)) \\ &= \frac{2\delta L}{c} (\omega_n - \omega'_n) - (\phi'(\omega'_n) - \phi(\omega'_n)), \end{aligned} \quad (6.6)$$

where in the last line we used the definition of the penetration depth (B.34). The first term can be estimated using  $\omega_n \approx n_{\text{He}}^{(\text{r})} \omega'_n$ , from which

$$\frac{2\delta L}{c} (\omega_n - \omega'_n) \approx 2\delta L \frac{\omega'_n}{c} (n_{\text{He}}^{(\text{r})} - 1) \approx 4\pi \frac{\delta L}{\lambda_0} (n_{\text{He}}^{(\text{r})} - 1) \sim \pi (n_{\text{He}}^{(\text{r})} - 1), \quad (6.7)$$

where we used  $\delta L \sim \lambda_0/4$ . At the same time, we could expect the second term to be much smaller. If we assume a perfect DBR, so that  $\phi'(\omega_0) = \phi(\omega_0) = \pi$  (where  $\omega_0 = 2\pi\lambda_0/c$  is the designed DBR optical frequency), we

<sup>a)</sup>The data is different from the results in section 6.1, since it was taken during a different cooldown, resulting in a slightly different cavity parameters.

can estimate this terms as

$$\begin{aligned}
\phi'(\omega'_n) - \phi(\omega'_n) &\approx \frac{\partial \phi'}{\partial \omega}(\omega'_n - \omega_0) - \frac{\partial \phi}{\partial \omega}(\omega'_n - \omega_0) \\
&\approx 2 \frac{\delta L}{c} n_{\text{He}}^{(r)}(\omega'_n - \omega_0) - 2 \frac{\delta L}{c}(\omega'_n - \omega_0) \\
&\approx 2\delta L \frac{(\omega'_n - \omega_0)}{c} (n_{\text{He}}^{(r)} - 1) \ll 2\delta L \frac{\omega'_n}{c} (n_{\text{He}}^{(r)} - 1),
\end{aligned} \tag{6.8}$$

where in going from the first to the second line we used equation (B.93) for the penetration depth dependence on the media outside the DBR. Thus, the second term is much smaller than the first one, and we can neglect it. This allows us to turn (6.6) into

$$\delta L \approx \frac{c}{4F} \frac{(n_{\text{He}}^{(r)} \omega'_n - \omega_n)}{(\omega'_n - \omega_n)} = \frac{L}{2} \frac{(n_{\text{He}}^{(r)} \omega'_n - \omega_n)}{(\omega'_n - \omega_n)}. \tag{6.9}$$

For the geometric cavity length  $L$  we can either use our previous estimate of  $\delta L \approx 0.5 \mu\text{m}$  to calculate  $L = L_{\text{eff}}^{(\text{opt})} - 2\delta L$ , or simply set  $L \approx L_{\text{eff}}^{(\text{opt})}$ . Since  $\delta L \ll L_{\text{eff}}^{(\text{opt})}$ , the latter introduces an error of only 1.5%, well below the statistical uncertainty. Either way, equation (6.9) yields  $\delta L = 0.64 \pm 0.01 \mu\text{m}$  for our data (the statistical uncertainty is most likely underestimated, since it is calculated over only 2 data points). This is still in a decent agreement with the other two estimates; the difference is most likely due to neglecting the second term in equation (6.6).

### 6.2.3 Analysis of OMIT/A data

Now we can perform a more in-depth analysis of the OMIT/A signal by systematically varying the power and the detuning of the control beam and measuring the relative amplitude  $a_{\text{rel}}$  of the OMIT/A response. The measurements described here and in the following sections are performed at a slightly different cavity length of  $84.1 \mu\text{m}$  and for a particular optical mode  $n_{\lambda/2}^{(\text{opt})} = 112$ . This corresponds to the mechanical frequency  $\omega_m = 2\pi \cdot 317.44 \text{ kHz}$  and the optical wavelength (in vacuum)  $\lambda_{\text{opt}} = 1538.30 \text{ nm}$ . The optical linewidth of this mode is measured to be  $\kappa = 2\pi \cdot 69 \text{ MHz}$ , and its external coupling is  $\kappa_{\text{ext}} = 2\pi \cdot 15 \text{ MHz}$ .<sup>b)</sup>

The results of the analysis are shown in Figure 6.4 along with theoretical fits. The dashed lines show the fit to the model described in section 2.7. Specifically, we use equation (2.147) and set  $a_{\text{rel}} = a_{\text{rel},-}$ , because in all measurements  $\Omega_p \approx -\omega_m$  (control beam detuning is positive, so the probe beam has lower frequency to be closer to the cavity resonance). While this model reproduces the magnitude behavior (top plot) very well, it systematically overestimates the relative phase of the response. To explain this deviation, we introduce an additional mechanism of the optomechanical coupling, which we generically call a ‘‘photothermal coupling’’.

### 6.2.4 Photothermal coupling

In this section we consider the photothermal coupling effects only in the classical limit; a full quantum treatment is presented in section 7.3. For consistency with the rest of the derivation, I will keep the operator notation for the cavity field and the mechanical motion. However, one should keep in mind that the derivation in this section should only be applied to the classical case.

The photothermal coupling arises usually arises due to some additional optical forces in the system, which are associated with an optical loss. For example, one possible origin of this force in our system is the light being absorbed in the mirror, which causes it to heat, thermally expand and, consequently, exert a force on the acoustic mode. There are two main distinguishing factors between the photothermal force and the standard radiation pressure. First: since this force is associated with loss, it is not described by a Hamiltonian; in other

<sup>b)</sup>As in subsection 6.2.2, the parameters do not precisely agree with the ones presented in the previous section, because the device was thermally cycled, causing slight mechanical changes. This is especially apparent in the optical linewidth, which is larger than the range given in subsection 6.1.2, most likely due to the cavity misalignment.

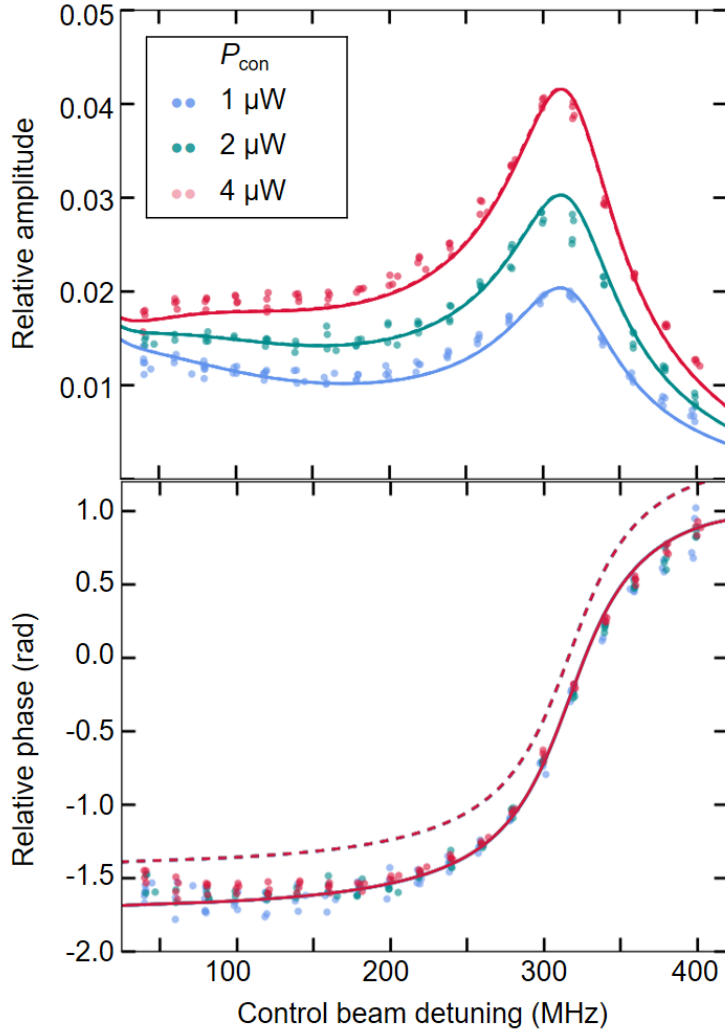


Figure 6.4: Amplitude (top) and phase (bottom) of the relative mechanical response amplitude  $a_{\text{rel}}$  extracted from the fits like the one shown on the right. The horizontal axis shows the detuning of the control beam from the cavity resonance  $\Delta_{\text{con}} = \nu_{\text{con}} - \nu_c$ . As this detuning is positive, the probe beam frequency is always lower than the mechanical frequency:  $\Omega_p = \nu_p - \nu_{\text{con}} = -\omega_m$ . Solid lines show a fit to the theoretical model with only two fit parameters  $g^{(0)}$  and  $g_{\text{pt}}^{(0)}$ . Dashed lines show the fit under the assumption of no photothermal coupling, i.e.,  $g_{\text{pt}}^{(0)} = 0$ ; they almost coincide with the solid lines on the top plot. Different colors correspond to different control beam powers.

words, it does not have an associated position-dependent resonance frequency shift, so its effects only appear in the mechanical equation of motion. Second: this force often has some low-pass filtering or delay due to the slow thermal response. This is in contrast with the radiation pressure force, which is always proportional to the instantaneous intracavity power.

To account for the delayed nature of the photothermal force, we describe its behavior with a relaxation differential equation

$$\tau_{\text{pt}} \dot{\hat{F}}_{\text{pt}} = -\hat{F}_{\text{pt}} + G_{\text{pt}} \hat{n}, \quad (6.10)$$

where  $\hat{F}_{\text{pt}}$  is the photothermal force,  $\tau_{\text{pt}}$  is the thermal reaction time,  $\hat{n} = \hat{a}^\dagger \hat{a}$  is the intracavity photon number ( $\hat{a}$  is the annihilation operator for the intracavity field) and  $G_{\text{pt}}$  is the DC proportionality coefficient between

the photon number and the photothermal force. In the Fourier domain this equation can be easily solved:

$$\hat{F}_{\text{pt}}[\omega] = \frac{G_{\text{pt}}}{1 - i\omega\tau_{\text{pt}}} \hat{n}[\omega]. \quad (6.11)$$

Since we are only interested in the force in a small frequency band around  $+\omega_{\text{m,eff}}$  (where it can efficiently drive the mechanical motion), we can substitute  $\omega \approx \omega_{\text{m,eff}}$  in the denominator of the expression above and transform back into time domain, obtaining

$$\hat{F}_{\text{pt}}(t) = \frac{G_{\text{pt}}}{1 - i\omega_{\text{m,eff}}\tau_{\text{pt}}} \hat{n}(t) \equiv g_{\text{pt}}^{(0)} \hat{n}(t), \quad (6.12)$$

with  $g_{\text{pt}}^{(0)}$  denoting the effective photothermal single-photon coupling, which in general can be complex (signifying the delayed response). The acoustic frequency in our system is fairly large ( $\sim 300$  MHz), so we expect the thermal reaction  $\tau_{\text{pt}}$  time to be much longer than the acoustic period. Hence, we can assume  $\omega_{\text{m,eff}}\tau_{\text{pt}} \gg 1$  and simplify  $g_{\text{pt}}^{(0)} \approx iG_{\text{pt}}/(\omega_{\text{m,eff}}\tau_{\text{pt}})$ . Since  $G_{\text{pt}}$  is real, we find that  $g_{\text{pt}}^{(0)}$  should be purely imaginary.

Now we can add the photothermal force into the mechanical equation of motion (2.50), which turns into

$$\begin{aligned} \dot{\hat{b}} &= -\left(\frac{\gamma_{\text{m}}}{2} + i\omega_{\text{m}}\right) \hat{b} - ig^{(0)} \hat{a}^\dagger \hat{a} - i\hat{F}_{\text{pt}} + \sqrt{\gamma_{\text{m}}}\hat{\eta} \\ &= -\left(\frac{\gamma_{\text{m}}}{2} + i\omega_{\text{m}}\right) \hat{b} - i(g^{(0)} + g_{\text{pt}}^{(0)}) \hat{a}^\dagger \hat{a} + \sqrt{\gamma_{\text{m}}}\hat{\eta}. \end{aligned} \quad (6.13)$$

The optical equation of motion stays the same as before (c.f. (2.49)):

$$\dot{\hat{a}} = -\frac{\kappa}{2} \hat{a} - ig^{(0)} \hat{a} (\hat{b} + \hat{b}^\dagger) + \sqrt{\kappa_{\text{ext}}} a_{\text{in}} e^{+i\omega_{\text{c}} t}. \quad (6.14)$$

We dropped the input vacuum noise terms  $\hat{\xi}_{\text{int}}$ ,  $\hat{\xi}_{\text{ext}}$  to underline that the present treatment is not applicable in the quantum domain. Note that  $g_{\text{pt}}^{(0)}$  enters the equation for  $\hat{b}$ , but not for  $\hat{a}$ .

Given this alteration, the OMIT/A derivation follows very closely the one presented in chapter 2. The important differences are in the definition of the optomechanical self-energy (equation (2.87))

$$\Sigma[\omega] = -i|\bar{a}|^2 g^{(0)} \left(g^{(0)} + g_{\text{pt}}^{(0)}\right) (\chi_{\text{c}}[\omega + \Delta] - \chi_{\text{c}}[\omega - \Delta]) \quad (6.15)$$

(the expressions for  $\gamma_{\text{m,eff}}$  and  $\omega_{\text{m,eff}}$  in terms of  $\Sigma$  stay the same) and in the OMIT/A relative amplitudes (equations (2.146) and (2.147)):

$$a_{\text{rel,+}} = -\frac{2|\bar{a}|^2 g^{(0)} \left(g^{(0)} + g_{\text{pt}}^{(0)}\right)}{\gamma_{\text{m,eff}}} \chi_{\text{c}}[\Delta + \omega_{\text{m,eff}}] \quad (6.16)$$

$$a_{\text{rel,-}} = \frac{2|\bar{a}|^2 g^{(0)} \left(g^{(0)} + \left(g_{\text{pt}}^{(0)}\right)^*\right)}{\gamma_{\text{m,eff}}} \chi_{\text{c}}[\Delta - \omega_{\text{m,eff}}]. \quad (6.17)$$

The only difference is the replacement of  $g^{(0)}$  in one of the terms by the full optical single-photon coupling  $g^{(0)} + g_{\text{pt}}^{(0)}$ .

## 6.2.5 Optomechanical coupling results

The data presented in Figure 6.4 was fit to equation (6.17), and the solid lines show the resulting fit. This fit describes well both the amplitude and the phase of the response. The only two free parameters in the fit were the two coupling rates  $g^{(0)}$  and  $g_{\text{pt}}^{(0)}$ ,<sup>c)</sup> and their resulting values are  $g^{(0)} = 2\pi \cdot (3.18 \pm 0.2)$  kHz and  $g_{\text{pt}}^{(0)} = i \cdot 2\pi \cdot (0.97 \pm 0.05)$  kHz.

<sup>c)</sup>It is only possible to fit them independently, because  $g^{(0)}$  is real and  $g_{\text{pt}}^{(0)}$  is imaginary. If both were real (or  $g_{\text{pt}}^{(0)}$  was a generic complex number), the fit would be under-constrained

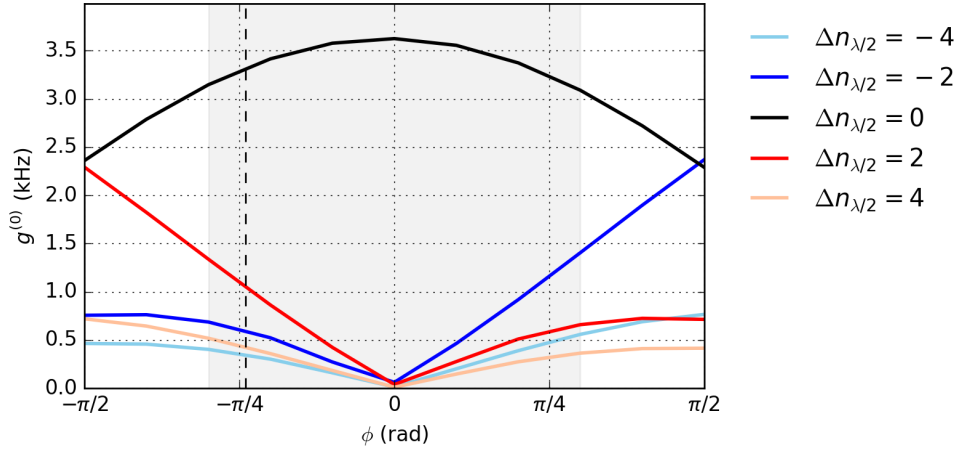


Figure 6.5: Calculated values of  $g^{(0)}$  as a function of reflection phase  $\phi$  (where a perfect mirror corresponds to  $\phi = 0$ ) for different values of the mode number mismatch  $\Delta n_{\lambda/2}$ . The vertical dashed line shows the value  $\phi = -0.24\pi$  estimated from the resonant optical wavelengths. The shaded gray area shows the range  $-0.3\pi < \phi < 0.3\pi$  estimated from the mismatched mechanical modes.

The radiation pressure coupling can be calculated theoretically using the approach outlined in section 4.7. The mechanical and the optical mode profiles are obtained from the known cavity parameters (mirror ROCs and cavity length) and corresponding wavelengths as described in section B.2. The main source of uncertainty in these calculations is the boundary condition of the optical mode, specifically, its reflection phase  $\phi(\omega)$ . While it can be calculated theoretically from the mirror stack parameters, it does not appear to match the experimentally obtained optical resonance frequencies, even though the DBR theory correctly reproduces the distance between the consecutive resonances (i.e., difference in the reflection phase between nearby modes). We attribute this to the fact that the reflection phase is much more sensitive to the exact DBR parameters, and small imperfections in the manufacturing process (e.g., varying layer thickness or refractive index) can strongly affect it.

We can estimate this phase by matching the obtained optical resonance wavelengths to the generic resonance formula (B.32), which yields  $\phi = -0.24\pi$ . Using this value, we obtain  $g^{(0)} = 2\pi \cdot 3.32$  kHz, which agrees reasonably well with the experimentally obtained value of  $g^{(0)} = 2\pi \cdot (3.18 \pm 0.2)$  kHz. We can also put a conservative constraint on the reflection phase by using the coupling to the nominally mismatched acoustic modes, which is the concept discussed in subsection 4.7.3. Figure 6.5 shows the coupling to the main mode, as well as to the four neighboring mismatched modes, as a function of  $\phi$ . We assume that we would be able to observe these mismatched modes if their coupling strength is  $> 45\%$  of the matched mode (i.e., their OMIT/A feature size is  $> 20\%$  that of the matched mode). Since we can not, in fact, detect them, we conclude that the phase angle  $\phi$  lies in the range  $-0.3\pi < \phi < 0.3\pi$ , meaning that the coupling to the main mode should lie between  $g^{(0)} = 2\pi \cdot 3.15$  kHz and  $g^{(0)} = 2\pi \cdot 3.6$  kHz.

## 6.3 Mechanical quality factor and heating

### 6.3.1 Mechanical quality factor measurements

As described in section 4.5, there are two main mechanisms for the acoustic loss: the intrinsic 3-phonon loss and the acoustic radiation loss. The 3-phonon loss is discussed in subsection 4.5.1, where it is shown that it leads to an intrinsic quality factor of  $Q_{\text{m,int}} = \chi/T^4$ , with  $\chi \approx 118 \text{ K}^4$ . The radiation loss (subsection 4.5.2) is temperature-independent, and it can be described by a constant mechanical finesse. A simple helium-glass interface corresponds to an acoustic finesse  $\mathcal{F}_{\text{ac}} \approx 300$ , which limits the quality factor to  $Q_{\text{m,rad}} = n_{\lambda/2}^{(\text{ac})} \mathcal{F}_{\text{ac}} = 5.6 \cdot 10^4$ . A more precise transfer matrix calculation (subsection B.5.4) based on the knowledge of the DBR stacks yields a slightly higher expected quality factor  $Q_{\text{m,rad}} = (7.7 \pm 0.5) \cdot 10^4$  (the error comes from uncertainties

in acoustic properties of the DBR materials); for details of this calculation, see Ref. [141]. Combining the two loss mechanisms, we obtain the relation for the total quality factor:

$$\frac{1}{Q_m} = \frac{1}{Q_{m,int}} + \frac{1}{Q_{m,rad}} = \frac{T^4}{\chi} + \frac{1}{Q_{m,rad}}. \quad (6.18)$$

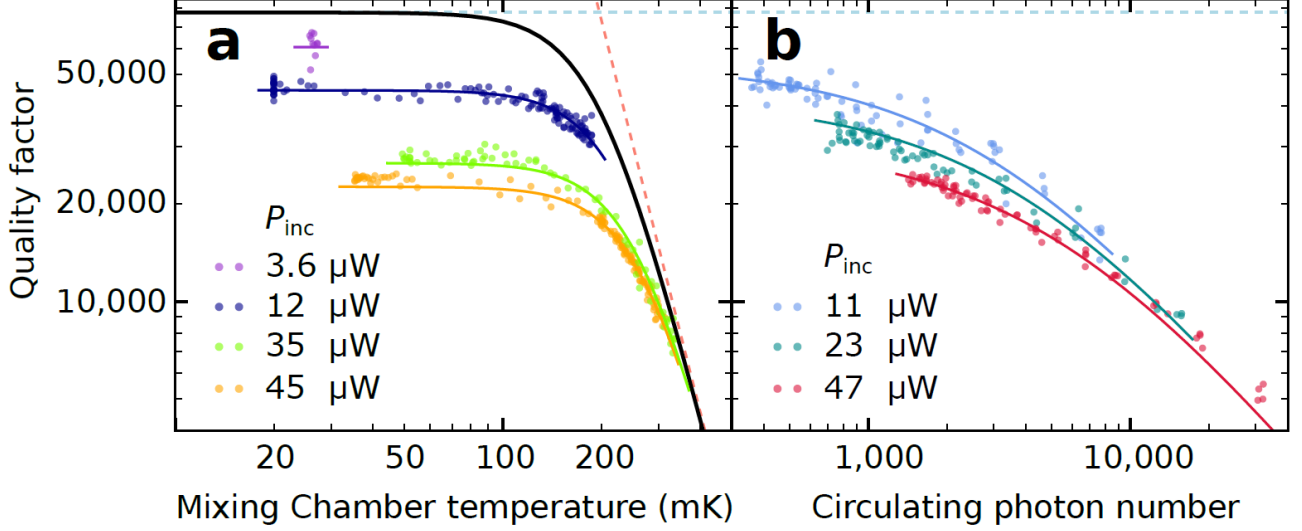


Figure 6.6: a) Mechanical quality factor  $Q_m$  as a function of mixing chamber temperature  $T_{MC}$  for various total incident laser powers  $P_{inc}$ . The black line shows the total expected quality factor (6.18) under the assumption  $T = T_{MC}$ ; the dashed blue line denotes the radiative loss  $Q_{m,rad}$ , while the dashed red line denotes the intrinsic loss  $Q_{m,int}$ . The solid lines are fits to the heating model (6.50). b) Mechanical quality factor  $Q_m$  as a function of the circulating photon number  $\bar{n}_c$  for various total incident laser power  $P_{inc}$ . The blue dashed line is the same as in (a). The solid lines are fits to the heating model (6.50).

To systematically investigate the acoustic loss, we performed OMIT/A measurements while varying the mixing chamber (MC) temperature  $T_{MC}$ , the average intracavity photon number  $\bar{n}_c$ , and the total incident laser power  $P_{inc}$ . The results are summarized in Figure 6.6. The first plot (Figure 6.6a) shows the measurements done when  $P_{inc}$  and the control beam detuning  $\Delta_{con}$  were held constant (so that  $\bar{n}_c$  was constant as well), while  $T_{MC}$  was varied. While the general behavior qualitatively agrees with the theoretical predictions (black line), the quality factor is consistently lower than expected. Furthermore, it seems to be generally lower for larger laser power  $P_{inc}$ . All of this suggests that there is some additional heating inside the device, and that the equilibrium helium temperature  $T$  is higher than  $T_{MC}$ .

The second plot (Figure 6.6b) sheds some more light on the potential loss mechanism. Different datasets shown in this plot are obtained for constant incident powers  $P_{inc}$  and for slightly varying (but low  $T_{MC} < 100$  mK) mixing chamber temperatures; changes in  $\bar{n}_c$  were achieved by altering the detuning of the control beam  $\Delta_{con}$ . Since this beam's contribution to the total circulating photon number scales as  $|\chi_c[\Delta_{con}]|^2 \sim 1/((\kappa/2)^2 + \Delta_{con}^2)$  (where  $\kappa$  is the optical linewidth), this allows us to change  $\bar{n}_c$  by a factor of  $\sim (2\omega_m/\kappa) \approx 80$ . The quality factor shown in the plot demonstrates a clear decreasing trend for growing circulating photon number, which suggests that the heating power scales with  $\bar{n}_c$ . In addition, it also goes down for higher incident powers given the same  $\bar{n}_c$ , so the heating power must also have some contribution due to  $P_{inc}$  which is independent of  $\bar{n}_c$ .

Combining the two heating sources, we can construct the expression for the total heat load:

$$\Phi = \mu P_{inc} + \nu \hbar \omega_L \kappa_{int} \bar{n}_c. \quad (6.19)$$

Here  $\omega_L$  is the laser frequency and  $\kappa_{\text{int}}$  is the internal loss rate of the optical mode, so that  $\hbar\omega_L\kappa_{\text{int}}\bar{n}_c$  is the power lost inside the cavity (i.e., the power contained in the light leaving the cavity but not returning back into the propagating fiber mode). The two coefficients  $\mu$  and  $\nu$ , denote, respectively, the fraction of the power incident on the cavity and the fraction of the power dissipated inside the cavity which contribute to heating.

### 6.3.2 Heating model

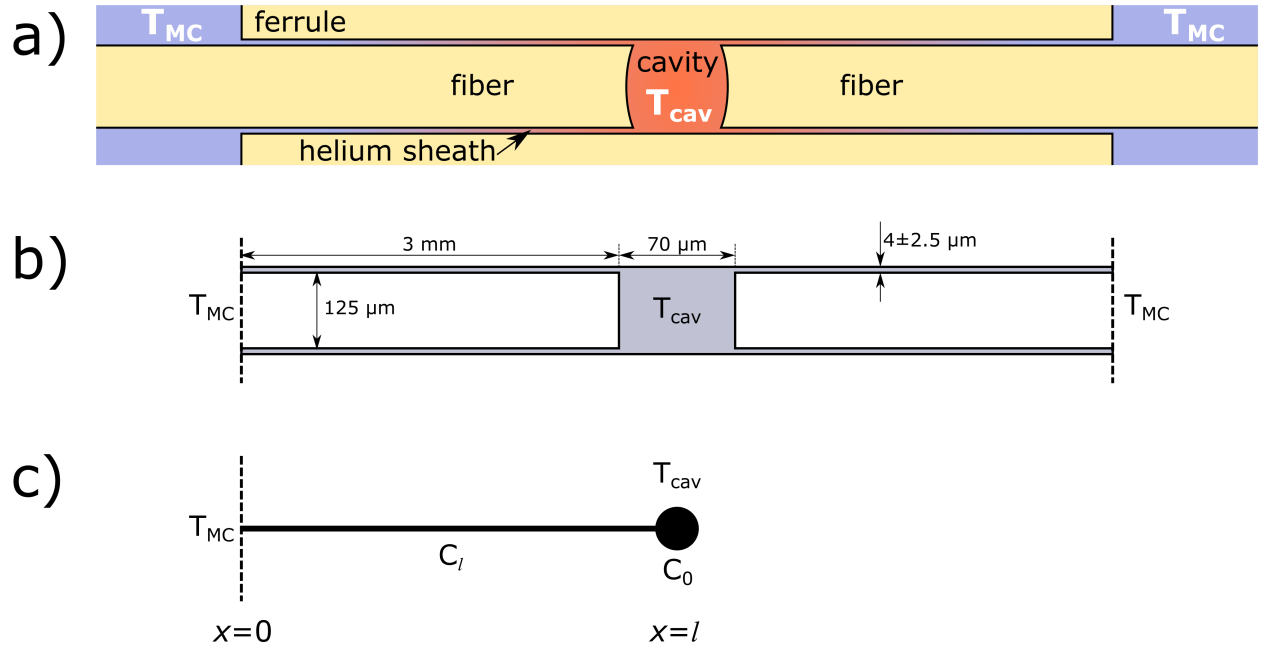


Figure 6.7: a) Schematic of the device (not to scale). The heat load is located inside the cavity (at temperature  $T_{cav}$ ), which is connected to the helium outside (at temperature  $T_{MC}$ ) via long narrow sheaths filled with helium.

b) Simplified geometry of the setup, along with the relevant dimensions.

c) The heating model. The cavity is modeled as a point heat capacity, which is connected to a reservoir through a one-dimensional heat-conducting channel.

To quantitatively describe the heating effects, we have developed a simple model of heat transport in the device. The steady-state solution of this model yields the dependence of the device temperature  $T_{cav}$  on the heat load  $\Phi$  and the temperature of the mixing chamber  $T_{MC}$ . The dynamical solution provides an expression for the thermal relaxation time of the helium inside the cavity, whose subsequent experimental measurements allow us to place additional constraints on the system parameters.

#### Heat transport equation

First, let us define the geometry of the device. Its general layout is shown in Figure 6.7a, and the simplified version in Figure 6.7b. The cavity is a cylindrical volume of helium confined between the two fiber faces inside the ferrule. It is thermally linked to a larger volume of helium outside the ferrule via two identical sheaths. We assume that the helium outside the ferrule has large heat capacity and a good thermal link to the mixing chamber, so its temperature does not depend on the power dissipated inside the cavity and is the same as the mixing chamber temperature  $T_{MC}$ .

Figure 6.7c shows the final simplified model. Since both sheaths are nearly identical, we replaced them with a single sheath with doubled cross-sectional area; due to its extreme aspect ratio, we can treat this sheath as

a one-dimensional channel with a heat capacity per unit length  $C_l$  and a thermal resistance per unit length  $R_l$ . Next, because the sheaths are long, narrow, and have low thermal conductivity, we can assume that the temperature inside the cavity is approximately homogeneous, so we can treat it as a point object with a heat capacity  $C_0$ . Thus, the whole system is represented as a point heat capacity located at  $x = l$  and experiencing heat load  $\Phi$ , which is connected to a reservoir at  $x = 0$  through a 1D channel. The reservoir is maintained at a constant temperature  $T_{MC}$ .

If we denote the temperature-dependent specific heat (per unit volume) of helium by  $c_V(T)$  and its thermal conductivity in the channel by  $\kappa(T)$ , we get for the parameters above

$$C_0(T) = V_{\text{cav}}c_V(T) \quad (6.20)$$

$$C_l(T) = A_{\text{sh}}c_V(T) \quad (6.21)$$

$$R_l(T) = (A_{\text{sh}}\kappa(T))^{-1}, \quad (6.22)$$

where  $V_{\text{cav}}$  is the volume of the cylindrical cavity and  $A_{\text{sh}}$  is the combined cross-sectional area of the sheaths.

The two equations governing the heat transport in the channel are[154]

$$j = -\frac{1}{R_l(T)} \frac{\partial T}{\partial x} \quad (6.23)$$

$$C_l(T) \frac{\partial T}{\partial t} = -\frac{\partial j}{\partial x}. \quad (6.24)$$

The first equation relates the heat current  $j(x)$  and the temperature gradient  $\frac{\partial T}{\partial x}$  (positive values of  $j$  denote heat flowing in the positive  $x$  direction, i.e., from the reservoir into the cavity), and the second one describes the heating of the helium inside the channel. The boundary condition at the reservoir is simply  $T(x = 0) = T_{MC}$ , while for the cavity it is expressed through a heat flow balance

$$\Phi = \left( C_0 \frac{\partial T}{\partial t} - j \right) \Big|_{x=l}. \quad (6.25)$$

This last relation shows that the power  $\Phi$  dissipated in the cavity is partially spent on increasing its temperature and partially transmitted into the channel. Because the thermal conductivity  $\kappa$  and heat capacity  $c_V$  are temperature-dependent, the equations above are in principle non-linear. Nevertheless, since both parameters have the same dependence  $c(T) = \delta_V T^3$ ,  $\kappa(T) = \epsilon_l T^3$ , we can transform the equations into linear ones with an appropriate substitution. For that, we express the material parameters as

$$C_0(T) = V_{\text{cav}}c_V(T) = \delta_0 T^3 \quad (6.26)$$

$$C_l(T) = A_{\text{sh}}c_V(T) = \delta_l T^3 \quad (6.27)$$

$$R_l(T) = (A_{\text{sh}}\kappa(T))^{-1} = (\epsilon_l T^3)^{-1}, \quad (6.28)$$

where  $\delta_0 = V_{\text{cav}}\delta_V$ ,  $\delta_l = A_{\text{sh}}\delta_V$  and  $\epsilon_l = A_{\text{sh}}\epsilon_V$ . Substituting these expressions into equations (6.23), (6.24) and boundary condition (6.25), we obtain

$$j(x) = -\epsilon_l T^3 \frac{\partial T}{\partial x} = -\frac{\epsilon_l}{4} \frac{\partial(T^4)}{\partial x} \quad (6.29)$$

$$-\frac{\partial j}{\partial x} = \delta_l T^3 \frac{\partial T}{\partial t} = \frac{\delta_l}{4} \frac{\partial(T^4)}{\partial t} \quad (6.30)$$

$$\Phi = \left( \delta_0 T^3 \frac{\partial T}{\partial t} - j \right) \Big|_{x=l} = \left( \frac{\delta_0}{4} \frac{\partial(T^4)}{\partial t} - j \right) \Big|_{x=l}. \quad (6.31)$$

Denoting  $u = T^4$ ,  $u_0 = T_{\text{MC}}^4$ , and using the first equation to express  $j$  leads to

$$\frac{\partial u}{\partial t} = \frac{\epsilon_l}{\delta_l} \frac{\partial^2 u}{\partial x^2} \quad (6.32)$$

$$u|_{x=0} = u_0 \quad (6.33)$$

$$\left( \frac{\partial u}{\partial t} + \frac{\epsilon_l}{\delta_0} \frac{\partial u}{\partial x} \right) \Big|_{x=l} = \frac{4\Phi}{\delta_0}. \quad (6.34)$$

Thus, the heat transport equation is expressed as a one-dimensional diffusion equation with the diffusion coefficient  $D = \epsilon_l/\delta_l$ .

### Steady state solution

First, we consider a steady state solution for a constant heat load  $\Phi$ . The diffusion equation turns into  $\frac{\partial^2 u}{\partial x^2} = 0$ , which has the general solution  $u = a + bx$ . The boundary condition at  $x = 0$  immediately yields  $a = u_0 = T_{\text{MC}}^4$ . From the second boundary condition we find  $b = \frac{\partial u}{\partial x} = \frac{4\Phi}{\epsilon_l}$ , which results in

$$u(x) = u_0 + \frac{4\Phi}{\epsilon_l} x, \quad (6.35)$$

From this, the temperature of the cavity can be determined as

$$T_{\text{cav}}^4 = u(l) = T_{\text{MC}}^4 + \frac{4\Phi}{\epsilon_l} l. \quad (6.36)$$

This relation provides the necessary connection between the mixing chamber temperature  $T_{\text{MC}}$ , the heat load  $\Phi$  and the device temperature  $T_{\text{cav}}$ . Together with equation (6.19), it can be used to model the heating behavior demonstrated in Figure 6.6 (see subsection 6.3.3).

### Transient dynamics

Next, we investigate the dynamics of this system. We consider the system to be in the steady state derived above, and then abruptly turn off the power source at  $t = 0$ . We then expect the cavity temperature to decay to  $T_{\text{MC}}$  exponentially with some characteristic time  $\tau_0$ , which we want to determine.

To find the time evolution of the temperature we use the eigenfunction expansion of the solution:

$$u(x, t) = u_0 + \sum_n T_n(t) v_n(x), \quad (6.37)$$

where  $v_n(x)$  is an eigenfunction of the Laplace operator with the appropriate boundary conditions

$$\frac{\partial^2 v_n}{\partial x^2} = -\lambda_n v_n \quad (6.38)$$

$$v_n(0) = 0 \quad (6.39)$$

$$\left( \frac{\epsilon_l}{\delta_l} \frac{\partial^2 v_n}{\partial x^2} + \frac{\epsilon_l}{\delta_0} \frac{\partial v_n}{\partial x} \right) \Big|_{x=l} = 0. \quad (6.40)$$

If we denote  $\lambda_n = k_n^2$  (choosing the opposite sign  $\lambda_n = -k_n^2$  results in the inability to satisfy both boundary conditions simultaneously, as well as an exponentially diverging time evolution), we get from the first two equations that  $v_n(x) = \sin(k_n x)$ . The boundary condition at  $x = l$  restricts the values of  $k_n$

$$-\frac{\epsilon_l}{\delta_l} k_n^2 \sin(k_n l) + \frac{\epsilon_l}{\delta_0} k_n \cos(k_n l) = 0, \quad (6.41)$$

which can be rewritten as

$$(k_n l) \tan(k_n l) = r_V \quad (6.42)$$

with  $r_V = \frac{l\delta_l}{\delta_0} = \frac{lA_{\text{sh}}}{V_{\text{cav}}} = \frac{V_{\text{sh}}}{V_{\text{cav}}}$  is the ratio of the sheath and the cavity volumes. The solutions for this equation exhaust all of the values  $k_n$ .

Now we can substitute the expansion back into equation (6.32) to obtain the equations for the time-dependent parts  $T_n$ :

$$\frac{\partial u}{\partial t} = \frac{\epsilon_l}{\delta_l} \frac{\partial^2 u}{\partial x^2} \quad (6.43)$$

$$\sum_n v_n \frac{\partial T_n}{\partial t} = \frac{\epsilon_l}{\delta_l} \sum_n T_n \frac{\partial^2 v_n}{\partial x^2} = -\frac{\epsilon_l}{\delta_l} \sum_n k_n^2 T_n v_n. \quad (6.44)$$

As the eigenfunctions are orthogonal,<sup>d)</sup> equation (6.44) has to be satisfied for each  $T_n$  independently

$$\frac{\partial T_n}{\partial t} = -\frac{\epsilon_l k_n^2}{\delta_l} T_n = -\frac{T_n}{\tau_n}, \quad (6.45)$$

where  $\tau_n = \frac{\delta_l}{\epsilon_l k_n^2}$  is the characteristic decay time. The solution for this equation is

$$T_n(t) = T_n(0) e^{-t/\tau_n}. \quad (6.46)$$

We are mostly interested in the longest relaxation time  $\tau_0$  corresponding to the smallest value of  $k_n$ , which we denote as  $k_0$

$$\tau_0 = \frac{\delta_l}{\epsilon_l} \frac{1}{k_0^2}. \quad (6.47)$$

With several percent error,  $k_0$  can be approximated by

$$(k_0 l)^{-2} \approx \left(\frac{2}{\pi}\right)^2 + r_V, \quad (6.48)$$

so the relaxation time becomes

$$\tau_0 \approx \frac{\epsilon_l}{\delta_l} l^2 \left(\frac{4}{\pi^2} + r_V\right) = \frac{\delta_l T^3 l}{\epsilon_l T^3 / l} \left(\frac{4}{\pi^2} + r_V\right) = \frac{cl^2}{\kappa} \left(\frac{4}{\pi^2} + r_V\right) = \frac{C_{\text{sh}}}{K_{\text{sh}}} \left(\frac{4}{\pi^2} + r_V\right), \quad (6.49)$$

where  $C_{\text{sh}} = cA_{\text{sh}}l = \delta_l T^3 l$  is the total heat capacity of the sheath, and  $K_{\text{sh}} = \kappa A_{\text{sh}}/l = \epsilon_l T^3 / l$  is the total thermal conductance of the sheath.

The expression above for the thermal relaxation time  $\tau_0$  depends only the sheath's heat capacity, thermal conductance, and the geometric parameter  $r_V$ . The heat capacity of the sheath can be known fairly well, since it only depends on its volume and the specific heat of liquid helium, which for low temperatures is well known [113]. Thermal conductivity, however, is much harder to evaluate *a priori*, since it depends upon the particular geometry of the conducting channel (which determines the mean phonon travel path between collisions with the boundaries) and the scattering properties of its wall. Therefore, measurements of  $\tau_0$  can provide an estimate for the thermal conductivity without the need for any assumptions about the specularly of reflections from the sheath surface.

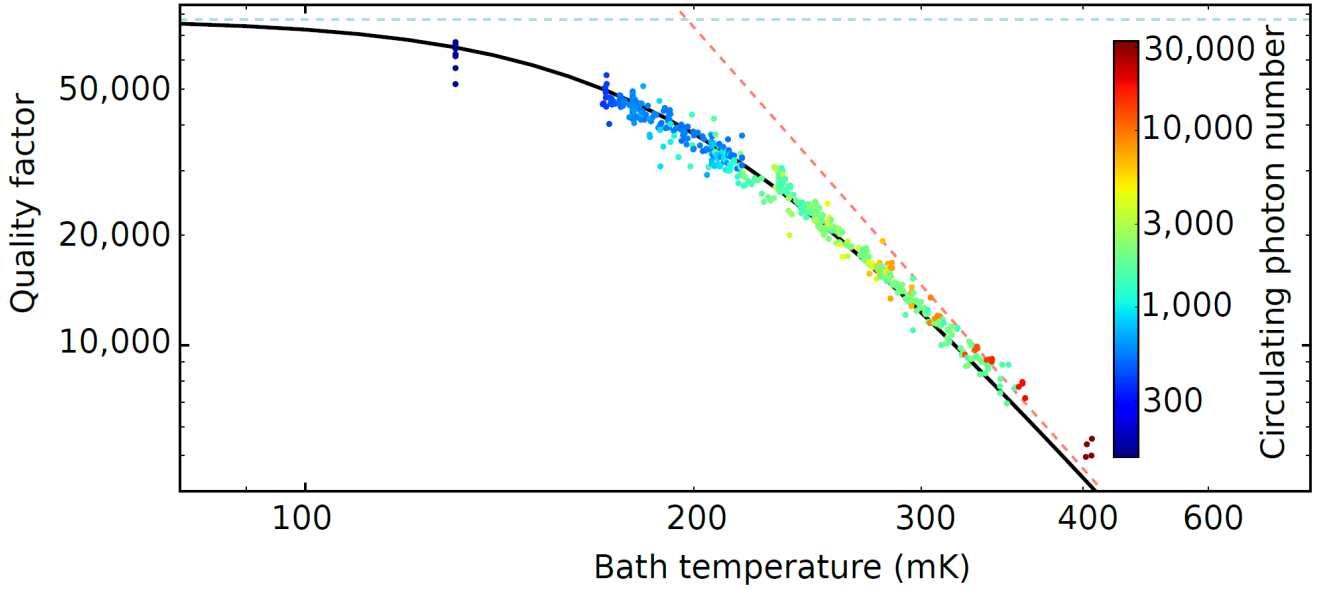


Figure 6.8: Mechanical quality factor  $Q_m$  as a function of the device temperature  $T_{\text{cav}}$  calculated from the heating model (6.36) and (6.19). This plot shows the same data as in Figures 6.6a and b, but with a rescaled horizontal axis; the dashed blue and red lines and the solid black line have the same meaning as Figure 6.6a. Marker colors denote the circulating photon number.

### 6.3.3 Fitting the quality factor measurements

Combining (6.18), (6.36) and (6.19) we arrive at the final expression for the mechanical quality factor in terms of observable system parameters:

$$\begin{aligned} \frac{1}{Q_m} &= \frac{1}{Q_{m,\text{rad}}} + \frac{T_{\text{cav}}^4}{\chi} = \frac{1}{Q_{m,\text{rad}}} + \frac{1}{\chi} \left( T_{\text{MC}}^4 + \frac{4\Phi}{\epsilon_l} l \right) \\ &= \frac{1}{Q_{m,\text{rad}}} + \frac{T_{\text{MC}}^4}{\chi} + \frac{4l}{\chi\epsilon_l} (\mu P_{\text{inc}} + \nu \hbar \omega_L \kappa_{\text{int}} \bar{n}_c). \end{aligned} \quad (6.50)$$

This expression was used to simultaneously fit all of the data shown in Figure 6.6. As independent parameters in the fit we chose  $Q_{m,\text{rad}}$  (the zero-temperature quality factor describing the radiation loss),  $\nu/\mu$  (the ratio of the two dimensionless heating coefficients) and  $\mu l/\epsilon_l$  (a combined parameter which characterizes the reaction of the device temperature to a given incident power); their extracted values are  $Q_{m,\text{rad}} = (70 \pm 2) \cdot 10^3$ ,  $\nu/\mu = 390 \pm 70$  and  $\mu l/\epsilon_l = (12 \pm 2) \text{ K}^4/\text{W}$ . The radiation loss quality factor is in a fairly good agreement with the theoretical prediction of  $Q_{m,\text{rad}} = (77 \pm 5) \cdot 10^3$  (subsection 6.3.1). The large value of the heating coefficients ratio  $\nu/\mu$  is consistent with the idea that a substantial fraction of the power inside the cavity leads to heating, while only a small portion of the incident power generates heat (i.e., most of the incident power is reflected). The ratio  $\mu l/\epsilon_l$  is harder to interpret, since we do not know the heat conductivity  $\epsilon_l/l$ ; however, the measurements described in the next subsection allow us to place some constraints on it, and thus obtain independent estimates of  $\mu$  and  $\nu$ .

<sup>d)</sup>Because of the non-trivial boundary condition (6.40), the orthogonality condition is expressed as  $\int_{x=0}^{x=l} v_n(x)v_m(x)dx + (l/r_V)v_n(l)v_m(l) \propto \delta_{n,m}$ , rather than the more common  $\int_{x=0}^{x=l} v_n(x)v_m(x)dx \propto \delta_{n,m}$ . One can check explicitly that the eigenfunctions  $v_n(x) = \sin(k_n x)$  with the condition on  $k_n$  given by equation (6.42) satisfy the first orthogonality relation, but not the second one. Nevertheless, existence of any orthogonality condition is enough to justify equation (6.45).

One way to obtain the correct orthogonality condition is to model the cavity heat capacity as a  $\delta$ -function in the channel heat capacity per unit length:  $C'_l(T, x) = C_l(T) + C_0(T)\delta(x-l)$ . This turns the boundary condition at  $x=l$  into a simple no-flow condition  $j|_{x=l} = 0$ , but forces us to use a generic orthogonality relation  $\int_{x=0}^{x=l} v_n(x)v_m(x)C'_l(x)dx = 0$ . Together with the definition of  $C'_l(T, x)$ , this relation is equivalent to the one presented above.

Figure 6.8 demonstrates the final output of the thermal model. There all of the quality factor data presented in Figure 6.6 is replotted as a function of the device temperature  $T_{\text{cav}}$  extracted from the thermal model for the parameters described above. Despite large differences in the circulating photon number and the incident power shown in Figure 6.6, all of the data now follows the theoretical curve (6.18), provided that the internal helium temperature  $T$  is interpreted as  $T_{\text{cav}}$ .

### 6.3.4 Thermal relaxation time

As we mentioned in the end of subsection 6.3.2, we can use the thermal relaxation time  $\tau_0$  to determine the thermal conductivity of the sheaths, which is otherwise hard to calculate.

We measure  $\tau_0$  by changing the circulating optical power (which is proportional to the power dissipated inside the cavity, and therefore to the heat load  $\Phi$ ) and monitoring the response of the temperature-dependent linewidth of the acoustic mode. The experiment is performed using the OMIT/A technique described in subsection 6.2.1, but with the probe beam frequency being fixed exactly one acoustic frequency away from the control beam:  $\Omega_p = \nu_p - \nu_{\text{con}} = -\omega_m$ . This way, the magnitude of the OMIA part of the probe beam reflection (described by equation (6.17)) is inversely proportional to the linewidth of the acoustic mode, which is a monotonic function of the device temperature. Hence, by observing the OMIA response as a function of time we can access the temperature dynamics. In practice, rather than measuring a step response to a change in the dissipated optical power, we perform a lock-in measurement in which we sinusoidally modulate the optical drive and record the magnitude and phase of the response of the OMIA signal amplitude.

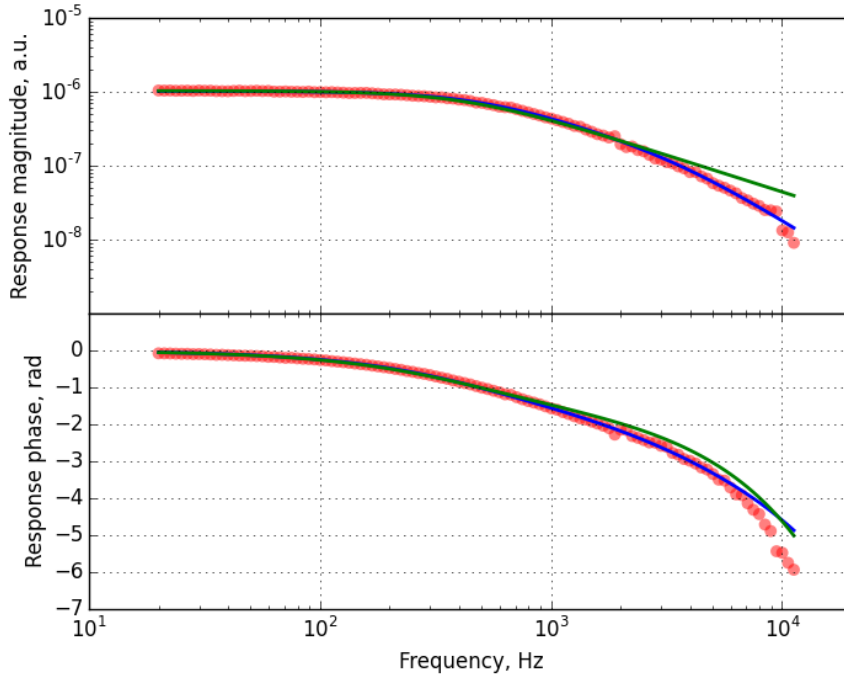


Figure 6.9: Amplitude and phase of the linewidth response as a function of the modulation frequency of the circulating optical power. The blue line is the fit to a double exponential (6.51); for comparison, the green line shows the fit to a simple exponential decay with a time delay, which corresponds to setting  $\tau_f = 0$  in equation (6.51).

The results are shown in figure 6.9. The data was fit to a double exponential decay with two time scales  $\tau_s$  and  $\tau_f$  and an additional time delay  $\tau_d$

$$\delta\gamma_{\text{m,int}}[\omega] \propto \frac{1}{1 + i\omega\tau_s} \frac{1}{1 + i\omega\tau_f} e^{i\omega\tau_d}. \quad (6.51)$$

We attribute the longer of the two decay times  $\tau_s \approx 350 \mu\text{s}$  to the thermal response. The shorter time  $\tau_f \approx 40 \mu\text{s}$  is only required to account for the data at frequencies above 2 kHz; it might arise from some other faster thermal process in the system (e.g., heating of the dielectric stack, or thermal equilibration of the helium inside the cavity), or from the mechanical response itself. Finally, the time delay  $\tau_d \approx 30 \mu\text{s}$  can be attributed to the sound propagation delay, as it is comparable to the ballistic phonon travel time in the sheath  $l/c_{\text{He}} \approx 12 \mu\text{s}$ . In interpreting the slowest time  $\tau_s$  as the thermal response time  $\tau_0$  we assumed that the thermal response is the slowest time scale in the system. Indeed, the observed time  $\tau_s \approx 350 \mu\text{s}$  is much larger than either optical ( $\kappa^{-1} \lesssim 3 \text{ ns}$ ) or mechanical ( $\gamma_m^{-1} \lesssim 20 \mu\text{s}$ ) lifetime, and we are not aware of any other similarly slow process occurring inside the device.

Finally, we use the measured value of  $\tau_0$  to estimate the thermal conductance. First, we need to calculate the heat capacity, for which we can use the known value for the specific heat  $c_V/T^3 = 8.3 \times 10^{-2} \text{ J}/(\text{mol} \cdot \text{K}^4)$  [113], which leads to the heat capacity per unit volume  $c_V/T^3 = 3 \times 10^3 \text{ J}/(\text{K}^4 \cdot \text{m}^3)$ . Next, we evaluate the volumes. The cavity has a diameter of  $d_{\text{cav}} = 133 \pm 5 \mu\text{m}$  and a length of  $l_{\text{cav}} = 70 \mu\text{m}$ , so its volume is  $V_{\text{cav}} = \frac{\pi}{4} d_{\text{cav}}^2 l_{\text{cav}} = (1.0 \pm 0.1) \times 10^{-12} \text{ m}^3$ . The sheaths have the same outer diameter  $d_{\text{cav}}$  (which is set by the inner diameter of the ferrule), inner diameter  $d_{\text{sh}} = 125 \mu\text{m}$  and length  $l = 3 \text{ mm}$ ; this means that the combined volume of two sheaths  $V_{\text{sh}} = A_{\text{sh}} l = 2 \frac{\pi}{4} (d_{\text{cav}}^2 - d_{\text{sh}}^2) l = (3.5 \div 16) \times 10^{-12} \text{ m}^3$ . The large spread in the volume estimates is due to the uncertainty in the sheath thickness  $h_{\text{sh}} = (d_{\text{cav}} - d_{\text{sh}})/2 = (1.5 \div 6.5) \mu\text{m}$ . From the volume estimates we obtain  $r_V = 0.06 \div 0.27$  and  $C_{\text{sh}}/T^3 = (1.0 \div 4.8) \times 10^{-8} \text{ J}/\text{K}^4$ . Using the experimental value for the time constant  $\tau_0 = 3.5 \times 10^{-4} \text{ s}$  we get  $K_{\text{sh}}/T^3 = \epsilon_l/l = (2.5 \div 7.8) \times 10^{-5} \text{ W}/\text{K}^4$ .

Now we can use this value of  $\epsilon_l/l$  to estimate the heating fractions  $\mu$  and  $\nu$  introduced in equation (6.19). From the experimentally obtained  $\mu l/\epsilon_l = (12 \pm 2) \text{ K}^4/\text{W}$  we get that  $\mu = (2.5 \div 10) \times 10^{-4}$  and, consequently,  $\nu \approx 400\mu = (0.1 \div 0.4)$ . This agrees with an intuitive expectation that a sizable fraction of the power lost inside the cavity (in our case, between 10% and 40%) contributes to the heat load. The rest of the optical power is lost to a combination of surface scattering losses (both due to the surface roughness and the mirror misalignment) and coupling into the non-propagating fiber modes (i.e., imperfect matching between the cavity mode and the traveling fiber mode).

Another way we can assess the validity of these thermal conductivity estimates is by using the theoretical expression for the thermal conductivity of a cylindrical channel[155]:

$$\kappa(T) = \frac{1}{3} c(T) c_{\text{He}} d_{\text{ch}} \frac{2-f}{f}, \quad (6.52)$$

which is applicable when the phonon mean free path is limited by scattering at the channel boundaries. Here  $d_{\text{ch}}$  is the diameter of the channel, and  $f$  is the fraction of diffusive phonon scattering events at the channel walls (the rest of the scattering events are assumed to be specular). This equation can be rewritten as

$$\frac{2-f}{f} = \frac{3}{c_{\text{He}} d_{\text{ch}}} \frac{\kappa(T)}{c(T)}. \quad (6.53)$$

We can apply this formula to the sheath by using equation (6.49) to express the ratio  $c/\kappa$ . With that, we find

$$\frac{2-f}{f} = \frac{3}{c_{\text{He}} d_{\text{ch}}} \frac{l^2}{\tau_0} \left( \frac{4}{\pi^2} + r_V \right). \quad (6.54)$$

If we approximate  $d_{\text{ch}}$  by twice the sheath thickness (to account for the non-cylindrical channel shape)  $d_{\text{ch}} \approx 2h_{\text{sh}} = (3 \div 13) \mu\text{m}$ , we will find that the diffusive scattering fraction  $f$  is between 3% for the minimal sheath thickness of  $1.5 \mu\text{m}$  and 20% for the maximal sheath thickness of  $6.5 \mu\text{m}$ . These values appear reasonable for the optically smooth glass surfaces of the ferrule and the fiber and a typical wavelength of thermal phonons  $\lambda_{\text{th}} = 2\pi \frac{\hbar c_{\text{He}}}{3k_{\text{B}} T} \gtrsim 10 \text{ nm}$  for  $T < 0.4 \text{ K}$ .

## 6.4 Performance and limitations

Now that we have described the device performance, we can ask how well it performs as a quantum optomechanics device. To provide a quantitative answer, we analyze two figures of merit: the optomechanical cooperativity  $\mathcal{C}$  (equation (2.152)) and the thermal optomechanical cooperativity  $\mathcal{C}_{\text{th}}$  (equation (3.1)).

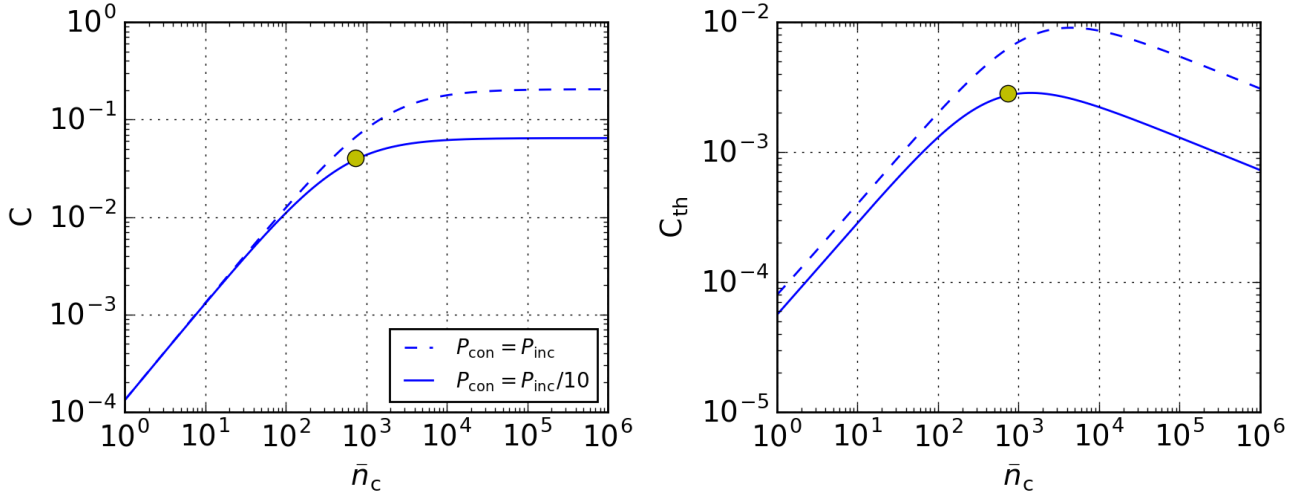


Figure 6.10: Cooperativity (left) and thermal cooperativity (right) of the first generation device as a function of the circulating photon number. In both plots dashed lines assume that all of the incident laser power is contained in the control beam, while solid lines assume that 10% of the total incident power is in the control beam. The yellow markers in both plots show the experimental results in our system for the highest achieved cooperativity. All of the plots assume  $T_{MC} = 0$ .

Both of these quantities grow with increasing circulating power. However, in our case heating due to the optical absorption leads to an increase of the helium temperature. As a consequence, the mechanical linewidth also increases, which causes the cooperativities to go down. Since the extra mechanical damping is proportional to the dissipated power, these two processes end up compensating each other, so the cooperativity saturates at high circulating powers. However, the thermal cooperativity has an extra factor of  $1/n_{th,m}$ , so at high temperatures it starts decreasing:  $C_{th} = C/n_{th,m} \propto 1/T \propto \bar{n}_c^{-1/4}$ . Therefore, it will have a maximum for some circulating photon number.

Figure 6.10 summarizes these processes and shows the dependence of both cooperativities on the circulating photon number. Since the heat load depends both on the circulating and on the incident power, we need to make some assumptions about the latter. The dashed lines show an ideal situation where all of the incident optical power is contained in the control beam. The solid lines depict a more realistic case where only 10% of the incident power is in the control beam. This is the highest reasonable fraction in the  $\phi$ M approach that we use, and is the highest fraction used in the experiments. The yellow markers show the best performance that we observed in the experiment, which corresponds to the OMIT/A sweeps at the top of the red curve in Figure 6.4. The cooperativity (left plot in Figure 6.10) was directly extracted from the OMIT/A feature size (equation (6.17)), and the thermal cooperativity was estimated assuming the mechanical bath temperature to be equal to the device temperature extracted from the theoretical model. The measured cooperativity  $C \approx 0.04$  matches fairly well with the expectations. However, both this observed value and the ideal saturation cooperativity  $C \approx 0.2$  are still significantly below 1, and the maximal thermal cooperativity is even lower (for comparison, cooperativities above  $10^4$  are routinely achieved[82, 156, 157], and the highest observed thermal cooperativity is 250[157]). This means that this device is still not well-suited for the quantum optomechanics applications. However, there are some straightforward ways to improve the performance, which is why we manufactured a new version of the device. The description of the new device and of the new experiments that we were able to perform with it is presented in Chapter 8.

# Chapter 7

## Undriven motion measurement theory

In this Chapter I will expand the general treatment of the undriven mechanical motion measurement given in section 2.6 to make it more applicable to the experiments performed with our superfluid helium device. We address four main points:

- We introduce the double control beam measurement scheme designed to simultaneously measure both motional sidebands in the resolved sideband regime, which allows for easier and more direct observation of sideband asymmetry (section 7.1).
- In addition to calculating the outgoing radiation, we also consider the measurement process and derive expressions for the photocurrent correlators (section 7.2).
- We introduce another measurable quantity: the sideband cross-correlator, and we discuss its interpretation and its quantum signatures (mostly discussed in subsection 7.2.2).
- Finally, we take into account the photothermal coupling, and determine how its presence affects measurement results and interpretations (section 7.3).

As only a handful of results derived here are actively used in the following chapters, I briefly summarize them in section 7.4.

### 7.1 Double control beam scheme

First, we lay out the double beam measurement scheme and describe the corresponding system dynamics, which ultimately lets us produce an expression for the outgoing radiation. The derivation is going to follow closely the one presented in chapter 2, specifically sections 2.3 and 2.6.

#### 7.1.1 Measurement schematic

One of the main goals of the experiments described in this work is to observe quantum optomechanics effects, starting with the sideband asymmetry. By sideband asymmetry we mean the perceived difference of one phonon between the Stokes and anti-Stokes sidebands, which is discussed in subsection 2.6.2. To measure this asymmetry, we need to detect undriven motion in both mechanical sidebands.

A standard way of observing undriven mechanical motion in the resolved sideband regime is shown in Figure 7.1a. There, a single drive (usually called the “measurement” or “control” beam) is detuned from the cavity resonance by about the mechanical frequency, so one of the motional sidebands (the one which is closer to the resonance) experiences a resonant cavity enhancement. However, this scheme does not allow us to detect both sidebands efficiently, because the off-resonant sideband (in Figure 7.1a this is the anti-Stokes, or “red” sideband) experiences very strong cavity filtering by a factor of  $\sim (4\omega_{\text{m,eff}}/\kappa)^2 \approx 3000$ . To detect this other sideband, we add a second control beam at a detuning  $+\omega_{\text{m,eff}}$  as shown in Figure 7.1b. This way, each beam produces a

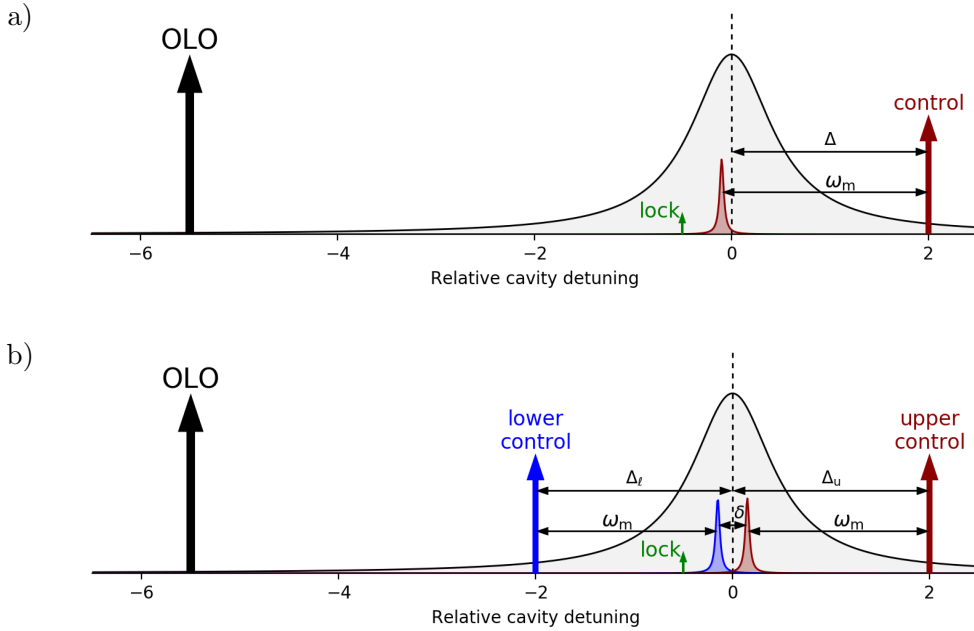


Figure 7.1: a) Optical tone configuration for the measurement of the undriven motion. The horizontal axis is scaled in units of optical cavity linewidths. Tones detunings and the mechanical motion linewidth are not to scale (except for the locking beam).  
b) Optical tone configuration for the simultaneous measurements of both mechanical sidebands. The horizontal axis is scaled in units of optical cavity linewidths. Tones detunings and the mechanical motion linewidth are not to scale (except for the locking beam).

single resonant sideband, which is different for different beams. As an added benefit, both mechanical sidebands are produced and measured simultaneously, so they represent the same mechanical motion. This means that in addition to measuring their individual PSDs we can also calculate their cross-correlator. As we show in section 7.2, this quantity allows us to extract the correlations between the mechanical motion and the optical vacuum noise, which reveals the action of RPSN on the mechanical oscillator (discussion of a related quantity, an optical quadrature correlator, and its relation to the RPSN, is given in Ref. [158]).

The double beam technique has already been demonstrated in Ref. [12], and a similar scheme involving switching detuning of a single control beam has been used in Ref. [80]. The latter scheme, however, is less convenient for us, as it does not allow for measuring the sideband cross-correlator (since the sidebands are measured one at a time). A different approach to simultaneous measurement of both sidebands is to apply a single control tone close to the cavity resonance to have approximately equal filtering of both sidebands. It has been adopted in many experiments [81, 83, 82, 156, 159], one of which [159] also demonstrated measurement of the sideband cross-correlator (via the optical quadrature correlator). However, a combination of high sideband resolution ( $\omega_m/\kappa \approx 15$ ) and strong optical heating prevents us from using this method efficiently.

To describe the scheme more quantitatively, let us denote the frequencies of the “upper” and “lower” control beam as respectively  $\omega_{\text{con,u}}$  and  $\omega_{\text{con,l}}$ . Thus, we expect the Stokes sideband coming from the upper beam to lie around  $\omega_{\text{con,u}} - \omega_{\text{m,eff}}$  and the anti-Stokes sideband of the lower beam to be at  $\omega_{\text{con,l}} + \omega_{\text{m,eff}}$ . If we choose the beams corresponding detunings such that  $\Delta_u = \omega_{\text{con,u}} - \omega_{\text{c0}} \approx \omega_{\text{m,eff}}$  and  $\Delta_l = \omega_{\text{con,l}} - \omega_{\text{c0}} \approx -\omega_{\text{m,eff}}$ , both of these sidebands will be close to resonance. To resolve them, and to avoid complications arising from a mechanical squeezing Hamiltonian [160, 161, 162, 163], we slightly shift them away from each other by increasing the frequency difference between the two control beams:  $|\Delta_u| + |\Delta_l| = \omega_{\text{con,u}} - \omega_{\text{con,l}} = 2\omega_{\text{m,eff}} + \delta$ , so the distance between the two sidebands becomes  $\delta$ . To keep the sidebands well resolved, but still both resonant with the cavity, we require  $\gamma_{\text{m,eff}} \ll \delta \ll \kappa$ . It is possible to do this in our system thanks to the large difference between the optical linewidth  $\kappa \approx 2\pi \cdot 20$  MHz and the mechanical linewidth  $\gamma_{\text{m,eff}} \approx 2\pi \cdot 3$  kHz. In the end, we typically

set  $\delta = 2\pi \cdot 200$  kHz.

### 7.1.2 Equations of motion and linearization

In order to describe the measurement process, we start with the standard optomechanical equations of motion (2.49), (2.50):

$$\dot{\hat{a}} = -\frac{\kappa}{2}\hat{a} - ig^{(0)}\hat{a}(\hat{b} + \hat{b}^\dagger) + \sqrt{\kappa_{\text{int}}}\hat{\xi}_{\text{int}} + \sqrt{\kappa_{\text{ext}}}\hat{\xi}_{\text{ext}} + \sqrt{\kappa_{\text{ext}}}a_{\text{in}}e^{+i\omega_{\text{c}0}t} \quad (7.1)$$

$$\dot{\hat{b}} = -\left(\frac{\gamma_{\text{m}}}{2} + i\omega_{\text{m}}\right)\hat{b} - ig^{(0)}\hat{a}^\dagger\hat{a} + \sqrt{\gamma_{\text{m}}}\hat{\eta}. \quad (7.2)$$

Here  $\hat{a}$  and  $\hat{b}$  are respectively the optical and the mechanical annihilation operators,  $g^{(0)}$  is the optomechanical coupling,  $\kappa_{\text{int}}$  and  $\kappa_{\text{ext}}$  are the internal and the external optical loss rates with the corresponding vacuum noise inputs  $\hat{\xi}_{\text{int}}$  and  $\hat{\xi}_{\text{ext}}$ ,  $a_{\text{in}}$  is the external classical drive,  $\kappa = \kappa_{\text{int}} + \kappa_{\text{ext}}$  is the total optical loss,  $\omega_{\text{m}}$  and  $\gamma_{\text{m}}$  are the mechanical frequency and damping, and  $\hat{\eta}$  is the mechanical thermal noise drive. The first equation is written in the frame rotating at the bare cavity frequency  $\omega_{\text{c}0}$ , hence the  $e^{+i\omega_{\text{c}0}t}$  factor in front of  $a_{\text{in}}$ .

Next, we specify the optical drive. It is comprised of two control tones denoted “lower” and “upper” in Figure 7.1, with the corresponding detunings  $\Delta_{\ell}$  and  $\Delta_{\text{u}}$ ; the later discussion will assume that  $\Delta_{\ell} \approx -\omega_{\text{m}}$  and  $\Delta_{\text{u}} \approx +\omega_{\text{m}}$ . Denoting the tones’ amplitudes by  $a_{\text{in},\ell}$  and  $a_{\text{in},\text{u}}$ , we can express the drive as  $a_{\text{in}}(t) = a_{\text{in},\ell}e^{-i\Delta_{\ell}t} + a_{\text{in},\text{u}}e^{-i\Delta_{\text{u}}t}$ .

After that, we apply the usual expansion of  $\hat{a}$  in powers of  $g^{(0)}$ , as in section 2.3. The zeroth order only includes the coherent drive and not the vacuum noise, and results in the equations of motion

$$\dot{a} = -\frac{\kappa}{2}a - ig^{(0)}a(b + b^*) + \sqrt{\kappa_{\text{ext}}}a_{\text{in}} \quad (7.3)$$

$$\dot{b} = -\left(\frac{\gamma_{\text{m}}}{2} + i\omega_{\text{m}}\right)b - ig^{(0)}|a|^2. \quad (7.4)$$

The radiation pressure force in the second equation  $-ig^{(0)}|a|^2$  has two components: one static and one at frequency  $|\Delta_{\text{u}} - \Delta_{\ell}| \approx 2\omega_{\text{m}}$ . Since both of these are far away from the mechanical resonance, and the radiation pressure force is relatively small, we can ignore them in our case and simply assume  $b = 0$ . To put it more quantitatively, these forces result in a dimensionless mechanical displacement on the order of  $z_0 \approx \frac{g^{(0)}}{\omega_{\text{m}}}\bar{n}_{\text{c}}$ , where  $\bar{n}_{\text{c}} = \overline{|a|^2}$  is the average intracavity photon number. We can ignore this displacement when considering the optical mode if its contribution to the cavity detuning is less than a cavity linewidth:  $z_0g^{(0)} \ll \kappa$ , which results in  $\bar{n}_{\text{c}} \ll \frac{\kappa\omega_{\text{m}}}{(g^{(0)})^2}$ . For our system this bound is about  $4 \cdot 10^8$ , which is much higher than the maximum circulating photon number used in the experiment  $\bar{n}_{\text{c}} \lesssim 10^4$ . Thus, ignoring the static mechanical displacement is justified, and the zeroth order solution for the optical mode becomes

$$\bar{a} = \bar{a}_{\ell}e^{-i\Delta_{\ell}t} + \bar{a}_{\text{u}}e^{-i\Delta_{\text{u}}t} \quad (7.5)$$

$$\bar{a}_{\ell} = \frac{\sqrt{\kappa_{\text{ext}}}a_{\text{in},\ell}}{\kappa/2 - i\Delta_{\ell}} \quad (7.6)$$

$$\bar{a}_{\text{u}} = \frac{\sqrt{\kappa_{\text{ext}}}a_{\text{in},\text{u}}}{\kappa/2 - i\Delta_{\text{u}}}. \quad (7.7)$$

Next, the linearized equations of motion are

$$\dot{\hat{d}} = -\frac{\kappa}{2}\hat{d} - ig^{(0)}(\hat{c}^\dagger + \hat{c})\bar{a}(t) + \sqrt{\kappa_{\text{int}}}\hat{\xi}_{\text{int}} + \sqrt{\kappa_{\text{ext}}}\hat{\xi}_{\text{ext}} \quad (7.8)$$

$$\dot{\hat{c}} = -\left(\frac{\gamma_{\text{m}}}{2} + i\omega_{\text{m}}\right)\hat{c} - ig^{(0)}(\bar{a}^*(t)\hat{d} + \hat{d}^\dagger\bar{a}(t)) + \sqrt{\gamma_{\text{m}}}\hat{\eta}, \quad (7.9)$$

where  $\hat{d}$  and  $\hat{c}$  are the first order expansion terms for the optical and mechanical modes respectively.

It is convenient to introduce a combined vacuum noise operator

$$\hat{\xi} = (\sqrt{\kappa_{\text{ext}}}\hat{\xi}_{\text{ext}} + \sqrt{\kappa_{\text{int}}}\hat{\xi}_{\text{int}})/\sqrt{\kappa}. \quad (7.10)$$

Because  $\kappa_{\text{int}} + \kappa_{\text{ext}} = \kappa$ , this operator has the same correlation properties (2.11)-(2.13) as  $\hat{\xi}_{\text{int,ext}}$ . Equation (7.8) for the optical mode can be rewritten as

$$\dot{\hat{d}} = -\frac{\kappa}{2}\hat{d} - ig^{(0)}(\hat{c}^\dagger + \hat{c})\bar{a}(t) + \sqrt{\kappa}\hat{\xi}. \quad (7.11)$$

After applying the Fourier transform (specifically, the ‘‘noise’’ Fourier transform defined in appendix A.2.2) and using some of its properties described in appendix A.2.3, the equations of motion become

$$\left(\frac{\kappa}{2} - i\omega\right)\hat{d}[\omega] = -ig^{(0)}\left(\bar{a}_\ell\left(\hat{c}[\omega - \Delta_\ell] + \hat{c}^\dagger[\omega - \Delta_\ell]\right) + \bar{a}_u\left(\hat{c}[\omega - \Delta_u] + \hat{c}^\dagger[\omega - \Delta_u]\right)\right) + \sqrt{\kappa}\hat{\xi}[\omega] \quad (7.12)$$

$$\left(\frac{\gamma_m}{2} - i(\omega - \omega_m)\right)\hat{c}[\omega] = -ig^{(0)}\left(\bar{a}_\ell^*\hat{d}[\omega + \Delta_\ell] + \bar{a}_u^*\hat{d}[\omega + \Delta_u] + \bar{a}_\ell\hat{d}^\dagger[\omega - \Delta_\ell] + \bar{a}_u\hat{d}^\dagger[\omega - \Delta_u]\right) + \sqrt{\gamma_m}\hat{\eta}[\omega]. \quad (7.13)$$

### 7.1.3 Solution, dynamical backaction and outgoing field

To solve equations (7.12), (7.13), we substitute the expression for  $\hat{d}$  (i.e., equation (7.12)) into the equation for  $\hat{c}$  (i.e., equation (7.13)). This produces 16 terms containing mechanical motion ( $\hat{c}$  or  $\hat{c}^\dagger$ ), which we can divide into several categories. First, there are 8 terms involving  $\hat{c}^\dagger$ . If the mechanical sidebands are far from each other ( $|\Delta_u - \Delta_\ell - 2\omega_m| \gg \gamma_{m,\text{eff}}$ ), these terms are off-resonant for the mechanical mode, and can be ignored. Of the remaining 8 terms, 4 include beating of the sideband of one control beam against the other beam, which would result in expressions like  $\hat{c}[\omega \pm (\Delta_u - \Delta_\ell)]$ ; since  $\Delta_u - \Delta_\ell \approx 2\omega_m \gg \gamma_{m,\text{eff}}$ , these terms are also very far off resonance and can be neglected. The last 4 terms produce a combination of the standard dynamic backaction effects of the beams (two terms per beam), and thus should be preserved. With the addition of the vacuum noise term, we obtain the following equation for the mechanical mode:

$$\begin{aligned} \left(\frac{\gamma_m}{2} - i(\omega - \omega_m)\right)\hat{c}[\omega] &= (g^{(0)})^2\left(|\bar{a}_\ell|^2(\chi_c[\omega - \Delta_\ell] - \chi_c[\omega + \Delta_\ell])\right. \\ &\quad \left.+ |\bar{a}_u|^2(\chi_c[\omega - \Delta_u] - \chi_c[\omega + \Delta_u])\right)\hat{c}[\omega] \\ &\quad - ig^{(0)}\left(\bar{a}_\ell^*\hat{d}_\xi[\omega + \Delta_\ell] + \bar{a}_\ell\hat{d}_\xi^\dagger[\omega - \Delta_\ell]\right. \\ &\quad \left.+ \bar{a}_u^*\hat{d}_\xi[\omega + \Delta_u] + \bar{a}_u\hat{d}_\xi^\dagger[\omega - \Delta_u]\right) \\ &\quad + \sqrt{\gamma_m}\hat{\eta}[\omega]. \end{aligned} \quad (7.14)$$

Here  $\chi_c[\omega] = (\kappa/2 - i\omega)^{-1}$  is the cavity susceptibility, and  $\hat{d}_\xi[\omega] = \chi_c[\omega]\sqrt{\kappa}\hat{\xi}[\omega]$  are the vacuum fluctuations of the intracavity field.

As in section 2.5, we can rewrite the mechanical equation of motion as

$$\hat{c}[\omega] = \chi_{m,\text{eff}}[\omega]\left(-i\hat{F}_{\text{RPSN}}[\omega] + \hat{F}_{\text{th}}[\omega]\right), \quad (7.15)$$

where the modified mechanical susceptibility is

$$\chi_{m,\text{eff}}[\omega] = (\gamma_m/2 - i(\omega - \omega_m) + i\Sigma[\omega])^{-1} \approx (\gamma_{m,\text{eff}}/2 - i(\omega - \omega_{m,\text{eff}}))^{-1}, \quad (7.16)$$

with the mechanical linewidth and the mechanical frequency modified by the dynamic backaction:

$$\gamma_{m,\text{eff}} = \gamma_m - 2\text{Im}\Sigma[\omega_{m,\text{eff}}] = \gamma_m + \delta\gamma_{m,\text{eff}} \quad (7.17)$$

$$\omega_{m,\text{eff}} = \omega_m + \text{Re}\Sigma[\omega_{m,\text{eff}}] = \omega_m + \delta\omega_{m,\text{eff}}. \quad (7.18)$$

The self-energy  $\Sigma[\omega]$  for the mechanical system is defined as

$$\Sigma[\omega] = i(g^{(0)})^2 (|\bar{a}_\ell|^2(\chi_c[\omega - \Delta_\ell] - \chi_c[\omega + \Delta_\ell]) + |\bar{a}_u|^2(\chi_c[\omega - \Delta_u] - \chi_c[\omega + \Delta_u])), \quad (7.19)$$

which is simply a sum of two contributions like (2.87), one for each beam. In the same vein, the radiation pressure force is

$$\hat{F}_{\text{RPSN}}[\omega] = g^{(0)} \left( \bar{a}_\ell^* \hat{d}_\xi[\omega + \Delta_\ell] + \bar{a}_\ell \hat{d}_\xi^\dagger[\omega - \Delta_\ell] + \bar{a}_u^* \hat{d}_\xi[\omega + \Delta_u] + \bar{a}_u \hat{d}_\xi^\dagger[\omega - \Delta_u] \right), \quad (7.20)$$

which is, again, a sum of two radiation pressure forces like (2.86). Finally, the thermal force is exactly the same as before (equation (2.85)):

$$\hat{F}_{\text{th}}[\omega] \equiv \sqrt{\gamma_m} \hat{\eta}[\omega]. \quad (7.21)$$

Note that the radiation pressure is still Hermitian:  $\hat{F}_{\text{RPSN}}^\dagger[\omega] = \hat{F}_{\text{RPSN}}[\omega]$ .

Now we are ready to find an expression for the intracavity field. Because we focus on the part of the spectrum close to the optical resonance  $\omega \approx 0$ , we can neglect the other two sidebands: the red sideband of the lower control beam, which corresponds to  $\hat{c}^\dagger[\omega - \Delta_\ell] \approx \hat{c}^\dagger[+\omega_m] \approx 0$ , and the blue sideband of the upper control beam, corresponding to  $\hat{c}[\omega - \Delta_u] \approx \hat{c}[-\omega_m] \approx 0$  (in addition, as we mentioned before, these sidebands are strongly filtered by the optical cavity response). The optical field thus becomes

$$\hat{d}[\omega] \approx \chi_c[\omega] \left( -ig^{(0)} \left( \bar{a}_\ell \hat{c}[\omega - \Delta_\ell] + \bar{a}_u \hat{c}^\dagger[\omega - \Delta_u] \right) + \sqrt{\kappa} \hat{\xi} \right) \quad (7.22)$$

Finally, the outgoing field can be calculated using the input-output relations (2.8):

$$\begin{aligned} \hat{d}_{\text{out}} &= \hat{\xi}_{\text{ext}} - \sqrt{\kappa_{\text{ext}}} \hat{d} \\ &= \hat{\xi}_{\text{ext}} - \sqrt{\kappa_{\text{ext}}} \chi_c[\omega] \left( -ig^{(0)} \left( \bar{a}_\ell \hat{c}[\omega - \Delta_\ell] + \bar{a}_u \hat{c}^\dagger[\omega - \Delta_u] \right) + \sqrt{\kappa} \hat{\xi} \right) \end{aligned} \quad (7.23)$$

The mechanical annihilation operator spectrum has peaks at  $+\omega_{\text{m,eff}}$ , while the creation operator (being its Hermitian conjugate) is peaked at  $-\omega_{\text{m,eff}}$ . Thus, if we denote the location of the red sideband (coming from the  $\hat{c}^\dagger$  term) as  $\omega_r$  and the location of the blue sideband (which comes from the  $\hat{c}$  term) as  $\omega_b$ , we get

$$\omega_r = \Delta_u - \omega_{\text{m,eff}} \quad (7.24)$$

$$\omega_b = \Delta_\ell + \omega_{\text{m,eff}}. \quad (7.25)$$

Because of the earlier choice of  $\Delta_\ell \approx -\omega_m$  and  $\Delta_u \approx +\omega_m$ , both of these frequencies are close to zero.

## 7.2 Photocurrent PSDs and a cross-correlator

### 7.2.1 Relating photocurrent to the outgoing field

Next, we need to relate the photocurrent PSD and cross-correlators to this outgoing field. As shown in equation (C.5) from appendix C.1, the photocurrent PSD can be found as

$$S_{ii}[\omega] = G^2 |a_{\text{OLO}}|^2 \left( S_{\hat{d}_{\text{out}}^\dagger, \hat{d}_{\text{out}}}[\omega - \omega_{\text{OLO}}] + S_{\hat{d}_{\text{out}}^\dagger, \hat{d}_{\text{out}}}[-\omega - \omega_{\text{OLO}}] + 1 \right), \quad (7.26)$$

with the outgoing field spectrum defined as

$$S_{\hat{d}_{\text{out}}^\dagger, \hat{d}_{\text{out}}}[\omega] = \left\langle \hat{d}_{\text{out}}^\dagger[\omega] \hat{d}_{\text{out}}[-\omega] \right\rangle. \quad (7.27)$$

In the following discussion we assume a negatively detuned OLO, that is,  $\omega_{\text{OLO}} < 0$  in the cavity frame.

Now, let us consider what would be the photocurrent  $i(t)$  and its corresponding Fourier transform  $i[\omega]$ . After mixing with the optical local oscillator, we expect the two mechanical sidebands of interest to be located

around  $\omega_{r,b} - \omega_{\text{OLO}}$  (i.e., the distance between the OLO at  $\omega_{\text{OLO}}$  and the sidebands at  $\omega_{r,b}$ ). Hence, we can define the shifted ‘‘local’’ Fourier transforms

$$i_{r,b}[\delta\omega] \equiv i[\omega_{r,b} - \omega_{\text{OLO}} + \delta\omega] \quad (7.28)$$

(note that unlike  $i[\omega]$  these do not correspond to any real function of time, so in general  $i_r[\omega] \neq (i_r[-\omega])^*$ ). The PSDs of the sidebands are then described by

$$\begin{aligned} S_{ii}^{(\text{rr})}[\delta\omega] &\equiv \langle i_r[\delta\omega](i_r[\delta\omega])^* \rangle = S_{ii}[-\omega_{\text{OLO}} + \omega_r + \delta\omega] \\ &= G^2 |a_{\text{OLO}}|^2 \times \\ &\quad \times (S_{\hat{d}_{\text{out}}, \hat{d}_{\text{out}}}^{\dagger}[-2\omega_{\text{OLO}} + \omega_r + \delta\omega] + S_{\hat{d}_{\text{out}}, \hat{d}_{\text{out}}}^{\dagger}[-\omega_r - \delta\omega] + 1) \end{aligned} \quad (7.29)$$

$$\begin{aligned} S_{ii}^{(\text{bb})}[\delta\omega] &\equiv \langle i_b[\delta\omega](i_b[\delta\omega])^* \rangle = S_{ii}[-\omega_{\text{OLO}} + \omega_b + \delta\omega] \\ &= G^2 |a_{\text{OLO}}|^2 \times \\ &\quad \times (S_{\hat{d}_{\text{out}}, \hat{d}_{\text{out}}}^{\dagger}[-2\omega_{\text{OLO}} + \omega_b + \delta\omega] + S_{\hat{d}_{\text{out}}, \hat{d}_{\text{out}}}^{\dagger}[-\omega_b - \delta\omega] + 1). \end{aligned} \quad (7.30)$$

Here  $S_{ii}^{(\text{rr})}[\delta\omega]$  and  $S_{ii}^{(\text{bb})}[\delta\omega]$  are the PSDs of the red and the blue sideband respectively, and  $\delta\omega$  is the frequency shift in the PSD from the sideband maximum.

While the second terms in the parentheses  $S_{\hat{d}_{\text{out}}, \hat{d}_{\text{out}}}^{\dagger}[-\omega_{r,b} - \delta\omega]$  correspond to the optical spectrum close to the cavity resonance, the first terms probe the spectrum roughly  $2\omega_{\text{OLO}}$  away from the cavity resonance, and therefore are insensitive to the cavity dynamics (more rigorously, the cavity susceptibility in the expression (7.23) is very small). Moreover, because of the normal ordering of the operators in  $S_{\hat{d}_{\text{out}}, \hat{d}_{\text{out}}}^{\dagger}$  the vacuum noise terms  $\hat{\xi}$  do not contribute. Thus, it is clear that  $S_{\hat{d}_{\text{out}}, \hat{d}_{\text{out}}}^{\dagger}[2\omega_{\text{OLO}}] \approx 0$ , and the PSDs simplify to

$$S_{ii}^{(\text{rr})}[\delta\omega] \approx G^2 |a_{\text{OLO}}|^2 (S_{\hat{d}_{\text{out}}, \hat{d}_{\text{out}}}^{\dagger}[-\omega_r - \delta\omega] + 1) \quad (7.31)$$

$$S_{ii}^{(\text{bb})}[\delta\omega] \approx G^2 |a_{\text{OLO}}|^2 (S_{\hat{d}_{\text{out}}, \hat{d}_{\text{out}}}^{\dagger}[-\omega_b - \delta\omega] + 1). \quad (7.32)$$

Next, we turn to the cross-correlator between the two sidebands. It is natural to define it as

$$S_{ii}^{(\text{rb})}[\delta\omega] \equiv \langle i_b[\delta\omega] i_r[-\delta\omega] \rangle = \langle i[-\omega_{\text{OLO}} + \omega_b + \delta\omega] i[-\omega_{\text{OLO}} + \omega_r - \delta\omega] \rangle. \quad (7.33)$$

Note that  $i_r$  is not complex conjugated, because it comes from  $\hat{c}^\dagger$  rather than  $\hat{c}$ . Similar to equation (C.4) from appendix C.1, we can use the definition of the Fourier transform  $i[\delta\omega]$  to express the result above through the time correlator  $C_{ii}(t, \tau)$ :

$$\begin{aligned} S_{ii}^{(\text{rb})}[\delta\omega] &= \int_{-\infty}^{+\infty} C_{ii}(t, \tau) e^{i(-2\omega_{\text{OLO}} + \omega_r + \omega_b)t} e^{i(\omega_b/2 - \omega_r/2 + \delta\omega)\tau} d\tau \\ &= G^2 (a_{\text{OLO}}^*)^2 \times \\ &\quad \times \int_{-\infty}^{+\infty} \left\langle : \left( e^{i\omega_b(t+\tau/2)} \hat{d}_{\text{out}} \left( t + \frac{\tau}{2} \right) \right) \left( e^{i\omega_r(t-\tau/2)} \hat{d}_{\text{out}} \left( t - \frac{\tau}{2} \right) \right) : \right\rangle e^{i\delta\omega\tau} d\tau. \end{aligned} \quad (7.34)$$

This expression can be greatly simplified if we recall from input-output theory[2] that the commutation relations of the outgoing fields are the same as the incoming ones. This implies that  $\hat{d}_{\text{out}}$  (just like  $\hat{\xi}_{\text{ext}}$ ) commute at different times, so the time ordering inside the ensemble averaging is irrelevant. Therefore, we can apply the Wiener-Khinchin theorem again and arrive at

$$S_{ii}^{(\text{rb})}[\delta\omega] = G^2 (a_{\text{OLO}}^*)^2 \left\langle \hat{d}_{\text{out}}[\omega_b + \delta\omega] \hat{d}_{\text{out}}[\omega_r - \delta\omega] \right\rangle. \quad (7.35)$$

## 7.2.2 Correlator values and interpretation

Now we have everything we need to calculate the PSDs (7.31), (7.32) and the cross-correlator (7.35) for the optical field (7.23) obtained earlier.

We start with the sideband PSDs  $S_{ii}^{(rr)}$  and  $S_{ii}^{(bb)}$ , which is proportional to  $S_{\hat{d}_{\text{out}}^\dagger, \hat{d}_{\text{out}}}[\omega]$ . As noted before, due to the normal ordering the terms containing the vacuum noise  $\hat{\xi}$  do not contribute. Thus, we are left with

$$\begin{aligned} S_{\hat{d}_{\text{out}}^\dagger, \hat{d}_{\text{out}}}[\omega] &= \left\langle \hat{d}_{\text{out}}^\dagger[\omega] \hat{d}_{\text{out}}[-\omega] \right\rangle \\ &= \kappa_{\text{ext}} |\chi_c[-\omega]|^2 (g^{(0)})^2 (|\bar{a}_\ell|^2 S_{\hat{c}^\dagger \hat{c}}[\omega + \Delta_\ell] + |\bar{a}_u|^2 S_{\hat{c} \hat{c}^\dagger}[\omega + \Delta_u]). \end{aligned} \quad (7.36)$$

We have also omitted two other terms involving the mechanical motion:  $\bar{a}_u^* \bar{a}_\ell \langle \hat{c}[\omega + \Delta_u] \hat{c}[-\omega - \Delta_\ell] \rangle$  and  $\bar{a}_\ell^* \bar{a}_u \langle \hat{c}^\dagger[\omega + \Delta_\ell] \hat{c}[-\omega - \Delta_u] \rangle$ . While not strictly zero, these terms are nevertheless small because the mechanical susceptibilities of the two terms in the product do not overlap. For example, in the first expression the two mechanical terms are centered around  $\omega = \omega_m - \Delta_u = -\omega_r$  and  $\omega = -\omega_m - \Delta_\ell = -\omega_b$ ; as we are working in the assumption  $|\omega_r - \omega_b| \gg \gamma_{m,\text{eff}}$  (well resolved sidebands, as discussed in subsection 7.1.1), the product of these two terms is always small.

Now we need to calculate the mechanical motion correlators:

$$S_{\hat{c}^\dagger, \hat{c}}[\omega] = |\chi_{m,\text{eff}}[-\omega]|^2 (S_{\hat{F}, \hat{F}}^{\text{RPSN}}[\omega] + S_{\hat{F}^\dagger, \hat{F}}^{\text{th}}[\omega]) \quad (7.37)$$

$$S_{\hat{c}, \hat{c}^\dagger}[\omega] = |\chi_{m,\text{eff}}[+\omega]|^2 (S_{\hat{F}, \hat{F}}^{\text{RPSN}}[\omega] + S_{\hat{F}, \hat{F}^\dagger}^{\text{th}}[\omega]). \quad (7.38)$$

The PSD of the thermal force is given by equations (2.117), (2.118):

$$S_{\hat{F}^\dagger, \hat{F}}^{\text{th}}[\omega] = \gamma_m n_{\text{th}} \quad (7.39)$$

$$S_{\hat{F}, \hat{F}^\dagger}^{\text{th}}[\omega] = \gamma_m (n_{\text{th}} + 1), \quad (7.40)$$

and the spectrum of the radiation pressure is similar to equation (2.119):

$$\begin{aligned} S_{\hat{F}, \hat{F}}^{\text{RPSN}}[\omega] &\equiv \left\langle \hat{F}_{\text{RPSN}}[\omega] \hat{F}_{\text{RPSN}}[-\omega] \right\rangle \\ &= (g^{(0)})^2 \kappa (|\bar{a}_\ell|^2 |\chi_c[\omega + \Delta_\ell]|^2 + |\bar{a}_u|^2 |\chi_c[\omega + \Delta_u]|^2). \end{aligned} \quad (7.41)$$

Like in section 2.6, its antisymmetric part still satisfies the criterion

$$\begin{aligned} S_{\hat{F}, \hat{F}}^{\text{RPSN}}[\omega_{m,\text{eff}}] - S_{\hat{F}, \hat{F}}^{\text{RPSN}}[-\omega_{m,\text{eff}}] &= (g^{(0)})^2 \kappa (|\bar{a}_\ell|^2 (|\chi_c[\omega_{m,\text{eff}} + \Delta_\ell]|^2 - |\chi_c[-\omega_{m,\text{eff}} + \Delta_\ell]|^2) \\ &\quad + |\bar{a}_u|^2 (|\chi_c[\omega_{m,\text{eff}} + \Delta_u]|^2 - |\chi_c[-\omega_{m,\text{eff}} + \Delta_u]|^2)) \\ &= -2\text{Im}\Sigma[\omega_{m,\text{eff}}] \equiv \delta\gamma_{m,\text{eff}}. \end{aligned} \quad (7.42)$$

We can once again define the effective RPSN phonon bath occupation (2.127)

$$n_{\text{RPSN}} = \frac{S_{\hat{F}, \hat{F}}^{\text{RPSN}}[-\omega_{m,\text{eff}}]}{\delta\gamma_{m,\text{eff}}}, \quad (7.43)$$

which results in exactly the same results for the mechanical motion PSD as before (equations (2.129) and (2.130)):

$$S_{\hat{c}^\dagger, \hat{c}}[\omega] = \frac{n_m \gamma_{m,\text{eff}}}{\gamma_{m,\text{eff}}^2/4 + (\omega + \omega_{m,\text{eff}})^2} \quad (7.44)$$

$$\begin{aligned} S_{\hat{c}, \hat{c}^\dagger}[\omega] &= \frac{(n_m + 1) \gamma_{m,\text{eff}}}{\gamma_{m,\text{eff}}^2/4 + (\omega - \omega_{m,\text{eff}})^2} \\ n_m &= \frac{n_{\text{RPSN}} \delta\gamma_{m,\text{eff}} + n_{\text{th},m} \gamma_m}{\gamma_{m,\text{eff}}}. \end{aligned} \quad (7.45)$$

With these spectra the PSD of the outgoing field is

$$S_{\hat{d}_{\text{out}}, \hat{d}_{\text{out}}}^{\text{ii}}[\omega] = \kappa_{\text{ext}} |\chi_c[-\omega]|^2 (g^{(0)})^2 \times \left( |\bar{a}_\ell|^2 \frac{n_m \gamma_{\text{m,eff}}}{\gamma_{\text{m,eff}}^2/4 + (\omega + \omega_b)^2} + |\bar{a}_u|^2 \frac{(n_m + 1) \gamma_{\text{m,eff}}}{\gamma_{\text{m,eff}}^2/4 + (\omega + \omega_r)^2} \right). \quad (7.46)$$

As expected, it is comprised of two Lorentzians centered at  $\omega = -\omega_r$  and  $\omega = -\omega_b$ . From (7.31), (7.32) the photocurrent PSDs of the individual sidebands are

$$S_{ii}^{(\text{rr})}[\delta\omega] \approx G^2 |a_{\text{OLO}}|^2 \left( \kappa_{\text{ext}} |\chi_c[\omega_r]|^2 (g^{(0)})^2 |\bar{a}_u|^2 \frac{(n_m + 1) \gamma_{\text{m,eff}}}{\gamma_{\text{m,eff}}^2/4 + \delta\omega^2} + 1 \right) \quad (7.47)$$

$$S_{ii}^{(\text{bb})}[\delta\omega] \approx G^2 |a_{\text{OLO}}|^2 \left( \kappa_{\text{ext}} |\chi_c[\omega_b]|^2 (g^{(0)})^2 |\bar{a}_\ell|^2 \frac{n_m \gamma_{\text{m,eff}}}{\gamma_{\text{m,eff}}^2/4 + \delta\omega^2} + 1 \right). \quad (7.48)$$

Both are Lorentzians with shot noise background, and with area under the Lorentzian proportional to  $n_m$  or  $n_m + 1$  for the blue and the red sideband respectively.

Now we switch to the cross-correlator (7.35), which is proportional to  $\langle \hat{d}_{\text{out}}[\omega_b + \delta\omega] \hat{d}_{\text{out}}[\omega_r - \delta\omega] \rangle$ . Because the normal ordering is not enforced, there will be terms involving the vacuum noise:

$$\begin{aligned} & \langle \hat{d}_{\text{out}}[\omega_b + \delta\omega] \hat{d}_{\text{out}}[\omega_r - \delta\omega] \rangle \\ & \approx -\kappa_{\text{ext}} (\chi_c[\omega_r] \chi_c[\omega_b]) (g^{(0)})^2 \bar{a}_\ell \bar{a}_u S_{\hat{c}, \hat{c}^\dagger}[\omega_{\text{m,eff}} + \delta\omega] \\ & \quad + i \left\langle \left( \hat{\xi}_{\text{ext}}[\omega_b + \delta\omega] - \sqrt{\kappa_{\text{ext}}} \chi_c[\omega_b] \hat{\xi}[\omega_b + \delta\omega] \right) \right. \\ & \quad \left. \times \left( \sqrt{\kappa_{\text{ext}}} \chi_c[\omega_r] g^{(0)} \left( \bar{a}_u \hat{c}^\dagger[-\omega_{\text{m,eff}} - \delta\omega] \right) \right) \right\rangle. \end{aligned} \quad (7.49)$$

The first term is just the mechanical motion PSD, similar to the sidebands' PSDs (as before, we assumed  $\delta\omega \sim \gamma_{\text{m,eff}} \ll |\omega_r - \omega_b|$  and neglected all off-resonant mechanical terms). The second term involves the correlations of the optical vacuum fluctuations with the mechanical motion, which are non-zero because the mechanical oscillator is driven by the radiation pressure shot noise arising from these vacuum fluctuations. Thus, this term directly represents the action of the radiation pressure shot noise on the mechanical oscillator.

Using expression (7.10) for  $\hat{\xi}$  and (7.20) for  $\hat{F}_{\text{RPSN}}$ , we get

$$\begin{aligned} \langle \hat{\xi}[\omega_b + \delta\omega] \hat{F}_{\text{RPSN}}[-\omega_{\text{m,eff}} - \delta\omega] \rangle &= g^{(0)} \bar{a}_\ell \langle \hat{\xi}[\omega_b + \delta\omega] \hat{d}_\xi^\dagger[-\omega_b - \delta\omega] \rangle \\ &= g^{(0)} \bar{a}_\ell \chi_c[-\omega_b] \sqrt{\kappa} \end{aligned} \quad (7.50)$$

$$\begin{aligned} \langle \hat{\xi}_{\text{ext}}[\omega_b + \delta\omega] \hat{F}_{\text{RPSN}}[-\omega_{\text{m,eff}} - \delta\omega] \rangle &= \sqrt{\kappa_{\text{ext}}} / \kappa \langle \hat{\xi}[\omega_b + \delta\omega] \hat{F}_{\text{RPSN}}[-\omega_{\text{m,eff}} - \delta\omega] \rangle \\ &= g^{(0)} \bar{a}_\ell \chi_c[-\omega_b] \sqrt{\kappa_{\text{ext}}}, \end{aligned} \quad (7.51)$$

so that

$$\begin{aligned} & \left\langle \left( \hat{\xi}_{\text{ext}}[\omega_b + \delta\omega] - \sqrt{\kappa_{\text{ext}}} \chi_c[\omega_b] \hat{\xi}[\omega_b + \delta\omega] \right) \hat{c}^\dagger[-\omega_{\text{m,eff}} - \delta\omega] \right\rangle \\ &= i (\chi_{\text{m,eff}}[\omega_{\text{m,eff}} + \delta\omega])^* \left\langle \left( \hat{\xi}_{\text{ext}}[\omega_b + \delta\omega] - \sqrt{\kappa_{\text{ext}}} \chi_c[\omega_b] \hat{\xi}[\omega_b + \delta\omega] \right) \hat{F}_{\text{RPSN}}[-\omega_{\text{m,eff}} - \delta\omega] \right\rangle \\ &= i (\chi_{\text{m,eff}}[\omega_{\text{m,eff}} + \delta\omega])^* \sqrt{\kappa_{\text{ext}}} (1 - \kappa \chi_c[\omega_b]) g^{(0)} \bar{a}_\ell \chi_c[-\omega_b] \\ &= -i (\chi_{\text{m,eff}}[\omega_{\text{m,eff}} + \delta\omega])^* \sqrt{\kappa_{\text{ext}}} g^{(0)} \bar{a}_\ell \chi_c[\omega_b]. \end{aligned} \quad (7.52)$$

Note that this expression depends on the full complex mechanical susceptibility, unlike, for example, the mechanical PSD, where only  $|\chi_{\text{m,eff}}|^2$  is present. This implies that it is sensitive to the phase response of the

mechanical oscillator, meaning that this term really is a correlator between the force and the displacement (simple force-force or displacement-displacement correlators would not depend on the force-displacement phase shift).

The complete noise correlator becomes

$$\left\langle \hat{d}_{\text{out}}[\omega_b + \delta\omega] \hat{d}_{\text{out}}[\omega_r - \delta\omega] \right\rangle \approx G_{\text{cc}} \left( S_{\hat{c}, \hat{c}^\dagger}[\omega_{\text{m,eff}} + \delta\omega] - (\chi_{\text{m,eff}}[\omega_{\text{m,eff}} + \delta\omega])^* \right) \quad (7.53)$$

$$G_{\text{cc}} = -\kappa_{\text{ext}} (\chi_c[\omega_r] \chi_c[\omega_b]) (g^{(0)})^2 \bar{a}_\ell \bar{a}_u. \quad (7.54)$$

where  $G_{\text{cc}}$  simply is a conversion factor between the displacement and the outgoing field.

Finally, the photocurrent cross-correlator is

$$\begin{aligned} S_{ii}^{(\text{rb})}[\delta\omega] &= G^2 (a_{\text{OLO}}^*)^2 G_{\text{cc}} (\omega_{\text{m,eff}} + \delta\omega] - (\chi_{\text{m,eff}}[\omega_{\text{m,eff}} + \delta\omega])^*) \\ &= G^2 (a_{\text{OLO}}^*)^2 G_{\text{cc}} \left( \frac{(n_m + 1)\gamma_{\text{m,eff}}}{\gamma_{\text{m,eff}}^2/4 + \delta\omega^2} - \frac{\gamma_{\text{m,eff}}/2 - i\delta\omega}{\gamma_{\text{m,eff}}^2/4 + \delta\omega^2} \right) \\ &= G^2 (a_{\text{OLO}}^*)^2 G_{\text{cc}} \frac{(n_m + 1/2)\gamma_{\text{m,eff}} - i\delta\omega}{\gamma_{\text{m,eff}}^2/4 + \delta\omega^2}. \end{aligned} \quad (7.55)$$

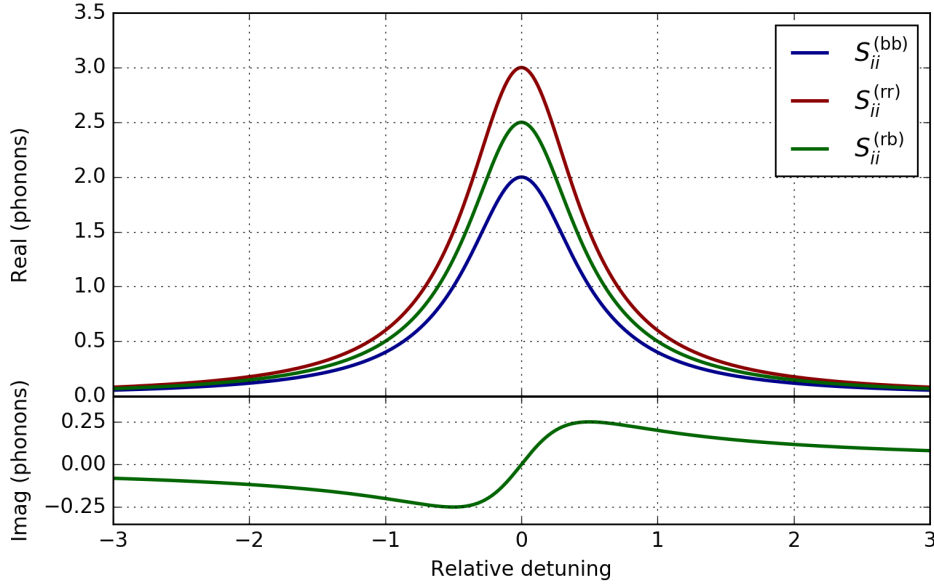


Figure 7.2: Illustration of the PSD of the Stokes sideband  $S_{ii}^{(\text{rr})}[\delta\omega]$  (red), the PSD of the anti-Stokes sideband  $S_{ii}^{(\text{bb})}[\delta\omega]$  (blue), and the sideband cross-correlator  $S_{ii}^{(\text{rb})}[\delta\omega]$  (green). The horizontal axis is normalized in units of the mechanical linewidth, and all three quantities have been shifted horizontally to share the same origin. The vertical axis is normalized in phonons, and the two PSDs have their shot noise background subtracted ( $S_{ii}^{(\text{rb})}[\omega]$  has no background). Imaginary parts of the PSDs ( $S_{ii}^{(\text{rr})}$  and  $S_{ii}^{(\text{bb})}$ ) are not plotted, since they are identically zero.

This expression is different from (7.47) and (7.48) in several important ways. First, there is no shot noise background present, as this noise is uncorrelated between the two sidebands (it is important to note that the measurement SNR is still affected by the shot noise; it just averages to zero instead of to some finite value). Second, the cross-correlator is complex, with an imaginary part that is antisymmetric in  $\delta\omega$  and has a magnitude of 1/2 of a phonon. Finally, the real Lorentzian part of the cross-correlator is proportional not to  $n_m$  (like in  $S_{ii}^{(\text{bb})}$ ) or  $n_m + 1$  (as in  $S_{ii}^{(\text{rr})}$ ), but to  $n_m + 1/2$ . As was shown above in the equation (7.53), this additional half of a phonon in the real part together with the anti-Lorentzian imaginary part can be combined to produce a

complex mechanical susceptibility. This susceptibility shows up because of the correlation between the random radiation pressure force noise and the mechanical displacement driven by this force, and thus is an unambiguous signature of the RPSN acting on the mechanical oscillator.

Figure 7.2 illustrates expressions (7.47), (7.48) and (7.55). The vertical axis has been normalized in units of phonons, so that the Lorentzian height corresponds to the phonon number factor. The data shown in the figure corresponds to the average phonon occupation  $n_m = 2$ , which is the height of the anti-Stokes sideband  $S_{ii}^{(bb)}$ . One can clearly see the difference in one phonon between the red and the blue sidebands, the difference in  $1/2$  of a phonon between the cross-correlator and either of the sidebands, and the magnitude of  $1/2$  of a phonon in the imaginary part of the cross-correlator.

## 7.3 Photothermal coupling

Since the current device demonstrates some degree of photothermal coupling, we need to check how its presence affects the results of the previous section.

### 7.3.1 Quantum treatment of the photothermal coupling

The quantum treatment of the photothermal coupling is a generalization of classical treatment from subsection 6.2.4, and is similar to Ref. [164]. In order to capture its non-unitary character, we model it as an additional optical loss and an extra mechanical force whose magnitude is proportional to the optical power lost to that channel. To describe this quantitatively, we first introduce an optical loss channel with a rate  $\kappa_{\text{pt}}$  and a corresponding vacuum noise  $\hat{\xi}_{\text{pt}}$ . This modifies the original equation of motion for the optical mode (7.1) to

$$\dot{\hat{a}} = -\frac{\kappa}{2}\hat{a} - ig^{(0)}(\hat{c}^\dagger + \hat{c})\hat{a} + \sqrt{\kappa_{\text{int}}}\hat{\xi}_{\text{int}} + \sqrt{\kappa_{\text{pt}}}\hat{\xi}_{\text{pt}} + \sqrt{\kappa_{\text{ext}}}(a_{\text{in}}e^{+i\omega c_0 t} + \hat{\xi}_{\text{ext}}). \quad (7.56)$$

The total damping is now a combination of all three loss rates:  $\kappa = \kappa_{\text{int}} + \kappa_{\text{pt}} + \kappa_{\text{ext}}$ . The vacuum noise  $\hat{\xi}_{\text{pt}}$  is uncorrelated with any other noise and is described by the same correlation relations (2.11)-(2.13). The amplitude of the field lost to that channel can be found from the input-output relations, just like (7.23) for the external coupling:

$$\hat{a}_{\text{out,pt}} = \hat{\xi}_{\text{pt}} - \sqrt{\kappa_{\text{pt}}}\hat{a}. \quad (7.57)$$

The corresponding power is simply

$$\hat{I}_{\text{out,pt}} = \hat{a}_{\text{out,pt}}^\dagger \hat{a}_{\text{out,pt}}. \quad (7.58)$$

The photothermal force is proportional to this intensity. As discussed in subsection 6.2.4, it can experience low-pass filtering, which we can model by writing a relaxation equation

$$\tau_{\text{pt}}\dot{\hat{F}}_{\text{pt}} = -\hat{F}_{\text{pt}} + \frac{G_{\text{pt}}}{\kappa_{\text{pt}}}\hat{I}_{\text{out,pt}}, \quad (7.59)$$

where  $G_{\text{pt}}$  is the DC proportionality coefficient between the intracavity photon number  $\bar{n}_c$  and the photothermal force (the extra factor of  $1/\kappa_{\text{pt}}$  compared to subsection 6.2.4 comes from the fact that it multiplies the outgoing photon flux, not the stored photon energy), and  $\tau_{\text{pt}}$  is the time constant of the low-pass filter. The solution of this equation (in the Fourier domain) is

$$\hat{F}_{\text{pt}}[\omega] = \frac{G_{\text{pt}}\hat{I}_{\text{out,pt}}[\omega]/\kappa_{\text{pt}}}{1 - i\omega\tau_{\text{pt}}}. \quad (7.60)$$

Like before, we assume that  $\omega \approx \omega_{\text{m,eff}}$ , since we are only interested in the forces in a small frequency band around  $\omega_{\text{m,eff}}$ . After this substitution and going back into the time domain, we obtain

$$\hat{F}_{\text{pt}}(t) = \frac{G_{\text{pt}}/\kappa_{\text{pt}}}{1 - i\omega_{\text{m,eff}}\tau_{\text{pt}}}\hat{I}_{\text{out,pt}}(t) = \frac{g_{\text{pt}}^{(0)}}{\kappa_{\text{pt}}}\hat{I}_{\text{out,pt}}(t), \quad (7.61)$$

where we defined the single-photon photothermal optomechanical coupling  $g_{\text{pt}}^{(0)} = G_{\text{pt}}/(1 - i\omega_{\text{m,eff}}\tau_{\text{pt}})$ . It is analogous to  $g^{(0)}$ , but it is in general complex (owing to the low-pass filtering) and appears only in the mechanical equation of motion, since its origin is non-unitary.

Next, we once again perform the first order expansion of the optical mode  $\hat{a} = \bar{a} + \hat{d}$ . This leads to the photothermal force

$$\begin{aligned}\hat{F}_{\text{pt}}(t) &= \frac{g_{\text{pt}}^{(0)}}{\kappa_{\text{pt}}} \hat{a}_{\text{out,pt}}^\dagger \hat{a}_{\text{out,pt}} \\ &= \frac{g_{\text{pt}}^{(0)}}{\kappa_{\text{pt}}} \left( \hat{\xi}_{\text{pt}}^\dagger - \sqrt{\kappa_{\text{pt}}}(\bar{a}^* + \hat{d}^\dagger) \right) \left( \hat{\xi}_{\text{pt}} - \sqrt{\kappa_{\text{pt}}}(\bar{a} + \hat{d}) \right) \\ &\approx g_{\text{pt}}^{(0)} |\bar{a}|^2 + g_{\text{pt}}^{(0)} (\bar{a}^* \hat{d} + \hat{d}^\dagger \bar{a}) - \frac{g_{\text{pt}}^{(0)}}{\sqrt{\kappa_{\text{pt}}}} (\bar{a}^* \hat{\xi}_{\text{pt}} + \hat{\xi}_{\text{pt}}^\dagger \bar{a}).\end{aligned}\quad (7.62)$$

In the following we ignore the static force term  $g_{\text{pt}}^{(0)} |\bar{a}|^2$  (this term is incorrect anyway, since we have used the low-passed proportionality coefficient  $A_{\text{pt,eff}}$  instead of the static  $A_{\text{pt}}$ ), just as for the radiation pressure.

After adding the photothermal force, the mechanical equation of motion becomes

$$\begin{aligned}\dot{\hat{c}} &= - \left( \frac{\gamma_{\text{m}}}{2} + i\omega_{\text{m}} \right) \hat{c} - ig^{(0)} \hat{a}^\dagger \hat{a} - i\hat{F}_{\text{pt}} + \sqrt{\gamma_{\text{m}}} \hat{\eta} \\ &= - \left( \frac{\gamma_{\text{m}}}{2} + i\omega_{\text{m}} \right) \hat{c} - i(g^{(0)} + g_{\text{pt}}^{(0)}) (\bar{a}^* \hat{d} + \hat{d}^\dagger \bar{a}) \\ &\quad + i \frac{g_{\text{pt}}^{(0)}}{\sqrt{\kappa_{\text{pt}}}} (\bar{a}^* \hat{\xi}_{\text{pt}} + \hat{\xi}_{\text{pt}}^\dagger \bar{a}) + \sqrt{\gamma_{\text{m}}} \hat{\eta}.\end{aligned}\quad (7.63)$$

Indeed, we see that the two optomechanical couplings  $g^{(0)}$  and  $g_{\text{pt}}^{(0)}$  enter the mechanical equation on equal footing, barring the vacuum noise term involving  $\hat{\xi}_{\text{pt}}$ . At the same time, only  $g^{(0)}$  appears in the optical equation (7.56), owing to the non-unitarity of  $g_{\text{pt}}^{(0)}$ .

### 7.3.2 Effects of the photothermal coupling

The rest follows fairly closely the derivation for case of pure radiation pressure. After transitioning into the Fourier domain and solving for  $\hat{c}[\omega]$ , we find, similarly to (7.15)

$$\hat{c}[\omega] = \chi_{\text{m,eff}}[\omega] \left( -i\hat{F}_{\text{OFSN}}[\omega] + \sqrt{\gamma_{\text{m}}} \hat{\eta}[\omega] \right). \quad (7.64)$$

Compared to (7.15), there are two modifications here. First, the expression for the mechanical susceptibility is still the same  $\chi_{\text{m,eff}}[\omega] = (\gamma_{\text{m}}/2 - i(\omega - \omega_{\text{m}}) + i\Sigma[\omega])^{-1}$ , but the self-energy is slightly different (similar to (6.15)):

$$\begin{aligned}\Sigma[\omega] &= ig^{(0)}(g^{(0)} + g_{\text{pt}}^{(0)}) \times \\ &\quad \times (|\bar{a}_\ell|^2 (\chi_{\text{c}}[\omega - \Delta_\ell] - \chi_{\text{c}}[\omega + \Delta_\ell]) + |\bar{a}_{\text{u}}|^2 (\chi_{\text{c}}[\omega - \Delta_{\text{u}}] - \chi_{\text{c}}[\omega + \Delta_{\text{u}}]))\end{aligned}\quad (7.65)$$

(this expression is proportional to  $g^{(0)}(g^{(0)} + g_{\text{pt}}^{(0)})$ , in contrast with  $(g^{(0)})^2$  in the radiation pressure case (7.19)). Second, the RPSN force  $\hat{F}_{\text{RPSN}}$  is replaced by a more general optical force shot noise (OFSN) force

$$\begin{aligned}\hat{F}_{\text{OFSN}}[\omega] &= g^{(0)} \left( \bar{a}_\ell^* \hat{d}_\xi[\omega + \Delta_\ell] + \bar{a}_\ell \hat{d}_\xi^\dagger[\omega - \Delta_\ell] + \bar{a}_{\text{u}}^* \hat{d}_\xi[\omega + \Delta_{\text{u}}] + \bar{a}_{\text{u}} \hat{d}_\xi^\dagger[\omega - \Delta_{\text{u}}] \right) \\ &\quad + g_{\text{pt}}^{(0)} \left( \bar{a}_\ell^* \hat{d}_{\text{pt}}[\omega + \Delta_\ell] + \bar{a}_\ell \hat{d}_{\text{pt}}^\dagger[\omega - \Delta_\ell] + \bar{a}_{\text{u}}^* \hat{d}_{\text{pt}}[\omega + \Delta_{\text{u}}] + \bar{a}_{\text{u}} \hat{d}_{\text{pt}}^\dagger[\omega - \Delta_{\text{u}}] \right),\end{aligned}\quad (7.66)$$

where the RPSN is associated with the same vacuum noise as before  $\hat{d}_\xi[\omega] = \chi_c[\omega]\sqrt{\kappa}\hat{\xi}[\omega]$ , while for the photothermal noise it is modified:

$$\hat{d}_{\text{pt}}[\omega] = \chi_c[\omega]\sqrt{\kappa}\hat{\xi}[\omega] - \frac{\hat{\xi}_{\text{pt}}}{\sqrt{\kappa_{\text{pt}}}}. \quad (7.67)$$

Since  $g_{\text{pt}}^{(0)}$  is in general complex, the optical force is no longer Hermitian:  $\hat{F}_{\text{OFSN}}^\dagger \neq \hat{F}_{\text{OFSN}}$ . Therefore, we need to calculate two different force noise spectra:

$$\begin{aligned} S_{\hat{F}, \hat{F}^\dagger}^{\text{OFSN}}[\omega] &\equiv \left\langle \hat{F}_{\text{OFSN}}[\omega] \hat{F}_{\text{OFSN}}^\dagger[-\omega] \right\rangle \\ &= |g^{(0)} + g_{\text{pt}}^{(0)}|^2 \kappa (|\bar{a}_\ell|^2 |\chi_c[\omega + \Delta_\ell]|^2 + |\bar{a}_u|^2 |\chi_c[\omega + \Delta_u]|^2) \\ &\quad - 2\text{Re} \left[ (g^{(0)} + g_{\text{pt}}^{(0)})^* g_{\text{pt}}^{(0)} (|\bar{a}_\ell|^2 \chi_c[-\omega - \Delta_\ell] + |\bar{a}_u|^2 \chi_c[-\omega - \Delta_u]) \right] \\ &\quad + \frac{|g_{\text{pt}}^{(0)}|^2}{\kappa_{\text{pt}}} (|\bar{a}_\ell|^2 + |\bar{a}_u|^2) \\ &= (g^{(0)})^2 \kappa (|\bar{a}_\ell|^2 |\chi_c[\omega + \Delta_\ell]|^2 + |\bar{a}_u|^2 |\chi_c[\omega + \Delta_u]|^2) \\ &\quad + 2\text{Re} \left[ g^{(0)} g_{\text{pt}}^{(0)} (|\bar{a}_\ell|^2 \chi_c[\omega + \Delta_\ell] + |\bar{a}_u|^2 \chi_c[\omega + \Delta_u]) \right] \\ &\quad + \frac{|g_{\text{pt}}^{(0)}|^2}{\kappa_{\text{pt}}} (|\bar{a}_\ell|^2 + |\bar{a}_u|^2) \end{aligned} \quad (7.68)$$

$$\begin{aligned} S_{\hat{F}^\dagger, \hat{F}}^{\text{OFSN}}[\omega] &\equiv \left\langle \hat{F}_{\text{OFSN}}^\dagger[\omega] \hat{F}_{\text{OFSN}}[-\omega] \right\rangle \\ &= (g^{(0)})^2 \kappa (|\bar{a}_\ell|^2 |\chi_c[\omega + \Delta_\ell]|^2 + |\bar{a}_u|^2 |\chi_c[\omega + \Delta_u]|^2) \\ &\quad + 2\text{Re} \left[ g^{(0)} g_{\text{pt}}^{(0)} (|\bar{a}_\ell|^2 \chi_c[-\omega - \Delta_\ell] + |\bar{a}_u|^2 \chi_c[-\omega - \Delta_u]) \right] \\ &\quad + \frac{|g_{\text{pt}}^{(0)}|^2}{\kappa_{\text{pt}}} (|\bar{a}_\ell|^2 + |\bar{a}_u|^2) \end{aligned} \quad (7.69)$$

(the PSDs differ only in the sign of the cavity susceptibility arguments in the second line; if  $g_{\text{pt}}^{(0)}$  is real, it is possible to use the relation  $(\chi_c[\omega])^* = \chi_c[-\omega]$  to show that both lines are the same). Nevertheless, the general property (7.42) of the antisymmetric component of the noise spectrum still holds:

$$\begin{aligned} S_{\hat{F}, \hat{F}^\dagger}^{\text{OFSN}}[\omega] - S_{\hat{F}^\dagger, \hat{F}}^{\text{OFSN}}[-\omega] &= (g^{(0)})^2 \kappa (|\bar{a}_\ell|^2 (|\chi_c[\omega + \Delta_\ell]|^2 - |\chi_c[-\omega + \Delta_\ell]|^2) \\ &\quad + |\bar{a}_u|^2 (|\chi_c[\omega + \Delta_u]|^2 - |\chi_c[-\omega + \Delta_u]|^2)) \\ &\quad + 2\text{Re} \left[ g^{(0)} g_{\text{pt}}^{(0)} (|\bar{a}_\ell|^2 (\chi_c[\omega_m + \Delta_\ell] - \chi_c[\omega_m - \Delta_\ell]) \right. \\ &\quad \left. + |\bar{a}_u|^2 (\chi_c[\omega_m + \Delta_u] - \chi_c[\omega_m - \Delta_u])) \right] \\ &= 2\text{Re} \left[ g^{(0)} (g^{(0)} + g_{\text{pt}}^{(0)}) (|\bar{a}_\ell|^2 (\chi_c[\omega_m + \Delta_\ell] - \chi_c[\omega_m - \Delta_\ell]) \right. \\ &\quad \left. + |\bar{a}_u|^2 (\chi_c[\omega_m + \Delta_u] - \chi_c[\omega_m - \Delta_u])) \right] \\ &= -2\text{Im}\Sigma[\omega_m] = \delta\gamma_{\text{m,eff}}. \end{aligned} \quad (7.70)$$

This result relies crucially on the presence of the  $\hat{\xi}_{\text{pt}}/\sqrt{\kappa_{\text{pt}}}$  term in the photothermal force noise, and on the fact that this noise is partially correlated with the intracavity field. Ignoring it and simply replacing the  $g^{(0)}$  by  $g^{(0)} + g_{\text{pt}}^{(0)}$  in the equation of motion for  $\hat{c}$  (which is sufficient for a classical treatment) would violate the above property and ultimately result in  $[\hat{c}, \hat{c}^\dagger] \neq 1$ .

Relation (7.70) allows us to follow the same route as for a purely radiation pressure coupled system. We can still define the effective occupation of the bath associated with the optical force

$$n_{\text{OFSN}} = \frac{S_{\hat{F}^\dagger, \hat{F}}^{\text{OFSN}}[-\omega_{\text{m,eff}}]}{\delta\gamma_{\text{m,eff}}} \quad (7.71)$$

and obtain the equilibrium occupation of the mechanical mode in the same way as in the expression (7.45) before:

$$n_{\text{m}} = \frac{n_{\text{OFSN}}\delta\gamma_{\text{m,eff}} + n_{\text{th}}\gamma_{\text{m}}}{\gamma_{\text{m,eff}}}. \quad (7.72)$$

With that, the expressions for the mechanical spectrum look the same as (7.44) and (7.45):

$$S_{\hat{c}^\dagger, \hat{c}}[\omega] = \frac{n_{\text{m}}\gamma_{\text{m,eff}}}{\gamma_{\text{m,eff}}^2/4 + (\omega + \omega_{\text{m,eff}})^2} \quad (7.73)$$

$$S_{\hat{c}, \hat{c}^\dagger}[\omega] = \frac{(n_{\text{m}} + 1)\gamma_{\text{m,eff}}}{\gamma_{\text{m,eff}}^2/4 + (\omega - \omega_{\text{m,eff}})^2}. \quad (7.74)$$

The difference is concealed in the definitions of the optomechanical self-energy  $\Sigma = \delta\omega_{\text{m,eff}} - i\delta\gamma_{\text{m,eff}}/2$  and the equilibrium mechanical occupation  $n_{\text{m}}$ .

Since equation (7.12) for the optical mode does not change (except for an additional loss channel), the general expression (7.36) for the PSD of the outgoing light still holds. Following that, the results for the PSDs of the red and blue sidebands are also the same as before (equations (7.47) and (7.48)).

To find  $S_{ii}^{(\text{rb})}$  we can still apply expression (7.49). In order to do so, we once again need to calculate the correlations between the vacuum noise and the mechanical motion, which follow from the generalized optical force noise:

$$\begin{aligned} \left\langle \hat{\xi}[\omega_{\text{b}} + \delta\omega] \hat{F}_{\text{OFSN}}^\dagger[-\omega_{\text{m,eff}} - \delta\omega] \right\rangle &= (g^{(0)} + g_{\text{pt}}^{(0)})^* \bar{a}_\ell \left\langle \hat{\xi}[\omega_{\text{b}} + \delta\omega] \hat{d}_\xi^\dagger[-\omega_{\text{b}} - \delta\omega] \right\rangle \\ &\quad - (g_{\text{pt}}^{(0)})^* \frac{\bar{a}_\ell}{\sqrt{\kappa_{\text{pt}}}} \left\langle \hat{\xi}[\omega_{\text{b}} + \delta\omega] \hat{\xi}_{\text{pt}}[-\omega_{\text{b}} - \delta\omega] \right\rangle \\ &= (g^{(0)} + g_{\text{pt}}^{(0)}) \bar{a}_\ell \chi_{\text{c}}[-\omega_{\text{b}}] \sqrt{\kappa} - (g_{\text{pt}}^{(0)})^* \frac{\bar{a}_\ell}{\sqrt{\kappa}} \end{aligned} \quad (7.75)$$

$$\left\langle \hat{\xi}_{\text{ext}}[\omega_{\text{b}} + \delta\omega] \hat{F}_{\text{OFSN}}^\dagger[-\omega_{\text{m,eff}} - \delta\omega] \right\rangle = (g^{(0)} + g_{\text{pt}}^{(0)})^* \bar{a}_\ell \chi_{\text{c}}[-\omega_{\text{b}}] \sqrt{\kappa_{\text{ext}}}. \quad (7.76)$$

These lead to

$$\begin{aligned} &\left\langle \left( \hat{\xi}_{\text{ext}}[\omega_{\text{b}} + \delta\omega] - \sqrt{\kappa_{\text{ext}}} \kappa \chi_{\text{c}}[\omega_{\text{b}}] \hat{\xi}[\omega_{\text{b}} + \delta\omega] \right) \hat{F}_{\text{OFSN}}^\dagger[-\omega_{\text{m,eff}} - \delta\omega] \right\rangle \\ &= \sqrt{\kappa_{\text{ext}}} (1 - \kappa \chi_{\text{c}}[\omega_{\text{b}}]) (g^{(0)} + g_{\text{pt}}^{(0)})^* \bar{a}_\ell \chi_{\text{c}}[-\omega_{\text{b}}] - \sqrt{\kappa_{\text{ext}}}[\omega_{\text{b}}] (g_{\text{pt}}^{(0)})^* \bar{a}_\ell \\ &= -\sqrt{\kappa_{\text{ext}}} g^{(0)} \bar{a}_\ell \chi_{\text{c}}[\omega_{\text{b}}], \end{aligned} \quad (7.77)$$

which is not dependent on the photothermal coupling. This means that the rest of the derivation follows the pure radiation pressure case, and we arrive at the same expression (7.55) as before.

## 7.4 Summary

To sum up, we have introduced the double control beam measurement scheme and described three main quantities that it provides: the two individual sidebands' PSDs, and their cross-correlator. We explored how these quantities show up in the photocurrent record, which produced final expression (7.47) and (7.48) for the sideband PSDs and equation (7.55) for the cross-correlator.

We have also identified quantum optomechanics signatures in the measurement results: a one-phonon difference between the two sideband magnitudes (sideband asymmetry), and a half-phonon difference between the cross-correlator and the sideband PSDs. We attribute the sideband asymmetry to the fundamental difference between the rates of absorption (Stokes) and emission (anti-Stokes) processes in the mechanical oscillator<sup>a)</sup>, and the cross-correlator features to the correlations between the optical vacuum noise and the mechanical motion, which arise from the action of RPSN on the mechanical mode.

Finally, we have included photothermal coupling into the model. We demonstrated that while it changes the mechanical mode parameters (equation (7.65)) and the effective optical bath occupation (equations (7.68), (7.69) and (7.71)), it does not affect expression (7.47), (7.48) and (7.55) for the measured quantities. Therefore, we have shown that the photothermal coupling does not distort the quantum optomechanics signatures.

---

<sup>a)</sup>A different interpretation is mentioned in section 2.6

# Chapter 8

## Second generation device

In this Chapter I will cover the results obtained in our second generation device. I start by listing its changes and improvements compared to the first generation device (section 8.1). Then I show the results of the OMIT/A characterization and the observation of the dynamical backaction effects (section 8.2). After that, I describe our approach to measuring and calibrating the undriven mechanical motion (section 8.3), we use to determine the mechanical bath temperature (section 8.4). Finally, I discuss the observed quantum optomechanical effects, specifically, the sideband asymmetry and the RPSN signatures (section 8.5).

### 8.1 Design improvements and device parameters

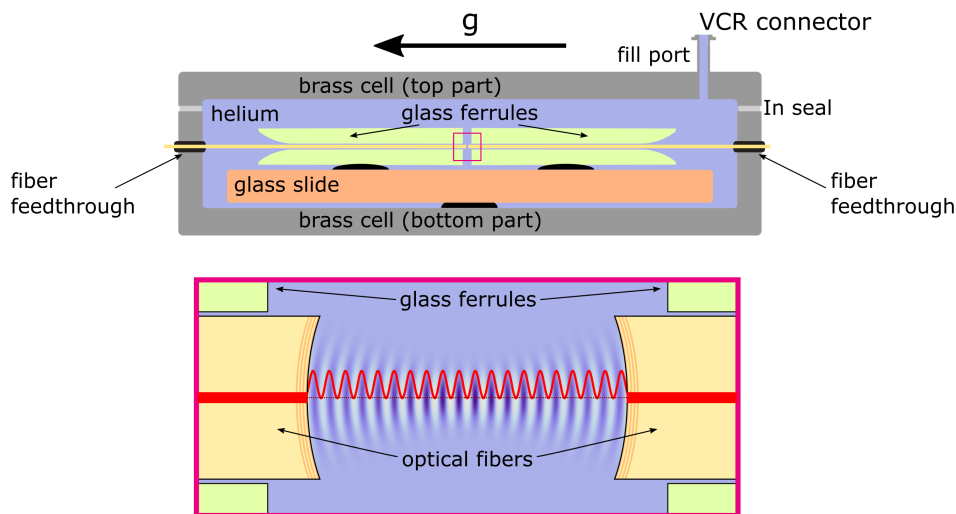


Figure 8.1: Top: Schematic of the second generation device cell. The black arrow on top shows the direction of gravity.

Bottom: Zoom-in of the cavity region denoted by the magenta rectangle in the top figure. Blue color variations denote the standing acoustic wave, with darker regions corresponding to higher helium density; red line shows the intensity profile of the standing optical wave inside the cavity.

In the previous chapter we demonstrated that the device performance was severely limited by heating caused by the light absorbed by the cavity mirrors. We have also shown that this heating is mostly due to the very poor thermal contact between the cavity volume and the rest of the helium. To improve the thermal conductivity, we altered the design as shown in Figure 8.1. The main difference compared to the first generation device (described in section 5.1, specifically Figure 5.1) is that instead of a single alignment ferrule we use two ferrules,

and the cavity is formed in the space between them. This way the cavity is in immediate contact with a larger helium bath, so we expect a much higher thermal conductivity and, as a result, much weaker heating effects.

In order to align the two ferrules, a single piece of fiber is threaded through both ferrules simultaneously, and then they are epoxied to a single glass slide. After the epoxy cures, the alignment fiber is removed, and the two ferrules effectively form a “super-ferrule”, whose alignment and robustness to thermal contraction is on par with a single ferrule. The rest of the device assembly proceeds as described in section 5.1.

There are also several less significant but still important improvements. First, the fibers’ OD (and, consequently, the ferrule ID) was changed from 125  $\mu\text{m}$  to 200  $\mu\text{m}$ . This made the fibers more mechanically robust, which allows for a better alignment of the two ferrules (a thinner alignment fiber might not be stiff enough to align the ferrules). Second, improvements in the fiber mirror manufacturing and optical coating quality let us produce better optical cavities. As a result, the optical linewidth decreased from 46 MHz (the best observed value for the first generation device) to 22.1 MHz. Finally, in an attempt to improve the acoustic quality factor, we implemented acoustic DBR structures below the optical ones using the same dielectric coating technique (they were, in fact, deposited in the same coating run). This resulted in a slight increase of the acoustic reflectivity, boosting the quality factor by about 50%. For more details on the acoustic DBR performance, see Ref. [141].

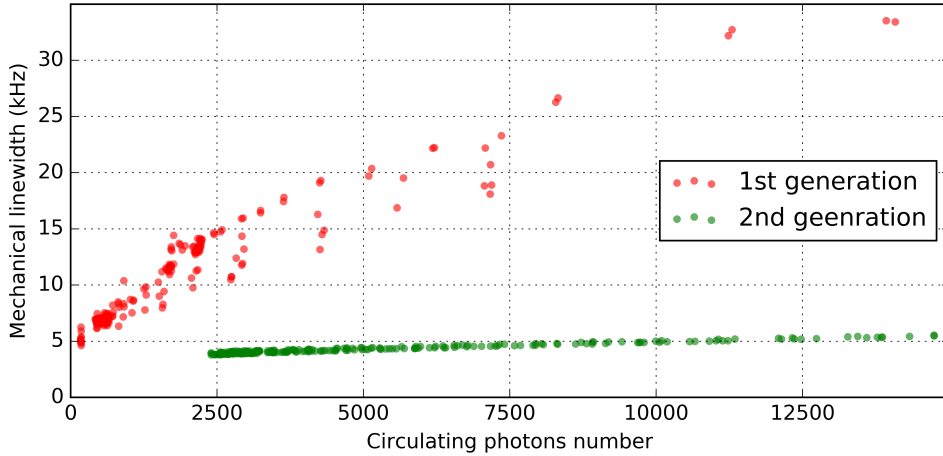


Figure 8.2: Comparison of the mechanical linewidths of the first generation device (red) and of the second generation device (green). All data has been taken for low mixing chamber temperature  $T_{\text{MC}} < 70$  mK.

As demonstrated in Figure 8.2, the design changes result in a great improvement of the mechanical quality factor. First, the temperature dependence of the mechanical loss is much weaker in the second generation device: compared to the first generation, the mechanical linewidth barely changes with power. Second, the zero-temperature limit is also better: the first generation device has the radiation quality factor of  $Q_{\text{m,int}} \approx 70,000$ , while in the second generation it is raised to  $Q_{\text{m,rad}} \approx 100,000$ .

The rest of the new device parameters are fairly similar to the first generation. The mirrors’ ROC are slightly bigger:  $r_1 = 496 \mu\text{m}$  and  $r_2 = 325 \mu\text{m}$ , compared to  $r_1 = 409 \mu\text{m}$  and  $r_2 = 282 \mu\text{m}$  for the old device. The cavity length was measured in the same way as for the first generation device (section 6.1), and the results are shown in Figure 8.3. The obtained effective lengths are  $L_{\text{eff}}^{(\text{opt})} = 66.54 \pm 0.07 \mu\text{m}$  for the optical mode and  $L_{\text{eff}}^{(\text{ac})} = 65.38 \pm 0.10 \mu\text{m}$  for the acoustic modes, yielding a similar penetration depth of  $\delta L = 0.58 \pm 0.06 \mu\text{m}$ . The estimates of the penetration depth from the difference between the filled and the empty cavity length are also fairly close:  $\delta L = 0.44 \pm 0.02 \mu\text{m}$ .

As in the first generation device, all of the optomechanical measurements shown below were performed during a separate cooldown, with the system parameters being slightly different from the data depicted in Figure 8.3. The cavity length was  $L_{\text{eff}}^{(\text{ac})} = 68.0 \pm 0.10 \mu\text{m}$  and the optical mode number was  $n_{\lambda/2}^{(\text{opt})} = 91$ , which corresponds to the optical wavelength (in vacuum) of  $\lambda_{\text{opt}} = 1529.6 \text{ nm}$  and the mechanical frequency

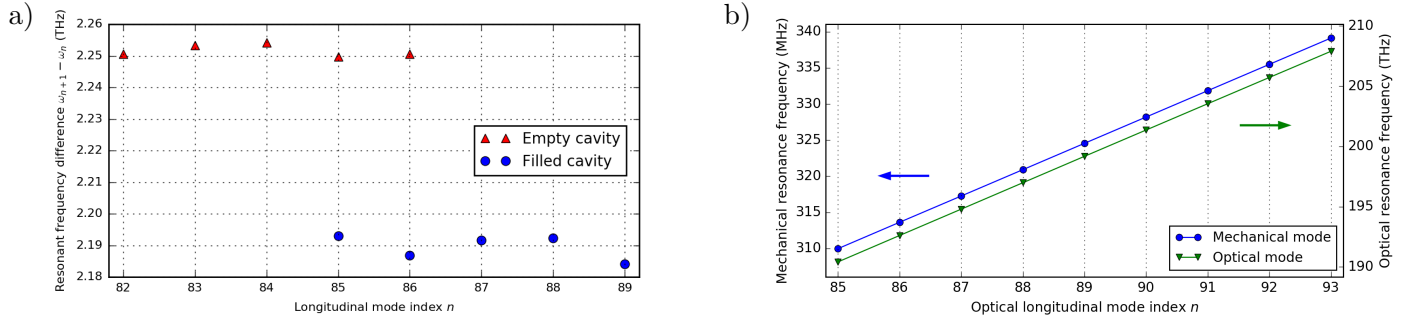


Figure 8.3: a) Frequency difference between the consecutive resonances  $\Delta\omega_n$  for different resonance indices  $n$  measured for an empty cavity (red) and for the same cavity filled with superfluid helium (blue). The longitudinal index  $n$  corresponds to the number of nodes of the standing optical wave inside the cavity, and is formally defined in equation (B.32).

b) Mechanical (blue) and optical (green) resonance frequencies as a function of optical longitudinal mode index. Note that the plots have different vertical axes scale. The vertical axes are rescaled for the data to have the same slope, and shifted for clarity.

Parameter	First generation	Second generation
$L$ , $\mu\text{m}$	84.1	68.0
$n_{\lambda/2}^{(\text{opt})}$	112	91
$\lambda_{\text{opt}}$ , nm	1538.3	1529.6
$\kappa/(2\pi)$ , MHz	69	22.1
$\kappa_{\text{ext}}/(2\pi)$ , MHz	15	9.7
$\omega_m/(2\pi)$ , MHz	317.44	319.24
$Q_{\text{m,rad}}$	60,000	100,000
$g^{(0)}/(2\pi)$ , kHz	3.18	3.60
$g_{\text{pt}}^{(0)}/(2\pi)$ , kHz	$i \cdot 0.97$	$i \cdot 0.83$

Table 8.1: Parameter comparison between the first and the second generation devices.

of  $\omega_m = 2\pi \cdot 319.24$  MHz. The optical cavity linewidth is still the same  $\kappa = 2\pi \cdot 22.1$  MHz, and the external coupling is  $\kappa_{\text{ext}} = 0.44\kappa = 2\pi \cdot 9.7$  MHz.

A list of most important parameters for the first and for the second generation devices is given in Table 8.1.

## 8.2 OMIT measurements and the dynamical backaction

Just as for the previous device, we start the characterization by performing OMIT/A measurements. This time, however, we can reach large enough intracavity power to observe the dynamical backaction effects (section 2.5), i.e., we can control the linewidth and frequency of the acoustic mode using the optomechanical interaction. The results are summarized in Figure 8.4. All of the data were fit simultaneously to the expectations of the optomechanical theory with the photothermal coupling, described in subsection 6.2.4. Specifically, we used equations (6.16) and (6.17) for the data in the left part of Figure 8.4 (OMIT/A response), and equation (6.17) (together with expressions (2.91), (2.92) for the optomechanical frequency and linewidth change) for the data in the right part. The only two free parameters are, as before, the radiation pressure single-photon optomechanical coupling  $g^{(0)}$  and the photothermal single-photon coupling  $g_{\text{pt}}^{(0)}$ ; as before, we assume the photothermal coupling

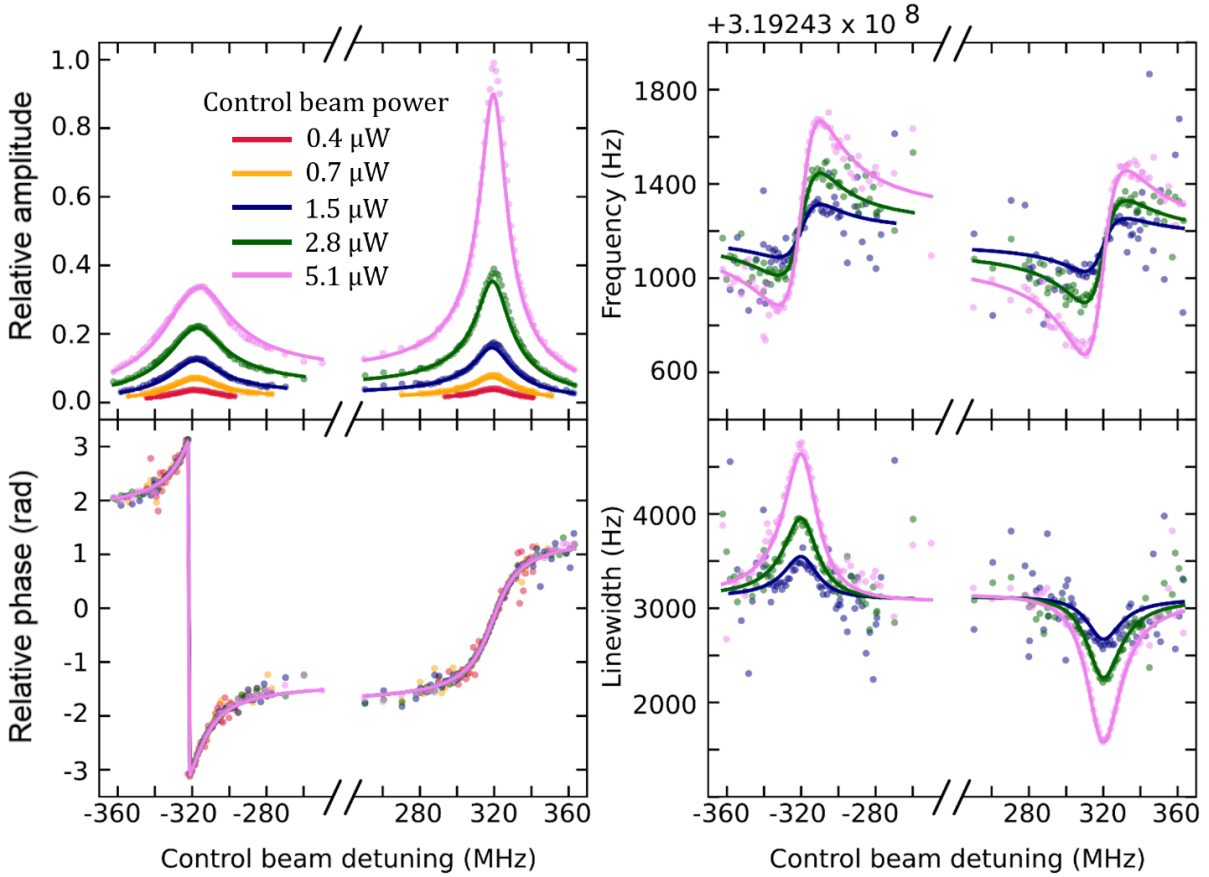


Figure 8.4: Left: relative amplitude (top) and phase (bottom) of the OMIT/A feature as a function of the control beam detuning for several control beam powers. The data is conceptually the same as in Figure 6.4, but shows much larger amplitude of the OMIT/A response. Solid lines are fits to the OMIT theory with photothermal coupling (subsection 6.2.4).

Right: change in the mechanical frequency (top) and damping (bottom) due to the dynamical backaction. This data is obtained in the same experiments as the data shown in the left part, but with the two lowest power datasets excluded due to poor SNR. The solid lines are the fits to the dynamical backaction theory with photothermal coupling (subsection 6.2.4).

to be purely imaginary. The results are  $g^{(0)} = 2\pi \cdot (3.60 \pm 0.1)$  kHz and  $g_{\text{pt}}^{(0)} = i \cdot 2\pi \cdot (0.83 \pm 0.1)$  kHz. Essentially the same results (within the statistical error) are obtained from an individual fit of the OMIT/A data (left half of Figure 8.4) or an individual fit of the dynamical backaction data (right half of Figure 8.4). Theoretical calculations like the ones in subsection 6.2.5 yield  $g^{(0)}$  lying between  $2\pi \cdot 3.55$  kHz and  $2\pi \cdot 4.1$  kHz, with the best estimate of the reflection angle  $\phi = -0.2\pi$  resulting in  $g^{(0)} = 2\pi \cdot 3.88$  kHz. While the agreement is slightly worse than for the first generation device, the experimental results are still within 10% from the theoretical expectations. The difference can be attributed to the uncertainties in the calibration of the optical power, of the external cavity coupling, or of the cavity geometric parameters (most likely, mirror ROCs).

### 8.3 Undriven motion measurement

Another experiment made possible by the improved cavity design is the measurement of the undriven mechanical motion, whose concept is described in sections 2.6 and 7.1. This motion arises due to the thermal noise coming from the mechanical bath, and thus represents thermal fluctuations of superfluid helium density inside the cavity. As the device temperature is very low, the magnitude of this motion is fairly small (the typical variation

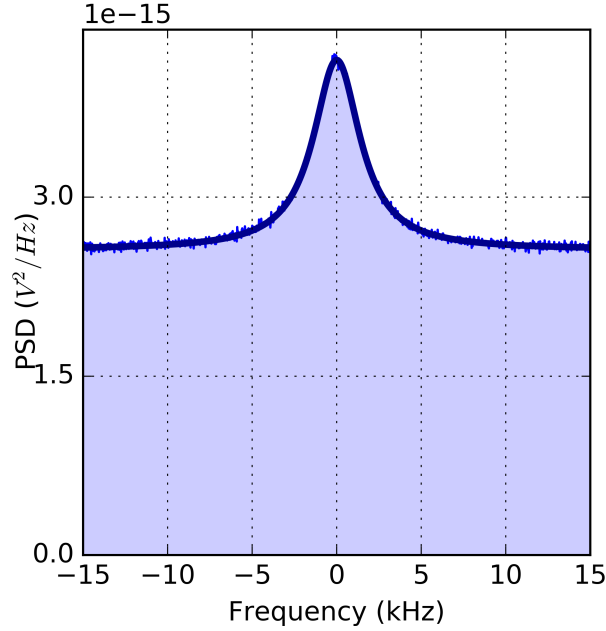


Figure 8.5: PSD of the voltage at the input of ZILI, which is proportional to the PSD of the photocurrent. The horizontal axis is shifted to have zero at the mechanical resonance frequency. Solid line shows the fit to a Lorentzian with a frequency-independent background (equation (8.1)).

in the relative helium density is about  $5 \cdot 10^{-9}$ , resulting in a cavity detuning of only 30 kHz), which requires long integration times to resolve in our system.

### 8.3.1 Measurement scheme

The optical tones that we use for the observation of the undriven motion are described in the previous chapter and are shown in Figure 7.1a,b. They are similar to the scheme used for the OMIT/A measurements (section 6.2), but this time the probe beam (which was used to produce an intensity beatnote that drives the mechanical mode) is absent, and instead of detecting the coherent response of the probe drive, the PSD of the photocurrent is calculated. Since most of the undriven motion measurement was performed in the double-beam configuration (Figure 7.1b), this is the measurement we will focus on. To describe a single-beam measurement scheme (Figure 7.1a), we only need to set one of the control beam powers to be zero.

Below is the outline of the PSD measurement procedure:

- (a) Lock the laser and the experimental cavity; as before, the cavity resonance is detuned by  $\nu_c \approx 2\pi \cdot 2100$  MHz from the OLO.
- (b) Set up the control beams by applying two microwave tones to the phase modulator. Usually, one of these tones is created by a dedicated microwave generator MWG 2, and the other by mixing up one of the ZILI outputs. We can denote the frequencies of these two microwave tones as  $\nu_{\text{con},\ell}$  for the lower frequency one (usually, the one output by MWG 2) and  $\nu_{\text{con},u}$  for the upper frequency one (created with the ZILI). Their corresponding detunings from the cavity resonance are  $\Delta_\ell = \nu_{\text{con},\ell} - \nu_c$  and  $\Delta_u = \nu_{\text{con},u} - \nu_c$ .

For the best sensitivity, the detunings of the control beams should be close to  $\pm\omega_{\text{m,eff}}$ , so that one of their mechanical sidebands is resonant with the optical cavity. This implies that the corresponding microwave frequencies are  $\nu_{\text{con},\ell} \approx \nu_c - \omega_{\text{m,eff}} \approx 2\pi \cdot 1780$  MHz and  $\nu_{\text{con},u} \approx \nu_c + \omega_{\text{m,eff}} \approx 2\pi \cdot 2420$  MHz.

- (c) Using the ZILI as a spectrum analyzer, measure the PSD of the photocurrent around  $\nu_{\text{con},\ell} + \omega_{\text{m,eff}}$  and  $\nu_{\text{con},u} - \omega_{\text{m,eff}}$ , which are the frequencies (in the microwave domain) of the mechanical sidebands closest

to the cavity resonance. We will denote the former photocurrent PSD (around  $\nu_{\text{con},\ell} + \omega_{\text{m,eff}}$ ) as  $S_{ii}^{(\ell\ell)}[\omega]$  and the latter PSD as  $S_{ii}^{(\text{uu})}[\omega]$ .

To obtain the photocurrent PSD, the ZILI demodulates the input signal at a given frequency (the center frequency of the PSD region of interest) and records the resulting demodulated quadratures at a reduced sampling rate (typically, about 200 kSa/s). This operation can be effectively thought of as recording the time-dependent photocurrent  $i(t)$ , but only corresponding to a narrow (half of the sampling frequency, i.e.,  $\sim 100$  kHz) frequency region of interest. After that, we apply the Fast Fourier Transform (FFT) algorithm in the post-processing and get the photocurrent Fourier transform  $i[\omega]$ , which is then used to produce the photocurrent PSD  $S_{ii}[\omega] = \langle |i[\omega]|^2 \rangle$ . In practice, the ensemble averaging  $\langle \dots \rangle$  is replaced by either time-averaging or data binning (averaging together neighboring data points).

This method of PSD calculation yields the same results as other approaches, for example, narrow-band filtering of the signal followed by a power detector (which is the method frequently used to calculate optical spectrum, and which we effectively implement with the TFPC in appendix D.2 and D.7). However, the fact that we obtain time record of the photocurrent  $i(t)$  becomes important for calculating the sideband cross-correlator, as described in section 7.2 and appendix D.9.

As described in appendix C.1.2, the obtained photocurrent PSDs correspond to the optical PSD around  $(\omega_{\text{OLO}} + \nu_{\text{con},\ell}) + \omega_{\text{m,eff}}$  for the lower control beam sideband, and around  $(\omega_{\text{OLO}} + \nu_{\text{con},\text{u}}) - \omega_{\text{m,eff}}$  for the upper control beam (where  $\omega_{\text{OLO}}$  is the frequency of the OLO). In the cavity frame  $\omega_{\text{OLO}}$  is the OLO detuning, which is fixed to be  $\omega_{\text{OLO}} = -\nu_{\text{c}}$  due to the cavity locking. This means that the measured photocurrent PSDs are centered around  $(\nu_{\text{con},\ell} - \nu_{\text{c}}) + \omega_{\text{m,eff}} = \Delta_{\ell} + \omega_{\text{m,eff}} = \omega_{\text{b}}$  and  $(\nu_{\text{con},\text{u}} - \nu_{\text{c}}) - \omega_{\text{m,eff}} = \Delta_{\text{u}} + \omega_{\text{m,eff}} = \omega_{\text{r}}$  respectively for the lower and the upper control beams, where  $\omega_{\text{r,b}}$  are defined in equation (7.28) in section 7.2. As shown in subsection 7.2.2 and equations (7.47) and (7.48), we expect these parts of the spectrum to contain the mechanical motional sidebands. These sidebands are manifest as Lorentzian peaks with width equal to the mechanical linewidth, and height proportional to the average mechanical phonon occupation  $n_{\text{m}}$  (for the anti-Stokes sideband) or  $n_{\text{m}} + 1$  (for the Stokes sideband). Figure 8.5 shows an example of one of the mechanical Lorentzians.

Both of the sidebands are fit to the general form of a Lorentzian with a frequency-independent background:

$$S_{ii}^{(\ell\ell)}[\omega] = A_{bg}^{(\ell\ell)} \left( 1 + L_{\text{rel}}^{(\ell\ell)} \frac{(\gamma_{\text{m,eff}}/2)^2}{(\gamma_{\text{m,eff}}/2)^2 + (\omega - (\nu_{\text{con},\ell} + \omega_{\text{m,eff}}))^2} \right) \quad (8.1)$$

$$S_{ii}^{(\text{uu})}[\omega] = A_{bg}^{(\text{uu})} \left( 1 + L_{\text{rel}}^{(\text{uu})} \frac{(\gamma_{\text{m,eff}}/2)^2}{(\gamma_{\text{m,eff}}/2)^2 + (\omega - (\nu_{\text{con},\text{u}} - \omega_{\text{m,eff}}))^2} \right), \quad (8.2)$$

from which we obtain the mechanical frequency  $\omega_{\text{m,eff}}$ , mechanical linewidth  $\gamma_{\text{m,eff}}$ , and the Lorentzian heights relative to the background  $L_{\text{rel}}^{(\ell\ell)}$  and  $L_{\text{rel}}^{(\text{uu})}$ . These relative heights are used to extract the mean phonon occupation  $n_{\text{m}}$  of the mechanical oscillator, as described in the next subsection.

### 8.3.2 Normalization scheme

For simplicity, we start by considering the lower control beam sideband PSD  $S_{ii}^{(\ell\ell)}$ , which corresponds to the anti-Stokes mechanical sideband described by equation (7.48). We can rewrite that expression as

$$\begin{aligned} S_{ii}^{(\text{bb})}[\delta\omega] &= G^2 |a_{\text{OLO}}|^2 \left( \kappa_{\text{ext}} |\chi_{\text{c}}[\omega_{\text{b}}]|^2 (g^{(0)})^2 |\bar{a}_{\ell}|^2 \frac{n_{\text{m}} \gamma_{\text{m,eff}}}{\gamma_{\text{m,eff}}^2/4 + \delta\omega^2} + 1 \right) \\ &= G^2 |a_{\text{OLO}}|^2 \left( 4 \frac{\kappa_{\text{ext}}}{\kappa} \frac{4(g^{(0)})^2 |\bar{a}_{\ell}|^2}{\kappa \gamma_{\text{m,eff}}} \frac{1}{1 + (2\delta\omega/\gamma_{\text{m,eff}})^2} n_{\text{m}} \frac{1}{1 + (2\omega_{\text{b}}/\kappa)^2} + 1 \right) \\ &= G^2 |a_{\text{OLO}}|^2 \left( 4\eta_{\kappa} \frac{\Gamma_{\text{meas},\ell}}{\gamma_{\text{m,eff}}} \frac{1}{1 + (2\omega_{\text{b}}/\kappa)^2} n_{\text{m}} \frac{1}{1 + (2\delta\omega/\gamma_{\text{m,eff}})^2} + 1 \right). \end{aligned} \quad (8.3)$$

Here  $\Gamma_{\text{meas},\ell} = \frac{4(g^{(0)})^2|\bar{a}_\ell|^2}{\kappa}$  is the measurement rate of the lower control beam, and  $\eta_\kappa = \frac{\kappa_{\text{ext}}}{\kappa}$  is the contribution to the measurement quantum efficiency due to the imperfect external coupling to the cavity.

If we compare equation (8.3) to the fit function (8.1), we see that their functional forms agree, and that the mechanical linewidths are consistent between the two expressions. To show that the mechanical frequencies agree as well, recall that  $S_{ii}^{(\text{bb})}$  was defined as (equation (7.30))  $S_{ii}^{(\text{bb})}[\delta\omega] = S_{ii}[\delta\omega + \omega_b - \omega_{\text{OLO}}]$ . Using the definition  $\omega_b = \Delta_\ell + \omega_{\text{m,eff}} = (\nu_{\text{con},\ell} - \nu_c) + \omega_{\text{m,eff}}$  and  $\omega_{\text{OLO}} = -\nu_c$  we can rewrite it as  $S_{ii}^{(\text{bb})}[\delta\omega] = S_{ii}[\delta\omega + \nu_{\text{con},\ell} + \omega_{\text{m,eff}}]$ , which agrees with the expression (8.1). Finally, the last fit parameter, the relative mechanical Lorentzian height, is expected to be

$$L_{\text{rel}}^{(\ell\ell)} = 4\eta_\kappa \frac{\Gamma_{\text{meas},\ell}}{\gamma_{\text{m,eff}}} \frac{1}{1 + (2\omega_b/\kappa)^2} n_{\text{m}}, \quad (8.4)$$

This expression is derived under the assumption of no additional loss or noise sources between the cavity output and the detector. Now, assume that there is a finite transmission from the cavity output to the photodetector  $\eta_\ell$ . It will affect the signal part of the PSD, but not the background, which will stay 1 in photon units. This is especially apparent in the normal-ordering description of the photodetection, where the background comes from the optical local oscillator, which is unaffected by the additional loss (at least, in the standard heterodyne measurement scheme, where the OLO is combined with the signal right at the PD input). Thus, the relative height is multiplied by  $\eta_\ell$

$$L_{\text{rel}}^{(\ell\ell)} = 4\eta_\kappa \eta_\ell \frac{\Gamma_{\text{meas},\ell}}{\gamma_{\text{m,eff}}} \frac{1}{1 + (2\omega_b/\kappa)^2} n_{\text{m}}. \quad (8.5)$$

Next, let us consider the effect of additional sources of noise on the way from the cavity to the photodetector. We denote their strength relative to the vacuum noise as  $n_{\text{add}} = \frac{1}{\eta_n} - 1$ , where  $\eta_n \leq 1$  represents the drop in the quantum efficiency due to this additional noise. With that, the noise background becomes  $1 + n_{\text{add}} = \frac{1}{\eta_n}$ , and the relative lorentzian height is further reduced to

$$L_{\text{rel}}^{(\ell\ell)} = 4\eta_\kappa \eta_\ell \eta_n \frac{\Gamma_{\text{meas},\ell}}{\gamma_{\text{m,eff}}} \frac{1}{1 + (2\omega_b/\kappa)^2} n_{\text{m}}. \quad (8.6)$$

Finally, there may be additional mechanisms reducing the signal-to-noise ratio which can not be readily attributed to loss or additional noise. For example, one such source of noise is the heterodyne non-ideality coming from the fact that OLO power is not infinitely larger than every other optical tone in the system (this mechanism is described quantitatively below). We can denote the quantum efficiency reduction of these residual mechanisms as  $\eta_r$  and get the final expression

$$\begin{aligned} L_{\text{rel}}^{(\ell\ell)} &= 4\eta_\kappa \eta_\ell \eta_n \eta_r \frac{\Gamma_{\text{meas},\ell}}{\gamma_{\text{m,eff}}} \frac{1}{1 + (2\omega_b/\kappa)^2} n_{\text{m}} \\ &= 4\eta_t \frac{\Gamma_{\text{meas},\ell}}{\gamma_{\text{m,eff}}} \frac{1}{1 + (2\omega_b/\kappa)^2} n_{\text{m}}, \end{aligned} \quad (8.7)$$

where  $\eta_t = \eta_\kappa \eta_\ell \eta_n \eta_r$  is the combined quantum efficiency of the measurement process. For a sideband close to the optical resonance  $|\omega_b| \ll \kappa$  the expression above simplifies to

$$L_{\text{rel}}^{(\ell\ell)} = 4\eta_t \frac{\Gamma_{\text{meas},\ell}}{\gamma_{\text{m,eff}}} n_{\text{m}}. \quad (8.8)$$

To calibrate the measurement rate  $\Gamma_{\text{meas},\ell}$  we use the OMIT/A data. The expression for the normalized amplitude of the OMIT/A feature is derived in subsection 6.2.4, equation (6.16):

$$\begin{aligned} a_{\text{rel},+} &= -\frac{2|\bar{a}|^2 g^{(0)} (g^{(0)} + g_{\text{pt}}^{(0)})}{\gamma_{\text{m,eff}}} \chi_c[\omega_b] \\ &= -\frac{g^{(0)} + g_{\text{pt}}^{(0)}}{g^{(0)}} \frac{\Gamma_{\text{meas},\ell}}{\gamma_{\text{m,eff}}} \frac{1}{1 - 2i\omega_b/\kappa}. \end{aligned} \quad (8.9)$$

The minus sign denotes that for a blue sideband (i.e., red-detuned control beam) the OMIT/A feature is a dip, so the Lorentzian is subtracted from the background. Similar to the motional sideband PSD, the expression can be further simplified for an on-resonance sideband:

$$a_{\text{rel},+} = -\frac{g^{(0)} + g_{\text{pt}}^{(0)}}{g^{(0)}} \frac{\Gamma_{\text{meas},\ell}}{\gamma_{\text{m,eff}}}. \quad (8.10)$$

If the photothermal coupling  $g_{\text{pt}}^{(0)}$  is known, then the measurement of  $a_{\text{rel},+}$  can be used to extract the ratio  $\Gamma_{\text{meas},\ell}/\gamma_{\text{m,eff}}$ . Knowing this ratio and  $\eta_t$ , one can then use formula (8.8) to relate the measured relative height of the Brownian motion peak  $L_{\text{rel}}^{(\ell\ell)}$  to the mechanical oscillator occupation  $n_{\text{m}}$ , and consequently rescale the vertical axis in the motional PSD data in units of phonons.

A similar calibration (using the same value of  $\eta_t$ , but a different individually determined measurement rate  $\Gamma_{\text{meas},\text{u}}$ ) is performed for the anti-Stokes acoustic sideband  $S_{ii}^{(\text{uu})}$ . Finally, to normalize the cross-correlator data  $S_{ii}^{(\text{rb})}$  we apply a scaling coefficient which is the geometric mean of the coefficients for the red and the blue sidebands.

The relevant contributions to the quantum efficiency in our setup are measured to be:

- Imperfect input cavity coupling  $\eta_{\kappa} = \kappa_{\text{ext}}/\kappa = 0.44 \pm 0.03$ .
- Optical loss between the cavity output and the optical amplifier  $\eta_{\ell} = 0.44$ . Its calibration procedure is described in appendix D.8.
- EDFA input noise  $\eta_{\text{n}} = 0.35 \div 0.40$  ( $\sim 4$  dB noise figure), depending on the total power incident on the amplifier. Its measurement procedure is described in appendix D.5.
- Imperfection of the heterodyne detection. The idealized description of the heterodyne detection usually assumes that the power in the OLO is much larger than in the rest of the optical field. If this assumption is relaxed, then the background of the motional sideband, which is proportional to the total laser power, becomes larger in comparison with the signal component, which comes only from the mixing with the OLO. As a result, the SNR degrades by the additional factor of  $\eta_{\text{r}} = P_{\text{OLO}}/P_{\text{tot}}$ , where  $P_{\text{OLO}}$  is the power in the OLO and  $P_{\text{tot}}$  is total power incident on the photodiode. In our measurements  $\eta_{\text{r}}$  varies between 0.7 and 0.95, depending on the strength of the microwave drives used to create the control beams.
- Image noise of the mixdown circuit. As mentioned in appendix D.3, the mixer circuit is not ideal, and it allows the noise from other parts of the spectrum (“image noise”) to be folded on top of the signal, which reduces the signal-to-noise ratio (SNR); thus the SNR of the “down-mixed” intermediate frequency (IF) signal on the output of the mixer can be higher than the SNR of the radio-frequency (RF) signal on the output of the photodetector.

The most common example of such a process is a standard (i.e., not image rejection) mixer, whose action can be thought of as multiplying the RF input by the microwave local oscillator (MWLO) signal at a frequency  $\nu_{\text{MWLO}}$  to produce the IF output. Since positive and negative frequencies at the IF output “fold” on top of each other, the signal at some frequency  $\nu_{\text{IF}}$  will be a sum of RF signals at  $\nu_{\text{MWLO}} + \nu_{\text{IF}}$  and  $\nu_{\text{MWLO}} - \nu_{\text{IF}}$ ; if only one of these contains actual signal (e.g., the brownian motion peak, in our case) but both have the same amount of noise, this “folding” reduces SNR by a factor of 2.

We performed calibrations of our image rejection mixer, as described in appendix section D.3. It turns out that at the relevant frequencies the added noise is suppressed by at least 22 dB, meaning that the associated quantum efficiency is  $\eta \geq 1 - 10^{-2.2} \approx 0.993$ . Therefore, we ignore this noise factor entirely.

- Electronic noise, mostly coming from the first microwave amplifier and the ZILI input preamplifier. This kind of noise is different from the other noise sources as it is additive rather than multiplicative, that is, its magnitude does not depend on the light incident on the photodiode. In particular, it is present when there is no incident power which makes it relatively easy to account for in the calibration: we measure it

beforehand with the laser and EDFA turned off, and then subtract it from the ZILI voltage PSD as the first step before applying other calibrations.

Combining these contributions, the total quantum efficiency  $\eta_t$  of the setup was between 0.05 and 0.08 depending on the measurement configuration. These estimates do not include electronics noise, because it is additive, so that its effect varies a lot depending on the optical power, measurement scheme, etc. Nevertheless, it is typically only about 1% of the total noise background (most of which is due to the EDFA noise). Hence it does not noticeably affect the numbers presented above, although we do take it into account in the calibration procedure. The relative error in the determination of the quantum efficiency is 7%, which almost entirely comes from the uncertainty in the relative input cavity coupling  $\eta_\kappa$ .

## 8.4 Thermal motion

In order to estimate the device heating and validate the normalization procedure, we performed thermal motion measurements for different MC temperatures and circulating powers. For each measurement we converted the mechanical phonon occupation  $n_m$  into the mechanical thermal bath occupation  $n_{\text{th},m}$  by taking into account optomechanical damping and radiation pressure shot noise (RPSN) heating, for which we use equation (7.72), where  $n_{\text{OFSN}}$  is defined in equations (7.71) and (7.69):

$$\begin{aligned}
n_m \delta\gamma_{m,\text{eff}} &= S_{\hat{F}^\dagger, \hat{F}}^{\text{OFSN}}[-\omega_{m,\text{eff}}] \\
&= 2\text{Re} \left[ g^{(0)} \left( g^{(0)} + g_{\text{pt}}^{(0)} \right) (|\bar{a}_\ell|^2 \chi_c[\omega_{m,\text{eff}} - \Delta_\ell] + |\bar{a}_u|^2 \chi_c[\omega_{m,\text{eff}} - \Delta_u]) \right] \\
&\quad + \frac{|g_{\text{pt}}^{(0)}|^2}{\kappa_{\text{pt}}} (|\bar{a}_\ell|^2 + |\bar{a}_u|^2) \\
&\approx 2\text{Re} \left[ g^{(0)} \left( g^{(0)} + g_{\text{pt}}^{(0)} \right) |\bar{a}_u|^2 \chi_c[\omega + \Delta_u] \right] + \frac{|g_{\text{pt}}^{(0)}|^2}{\kappa_{\text{pt}}} (|\bar{a}_\ell|^2 + |\bar{a}_u|^2), \tag{8.11}
\end{aligned}$$

where we dropped the RPSN coming from the lower control beam as  $|\chi_c[\omega_{m,\text{eff}} - \Delta_\ell]| \approx |\chi_c[2\omega_{m,\text{eff}}]| \ll |\chi_c[\omega_{m,\text{eff}} + \Delta_\ell]|$ . We additionally assume almost resonant sidebands  $|\omega_{m,\text{eff}} - \Delta_u| \ll \kappa$ , we can approximate  $\chi_c[\omega_{m,\text{eff}} - \Delta_u] \approx \chi_c[0] = 2/\kappa$  and simplify further:

$$n_m \delta\gamma_{m,\text{eff}} \approx 4 \frac{(g^{(0)})^2}{\kappa} |\bar{a}_u|^2 + \frac{|g_{\text{pt}}^{(0)}|^2}{\kappa_{\text{pt}}} (|\bar{a}_\ell|^2 + |\bar{a}_u|^2). \tag{8.12}$$

The first term in this expression corresponds to the RPSN, and it only depends on independently measured parameters. In our measurements we had  $|\bar{a}_\ell|^2 \approx |\bar{a}_u|^2 < 1200$ , so the RPSN added at most about one phonon worth of mechanical energy, in the sense that its contribution to the term  $n_{\text{OFSN}} \delta\gamma_{m,\text{eff}} / \gamma_{m,\text{eff}}$  in equation (7.72) was not more than one. The second term, however, involves the photothermal channel loss rate  $\kappa_{\text{pt}}$ , which we can not access experimentally. There are several ways of estimating this loss quantity.

One way is to assume that all of the internal cavity loss contributes to the photothermal force. This means that  $\kappa_{\text{int}} = 0$  and, consequently,  $\kappa_{\text{pt}} = \kappa - \kappa_{\text{ext}} \approx 0.56\kappa$ . With that assumption, the photothermal force noise (second term in equation (8.12)) is about 5% of the RPSN (first term in equation (8.12)), or about 0.05 phonons. This is much smaller than many statistical and systematic uncertainties in our measurement of  $n_m$ , so it can safely be ignored.

The other way is to use the absorption of the DBR mirrors to estimate the amount of power dissipated in the cavity. Room-temperature calorimetry measurements performed by the coating company yield an estimate of the optical absorption  $a = 3$  ppm (per single reflection) for laser wavelength  $\lambda_{\text{opt}} = 1064$  nm[165]. Given the cavity finesse  $\mathcal{F} \approx 100,000$ , we can calculate the fraction of optical losses associated with absorption to be  $a\mathcal{F}/(2\pi) \approx 0.05$  per mirror, or 0.1 total. Therefore, we can assume  $\kappa_{\text{pt}} \approx 0.1\kappa$ , so that the added phonon number is  $\sim 25\%$  of RPSN contribution, i.e., about 0.25 phonons. This is still small enough that we can ignore it while interpreting thermal motion data (and it is even smaller for the majority of measurements, where  $\bar{n}_c < 1000$

and this contribution is  $< 0.1$  phonon), where the typical thermal bath occupation is  $\sim 10$  phonons. Thus, in the analysis we ignore the photothermal force contribution to the optical noise and assume  $n_{\text{OFSN}} = n_{\text{RPSN}}$ , where  $n_{\text{RPSN}}$  is calculated for the purely radiation pressure case and is defined in equation (7.43).

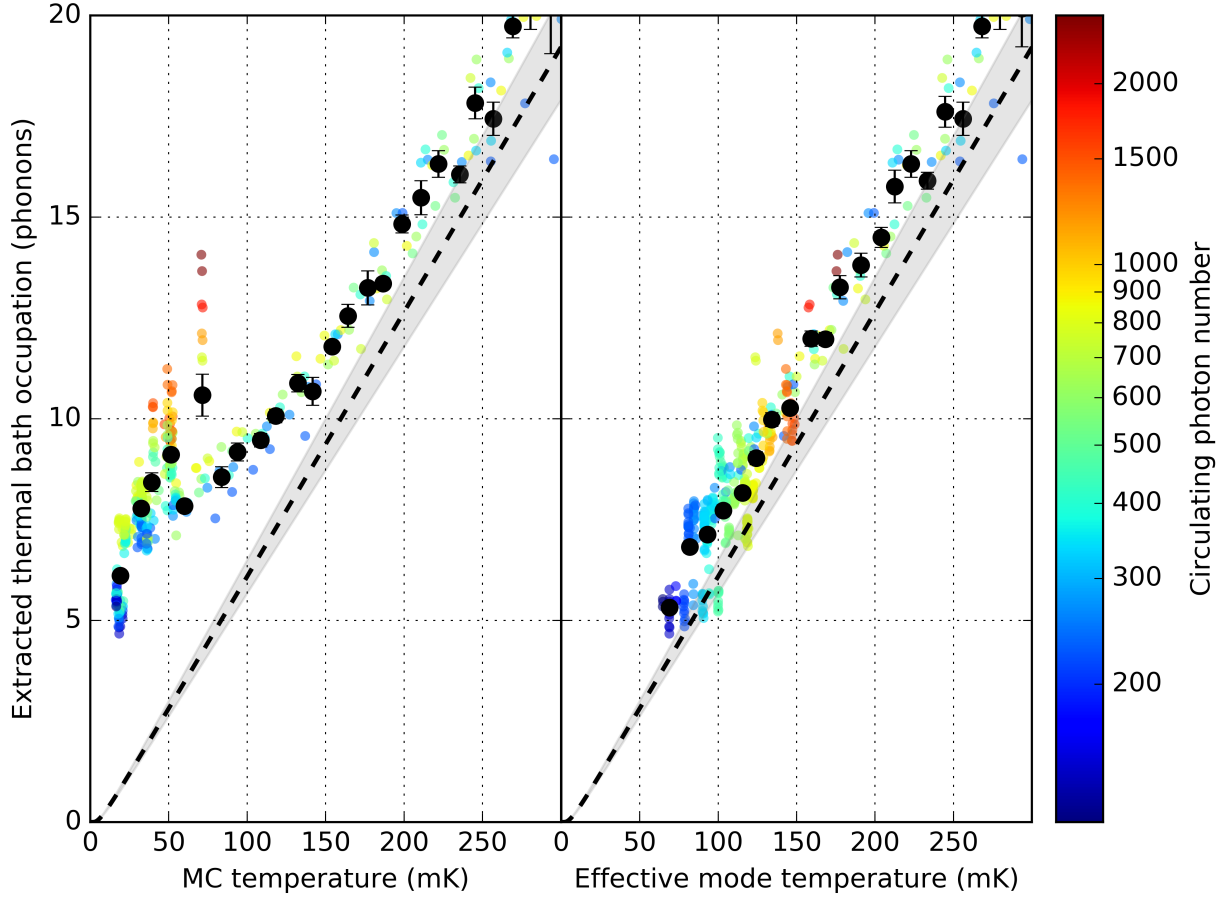


Figure 8.6: Left: thermal phonon occupation of the mechanical bath  $n_{\text{th,m}}$  as a function of the mixing chamber (MC) temperature  $T_{\text{MC}}$ . Marker color encodes the circulating photon number. The dashed lines shows the expectations  $n_{\text{th,m}} = n_{\text{th}}(T_{\text{MC}})$ , where  $n_{\text{th}}(T)$  is defined in (2.10). The grey area around this line shows the systematic uncertainty in determining  $n_{\text{th,m}}$ ; it mostly comes from the uncertainty in calibration of  $\eta_{\kappa} = \kappa_{\text{ext}}/\kappa$ .

Right: Same data as in the left part, but with the horizontal axis rescaled to represent the effective bath temperature extracted from the thermal model.

With this simplification, we can now calculate the mechanical thermal bath occupation  $n_{\text{th,m}}$  given the mechanical mode occupation  $n_{\text{m}}$ . The result of this analysis is shown in the left part of Figure 8.6, which plots  $n_{\text{th,m}}$  as a function of the MC temperature  $T_{\text{MC}}$ . For  $T_{\text{MC}} \gtrsim 150$  mK the experimental results agree pretty well with the expectation that the bath temperature is equal to  $T_{\text{MC}}$  (i.e.,  $n_{\text{th,m}} = n_{\text{th}}(T_{\text{MC}}) = (\exp(\hbar\omega_{\text{m,eff}}/k_{\text{B}}T_{\text{MC}}) - 1)^{-1}$ ). However, for lower temperatures the experimental values are higher than theoretical expectations, and are generally larger for high circulating photon numbers. This implies that there is still some optical heating present in our system, which causes the helium bath temperature to be higher than  $T_{\text{MC}}$ .

It turns out that the heating mechanism in the second generation device is very different from the first generation device (section 6.3). The behavior of that device was explained fairly well by assuming that the helium temperature distribution inside the cavity is homogeneous, and that the heating occurs because of the low thermal conductivity of the helium sheaths connecting the cavity with a large helium bath. The current device, however, fails to be described by a similar model, and seems to exhibit highly inhomogeneous temperature

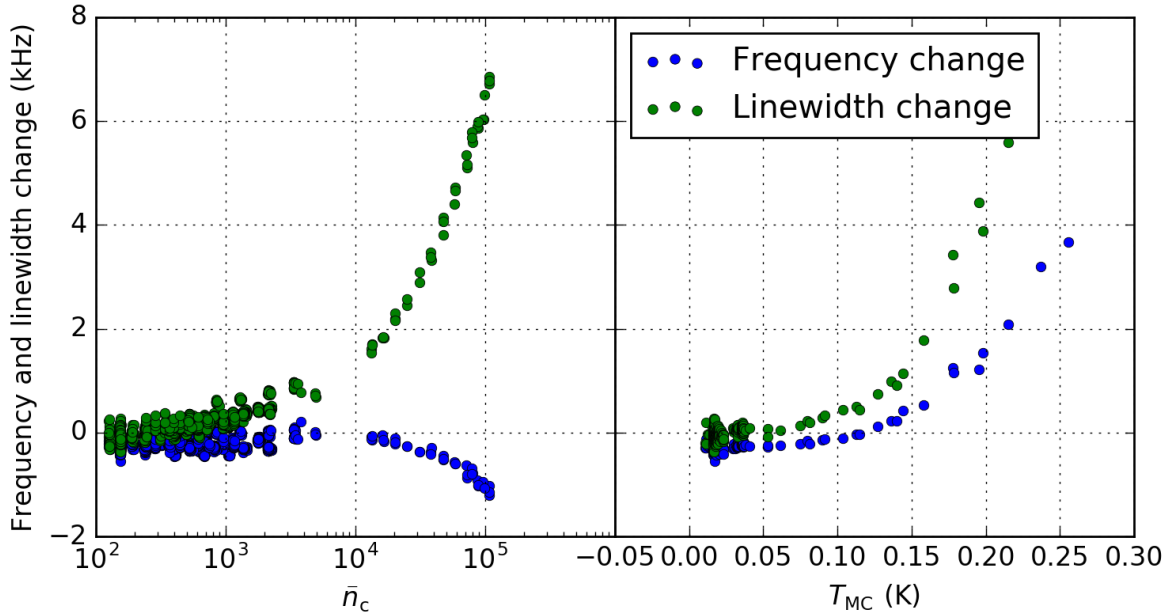


Figure 8.7: Change in the mechanical frequency (blue) and the mechanical linewidth (green) as a function of the circulating photon number (left) or the MC temperature (right). The temperature in the left plot was kept below 100 mK, and the circulating photon number in the right plot is below 300.

profile. This is especially apparent if we include behavior of the mechanical linewidth and frequency (as shown in Figure 8.7), which is qualitatively different between the MC heating (which raises device temperature uniformly) and optical heating. For example, increasing  $T_{MC}$  leads to increase in mechanical frequency, while increasing  $\bar{n}_c$  decreases the mechanical frequency (meanwhile, both processes cause growth in  $n_{th,m}$ , as can be seen from Figure 8.6).

To explain this behavior, we developed a model which assumes that the optical absorption and heating happens in a localized manner, and so creates hot-spots on the mirror surfaces. Immediately next to these hot-spots (10 ÷ 500 nm) the heat flux density is very large, so the thermal transport is in the highly nonlinear Gorter-Mellink regime[166, 167], where the thermal conductivity becomes very low. Because of that, the temperature at the hot-spots can be very high (1 ÷ 2 K, compared to  $\lesssim$  300 mK of the bulk helium), which results in complicated behavior of the mechanical linewidth, frequency and bath occupation. The full model is fairly complicated, so I do not present it here; for an extensive quantitative treatment see Ref. [141]. Nevertheless, we can use this model to calculate the effective thermal bath temperature  $T_{eff}$ , and then rescale the horizontal axis in Figure 8.6 to reflect this temperature. The results of this rescaling are shown in the right part of Figure 8.6. It demonstrates a much better agreement between the experiment and the expectations over large range of temperatures and circulating photon numbers.

## 8.5 Quantum signatures

Finally, let us consider signatures of the quantum optomechanics in the measured undriven motion. As was described in Chapter 7, the effects that we are looking for are the sideband asymmetry and the correlations between the mechanical motion and the vacuum noise background (which is a signature of RPSN). To observe them, we need to measure PSDs of both sidebands and their cross-correlator. An example of one such measurement is shown in Figure 8.8, which plots the normalized PSDs and the normalized sideband cross-correlator. The observations seem to be in a good qualitative agreement with the theory expectations (7.47), (7.48) and (7.55): the difference between the Stokes and the anti-Stokes sideband is close to one phonon (the expected value for the sideband asymmetry), the real part of the cross-correlator lies exactly between two sideband PSDs, and its imaginary part has a span of 1/2 of a phonon.

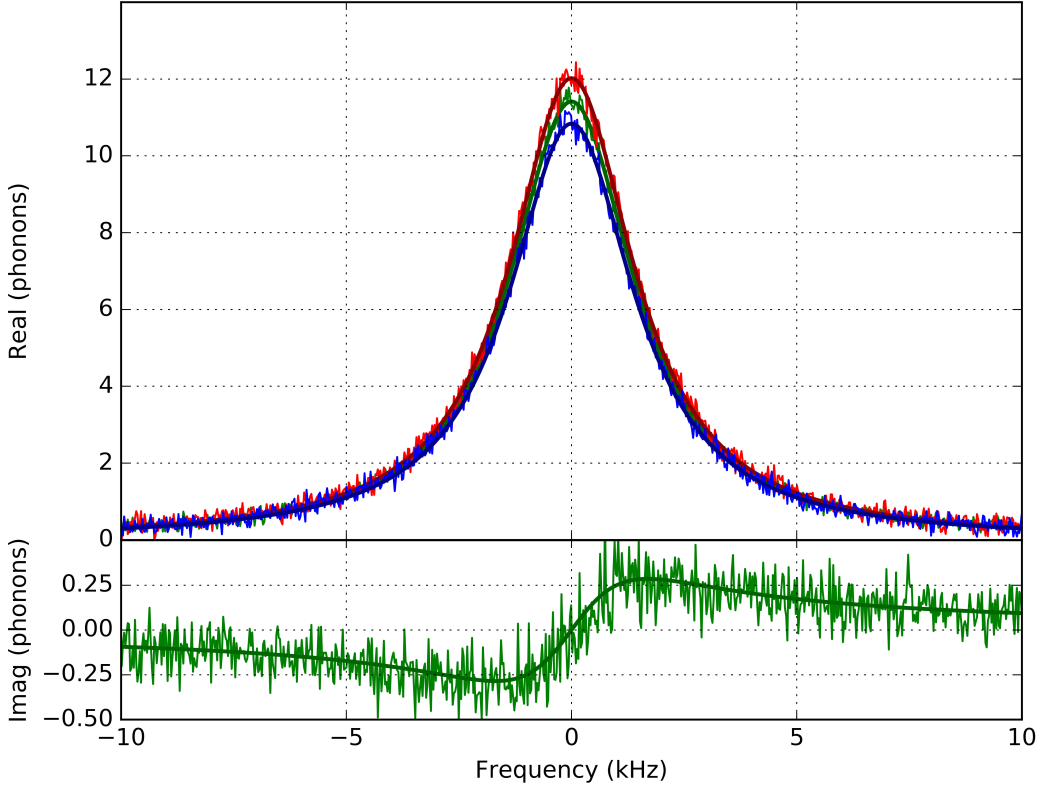


Figure 8.8: PSD of the Stokes sideband  $S_{ii}^{(\text{rr})}[\delta\omega]$  (red), PSD of the anti-Stokes sideband  $S_{ii}^{(\text{bb})}[\delta\omega]$  (blue), and sideband cross-correlator  $S_{ii}^{(\text{rb})}[\delta\omega]$  (green). All three quantities have been shifted horizontally to share the same origin, and the two PSDs have their background subtracted ( $S_{ii}^{(\text{rb})}[\omega]$  has no background). The vertical axis is normalized in phonons, as described in subsection 8.3.2. Imaginary parts of the PSDs ( $S_{ii}^{(\text{rr})}$  and  $S_{ii}^{(\text{bb})}$ ) are not plotted, since they are identically zero. The solid lines show fits to a Lorentzian lineshape (top plot) or an anti-Lorentzian lineshape (bottom plot). The average mechanical phonon occupation for this data is  $n_m \approx 11$ .

To examine the results quantitatively, we first fit the PSDs to a Lorentzian lineshape

$$S_{ii}^{(\text{xx})}[\delta\omega] = S_{\text{bg}}^{(\text{xx})} + n_m^{(\text{xx})} \frac{(\gamma_{\text{m,eff}}/2)^2}{(\gamma_{\text{m,eff}}/2)^2 + \delta\omega^2} \quad (8.13)$$

(where the superscript  $(xx)$  can stand for  $(\text{rr})$  for the Stokes sideband or  $(\text{bb})$  for the anti-Stokes sideband), and the cross-correlator to a combination of a real Lorentzian and an imaginary anti-Lorentzian part, as suggested by (7.55):

$$S_{ii}^{(\text{rb})}[\delta\omega] = \frac{e^{i\phi_{\text{rb}}} \left( n_m^{(\text{rb})} \gamma_{\text{m,eff}} - 2i f_m^{(\text{rb})} \delta\omega \right) \gamma_{\text{m,eff}}/4}{(\gamma_{\text{m,eff}}/2)^2 + \delta\omega^2}. \quad (8.14)$$

Here the factor of  $\gamma_{\text{m,eff}}/4$  in the numerator is added in order for  $n_m^{(\text{rb})}$  to correspond to the Lorentzian height, and the angle  $\phi_{\text{rb}}$  is a fit parameters added to accommodate for potential errors in calibration of the angle of the cross-correlator (described in appendix D.9). In practice, fixing  $\phi_{\text{rb}} = 0$  does not significantly affect the results, as it is usually fairly small:  $\phi_{\text{rb}} < 20$  mrad. Nevertheless, it provides a useful assessment for the quality of the phase calibration.

To extract the quantum effects, we calculate three independent signatures: the sideband asymmetry  $n_m^{(rr)} - n_m^{(bb)}$ , which is expected to be one phonon; the difference between the real part of the cross-correlator and the anti-Stokes sidebands magnitudes  $n_m^{(rb)} - n_m^{(bb)}$ , which should be 1/2 of a phonon; and the span of the imaginary part of the cross-correlator  $f_m^{(rb)}$ , which is also expected to be 1/2 of a phonon. We then repeatedly measure these three quantities while varying different system parameters such as MC temperature, control beam powers, and total incident power.

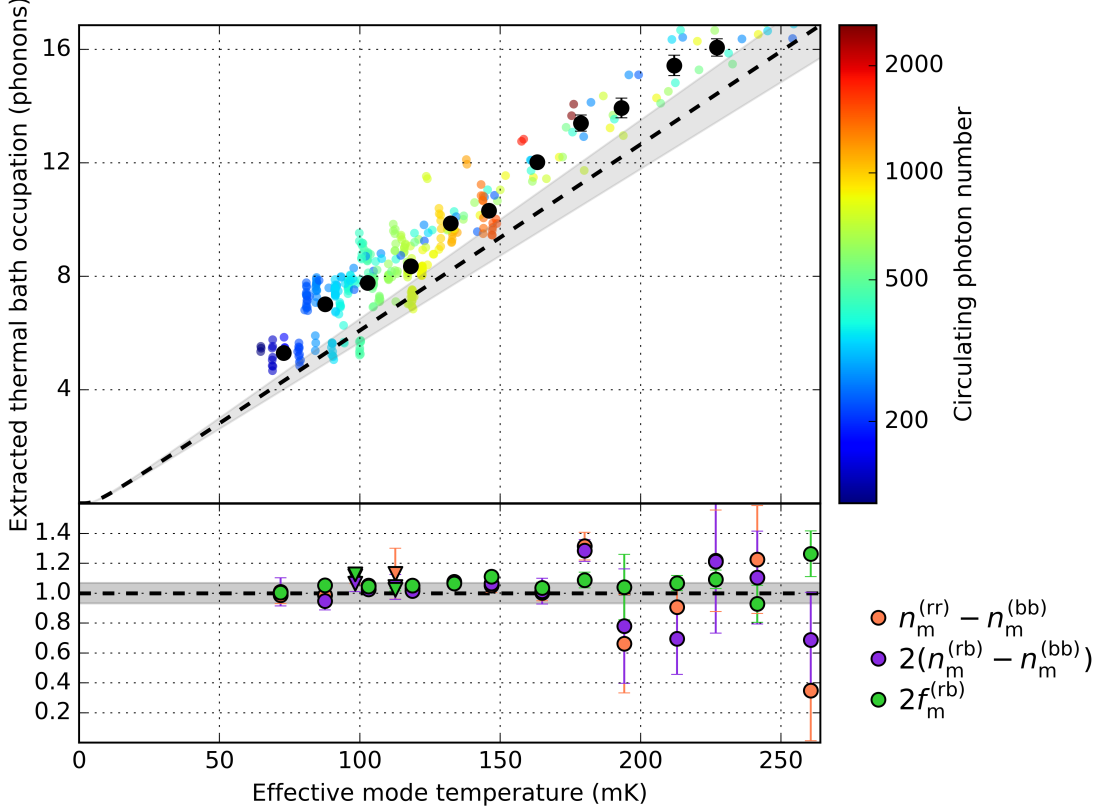


Figure 8.9: Top: occupation of the thermal mechanical bath as a function of the effective bath temperature extracted from the thermal model. This plot is the same as the right panel of Figure 8.6, and serves here as a reference.

Bottom: Three quantum signatures:  $n_m^{(rr)} - n_m^{(bb)}$ ,  $n_m^{(rb)} - n_m^{(bb)}$  and  $f_m^{(rb)}$ , plotted as a function of the effective bath temperature. The latter two quantities are multiplied by 2 to have their expected values equal 1 (dashed line). The grey area around the dashed line show the statistical uncertainty due to the imperfect motion measurement calibration. Circular markers denote the data taken with approximately balanced control beams (less than 15% power difference); triangle markers correspond to the data taken with purposefully imbalanced control beams (power ratio between 1.5 and 3.5). The data were averaged with a 20 mK window, and the error bars show the statistical error of the averages.

The results are shown in Figure 8.9, where the data is plotted against the effective mechanical bath temperature extracted from the thermal model described in section 8.4. The experiment shows good agreement with expectations in a large range of effective mode temperatures (from 70 to 250 mK), which confirms the validity of the calibration procedure and the quantum behavior of the optomechanical system. In addition, we have performed a series of measurements with deliberately unbalanced control beam powers (by a factor of 2), which still demonstrate the same values of all three signatures (shown with triangle markers in Figure 8.9).

The agreement between the experimental data and the theory also implicitly shows that our assumptions about the ratio between the radiation pressure optomechanical coupling  $g^{(0)}$  and the photothermal coupling  $g_{pt}^{(0)}$  were correct. To see that, consider equation (8.10) which is used to extract the ratios  $\Gamma_{meas,\ell}/\gamma_{m,eff}$  and

$\Gamma_{\text{meas,u}}/\gamma_{\text{m,eff}}$  from the OMIT/A amplitudes  $a_{\text{rel,+}}$  and  $a_{\text{rel,-}}$ . In order for this to work, we need to know the ratio of  $g_{\text{pt}}^{(0)}/g^{(0)}$ . Previously we extracted this ratio by assuming that the photothermal force is very filtered, so  $g_{\text{pt}}^{(0)}$  has to be purely imaginary; were it not the case, we would not have had enough experimental data to determine it independently of  $g^{(0)}$ .

Indeed, all of the “classical” optomechanical signatures that we have considered, such as the OMIT/A response amplitude (equation (6.16)) or the magnitude of the dynamical backaction (equation (7.19)) always depend on the product  $g^{(0)}(g^{(0)}+g_{\text{pt}}^{(0)})$ . This is a consequence of those experiments having a “loop” design, where an excitation starts and ends in the same element (either optical, or mechanical), and only temporarily passes through the other one. For example, in the OMIT/A experiment the probe beam excitation starts in the optical domain, then gets written on the mechanical motion through the optical force, and after that gets transferred back into the optical domain as a control beam sideband. Similarly, in the dynamical backaction description an excitation starts in the mechanical domain, then gets converted into a modulation of the intracavity field, and later acts back on the mechanical oscillator. Thus, the effect of both of these processes is going to be proportional to the product of the two conversion rates. Since the conversion rate from the mechanical to the optical domain is  $g^{(0)}$  (as in equation (7.56)), and the rate of the opposite process is  $g^{(0)}+g_{\text{pt}}^{(0)}$  (as can be seen in equation (7.63)), their product is  $g^{(0)}(g^{(0)}+g_{\text{pt}}^{(0)})$ , and this is the only combination accessible through the OMIT/A or the dynamical backaction measurements.

In a way, the measurements of the quantum signatures and, to a lesser extent, the measurements of the thermal motion provide a way around this problem by giving us a “mechanical drive” with a well-defined amplitude (either mechanical zero point fluctuations, or environment thermal noise). Thus, the measured effect does not rely on the light acting on the mechanical motion, so it only depends on the radiation pressure coupling  $g^{(0)}$ , as can be seen in, e.g., equation (7.47). This lets us measure the radiation pressure coupling  $g^{(0)}$  in an independent experiment, confirming that there is no “stray” real-valued photothermal coupling in our system, which would obscure quantum effects.

Hence, in the end, the agreement shown in Figure 8.9 confirms our initial assumption about predominantly unitary optomechanical interaction, meaning that it can in principle be used to initialize, manipulate and read out the quantum state of the mechanical system with minimal information loss. Therefore, the acoustic modes in superfluid helium could potentially serve as a quantum memory or a quantum bus in hybrid optomechanical systems.

# Chapter 9

## Conclusion and future directions

### 9.1 Device performance

As we showed in the previous Chapter, the second generation device has significantly better performance than the first generation device (see, e.g., Figure 8.2 and Table 8.1). This allowed us to perform qualitatively different measurements, such as dynamical backaction (section 8.2) and quantum sideband asymmetry (section 8.5). Now I want to discuss the improvements more quantitatively by calculating the cooperativity and the thermal cooperativity for the new device.

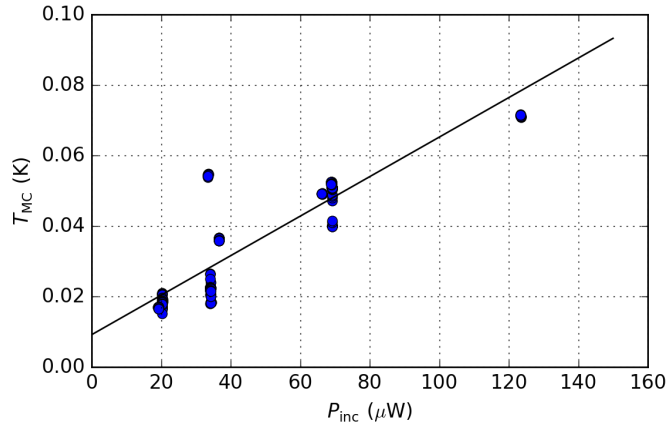


Figure 9.1: Experimental dependence of the MC temperature on the total optical power incident on the cavity (blue dots) and its linear fit (black line).

Similar to the first generation device, the performance is ultimately limited by the optical heating, which degrades the mechanical mode parameters. To calculate the dependence of the mechanical linewidth (used for both cooperativities) and the effective mechanical bath temperature (needed for the thermal cooperativity) on the circulating photon number, we used our thermal model outlined in section 8.4 and described in detail in Ref. [141]. Unlike the first generation device (see section 6.3 and equation (6.50)), this model does not explicitly include the incident laser power, in the sense that given the same  $\bar{n}_c$  and  $T_{\text{MC}}$  the incident power does not affect the results. However, as the dilution refrigerator has a limited cooling capability, the MC temperature does depend on the incident power (and seems to be roughly independent of the circulating photon number, given the same incident power). This dependence, along with a linear fit, is shown in Figure 9.1. We use the parameters of this linear fit to estimate the MC temperature for a given incident power, and then use this MC temperature in the heating model.

The results of these calculations are demonstrated in Figure 9.2, where we plot the cooperativity and the thermal cooperativity as a function of the circulating photon number. Each plot has three lines. The dotted

line shows the results obtained when the MC heating is neglected, and its temperature is set to zero. Thus, this data represents a perfect case of an infinite cooling power of the refrigerator. Next, the dashed line takes this heating into account, and to calculate the incident power for a given intracavity photon number it assumes that only control beams are incident on the cavity. Finally, the solid line represents the assumption of 10% of the total incident power being in the control beams (i.e., the incident power for a given  $\bar{n}_c$  is 10 times larger than for the dashed line, while all other parameters are kept the same).

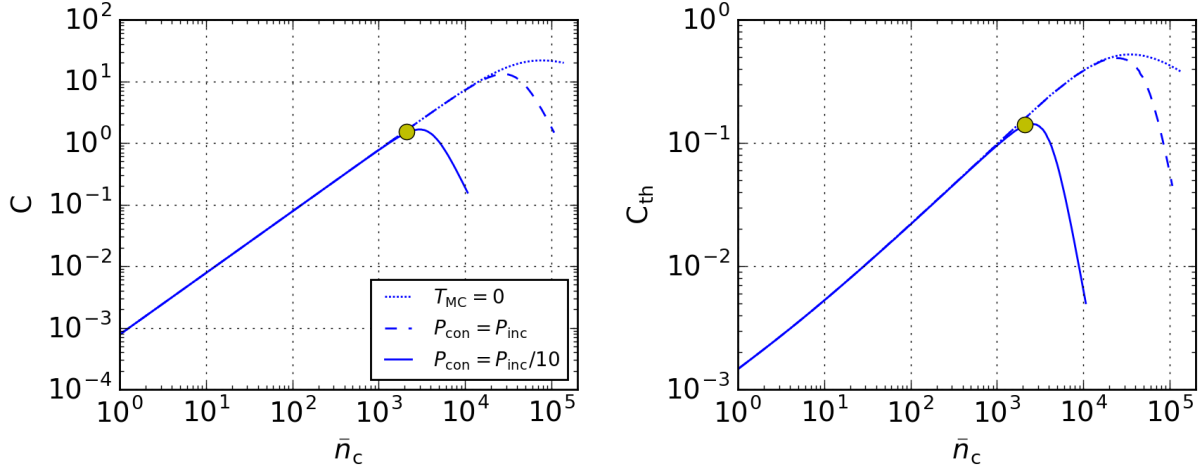


Figure 9.2: Cooperativity (left) and thermal cooperativity (right) of the second generation device as a function of the circulating photon number. Dotted lines show the results for a fixed zero MC temperature, dashed lines assume that all of the incident laser power is contained in the control beam, while solid lines assume that 10% of the total incident power is in the control beam. The yellow markers in both plots show the experimental results in our system for the highest observed cooperativity. All of the plots assume  $T_{MC} = 0$ .

The yellow markers show the maximum measured cooperativity of about 1.5, which corresponds to a thermal cooperativity of about 0.14. Both of these values seem to be close to their maximum expected values according to the model described by the solid blue lines. While these values are still smaller than the best observed in the field ( $\mathcal{C} > 10^4$ [82, 156, 157] and  $\mathcal{C}_{th} \approx 250$ [157]), they nevertheless represent an improvement by a factor of 30 compared to the first generation device, and they are large enough to allow us to observe quantum optomechanical effects.

### 9.1.1 Comparison to other superfluid helium optomechanics experiments

Now let us compare these results to other superfluid optomechanics experiments, which are described in section 4.3.2. Since the Helmholtz resonator experiments[131, 132] are not yet in the cavity optomechanics settings, we will not consider them here, and we will focus on the other two experiments: density waves in a MW resonator[126] and third sound waves on a microtoroid[127]. One should keep in mind that those experiments were not necessarily designed with a goal of maximizing the optomechanical cooperativity, so the comparison could be unfair.

The MW resonator experiment[126] demonstrated very high mechanical quality factor  $Q_m > 10^8$ [112], more than 3 orders of magnitude larger than the highest  $Q_{m,rad} \approx 10^5$  in our device. The “optical” linewidth  $\kappa = 2\pi \times 230$  Hz was also smaller than in our device ( $\kappa = 2\pi \cdot 22.1$  MHz), mostly due to the smaller overall frequency scale: the MW quality factor in that work is about 5 times larger than the optical quality factor in our device. On the other hand, because of this smaller frequency scale and larger mechanical mode volume, the optomechanical coupling was much weaker  $g^{(0)} \approx 2\pi \cdot 6.7 \cdot 10^{-9}$  Hz. This results in a fairly small cooperativity: for the maximal reported cavity photon number  $\bar{n}_c \approx 3 \cdot 10^8$  the cooperativity is about  $4 \cdot 10^{-6}$ . Another potential issue for the quantum optomechanics applications is the classical MW noise. Even for the cooperativity reported

above the MW drive power was about 4 nW, which corresponds to a shot noise PSD of  $-145$  dBc/Hz. Reducing classical phase noise below this level at only  $\omega_m \approx 2\pi \cdot 8$  kHz detuning away from the MW pump tone might be a challenging engineering problem, and it becomes proportionally harder if higher cooperativity is desired.

The third sound optomechanics devices[127] utilized an optical mode with wavelength  $\lambda_{\text{opt}} = 1.555$   $\mu\text{m}$  and linewidth  $\kappa = 2\pi \times 22$  MHz, which is very close to our parameters. The mechanical mode had a significantly lower frequency:  $\sim 500$  kHz, meaning that the device was in the fairly unresolved sideband regime. In that work the authors were able to optomechanically damp the mechanical mode by about a factor of 4, which corresponds to a cooperativity of  $\sim 5$ . However, the optomechanical coupling was dominated by photothermal forces; if only the radiation pressure force is taken into account, the cooperativity goes down to  $\sim 0.1$ [168], with a corresponding thermal cooperativity  $\sim 10^{-5}$  for the 300 mK base temperature of a  $^3\text{He}$  cryostat. Additionally, as shown in section 7.3, the photothermal coupling can add a lot of additional force noise acting on the mechanical resonator, which makes it less suitable for quantum optomechanics applications.

## 9.2 Future directions

Now I want to describe possible ways to improve and expand our measurements of the superfluid helium optomechanics.

### 9.2.1 Acoustic wave optomechanics

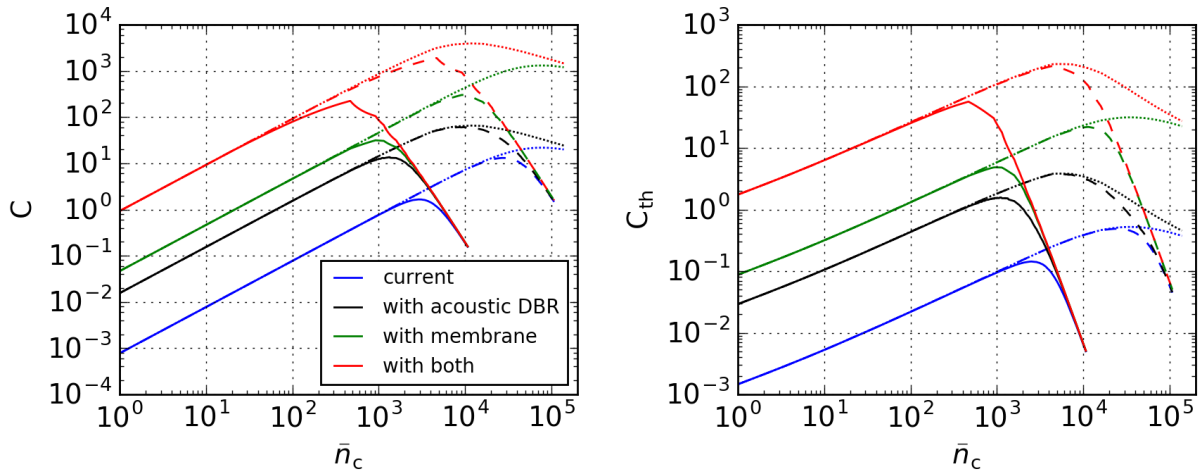


Figure 9.3: Cooperativity (left) and thermal cooperativity (right) of the second generation device, including potential improvements. The lines style (dotted, dashed or solid) is the same as described in the caption of Figure 9.2. The line color encodes possible improvements: blue lines correspond to the current version of the device, black lines assume additional acoustic DBR mirrors, green lines assume presence of additional membrane barriers inside the cavity, and red lines assume both improvements (acoustic DBRs and membranes) together.

We have discussed in section 8.4 that the second generation device performance is mainly limited by optical heating. However, since the heating is mostly restricted to very tightly localized spots right at the mirrors' surface, it is hard to significantly reduce its effect on the mechanical mode. Nevertheless, there are still some improvements which could increase the cooperativity or the thermal cooperativity at least in some range of optical powers:

- a) One effect which is straightforward to address is the dilution refrigerator cooling efficiency. As can be seen in Figure 9.2, it strongly affects the performance of our device, reducing the maximum achievable cooperativity by a factor of 2 to 10 (depending on the fraction of the control beam in the total incident

power). Since we have not yet tried to optimize the refrigerator operation in the presented experiments, there are still some potential gains in trying that.

- b) Another limiting factor is the low-temperature acoustic quality factor, which is currently determined only by the impedance mismatch between helium and glass (see subsection 4.5.2). It is possible to improve this by implementing an acoustic DBR structure similar to the optical DBR which we use in the fiber mirrors forming the cavity. As mentioned in subsection 4.5.2, this path is associated with complications due to a large (factor of 20) sound wavelength mismatch between the sound in helium and in glass, which means that the sound inside glass does not obey the paraxial approximations. Nevertheless, as discussed in detail in Ref. [141], it is possible to find some cavity parameters which would improve the acoustic reflectivity of the fiber mirrors by about a factor of 20 with realistic DBR parameters (2 acoustic layer pairs). The projected device performance with this improvement is shown with black lines in Figure 9.3.
- c) Related to the previous point, one can try to improve the system by transitioning from microscopic fiber cavities to macroscopic (1 ÷ 10 cm long) ones. Since most of the acoustic losses (the radiation into glass mirrors and the thermal heating effects) occur immediately next to the mirror surfaces, their relative contribution should become smaller, and the acoustic quality factor should go up proportionally to the cavity length. Similarly, assuming that the optical finesse stays the same, the optical quality factor will go up in the same manner. On the other hand, the optomechanical coupling  $g^{(0)}$  will be reduced, as  $g^{(0)} \propto V_{\text{mode}}^{-1/2}$  (see section 4.7.2), and the mode volume  $V_{\text{mode}}$  increases for larger cavities. We can estimate it as  $V_{\text{mode}} \propto Lw_0^2$  where  $w_0 = \sqrt{z_R \lambda / \pi} \propto \sqrt{z_R} \propto \sqrt{L}$  is the mode waist (see section B.2), which implies that  $V_{\text{mode}} \propto L^2$  and, consequently,  $g^{(0)} \propto L^{-1}$ . Combining all of these dependencies, we arrive at the conclusion that the cooperativity should stay constant given the same circulating photon number. At the same time, since both thermal and radiation acoustic losses scale as  $L^{-1}$ , the maximum reasonable number of photons (i.e., the number at which thermal loss is approximately equal to the radiative loss) stay the same, so the maximum achievable cooperativity is not affected.

On the other hand, some applications might gain from an increased acoustic quality factor. For example, switching to a 5 cm-long cavity should decrease the mechanical linewidth by a factor of  $10^3$ , down to only several Hz, which means that it would be possible to measure the acoustic mode frequency with a precision of  $\sim 10^{-9}$ . This opens a possibility for precise measurements of the helium properties and their dependence on, e.g., temperature or pressure.

- d) Finally, it still could be possible to better isolate the standing acoustic wave from the mirrors without sacrificing the optomechanical coupling. To do that, we can incorporate inside the cavity additional barriers with low optical absorption and high acoustic reflectivity. One candidate for such barrier are  $\text{Si}_3\text{N}_4$  membranes[34], which are known to have low optical absorption and scattering ( $\text{Im}\{n_r\} < 1.5 \cdot 10^{-6}$ [36]) and high mechanical quality factors ( $> 10^7$  for commercially available membranes[169]). The absorption issues can be further alleviated by placing the membranes close to the nodes of the optical mode, where the light intensity is small, so its absorption and scattering is minimized.

The acoustic reflection off such membranes is discussed in subsection B.5.5. To use the expressions derived there, we need to make some assumptions about the membrane mechanical response function  $\tilde{K}$ . In general, this can be expressed as

$$\tilde{K}^{-1} = \frac{1}{\sigma} \sum_n c_n \frac{1}{\omega_n^2 - \omega^2}, \quad (9.1)$$

where  $\sigma$  is the membrane surface density, and the sum goes over all membrane modes with frequencies  $\omega_n$ . Prefactors  $c_n$  denote the participation ratios (for a pressure distribution given by the transverse acoustic mode profile) for the corresponding modes; they are assumed to be normalized as  $\sum_n c_n^2 = 1$ . This expression is fairly complicated and is dependent on the details of the membrane geometry. Hence, for simplicity we will assume a low-frequency patterned trampoline membrane[43], for which the fundamental frequency is  $\omega_0 \sim 40$  kHz, almost 4 order of magnitude smaller than the acoustic frequency  $\omega$ . This

means that we can approximate the membrane as a freely-suspended mass by assuming  $\omega_0 \approx 0$  and  $c_n \approx \delta_{n,0}$  (for realistic pad/tether ratio of such membrane it is possible to achieve  $c_0 \gtrsim 0.9$ ), so that  $\tilde{K} \approx -\sigma\omega^2/(\sum_n c_n) \approx -\sigma\omega^2$  (see also subsection B.5.5). This results in the acoustic transmission coefficient (equation (B.121))

$$T^{(\text{mb})} = \frac{1}{1 + \left(\tilde{K}/(2\omega\mathcal{Z})\right)^2} = \frac{1}{1 + (\sigma\omega/(2\mathcal{Z}))^2}. \quad (9.2)$$

Assuming the membrane thickness of 100 nm and  $\text{Si}_3\text{N}_4$  density of  $2.7 \cdot 10^3 \text{ kg/m}^3$ , we get  $\sigma\omega/(2\mathcal{Z}) \approx 7.9$  and the transmission of only  $T^{(\text{mb})} \approx 1.6\%$ . Provided that the membranes are positioned correctly inside the cavity, such barriers can increase the mechanical quality factor by about  $1/T^{(\text{mb})} \approx 60$  (even more for larger membrane thicknesses) without noticeably decreasing the optomechanical coupling. What is more important, unlike the acoustic DBR structures, the membranes also isolate the mechanical mode from the mirror surfaces, which proportionally reduces the optical heating effects leading to an improved optical power handling. The effect of adding the membrane barriers are also shown in Figure 9.3. The green lines show the improvements for the barriers alone, and the red lines show the potential cooperativities if both upgrades (acoustic DBRs and membrane barriers) are implemented.

To sum up, as can be seen in Figure 9.3, by implementing all of these improvements we should be able to increase the cooperativities by more than 3 orders of magnitude and approach  $\mathcal{C} > 10^3$  and  $\mathcal{C}_{\text{th}} > 10^2$ , well in the high thermal cooperativity regime.

Another possible way to proceed with the current device is to perform different kinds of quantum experiments allowed by the current parameters. One such experiment involves using short laser pulses and single-photon detectors for heralded generation of non-classical mechanical states[64]. Provided that the heating effects arise slowly compared to the pulse time, this scheme can yield large instantaneous measurement rates, while maintaining high mechanical quality factor and low effective mechanical temperature.

## 9.2.2 Other superfluid helium excitations

Finally, we could pursue superfluid helium optomechanics with excitations which are not acoustic waves. We have already described one such experiment[127], which studied the third sound in superfluid helium. There are two other possibilities which we are currently exploring:

- a) We can use a half-filled optical cavity to study surface waves on superfluid helium[141]. Compared to the sound waves, these excitations have a much lower frequency (about 500 Hz for the fundamental mode), but a comparable optomechanical coupling ( $g^{(0)} \sim 500 \text{ Hz}$ ). In addition, unlike the acoustic Gaussian modes, there will be multiple surface modes with approximately equal couplings to the optical mode. This results in a qualitatively different optomechanics regime:  $g^{(0)} \sim \omega_m \ll \kappa$  (unlike  $g^{(0)} \ll \kappa \ll \omega_m$  for the current device), and a large number of tightly-spaced mechanical modes, which can lead to rich multi-mode physics (e.g., creation of multipartite optomechanical mixing[170] or entanglement[171, 172], or achieving a boost in the optomechanical coupling[173]). Some possible issues with this device are still unclear mechanical loss mechanism, and possibly increased sensitivity to external acoustic noise.
- b) The other approach is to build a device consisting only of superfluid helium[174]. The device itself is a magnetically levitated droplet of superfluid helium with  $\sim 1 \text{ mm}$  diameter, where the optical mode is a WGM mode of this spherical resonator, and the mechanical mode is one of the droplet vibrational modes. Since helium itself has very low optical absorption and low mechanical loss, and there are no other materials present, this system has a potential of having very high optical and mechanical quality factors, possibly even achieving strong single-photon coupling regime  $g^{(0)} \gtrsim \kappa$ .

Another interesting feature of this system is the presence of mechanical degrees of freedom which are not harmonic oscillators. Specifically, the optical mode frequency depends on the droplet circumference, so it is sensitive to the rotational motion (which changes this circumference due to centrifugal forces). This is a

qualitatively different and so far unexplored regime in optomechanics, and it may yield many interesting experimental and theoretical results.

### 9.3 Summary and conclusions

In this work we have demonstrated an optomechanical device where the mechanical mode is a standing acoustic wave in superfluid helium. The first generation of this device demonstrated moderate cooperativity, but it still allowed us to drive the mechanical oscillator and measure its displacement using only light. We used these measurements to systematically explore how the the mechanical properties depend on the MC temperature and the laser power, and clearly identified the poor thermal contact between the cavity and the large helium bath as a limiting factor for the device performance. We have also demonstrated that the optomechanical coupling is predominantly electrostrictive in origin, although we have detected the presence of photothermal coupling as well.

The second generation device, whose design addressed the thermalization issues, showed an improvement by a factor of 30 in the optomechanical cooperativity. This let us perform experiments in which we modified the mechanical mode parameters (linewidth and frequency) using light via the dynamical backaction. It also allowed us to measure the undriven motion of the mechanical oscillator, which was used (in combination with the mechanical linewidth and frequency data) to develop a model describing optical heating in this new device. The undriven motion measurements also exhibited quantum optomechanics effects: the difference in the magnitudes of the two motional sidebands (sideband asymmetry) demonstrated the fundamental difference in rates between the Stokes and anti-Stokes scattering processes, while the cross-correlator between the two mechanical sidebands revealed the correlations between the mechanical motion and the optical vacuum noise, which are created by the RPSN. This constitutes the first observation of quantum optomechanics effects in a fluid.

Looking into the future, there are several avenues for improvement. So far, it seems like all of the shortcomings of our system (acoustic loss, optical loss, heating problems) stem from the properties of the container (i.e., the Fabry-Perot cavity), not from the properties of helium itself. As outlined in subsection 9.2.1, we can improve the performance by either making the container better, or getting rid of it entirely and building a purely superfluid device. Both approaches have their advantages. Improving the container is more incremental and easier to implement, and it could provide better control over system parameters, since many of them (such as optical and mechanical linewidth, and optomechanical coupling) are defined by controllable system geometry (cavity length, mirrors ROC and reflectivity, etc.). On the other hand, a 100% superfluid device can ultimately provide better performance, since helium itself is pretty ideal.

In terms of making more “interesting” kinds of systems (i.e., systems containing more than the standard optomechanics Hamiltonian with a single optical and mechanical modes), there are also several approaches. One of them is to rely on helium. Unfortunately, the flip side of helium being close to “ideal” is that its density waves are somewhat “boring”, especially at very low ( $< 100$  mK) temperatures: helium is a fluid (which means that it has no shear modulus, and that its modes have to be defined by the external geometry); it has zero viscosity; one cannot vary its chemical composition (the only variable is the isotopic  $^3\text{He}/^4\text{He}$  ratio, which generally should be kept as low as possible to achieve the highest mechanical quality factor[112, 175]); and it is fairly linear, at least at the typical acoustic mode ZPF levels (the typical relative density variations due to ZPF in our device are  $\sim 10^{-9}$ ). However, superfluid helium does have unusual macroscopic quantum properties, which can be exploited to create more interesting situations. First, due to its zero viscosity it can maintain a rotational flow indefinitely, which leads to new kinds of behavior, such as creation of quantized vortices[95]. Second, excited helium atoms can form long-lived ( $\sim 10$  s) excimers[105] with more accessible (compared to He atoms) optical transitions. Third, superfluid helium does have a quantum order parameter, which is somewhat similar to the order parameter in superconductors. This means that it is in principle possible to create a superfluid analogue of the superconducting Josephson junction[176, 177, 178], thus introducing a very strong non-linearity to the helium flow, potentially even on a single ZPF level. Such non-linearities could allow for the creation of a quantum anharmonic oscillator, resulting in a mechanical two-level system and paving a way to the quantum non-linear optomechanics. Finally, the levitated superfluid droplet system can provide access to

rotational degrees of freedom, which so far have not been investigated in optomechanical systems.

Another way to expand the system is to embed other elements in helium, thus creating hybrid optomechanical systems. I have already mentioned intrinsic helium excitation such as excimers and vortices. In addition, as described in section 4.1, helium can serve as a host to many other different systems, such as electrons (both in bulk and on the surface), atoms, molecules, or nanoparticles. Most of these systems should have some degree of coupling to the helium pressure (i.e., acoustic waves), or to the position on the surface (i.e., surface waves). This could create a “hosted system”  $\leftrightarrow$  “helium waves”  $\leftrightarrow$  “light” interaction, where acoustic/surface waves serve as a mediator if the hosted system does not interface with light directly. As we have demonstrated with our work, the helium $\leftrightarrow$ light interaction is dominated by the radiation pressure, which means that this part of the interface should not introduce extra noise or information loss.

One fairly successful example of such a hybrid system in the solid-state optomechanics is the MW  $\leftrightarrow$  optical transducer[85], where a mechanical membrane mediates interaction between these two electromagnetic domains. As strange as it might seem, currently this is the most promising candidate for this quantum kind of information transfer. One could imagine a similar system implemented using helium surface waves and electrons on its surface[101], where the electrons couple to a MW resonator, while helium waves interact with an optical cavity.

In the end, I do believe that superfluid helium still has a lot to offer to the field of optomechanics, whether it is in creating canonical devices with outstanding performance, serving as a mediator in hybrid systems, or forming qualitatively new kinds of optomechanical interactions. It is safe to assume that the potential of superfluid helium optomechanics is far from being exhausted.

# Appendices

# Appendix A

## Mathematical definitions

This Appendix chapter introduces several mathematical definitions and relations used throughout the thesis.

### A.1 Correlator and power spectral density

#### A.1.1 Correlator

We define the time-dependent correlator of two operators as

$$C_{\hat{a},\hat{b}}(t, \tau) \equiv \langle \hat{a}(t - \tau/2)\hat{b}(t + \tau/2) \rangle, \quad (\text{A.1})$$

where  $\langle \dots \rangle$  represents an ensemble average. The same definition applies if  $a$  and  $b$  are classical variables instead of operators (in which case their order inside the correlator does not matter).

In many cases the correlator does not depend on the common time  $t$ ; for stochastic variables or operators, this would correspond to a stationary random process. In this case we will omit the first argument:

$$C_{\hat{a},\hat{b}}(\tau) \equiv C_{\hat{a},\hat{b}}(0, \tau) \equiv \langle \hat{a}(-\tau/2)\hat{b}(\tau/2) \rangle = \langle \hat{a}(0)\hat{b}(\tau) \rangle. \quad (\text{A.2})$$

The last equality directly follows from the  $t$ -independence of the correlator, so that  $C_{\hat{a},\hat{b}}(0, \tau) = C_{\hat{a},\hat{b}}(\tau/2, \tau)$ .

#### A.1.2 Power spectral density

We broadly define a double-sided time-dependent power spectral density (PSD) as a Fourier transform of the corresponding correlator

$$S_{\hat{a},\hat{b}}(t, \omega) \equiv \int_{-\infty}^{+\infty} C_{\hat{a},\hat{b}}(t, \tau) e^{+i\omega\tau} d\tau. \quad (\text{A.3})$$

The usual narrow definition corresponds to the case of a stationary process and a single variable:

$$S_{\hat{x},\hat{x}}[\omega] \equiv \int_{-\infty}^{+\infty} C_{\hat{x},\hat{x}}(\tau) e^{+i\omega\tau} d\tau. \quad (\text{A.4})$$

This definition specifies the PSD in unit<sup>2</sup>/Hz not in unit<sup>2</sup>/(s<sup>-1</sup>) in the sense that the RMS magnitude of  $\hat{x}$  is obtained by integration over an ordinary frequency  $f = \omega/(2\pi)$  and not an angular frequency  $\omega$ :

$$\langle \hat{x}^2 \rangle \equiv C_{\hat{x},\hat{x}}(0) = \int_{-\infty}^{+\infty} S_{\hat{x},\hat{x}}[2\pi f] df = \int_{-\infty}^{+\infty} S_{\hat{x},\hat{x}}[\omega] \frac{d\omega}{2\pi}. \quad (\text{A.5})$$

### A.1.3 Properties

There are two important properties of correlators and power spectral densities which are applicable in many cases:

- (1) If  $\hat{b} = \hat{a}^\dagger$  (which for a single-operator PSD would correspond to a Hermitian operator  $\hat{x}$ ), then the correlator obeys the relation

$$\begin{aligned} (C_{\hat{a},\hat{a}^\dagger}(t, \tau))^* &= \langle \hat{a}(t - \tau/2)\hat{a}^\dagger(t + \tau/2) \rangle^* = \langle (\hat{a}^\dagger)^\dagger(t + \tau/2)\hat{a}^\dagger(t - \tau/2) \rangle \\ &= \langle \hat{a}(t + \tau/2)\hat{a}^\dagger(t - \tau/2) \rangle = C_{\hat{a},\hat{a}^\dagger}(t, -\tau), \end{aligned} \quad (\text{A.6})$$

so the corresponding PSD is real:

$$\begin{aligned} (S_{\hat{a},\hat{a}^\dagger}(t, \omega))^* &= \int_{-\infty}^{+\infty} C_{\hat{a},\hat{a}^\dagger}^*(t, \tau) e^{+i\omega\tau} d\tau \\ &= \int_{-\infty}^{+\infty} C_{\hat{a},\hat{a}^\dagger}(t, -\tau) e^{-i\omega\tau} d\tau = S_{\hat{a},\hat{a}^\dagger}(t, \omega). \end{aligned} \quad (\text{A.7})$$

- (2) If the operator  $\hat{x}$  commutes at different times (for example, if it is simply a classical variable), the autocorrelator is symmetric in time  $C_{\hat{x},\hat{x}}(t, -\tau) = C_{\hat{x},\hat{x}}(t, \tau)$ , and the PSD becomes symmetric as well

$$\begin{aligned} S_{\hat{x},\hat{x}}(t, -\omega) &= \int_{-\infty}^{+\infty} C_{\hat{x},\hat{x}}(t, \tau) e^{-i\omega\tau} d\tau \\ &= \int_{-\infty}^{+\infty} C_{\hat{x},\hat{x}}(t, -\tau) e^{-i\omega\tau} d\tau = S_{\hat{x},\hat{x}}(t, \omega). \end{aligned} \quad (\text{A.8})$$

Thus, an asymmetric power spectrum inherently corresponds to a non-classical variable.

## A.2 Fourier transform

In this work I am using two different variations of Fourier transform defined for two different scenarios. Both of these use “physicist’s notation” where a positive frequency exponent is expressed as  $e^{-i\omega t}$ .

### A.2.1 “Coherent” Fourier transform

For dealing with coherent signals, it is convenient to use the following Fourier transform definition:

$$\mathcal{F}_c \{f(t)\} [\omega] \equiv f^{(c)}[\omega] \equiv \frac{1}{2\pi} \int_{-\infty}^{+\infty} f(t) e^{+i\omega t} dt. \quad (\text{A.9})$$

From the orthogonality relations

$$\int_{-\infty}^{+\infty} e^{+i\omega t} e^{-i\omega' t} dt = 2\pi \delta(\omega - \omega') \quad (\text{A.10})$$

$$\int_{-\infty}^{+\infty} e^{+i\omega t} e^{-i\omega' t} d\omega = 2\pi \delta(t - t') \quad (\text{A.11})$$

the corresponding inverse Fourier transform is simply

$$\mathcal{F}_c^{-1} \{f^{(c)}[\omega]\} (t) \equiv \int_{-\infty}^{+\infty} f^{(c)}[\omega] e^{-i\omega t} d\omega = f(t). \quad (\text{A.12})$$

For a coherent signal  $f(t) = Ae^{-i\omega_0 t}$  this kind Fourier transform yields  $f^{(c)}[\omega] = A\delta(\omega - \omega')$

## A.2.2 “Noise” Fourier transform

For stochastic variables it is more appropriate to use a “windowed” Fourier transform (for the motivation of this definition, see, e.g., Ref. [10]):

$$\mathcal{F}_n \{f(t)\} [\omega] \equiv f^{(n)}[\omega] \equiv \lim_{T \rightarrow \infty} \frac{1}{\sqrt{T}} \int_{-T/2}^{+T/2} f(t) e^{+i\omega t} dt. \quad (\text{A.13})$$

This normalization allows one to easily calculate time-independent power spectral densities using the Wiener-Khinchin theorem:

$$S_{\hat{a}, \hat{b}}[\omega] = \langle \hat{a}^{(n)}[\omega] \hat{b}^{(n)}[-\omega] \rangle. \quad (\text{A.14})$$

This theorem holds if the two processes have a finite correlation time, i.e., if  $C_{\hat{a}, \hat{b}}(\tau)$  goes to zero for large  $\tau$ .

## A.2.3 Properties and conventions

Below are some common useful properties of Fourier transforms which apply to both definitions above:

$$\mathcal{F} \left\{ \frac{d}{dt} f(t) \right\} [\omega] = -i\omega \mathcal{F} \{f(t)\} [\omega] \quad (\text{A.15})$$

$$\mathcal{F} \{f(t) e^{-i\omega_0 t}\} [\omega] = \mathcal{F} \{f(t)\} [\omega - \omega_0] \quad (\text{A.16})$$

$$\mathcal{F} \{f(t - \tau_0)\} [\omega] = \mathcal{F} \{f(t)\} [\omega] e^{+i\omega \tau_0} \quad (\text{A.17})$$

$$\mathcal{F} \{f^*(t)\} [\omega] = (\mathcal{F} \{f(t)\} [-\omega])^*. \quad (\text{A.18})$$

The last property means that the notation like  $f^*[\omega]$  is ambiguous, as it can mean either  $\mathcal{F} \{f^*\} [\omega]$  or  $(\mathcal{F} \{f\} [\omega])^* = \mathcal{F} \{f^*\} [-\omega]$ . In this work we adopt the first meaning, and the second one will be always denoted explicitly by parentheses:

$$f^*[\omega] \equiv \mathcal{F} \{f^*\} [\omega] \quad (\text{A.19})$$

$$(f[\omega])^* \equiv (\mathcal{F} \{f\} [\omega])^*. \quad (\text{A.20})$$

Furthermore, we will omit the superscript <sup>(c)</sup> or <sup>(n)</sup> denoting which kind of Fourier transform is used if it is obvious from the context, or if it is not important for the discussion.

# Appendix B

## Mode-related derivations

### B.1 Cavity frequency perturbation

In this section we derive the expression for the change in the cavity resonant frequency due to a perturbation of the medium inside it.

We start with the Maxwell equations and the assumption of no net charges  $\rho_q = 0$  or currents  $\mathbf{j}_q = 0$ :

$$\nabla \cdot \mathbf{B} = 0 \quad (\text{B.1})$$

$$\nabla \cdot \mathbf{D} = 0 \quad (\text{B.2})$$

$$\nabla \times \mathbf{H} = \frac{\partial \mathbf{D}}{\partial t} \quad (\text{B.3})$$

$$\nabla \times \mathbf{E} = -\frac{\partial \mathbf{B}}{\partial t}. \quad (\text{B.4})$$

Here  $\mathbf{E}$  is the electric field,  $\mathbf{B}$  is the magnetic field,  $\mathbf{D}$  is the electric displacement field and  $\mathbf{H}$  is the magnetic  $H$ -field. In addition to the equations above, we assume the standard linear isotropic media relations:

$$\mathbf{D} = \epsilon \mathbf{E} \quad (\text{B.5})$$

$$\mathbf{B} = \mu \mathbf{H}, \quad (\text{B.6})$$

where  $\epsilon$  is the electric permittivity and  $\mu$  is the magnetic permeability. Because we are focusing on dielectric effects, we will assume that the material has no special magnetic properties:  $\mu = \mu_0$ , where  $\mu_0$  is the vacuum permeability. Also, for notational simplicity we denote  $\epsilon = \epsilon_0 \epsilon^{(r)}$ , where  $\epsilon_0$  is the vacuum permittivity and  $\epsilon^{(r)}$  is the relative permittivity of the material, which may be position dependent.

From the equations above we can obtain the wave equation for the  $\mathbf{D}$ -field:

$$\frac{\partial^2 \mathbf{D}}{\partial t^2} = \frac{1}{\mu_0} \nabla \times \frac{\partial \mathbf{B}}{\partial t} = -\frac{1}{\mu_0} \nabla \times (\nabla \times \mathbf{E}) = -\frac{1}{\mu_0} \nabla (\nabla \cdot \mathbf{E}) + \frac{1}{\mu_0} \nabla^2 \mathbf{E}. \quad (\text{B.7})$$

Note that  $\epsilon$  can in principle vary in space, so that  $\nabla \cdot \mathbf{E}$  does not have to be zero.

Next, we assume that the electric field corresponds to some mode at frequency  $\omega$ , so that  $\mathbf{E}(t) = \mathbf{E} e^{-i\omega t}$ , and that the permittivity is constant in time. Then using the relation between  $\mathbf{E}$  and  $\mathbf{D}$  we get

$$\nabla (\nabla \cdot \mathbf{E}) - \nabla^2 \mathbf{E} = -\mu_0 \epsilon_0 \frac{\partial^2 (\epsilon^{(r)} \mathbf{E})}{\partial t^2} = \frac{\omega^2}{c^2} \epsilon^{(r)} \mathbf{E}, \quad (\text{B.8})$$

where  $c = 1/\sqrt{\epsilon_0 \mu_0}$  is the speed of light.

This equation along with the boundary conditions determines the frequency and the spatial profile of the optical mode. For the boundary condition we assume perfectly reflecting (i.e., ideally conducting) walls  $\mathbf{E}^{(t)}|_{\partial V} = 0$ , where  $\mathbf{E}^{(t)}$  is the transverse (i.e., parallel to the boundary) electric field. If the mode confinement is more ‘‘loose’’

(e.g., DBR mirrors for Fabry-Perot cavities, or evanescently decaying field for WGM resonators), we can imagine such walls being very far away where they do not significantly perturb the modes.

Now we can employ first-order perturbation theory to determine the change in the resonance frequency due to a perturbation in the electrical permittivity. First, imagine we have an initial permittivity profile  $\epsilon_0^{(r)}(\mathbf{r})$  and, correspondingly, some mode with field magnitude  $\mathbf{E}_0(\mathbf{r})$  and frequency  $\omega_0$ . The field satisfies the equation

$$\nabla(\nabla \cdot \mathbf{E}_0) - \nabla^2 \mathbf{E}_0 = \frac{\omega_0^2}{c^2} \epsilon_0^{(r)} \mathbf{E}_0. \quad (\text{B.9})$$

Now let us introduce a small perturbation to the permittivity  $\delta\epsilon^{(r)}$ . This perturbation will cause changes in the field profile  $\delta\mathbf{E}$  and the resonant frequency  $\delta\omega$ . The resulting equation is

$$\nabla(\nabla \cdot (\mathbf{E}_0 + \delta\mathbf{E})) - \nabla^2(\mathbf{E}_0 + \delta\mathbf{E}) = \frac{(\omega_0 + \delta\omega)^2}{c^2} (\epsilon_0^{(r)} + \delta\epsilon^{(r)}) (\mathbf{E}_0 + \delta\mathbf{E}). \quad (\text{B.10})$$

Next, we can use the unperturbed equation (B.9) to get rid of the zeroth-order terms, and then discard terms which are higher than first order in  $\delta\omega$ ,  $\delta\epsilon^{(r)}$  and  $\delta\mathbf{E}$

$$\nabla(\nabla \cdot \delta\mathbf{E}) - \nabla^2 \delta\mathbf{E} = \frac{2\omega_0 \delta\omega}{c^2} \epsilon_0^{(r)} \mathbf{E}_0 + \frac{\omega_0^2}{c^2} \delta\epsilon^{(r)} \mathbf{E}_0 + \frac{\omega_0^2}{c^2} \epsilon_0^{(r)} \delta\mathbf{E}. \quad (\text{B.11})$$

All we need from this equation is an expression for  $\delta\omega$  in terms of the known unperturbed mode parameters  $\mathbf{E}_0$ ,  $\epsilon_0^{(r)}$ ,  $\omega_0$ , and the perturbation  $\delta\epsilon^{(r)}$ . This means that we do not need to completely solve this equation and find  $\delta\mathbf{E}$ , if we can get rid of it in the final expression.

In order to do that, we multiply the left and the right parts of equation (B.11) by  $\mathbf{E}_0$  and integrate the resulting product over the whole space:

$$\begin{aligned} & \int_V \mathbf{E}_0 \cdot \nabla(\nabla \cdot \delta\mathbf{E}) dV - \int_V \mathbf{E}_0 \cdot \nabla^2 \delta\mathbf{E} \\ &= \int_V \frac{2\omega_0 \delta\omega}{c^2} \epsilon_0^{(r)} |\mathbf{E}_0|^2 dV + \int_V \frac{\omega_0^2}{c^2} \delta\epsilon^{(r)} |\mathbf{E}_0|^2 dV + \int_V \frac{\omega_0^2}{c^2} \epsilon_0^{(r)} \delta\mathbf{E} \cdot \mathbf{E}_0 dV. \end{aligned} \quad (\text{B.12})$$

Using integration by parts and the boundary conditions  $\mathbf{E}_0^{(t)}|_{\partial V} = \delta\mathbf{E}^{(t)}|_{\partial V} = 0$ , we can show that in the left-hand side

$$\begin{aligned} & \int_V \mathbf{E}_0 \cdot \nabla(\nabla \cdot \delta\mathbf{E}) dV - \int_V \mathbf{E}_0 \cdot \nabla^2 \delta\mathbf{E} \\ &= \int_V \delta\mathbf{E} \cdot \nabla(\nabla \cdot \mathbf{E}_0) dV - \int_V \delta\mathbf{E} \cdot \nabla^2 \mathbf{E}_0 \end{aligned} \quad (\text{B.13})$$

With that we can rearrange the terms to get

$$\begin{aligned} & \int_V \frac{2\omega_0 \delta\omega}{c^2} \epsilon_0^{(r)} |\mathbf{E}_0|^2 dV + \int_V \frac{\omega_0^2}{c^2} \delta\epsilon^{(r)} |\mathbf{E}_0|^2 dV \\ &= \int_V \delta\mathbf{E} \cdot \nabla(\nabla \cdot \mathbf{E}_0) dV - \int_V \delta\mathbf{E} \cdot \nabla^2 \mathbf{E}_0 - \int_V \frac{\omega_0^2}{c^2} \epsilon_0^{(r)} \delta\mathbf{E} \cdot \mathbf{E}_0 dV \\ &= \int_V \delta\mathbf{E} \cdot \left( \nabla(\nabla \cdot \mathbf{E}_0) - \nabla^2 \mathbf{E}_0 - \frac{\omega_0^2}{c^2} \epsilon_0^{(r)} \mathbf{E}_0 \right) = 0. \end{aligned} \quad (\text{B.14})$$

The last line is zero, since  $\mathbf{E}_0$  obeys the unperturbed equation (B.9).

Finally, from this equation we obtain the change in the resonance frequency

$$\frac{\delta\omega}{\omega_0} = -\frac{1}{2} \frac{\int_V \delta\epsilon^{(r)} |\mathbf{E}_0|^2 dV}{\int_V \epsilon_0^{(r)} |\mathbf{E}_0|^2 dV}. \quad (\text{B.15})$$

If the initial permittivity is uniform  $\epsilon_0^{(r)}(\mathbf{r}) = \epsilon_0^{(r)}$ , we can modify the expression above to get a more intuitive expression

$$\frac{\delta\omega}{\omega_0} = -\frac{\int_V (\delta\epsilon^{(r)}/2\epsilon_0^{(r)}) |\mathbf{E}_0|^2 dV}{\int_V |\mathbf{E}_0|^2 dV} = -\frac{\int_V \frac{\delta n}{n_0} |\mathbf{E}_0|^2 dV}{\int_V |\mathbf{E}_0|^2 dV}, \quad (\text{B.16})$$

where  $n_0 = \sqrt{\epsilon_0^{(r)}}$  is the unperturbed refractive index of the medium and  $\delta n$  is its perturbation.

If we assume that  $\delta n$  is also constant everywhere, we get just  $\frac{\delta\omega}{\omega_0} = -\frac{\delta n}{n_0}$ : the perturbation in the refractive index changes the cavity's effective size and, therefore, its resonant frequency. If, however,  $\delta n$  varies in space, the regions with higher intensity should contribute more to the overall perceived change in  $n$ ; in this case we can see the numerator as a weighed average of  $\delta n$ , while the denominator is just a normalization coefficient.

## B.2 Cavity modes

In this section we consider Gaussian modes inside a Fabry-Perot cavity, and derive expressions for their spatial profiles and frequencies.

### B.2.1 Gaussian beam

We start with a Gaussian beam[152], which is a solution for the wave equation in the paraxial approximation. A beam with a waist at  $z = 0$  and propagating in  $+z$  direction can be expressed in terms of the complex radius of curvature  $\tilde{q}(z) = \tilde{q}_0 + z$  as

$$u(x, y, z) = e^{ikz} \frac{\tilde{q}_0}{\tilde{q}(z)} \exp\left(ik \frac{x^2 + y^2}{2\tilde{q}(z)}\right), \quad (\text{B.17})$$

where  $k = \omega/c$  is the beam's wave-vector,  $\omega$  is its frequency and  $\tilde{q}_0$  can be expressed in terms of the beam waist  $w_0$  as  $\tilde{q}_0 = -iw_0^2 k/2$ . Equation (B.17) can be rewritten in terms of a position-dependent beam width  $w(z)$ , radius of curvature (ROC)  $R(z)$ , and Gouy phase shift  $\psi_G(z)$  as

$$u(x, y, z) = e^{ikz} e^{-i\psi_G(z)} \frac{w_0}{w(z)} \exp\left(-\frac{x^2 + y^2}{(w(z))^2} + ik \frac{x^2 + y^2}{2R(z)}\right) \quad (\text{B.18})$$

$$w(z) = w_0 \sqrt{1 + (z/z_R)^2} \quad (\text{B.19})$$

$$R(z) = z \left(1 + (z_R/z)^2\right) \quad (\text{B.20})$$

$$\tan \psi_G(z) = z/z_R, \quad (\text{B.21})$$

where  $z_R = i\tilde{q}_0 = w_0^2 k/2$  is the Rayleigh range, which characterizes divergence of the beam (it can be thought of as the longitudinal extent of the beam waist). The interpretation of  $R(z)$  as the ROC of the beam can be made more apparent by approximating the phase around some point  $z = z_0$  as

$$\phi(x, y, z) \approx \phi(0, 0, z_0) + ik \left( \frac{x^2 + y^2}{2R_0} + (z - z_0) \right), \quad (\text{B.22})$$

where  $R_0 \equiv R(z_0)$  and we have neglected the spatial dependence of the slowly changing Gouy phase  $\psi_G$  and the ROC  $R$ . From this, a surface of constant phase obeys the equation  $x^2 + y^2 + 2R_0(z - z_0) = 0$ , which up to terms quadratic in  $z - z_0$  describes a spherical surface of radius  $R_0$ :  $x^2 + y^2 + (z - z_0 + R_0)^2 = R_0^2$ .

### B.2.2 Gaussian modes

A Gaussian beam can be confined to a standing mode with two spherical mirrors, which form a Fabry-Perot cavity. In order to satisfy the boundary condition imposed by the mirrors, the mode needs to obey two

conditions. First, its radius of curvature  $R(z)$  should be equal to the corresponding ROCs of the mirrors at their surface (with appropriate signs):  $R(z_1) = -R_1$ ,  $R(z_2) = R_2$ , where  $z_{1,2}$  are the positions of the mirrors and  $R_{1,2}$  are their ROCs, with positive  $R$  corresponding to a concave mirror. This fixes the Rayleigh range to

$$z_R = \frac{\sqrt{g_1 g_2 (1 - g_1 g_2)}}{g_1 + g_2 - 2g_1 g_2} L, \quad (\text{B.23})$$

where  $L$  is a length of the resonator and  $g_{1,2} \equiv 1 - L/R_{1,2}$  are so-called  $g$ -parameters. The resonator is stable only when the argument of the square root is positive, that is for  $0 < g_1 g_2 < 1$ .

The second requirement comes from the wave nature of light, and it restricts the round-trip phase of the beam to be a multiple of  $2\pi$ . We express it as

$$2k_n L - 2\Delta\psi_G + (\phi_1 + \phi_2) = 2\pi n, \quad (\text{B.24})$$

where an integer  $n$  is a longitudinal number of the mode,  $k_n = \omega_n/c$  is the corresponding wave-vector,  $\Delta\psi_G = \psi_G(z_2) - \psi_G(z_1)$  is the Gouy phase shift acquired by the beam between the two mirrors, and  $\phi_{1,2}$  are the reflection phases of the mirrors. For mirrors made of ideal conductors (corresponding to zero electric field on the surface) these phases are simply  $\pi$ ; however, for distributed Bragg reflector (DBR) mirrors these can be arbitrary and, in principle, wavelength-dependent (see section B.4).

The corresponding mode profile is

$$u_n(x, y, z) = e^{i\phi_0} e^{ik_n z} e^{-i\psi_G(z)} \frac{w_0}{w(z)} \exp\left(-\frac{x^2 + y^2}{(w(z))^2} + ik_n \frac{x^2 + y^2}{2R(z)}\right) + \text{c.c.}, \quad (\text{B.25})$$

which is the real part of the Gaussian beam expression (B.18) with an overall mode phase  $\phi_0$ . The zero of the  $z$ -axis is defined to be at the mode waist, and the corresponding mirror positions are

$$z_1 = -\frac{g_2(1 - g_1)}{g_1 + g_2 - 2g_1 g_2} L \quad (\text{B.26})$$

$$z_2 = \frac{g_1(1 - g_2)}{g_1 + g_2 - 2g_1 g_2} L = z_1 + L. \quad (\text{B.27})$$

One can check that given the Rayleigh range (B.23) the mode ROC obeys the boundary conditions  $R(z_1) = -R_1$  and  $R(z_2) = R_2$ . Finally, in order to produce the correct reflection phases  $\phi_{1,2}$ , the overall phase of the mode  $\phi_0$  has to satisfy

$$\phi_0 + k_n z_2 - \psi_G(z_2) = -\phi_2/2 \pmod{2\pi}. \quad (\text{B.28})$$

Since  $k_n$  obeys the resonant frequency condition (equation (B.23)), the phase requirement on the other mirror surface

$$\phi_0 + k_n z_1 - \psi_G(z_1) = \phi_1/2 \pmod{2\pi} \quad (\text{B.29})$$

is satisfied automatically.

### B.2.3 Resonance frequencies and free spectral range

It turns out[152] that the full Gouy phase shift is independent of the wavelength and is equal to

$$\Delta\psi_G = \arccos(\pm\sqrt{g_1 g_2}), \quad (\text{B.30})$$

where the positive sign corresponds to  $g_1, g_2 > 0$ , and the negative sign to  $g_1, g_2 < 0$ . This results in the following expression for resonant frequencies of a Fabry-Perot cavity formed by perfect conductor mirrors:

$$\omega_n = ck_n = 2\pi F \left( n + \frac{\Delta\psi_G}{\pi} \right), \quad (\text{B.31})$$

where  $F = c/(2L)$  is the free spectral range (FSR) of the cavity. The frequency difference between the consecutive modes is simply equal to the FSR:  $\Delta\omega_n \equiv \omega_{n+1} - \omega_n = 2\pi F$ . For mirrors with arbitrary reflection phase  $\phi_{1,2}(\omega)$  the resonance condition becomes

$$\omega_n = 2\pi F \left( n + \frac{\Delta\psi_G}{\pi} - \frac{\phi_1(\omega_n) + \phi_2(\omega_n)}{2\pi} \right), \quad (\text{B.32})$$

and the distance between the consecutive modes can be expressed as

$$\Delta\omega_n = 2\pi F_{\text{eff}}. \quad (\text{B.33})$$

Here  $F_{\text{eff}} = c/(2L_{\text{eff}})$  is the FSR corresponding to the effective cavity length  $L_{\text{eff}} = L + \delta L_1(\omega_n) + \delta L_2(\omega_n)$ , where  $\delta L_i(\omega)$  is the penetration depth of  $i^{\text{th}}$  mirror defined as

$$\delta L_i(\omega) = \frac{c}{2} \frac{\partial(\phi_i)}{\partial\omega}. \quad (\text{B.34})$$

Note that equation (B.34) does not imply  $\phi_i = 2\omega\delta L_i/c$ , that is, the penetration depth is defined in terms of the differential response of the mirror's reflection phase (the difference is similar to, e.g., group velocity vs. phase velocity). Thus, while knowing the penetration depth is enough to find the frequency difference between the nearby modes, it is not enough to predict their absolute frequencies.

Finally, we need to consider what happens if the cavity is filled with a uniform dielectric with refractive index  $n_0$ . The only difference this introduces in the equations above is the factor of  $n_0$  in the relationship between the mode's frequency  $\omega_n$  and its wave-vector  $k_n$ . We can account for this by replacing  $L$  with  $Ln_0$  in the definitions for  $F$  and  $F_{\text{eff}}$  in (B.32) and (B.33). In addition, the dielectric could change the mirrors' reflection phase  $\phi_i$  and the corresponding penetration depth  $\delta L_i$  (an example of this effect is given in subsection B.4.2), so those need to be adjusted accordingly.

### B.3 Transfer matrix formalism

In this section we introduce the transfer matrix formalism for solving 1D propagation of EM waves. We then use it to derive expressions for the resonant frequency and the linewidth of a simple Fabry-Perot cavity, and later employ it in considering optical DBR (section B.4).

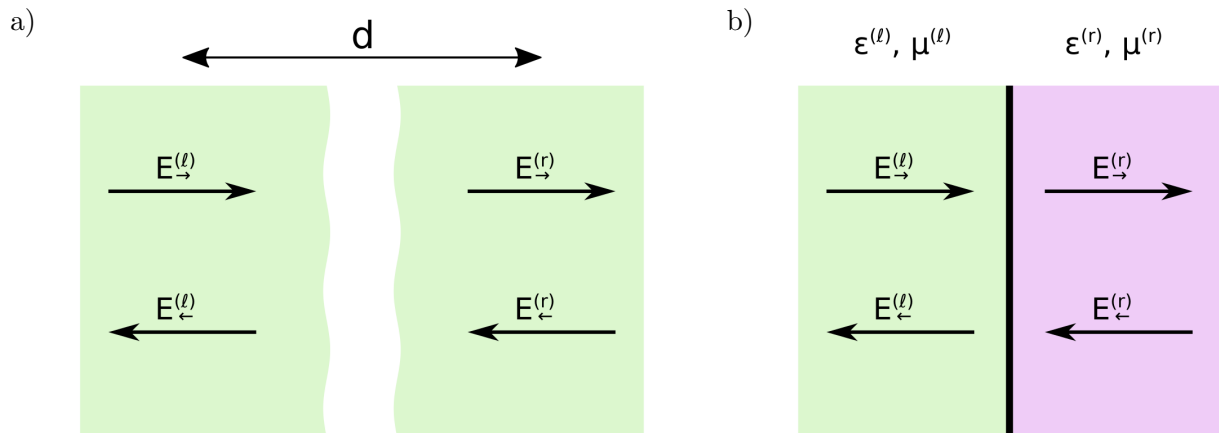


Figure B.1: a) Schematic of the transfer matrix description of wave propagation. b) Schematic of the transfer matrix description of a material boundary.

### B.3.1 Definition

A transfer matrix describes a linear relation between the incoming and the outgoing electrical fields on one side and on the other:

$$\begin{pmatrix} E_{\rightarrow}^{(r)} \\ E_{\leftarrow}^{(r)} \end{pmatrix} = M \cdot \begin{pmatrix} E_{\rightarrow}^{(\ell)} \\ E_{\leftarrow}^{(\ell)} \end{pmatrix}, \quad (\text{B.35})$$

where  $E$  is the electric field, arrows show the direction of propagation, and  $(\ell)$  and  $(r)$  denote two sides of an optical element (schematic illustrations are shown in Figure B.1). The most important property of these matrices is that they are easily “stackable”, in the sense that the transfer matrix of a sequence of two elements is a product of the two transfer matrices. For the definition given in equation (B.35) the product is reversed, i.e., the rightmost matrix corresponds to the first (leftmost) element.

### B.3.2 Common cases

Below we derive transfer matrices for the most common situations.

1. Propagation (shown in Figure B.1a).

Propagation simply adds a phase shift to the forward and the backward waves without mixing them:

$$M^{(p)}(k, d) = \begin{pmatrix} e^{ikd} & 0 \\ 0 & e^{-ikd} \end{pmatrix}. \quad (\text{B.36})$$

Here  $d$  is the propagation distance and  $k$  is the wave-vector. For a wave of a frequency  $\omega$  propagating through a media with a dielectric constant  $\epsilon$  and a magnetic permeability  $\mu$  the wave-vector is

$$k = n \frac{\omega}{c} \quad (\text{B.37})$$

$$n = \sqrt{\frac{\epsilon\mu}{\epsilon_0\mu_0}}, \quad (\text{B.38})$$

where  $n$  is the refractive index of the media.

2. Boundary between two different media (shown in Figure B.1b).

To derive the relation at the boundary, we have to consider the boundary conditions. Assuming that the boundary is non-singular (i.e., it has zero surface conductivity or polarizability), the continuity conditions are

$$E^{(\ell)} = E^{(r)} \quad (\text{B.39})$$

$$H^{(\ell)} = H^{(r)}, \quad (\text{B.40})$$

where  $H = B/\mu$  is the magnetic  $H$ -field. From the Maxwell's equations the electric and the magnetic fields can be expressed as

$$E^{(\ell,r)} = E_{\rightarrow}^{(\ell,r)} + E_{\leftarrow}^{(\ell,r)} \quad (\text{B.41})$$

$$H^{(\ell,r)} = \frac{E_{\rightarrow}^{(\ell,r)} - E_{\leftarrow}^{(\ell,r)}}{\mathcal{Z}^{(\ell,r)}}, \quad (\text{B.42})$$

with  $\mathcal{Z}^{(\ell,r)} \equiv \sqrt{\frac{\mu^{(\ell,r)}}{\epsilon^{(\ell,r)}}}$  is the wave impedance of the media. These relations result in the transfer matrix

$$M^{(b)}(\mathcal{Z}^{(\text{rel})}) = \frac{1}{2} \begin{pmatrix} 1 + \mathcal{Z}^{(\text{rel})} & 1 - \mathcal{Z}^{(\text{rel})} \\ 1 - \mathcal{Z}^{(\text{rel})} & 1 + \mathcal{Z}^{(\text{rel})} \end{pmatrix}, \quad (\text{B.43})$$

where  $\mathcal{Z}^{(\text{rel})} = \mathcal{Z}^{(r)}/\mathcal{Z}^{(\ell)}$  is the relative wave impedance of the two media. If the media have the same magnetic permeability (for example, both are non-magnetic, i.e.,  $\mu^{(\ell)} = \mu^{(r)} = \mu_0$ ), then  $\mathcal{Z}^{(\text{rel})} = 1/n^{(\text{rel})}$ , where  $n^{(\text{rel})} = n^{(r)}/n^{(\ell)}$  is the relative refractive index of the two media.

### 3. Dielectric slab in vacuum.

Let us now consider a dielectric slab of width  $d$  and refractive index  $n^{(d)} = \sqrt{\epsilon^{(d)}/\epsilon_0}$ , where  $\epsilon^{(d)}$  is its dielectric constant. The transfer matrix in this situation can be obtained by combining the two previous cases:

$$\begin{aligned} M^{(\text{ds})}(d, n^{(d)}) &= M^{(\text{b})}(1/n^{(d)})M^{(\text{p})}(k, d)M^{(\text{b})}(n^{(d)}) \\ &= \cos(kd) \begin{pmatrix} 1 & 0 \\ 0 & 1 \end{pmatrix} + i \frac{\sin(kd)}{2n^{(d)}} \begin{pmatrix} 1 + (n^{(d)})^2 & 1 - (n^{(d)})^2 \\ 1 - (n^{(d)})^2 & -1 - (n^{(d)})^2 \end{pmatrix}. \end{aligned} \quad (\text{B.44})$$

Note that here  $k = \omega n^{(d)}/c$  is the wave-vector inside the dielectric.

### 4. Thin dielectric layer.

A thin dielectric layer describes the situation where the slab thickness is negligible compared to the optical wavelength (both in vacuum and in the dielectric). Formally, we obtain this case by considering  $M^{(\text{ds})}$  in the limit  $\epsilon^{(d)} \rightarrow \infty$ ,  $k_0 d \rightarrow 0$  and  $k_0 \epsilon^{(d)} d \rightarrow \text{const}$ :

$$M^{(\text{dl})}(\xi) = \begin{pmatrix} 1 + i\xi & i\xi \\ -i\xi & 1 - i\xi \end{pmatrix}, \quad (\text{B.45})$$

where  $\xi = k_0 d \epsilon^{(d)}/(2\epsilon_0)$ . Note that although the layer is assumed to be thin enough that it does not affect phase of the passing waves (since  $kd = k_0 d n^{(d)} = 2\xi/n^{(d)} \rightarrow 0$ ),  $\xi$  can take any value, including  $\xi > 1$ .

A useful property of this transfer matrix is the ease of combining two consecutive layers:  $M^{(\text{dl})}(\xi_1)M^{(\text{dl})}(\xi_2) = M^{(\text{dl})}(\xi_1 + \xi_2)$ .

## B.3.3 Scattering matrix

Another important class of objects is scattering matrices. They connect the same four quantities (incoming and outgoing fields) as the transfer matrices, but in a different way:

$$\begin{pmatrix} E_{\leftarrow}^{(\ell)} \\ E_{\rightarrow}^{(r)} \end{pmatrix} = S \begin{pmatrix} E_{\rightarrow}^{(\ell)} \\ E_{\leftarrow}^{(r)} \end{pmatrix}, \quad (\text{B.46})$$

that is, it expresses scattered waves  $E_{\leftarrow}^{(\ell)}$  and  $E_{\rightarrow}^{(r)}$  in terms of the incident ones  $E_{\rightarrow}^{(\ell)}$  and  $E_{\leftarrow}^{(r)}$ . In the ordering given above the diagonal elements correspond to reflection, and off-diagonal elements describe transmission. These matrices describe optical objects in a more intuitive sense (the matrix elements have clear meaning of reflection and transmission), and they can be readily generalized for an arbitrary number of ports (not just two for a simple 1D object). However, they do not combine as easily as the transfer matrices: scattering matrix of the combination of two elements is not simply a product of their scattering matrices.

Barring some degenerate cases (e.g., perfect reflector or perfect absorber), there is a one-to-one correspondence between scattering matrices and transfer matrices:

$$S(M) = \frac{1}{M_{22}} \begin{pmatrix} -M_{21} & 1 \\ M_{11}M_{22} - M_{12}M_{21} & M_{12} \end{pmatrix} \quad (\text{B.47})$$

$$M(S) = \frac{1}{S_{12}} \begin{pmatrix} S_{12}S_{21} - S_{11}S_{22} & S_{22} \\ -S_{11} & 1 \end{pmatrix}. \quad (\text{B.48})$$

Using these, we can write a scattering matrix of a thin dielectric layer as

$$S^{(\text{dl})}(\xi) = \frac{1}{1 - i\xi} \begin{pmatrix} i\xi & 1 \\ 1 & i\xi \end{pmatrix}, \quad (\text{B.49})$$

so its transmission and reflection coefficients are

$$t^{(\text{dl})} = -\frac{i}{i + \xi} \quad (\text{B.50})$$

$$T^{(\text{dl})} = |t^{(\text{dl})}|^2 = \frac{1}{1 + \xi^2} \quad (\text{B.51})$$

$$r^{(\text{dl})} = -\frac{\xi}{i + \xi} \quad (\text{B.52})$$

$$R^{(\text{dl})} = |r^{(\text{dl})}|^2 = \frac{\xi^2}{1 + \xi^2} = 1 - T^{(\text{dl})}. \quad (\text{B.53})$$

Here  $t^{(\text{dl})}$  and  $r^{(\text{dl})}$  are amplitude reflection and transmission coefficients, while  $T^{(\text{dl})}$  and  $R^{(\text{dl})}$  are the corresponding power coefficients. These expressions suggest that a lossless mirror with transmittivity  $T$  can be modeled as a dielectric layer of strength  $\xi^{(\text{m})}(T) = \sqrt{\frac{1-T}{T}}$ . Note that  $\lim_{T \rightarrow 0} \xi^{(\text{m})}(T) = \infty$ , that is, for a perfect reflector one needs an infinite strength mirror.

### B.3.4 Cavities

Now we describe of a Fabry-Perot cavity using the transfer matrix formalism. To keep the discussion general, let us denote the transfer matrix of the cavity content as  $M^{(\text{cav})}(\omega)$ , where  $\omega$  is the frequency of the circulating light. This matrix does not include the input and output mirrors, but it includes everything else in the cavity, i.e., it connect the fields at the leftmost side of the cavity (on the right side of the input mirror) to the fields of the rightmost side (on the left side of the output mirror). For example, for an empty cavity of length  $L$  this matrix is simply a propagation matrix  $M^{(\text{cav})}(\omega) = M^{(\text{p})}(\omega/c, L)$ .

If we include the input mirror of transmittivity  $T_{\text{in}}$  and the output mirror of transmittivity  $T_{\text{out}}$ , the total transfer matrix describing the cavity becomes

$$M(\omega) = M^{(\text{dl})}(\xi^{(\text{out})}) \cdot M^{(\text{cav})}(\omega) \cdot M^{(\text{dl})}(\xi^{(\text{in})}), \quad (\text{B.54})$$

where  $\xi^{(\text{in,out})} = \xi^{(\text{m})}(T_{\text{in,out}})$  are the dielectric mirror strengths required to achieve the necessary transmission coefficients. Now we can use this transfer matrix to obtain the corresponding scattering matrix and get the cavity transmission and reflection coefficients:

$$t = S_{21} = \frac{M_{11}M_{22} - M_{12}M_{21}}{M_{22}} \quad (\text{B.55})$$

$$r = S_{11} = -\frac{M_{21}}{M_{22}}. \quad (\text{B.56})$$

The resonance of a cavity corresponds to a pole of its transmission or reflection coefficient. From the equations above it is clear that the poles of  $r$  and  $t$  correspond to zeros of  $M_{22}$ , which yields the equation for the resonant frequencies of the cavity:

$$M_{22}(\omega_{\text{res}}) = 0. \quad (\text{B.57})$$

The root will in general be complex, with real and imaginary parts corresponding to the frequency and linewidth of the resonance.

As an instructive and useful example, let us consider an empty cavity made of length  $L$  formed by two mirrors with transmission coefficients  $T_{\text{in}}$  and  $T_{\text{out}}$ . The cavity transfer matrix is a propagation matrix  $M^{(\text{p})}(k, L)$  with  $k = \omega/c$  for the empty cavity, so the total transfer matrix is

$$M(\omega) = M^{(\text{dl})}(\xi^{(\text{in})})M^{(\text{p})}(\omega/c, L) \cdot M^{(\text{dl})}(\xi^{(\text{out})}), \quad (\text{B.58})$$

where  $\xi^{(\text{in,out})} = \sqrt{R_{\text{in,out}}/T_{\text{in,out}}}$  with  $R_{\text{in,out}} = 1 - T_{\text{in,out}}$  being the corresponding power reflection coefficients. For simplicity, we will assume high-reflectivity mirrors  $T_{\text{in,out}} \ll 1$

The important transfer matrix element is

$$M_{22}(\omega) = e^{-i\omega L/c}(1 - i\xi^{(\text{in})})(1 - i\xi^{(\text{out})}) + e^{i\omega L/c}\xi^{(\text{in})}\xi^{(\text{out})}, \quad (\text{B.59})$$

which leads to the equation for the resonant frequency

$$e^{2i\omega_{\text{res}}L/c} = 1 + i \left( \sqrt{\frac{T_{\text{in}}}{R_{\text{in}}}} + \sqrt{\frac{T_{\text{out}}}{R_{\text{out}}}} \right) - \sqrt{\frac{T_{\text{in}}T_{\text{out}}}{R_{\text{in}}R_{\text{out}}}}. \quad (\text{B.60})$$

The solution for this equation is (up to terms of the order  $T_{\text{in,out}}^{3/2}$ )

$$2\omega_{\text{res}}L/c = 2\pi n + \left( \sqrt{\frac{T_{\text{in}}}{R_{\text{in}}}} + \sqrt{\frac{T_{\text{out}}}{R_{\text{out}}}} \right) - i \left( \frac{T_{\text{in}}}{R_{\text{out}}} + \frac{T_{\text{out}}}{R_{\text{out}}} \right), \quad (\text{B.61})$$

where  $n$  is the mode index, similar to the one defined in subsection B.2.3. We can identify the real part of  $\omega_{\text{res}}$  as the resonant frequency

$$\omega_n = \text{Re} \{ \omega_{\text{res}} \} = 2\pi nF + \left( \sqrt{\frac{T_{\text{in}}}{R_{\text{in}}}} + \sqrt{\frac{T_{\text{out}}}{R_{\text{out}}}} \right) F \approx 2\pi nF \quad (\text{B.62})$$

(where  $F = c/(2L)$  is the FSR defined in subsection B.2.3), and the imaginary part as the corresponding linewidth

$$\kappa = -2\text{Im} \{ \omega_{\text{res}} \} = F \left( \frac{T_{\text{in}}}{R_{\text{out}}} + \frac{T_{\text{out}}}{R_{\text{out}}} \right) \approx F (T_{\text{in}} + T_{\text{out}}). \quad (\text{B.63})$$

The cavity finesse, which is defined as the ratio of the FSR to the linewidth

$$\mathcal{F} = \frac{2\pi F}{\kappa}, \quad (\text{B.64})$$

is equal to

$$\mathcal{F} = \frac{2\pi}{T_{\text{in}} + T_{\text{out}}}. \quad (\text{B.65})$$

This quantity is convenient to characterize Fabry-Perot cavities, since unlike the quality factor  $Q = \omega_n/\kappa = n\mathcal{F}$  it only depends on the mirror parameters and not on the total cavity length (at least, in the perfect 1D case where we neglect clipping and diffraction losses).

### B.3.5 Perfect mirrors approximation

Equation (B.57) can be simplified if we take the limit of perfectly reflecting input and output mirrors. As we have shown in the previous section, this corresponds to the infinite mirror dielectric strength  $\xi_{\text{in,out}} \rightarrow \infty$ . In this limit the mirror transfer matrix (B.45) becomes

$$M^{(\text{mir})} \approx i\xi \begin{pmatrix} 1 & 1 \\ -1 & -1 \end{pmatrix}. \quad (\text{B.66})$$

After substituting this matrix for the mirrors in equation (B.54), resonant condition (B.57) turns into

$$\left( M_{11}^{(\text{cav})} + M_{22}^{(\text{cav})} - M_{12}^{(\text{cav})} - M_{21}^{(\text{cav})} \right) (\omega_{\text{res}}) = 0. \quad (\text{B.67})$$

In the simple case of the empty cavity mentioned above this immediately leads to  $e^{2i\omega_{\text{res}}L/c} = 1$ , which corresponds to the familiar condition of the roundtrip length being a multiple of the optical wavelength.

Relation (B.67) can be derived in a different way, starting from the perfect reflector boundary condition of having a zero electric field on the surface. On the left side of the cavity it leads to  $E_{\leftarrow}^{(\ell)} = -E_{\rightarrow}^{(\ell)}$ , while similarly on the right  $E_{\leftarrow}^{(r)} = -E_{\rightarrow}^{(r)}$ . However, these four fields are also related through the cavity transfer matrix  $M^{(\text{cav})}$ , which leads to the condition

$$\begin{aligned} 0 &= E_{\rightarrow}^{(r)} + E_{\leftarrow}^{(r)} = \left( M_{11}^{(\text{cav})} E_{\rightarrow}^{(\ell)} + M_{12}^{(\text{cav})} E_{\leftarrow}^{(\ell)} \right) + \left( M_{21}^{(\text{cav})} E_{\rightarrow}^{(\ell)} + M_{22}^{(\text{cav})} E_{\leftarrow}^{(\ell)} \right) \\ &= \left( M_{11}^{(\text{cav})} - M_{12}^{(\text{cav})} + M_{21}^{(\text{cav})} + M_{22}^{(\text{cav})} \right) E_{\rightarrow}^{(\ell)}. \end{aligned} \quad (\text{B.68})$$

If the circulating field  $E_{\rightarrow}^{(\ell)}$  is non-zero, the equation above is equivalent to (B.67).

## B.4 Distributed Bragg reflectors

### B.4.1 Finite DBR

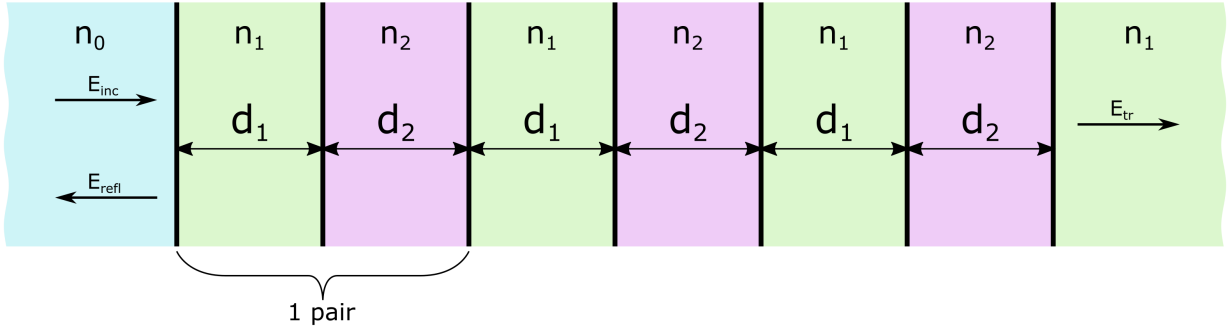


Figure B.2: Schematic of a distributed Bragg reflector (DBR). The DBR shown here corresponds to  $N = 3$  layer pairs.

In this section I want to briefly consider distributed Bragg reflector (DBR) mirrors. A DBR is a stack of dielectric layers, which is comprised of  $N$  identical layer pairs, as shown in Figure B.2. Each pair consists of two dielectric layers made out of materials with dissimilar refractive coefficients. Let us denote the refractive coefficients of the two dielectrics as  $n_1$  and  $n_2$ , the corresponding layer thicknesses as  $d_1$  and  $d_2$ , and the wave-vector of light (in vacuum) as  $k_0$ . With these definitions, the transfer matrix of a single pair is expressed as

$$M^{(\text{pair})} = M^{(\text{b})}(n_2/n_1) \cdot M^{(\text{p})}(n_2 k_0, d_2) \cdot M^{(\text{b})}(n_1/n_2) \cdot M^{(\text{p})}(n_1 k_0, d_1). \quad (\text{B.69})$$

This matrix describes (reading right to left) light propagating through the first dielectric layer, then entering the second layer, propagating through that, and finally entering back into the first dielectric at the start of the next pair (remember that the transfer matrix describing a wave going from a material with refractive index  $n_1$  into a material with refractive index  $n_2$  is  $M^{(\text{b})}(\mathcal{Z}^{(2)}/\mathcal{Z}^{(1)}) = M^{(\text{b})}(n_1/n_2)$ ). The total transfer matrix of  $N$  layers, including the light entering from some outside material with the refractive index  $n_0$ , is

$$M^{(\text{DBR})} = \left( M^{(\text{pair})} \right)^N \cdot M^{(\text{b})}(n_0/n_1). \quad (\text{B.70})$$

In an ideal DBR the layers are assumed to be  $\lambda/4$  thick, i.e.,  $k_0 n_1 d_1 = k_0 n_2 d_2 = \pi/2$ . In this case both propagation matrices are equal to

$$M^{(\text{p})}(n_1 k_0, d_1) = M^{(\text{p})}(n_2 k_0, d_2) = \begin{pmatrix} i & 0 \\ 0 & -i \end{pmatrix}, \quad (\text{B.71})$$

so the transfer matrix of a single pair is

$$M^{(\text{pair})} = -\frac{1}{2n_r} \begin{pmatrix} 1 + n_r^2 & 1 - n_r^2 \\ 1 - n_r^2 & 1 + n_r^2 \end{pmatrix}, \quad (\text{B.72})$$

and the transfer matrix of  $N$  pairs is

$$\left(M^{(\text{pair})}\right)^N = \frac{(-1)^N}{2n_r^N} \begin{pmatrix} 1 + n_r^{2N} & 1 - n_r^{2N} \\ 1 - n_r^{2N} & 1 + n_r^{2N} \end{pmatrix}, \quad (\text{B.73})$$

where  $n_r = n_2/n_1$ . The total DBR transfer matrix is

$$M^{(\text{DBR})} = \frac{(-1)^N}{2n_r^N} \begin{pmatrix} 1 + (n_1/n_0)n_r^{2N} & 1 - (n_1/n_0)n_r^{2N} \\ 1 - (n_1/n_0)n_r^{2N} & 1 + (n_1/n_0)n_r^{2N} \end{pmatrix}. \quad (\text{B.74})$$

The amplitude transmission coefficient of the whole DBR mirror can be obtained using equation (B.55):

$$t = \frac{2(n_1/n_0)(-1)^N}{n_r^{-N} + (n_1/n_0)n_r^N}. \quad (\text{B.75})$$

If we assume  $N \gg 1$ , then the power transmission coefficient can be approximated as

$$T = |t|^2 \approx \begin{cases} 4(n_1/n_0)^2 n_r^{2N}, & 0 < n_r < 1 \\ 4n_r^{-2N}, & n_r > 1. \end{cases} \quad (\text{B.76})$$

Thus, unless  $n_r = 1$  (i.e., both materials are the same), the transmission coefficient decreases exponentially with  $N$ , so it can be made arbitrarily small by adding more layers. In practice, high-quality mirror DBR coatings routinely achieve  $T \approx 10^{-6}$ .

### B.4.2 Infinite DBR approximation and penetration depth

It is also useful to consider the case of an infinite DBR, but with a potentially mismatched incident light wavelength (i.e., with layer thicknesses not being exactly  $\lambda/4$ ). This will allow us estimate the penetration depth (defined in equation (B.34) in subsection B.2.3) of a DBR in the perfect reflectivity limit.

Let us start again by considering just  $N$  layer pairs without the outside material. If we assume that the light is only incident from the left, and if we normalize this incident amplitude to be 1, we can write the transfer relations as

$$\begin{pmatrix} t \\ 0 \end{pmatrix} = \left(M^{(\text{pair})}\right)^N \cdot \begin{pmatrix} 1 \\ r \end{pmatrix}. \quad (\text{B.77})$$

Here  $r$  and  $t$  are the amplitudes of the reflected and the transmitted wave respectively, and with our normalization they are simply equal to the reflection and the transmission coefficients. Next, let us assume that the single pair transfer matrix  $M^{(\text{pair})}$  has a complete set of eigenvectors  $v_{1,2}$  and eigenvalues  $\lambda_{1,2}$ ,<sup>a)</sup> and let us decompose the transmission vector in terms of these eigenvectors as

$$\begin{pmatrix} t \\ 0 \end{pmatrix} = t(a_1 v_1 + a_2 v_2), \quad (\text{B.78})$$

where  $a_{1,2}$  are the decomposition coefficients. Using that decomposition, we can invert the relation (B.77) to obtain

$$\begin{pmatrix} 1 \\ r \end{pmatrix} = t \left( a_1 \lambda_1^{-N} v_1 + a_2 \lambda_2^{-N} v_2 \right). \quad (\text{B.79})$$

---

<sup>a)</sup>The only way the Jordan normal form of  $M^{(\text{pair})}$  could be non-diagonal is if  $\lambda_1 = \lambda_2$ , and, as we show later, this implies that the DBR does not actually serve as a reflector.

First, let us imagine that  $|\lambda_1| = |\lambda_2|$ ; since  $\lambda_1\lambda_2 = \det(M^{(\text{pair})}) = 1$ , this would imply that  $|\lambda_1| = |\lambda_2| = 1$ . However, this means that the RHS magnitude stays approximately the same (on the order of  $t$ ) regardless of the number of layers  $N$ , which means that the DBR transmission does not depend on  $N$ .<sup>b)</sup>

Since we only want to consider DBRs which get progressively more reflective as  $N$  grows, we have to assume that  $|\lambda_1| \neq |\lambda_2|$ . Let us then WLOG denote the smaller eigenvalue as  $\lambda_1$  and the bigger one as  $\lambda_2$ ; since  $\lambda_1\lambda_2 = 1$ , its means that  $|\lambda_1| < 1$  and  $|\lambda_2| > 1$ . Then for very large  $N$  such that  $|\lambda_1|^{-N} \gg |\lambda_2|^{-N}$  we can approximate (B.79) as

$$\begin{pmatrix} 1 \\ r \end{pmatrix} \approx ta_1\lambda_1^{-N}v_1 \propto v_1. \quad (\text{B.81})$$

Thus, to find the reflection phase, we simply need to examine the eigenvector corresponding to the smaller eigenvalue.

Finally, we can consider what would happen if the DBR is preceded by some other objects, e.g., if the wave enters from a different material as we assumed in the previous subsection. If we denote the transfer matrix leading to the DBR pairs stack as  $M^{(s)}$ , the new transfer relations can be expressed as

$$\begin{pmatrix} t \\ 0 \end{pmatrix} = \left(M^{(\text{pair})}\right)^N \cdot M^{(s)} \cdot \begin{pmatrix} 1 \\ r \end{pmatrix}. \quad (\text{B.82})$$

Following the same route, we can arrive at an analogue of equation (B.81):

$$M^{(s)} \cdot \begin{pmatrix} 1 \\ r \end{pmatrix} \approx ta_1\lambda_1^{-N}v_1 \propto v_1, \quad (\text{B.83})$$

so in the end

$$\begin{pmatrix} 1 \\ r \end{pmatrix} \propto \left(M^{(s)}\right)^{-1} \cdot v_1. \quad (\text{B.84})$$

This means that the reflection amplitude is

$$r = \frac{\left[\left(M^{(s)}\right)^{-1} \cdot v_1\right]_2}{\left[\left(M^{(s)}\right)^{-1} \cdot v_1\right]_1}. \quad (\text{B.85})$$

(where a subscript outside parentheses is a vector index).

Now let us consider a mismatched DBR. Specifically, let us assume that the DBR is perfectly matched for some wave-vector  $k_{0,m}$ , but the incident light has a different wave-vector  $k_0 \neq k_{0,m}$ . We can account for the mismatch by replacing the ideal propagation matrix (B.71) with

$$M^{(\text{D})}(n_1k_0, d_1) = M^{(\text{D})}(n_1k_0, d_1) = \begin{pmatrix} ie^{i\delta} & 0 \\ 0 & -ie^{-i\delta} \end{pmatrix}, \quad (\text{B.86})$$

where  $\delta = k_0n_1d_1 - \pi/2 = k_0n_2d_2 - \pi/2 = (k_{0,m}/k_0 - 1)\pi/2$  is the extra phase acquired due to the mismatch.

With this, a single pair transfer matrix becomes

$$M^{(\text{pair})} = -\frac{1}{4n_r} \begin{pmatrix} (n_r - 1)^2 + e^{2i\delta}(n_r + 1)^2 & (1 + e^{-2i\delta})(n_r^2 - 1) \\ (1 + e^{2i\delta})(n_r^2 - 1) & (n_r - 1)^2 + e^{-2i\delta}(n_r + 1)^2 \end{pmatrix}. \quad (\text{B.87})$$

---

<sup>b)</sup>More rigorously, since  $|\lambda_1| = 1$ , we can represent it as  $\lambda_1 = e^{i\phi}$ . For an arbitrary small precision  $\epsilon$  we can choose  $N$  such that  $|N\phi| < \epsilon \pmod{2\pi}$  (which is always possible, following from Dirichlet's approximation theorem), which leads to  $\lambda_1^N = 1 + O(\epsilon)$  and  $\lambda_2^N = 1/\lambda_1^N = 1 + O(\epsilon)$ . However, this would mean that

$$\begin{pmatrix} 1 \\ r \end{pmatrix} \approx t(a_1v_1 + a_2v_2), = \begin{pmatrix} t \\ 0 \end{pmatrix}, \quad (\text{B.80})$$

leading to  $t = 1$  and  $r = 0$ , i.e., DBR being perfectly transmitting for an arbitrary large  $N$ .

The full expression for the eigenvalues and the eigenvectors are too cumbersome and not very illuminating; instead, we can expand them to the first order in  $\delta$  to get

$$\begin{aligned} \lambda_1 &= -n_r & \lambda_2 &= -1/n_r \\ v_1 &= \begin{pmatrix} -1 - i\frac{2}{n_r-1}\delta \\ 1 \end{pmatrix} & v_2 &= \begin{pmatrix} 1 - i\frac{2n_r}{n_r-1}\delta \\ 1 \end{pmatrix}. \end{aligned} \quad (\text{B.88})$$

From this, depending on the magnitude of  $n_r$ , the reflection coefficient is

$$r = \begin{cases} -1 - i\frac{2}{1-n_r}\delta, & 0 < n_r < 1 \\ 1 + i\frac{2n_r}{n_r-1}\delta, & n_r > 1, \end{cases} \quad (\text{B.89})$$

so the reflection phase (in the first order in  $\delta$ ) becomes

$$\phi = \begin{cases} \frac{2}{1-n_r}\delta, & 0 < n_r < 1 \\ \frac{2n_r}{n_r-1}\delta, & n_r > 1. \end{cases} \quad (\text{B.90})$$

We can find the corresponding penetration depth using equation (B.34):

$$\delta L = \frac{c}{2} \frac{\partial \phi}{\partial \omega} = \frac{1}{2} \frac{\partial \phi}{\partial k_0} = \frac{1}{2} \frac{d\delta}{dk_0} \frac{\partial \phi}{\partial \delta} = \frac{\lambda_0}{4} \begin{cases} \frac{n_r}{1-n_r}, & 0 < n_r < 1 \\ \frac{1}{n_r-1}, & n_r > 1. \end{cases} \quad (\text{B.91})$$

We have used the fact that the stack is almost matched, so  $\frac{d\delta}{dk_0} = n_1 d_1 \approx \lambda_0/4$ , where  $\lambda_0 = 2\pi/k_0$  is the vacuum wavelength. Note that this expression is symmetric with respect to  $n_r \rightarrow 1/n_r$  (which corresponds to switching the layers' order), that is, the penetration depth does not depend on which layer goes first.

If we account for the boundary between the first layer and the outer material with the refractive index  $n_0$ , the reflection coefficient turns into

$$r = \begin{cases} -1 - i\frac{n_0}{n_1} \frac{2}{1-n_r}\delta, & 0 < n_r < 1 \\ 1 + i\frac{n_1}{n_0} \frac{2n_r}{n_r-1}\delta, & n_r > 1, \end{cases} \quad (\text{B.92})$$

and the penetration depth becomes

$$\delta L = \frac{\lambda_0}{4} \begin{cases} \frac{n_0}{n_1} \frac{n_r}{1-n_r}, & 0 < n_r < 1 \\ \frac{n_1}{n_0} \frac{1}{n_r-1}, & n_r > 1. \end{cases} \quad (\text{B.93})$$

## B.5 One-dimensional propagation of acoustic waves

Here we will derive equations governing propagation of 1D longitudinal acoustic waves, and then introduce a transfer matrix formalism (very similar to the one in section B.3) for these waves. After that, we use it to derive the acoustic reflection coefficient for a material boundary.

### B.5.1 Wave equation

We will describe a wave by its displacement profile  $\chi(x, t)$ . The first equation governing the wave motion is essentially Newton's second law applied to a tiny slab of material between  $x + \chi(x)$  and  $x + dx + \chi(x + dx)$ . The total mass of this slab is  $dm = \rho_0 A dx$ , where  $\rho_0$  is the density of a non-strained material and  $A$  is the cross-sectional area of the wave. The acceleration of the COM of this slab is (up to first order in  $dx$ ) the second time derivative of the wave displacement:  $a(x) = \frac{\partial^2 \chi}{\partial t^2}$ . Finally, the net force acting on the slab can be calculated as  $dF = (p(x) - p(x + dx))A$ , where  $p(x, t)$  is the (longitudinal) stress inside the material. This lets us write Newton's second law as

$$\rho_0 A \frac{\partial^2 \chi}{\partial t^2} dx = a(x) dm = dF = (p(x) - p(x + dx))A, \quad (\text{B.94})$$

which yields a partial differential equation

$$\rho_0 \frac{\partial^2 \chi}{\partial t^2} = -\frac{\partial p}{\partial x}. \quad (\text{B.95})$$

The second equation relates the pressure profile  $p(x)$  to the wave displacement  $\chi(x)$ , and it comes from the material properties. We assume the standard linear isotropic Young's law

$$p(x) = E\epsilon(x) = E \left( -\frac{\partial \chi}{\partial x} \right), \quad (\text{B.96})$$

where  $\epsilon(x)$  is the compressional strain and  $E$  is the material's Young's modulus. Combining the equations (B.95) and (B.96) we obtain the wave equation

$$\frac{\partial^2 \chi}{\partial t^2} = \frac{E}{\rho_0} \frac{\partial^2 \chi}{\partial x^2} \equiv c_s^2 \frac{\partial^2 \chi}{\partial x^2}, \quad (\text{B.97})$$

where  $c_s \equiv \sqrt{E/\rho_0}$  is the sound velocity in the material.

### B.5.2 Energy density and energy flux

The mechanical energy of the wave consists of two parts: kinetic and potential. The kinetic energy of a slice of material between  $x + \chi(x)$  and  $x + dx + \chi(x + dx)$  with a velocity  $v(x) = \frac{\partial \chi}{\partial t}$  is

$$dK = \frac{dm}{2} v^2(x) = \frac{\rho_0}{2} \left( \frac{\partial \chi}{\partial t} \right)^2 Adx. \quad (\text{B.98})$$

The potential energy can be calculated using the strain  $\epsilon(x)$  as

$$dP = \frac{E}{2} \epsilon^2(x) dV = \frac{E}{2} \left( \frac{\partial \chi}{\partial x} \right)^2 Adx. \quad (\text{B.99})$$

Thus, the total energy density for a unit cross-sectional area is

$$u_s = \frac{dK + dP}{Adx} = \frac{\rho_0}{2} \left( \frac{\partial \chi}{\partial t} \right)^2 + \frac{E}{2} \left( \frac{\partial \chi}{\partial x} \right)^2. \quad (\text{B.100})$$

If we examine the time derivative of the energy density, we obtain

$$\begin{aligned} \frac{\partial u_s}{\partial t} &= \rho_0 \frac{\partial \chi}{\partial t} \frac{\partial^2 \chi}{\partial t^2} + E \frac{\partial \chi}{\partial x} \frac{\partial^2 \chi}{\partial x \partial t} = \rho_0 c_s^2 \frac{\partial^2 \chi}{\partial x^2} \frac{\partial^2 \chi}{\partial t^2} + E \frac{\partial \chi}{\partial x} \frac{\partial^2 \chi}{\partial x \partial t} \\ &= \frac{\partial}{\partial x} \left( E \frac{\partial \chi}{\partial x} \frac{\partial \chi}{\partial t} \right) = -\frac{\partial p_s}{\partial x}, \end{aligned} \quad (\text{B.101})$$

where we have defined  $p_s = -E \frac{\partial \chi}{\partial x} \frac{\partial \chi}{\partial t}$ . This equation reminds one of the general form of the 1D continuity equation  $\frac{\partial \rho}{\partial t} = -\frac{\partial j}{\partial x}$ , where  $\rho$  and  $j$  are correspondingly the density and flux of some conserved quantity. From this correspondence we can identify  $p_s$  as the energy flux (per unit cross-sectional area) carried by the acoustic waves.

A right-moving wave with frequency  $\omega$  and amplitude  $\chi_0$  can be expressed as  $\chi(x, t) = \chi_0 \sin(kx - \omega t + \phi_0)$ , where  $k = \omega/c_s$  is the wave-vector and  $\phi_0$  is an overall phase. The instantaneous energy density for this wave is

$$\begin{aligned} u_s(x, t) &= \frac{\chi_0^2}{2} (\rho_0 \omega^2 + Ek^2) \sin^2(kx - \omega t + \phi_0) \\ &= \rho_0 \omega^2 \chi_0^2 \sin^2(kx - \omega t + \phi_0), \end{aligned} \quad (\text{B.102})$$

and after averaging over the wave period it becomes

$$\overline{u_s}(x) = \frac{\rho_0 \omega^2}{2} \chi_0^2. \quad (\text{B.103})$$

We can write similar expressions for the energy flux:

$$p_s(x, t) = \chi_0^2 E k \omega \cos^2(kx - \omega t + \phi_0) = \mathcal{Z} \omega^2 \chi_0^2 \cos^2(kx - \omega t + \phi_0) \quad (\text{B.104})$$

$$\overline{p_s}(x) = \frac{\mathcal{Z} \omega^2}{2} \chi_0^2, \quad (\text{B.105})$$

where

$$\mathcal{Z} = \frac{E}{c_s} = \sqrt{E \rho_0} = c_s \rho_0 \quad (\text{B.106})$$

is the acoustic impedance.

### B.5.3 Boundary conditions

An interface between two materials should satisfy two conditions. First, the wave displacement should be the same:

$$\chi^{(\ell)} = \chi^{(r)}, \quad (\text{B.107})$$

where  $\chi_{\ell, r}$  are the displacement profiles on the left and on the right side of the boundary respectively. Second, we assume that the boundary does not produce any additional stress, so the pressure on both sides should also be the same:

$$-E^{(\ell)} \frac{\partial \chi^{(\ell)}}{\partial x} = p^{(\ell)} = p^{(r)} = -E^{(r)} \frac{\partial \chi^{(r)}}{\partial x}. \quad (\text{B.108})$$

### B.5.4 Transfer matrix description for sound

Given the wave equation and the boundary conditions, we can apply exactly the same transfer matrix approach that we used for light (section B.3) to the sound waves. Similarly to the EM waves definition (B.35), we define a sound transfer matrix as describing a relation between the sound amplitudes  $\chi$  on the left and on the right side of an object:

$$\begin{pmatrix} \chi_{\rightarrow}^{(r)} \\ \chi_{\leftarrow}^{(r)} \end{pmatrix} = M \cdot \begin{pmatrix} \chi_{\rightarrow}^{(\ell)} \\ \chi_{\leftarrow}^{(\ell)} \end{pmatrix}. \quad (\text{B.109})$$

Given this definition, the propagation matrix looks exactly the same as for the light (B.36):

$$M^{(p)}(k, d) = \begin{pmatrix} e^{ikd} & 0 \\ 0 & e^{-ikd} \end{pmatrix}. \quad (\text{B.110})$$

The only difference is the relation between the wave-vector and the frequency  $k = \omega/c_s$ .

The boundary transfer matrix can be calculated using the boundary conditions (B.107), (B.108), and it is slightly different than (B.43)

$$M^{(b)}(\mathcal{Z}^{(\text{rel})}) = \frac{1}{2\mathcal{Z}^{(\text{rel})}} \begin{pmatrix} 1 + \mathcal{Z}^{(\text{rel})} & 1 - \mathcal{Z}^{(\text{rel})} \\ 1 - \mathcal{Z}^{(\text{rel})} & 1 + \mathcal{Z}^{(\text{rel})} \end{pmatrix}, \quad (\text{B.111})$$

with  $\mathcal{Z}^{(\text{rel})} = \mathcal{Z}^{(r)}/\mathcal{Z}^{(\ell)}$ , where  $\mathcal{Z}^{(r, \ell)}$  are the acoustic impedances of the two media.<sup>c)</sup>

<sup>c)</sup>To regain the same expression as (B.43) we would need to define transfer matrices in terms of pressure  $p(x, t)$  instead of displacement  $\chi(x, t)$ .

Now we can use relations (B.55) and (B.56) to calculate the amplitude transmissions and reflection coefficients for a material boundary:

$$t^{(b)} = \frac{2}{\mathcal{Z}^{(\text{rel})} + 1} \quad (\text{B.112})$$

$$r^{(b)} = \frac{\mathcal{Z}^{(\text{rel})} - 1}{\mathcal{Z}^{(\text{rel})} + 1}. \quad (\text{B.113})$$

Note that  $|t^{(b)}|^2 + |r^{(b)}|^2 \neq 1$ , since the reflected and transmitted waves travel in different media. To accommodate for that, we can define the power reflection and transmission coefficients which take the impedance difference into account:

$$T^{(b)} = |t^{(b)}|^2 \frac{\mathcal{Z}^{(r)}}{\mathcal{Z}^{(\ell)}} = \frac{4\mathcal{Z}^{(\text{rel})}}{(\mathcal{Z}^{(\text{rel})} + 1)^2} \quad (\text{B.114})$$

$$R^{(b)} = |r^{(b)}|^2 = \frac{(\mathcal{Z}^{(\text{rel})} - 1)^2}{(\mathcal{Z}^{(\text{rel})} + 1)^2}. \quad (\text{B.115})$$

These coefficients describe the powers in respectively the transmitted and the reflected waves relative to the incident power, and with these it is easy to show that the energy is conserved:  $T^{(b)} + R^{(b)} = 1$ .

### B.5.5 Interaction with a movable boundary

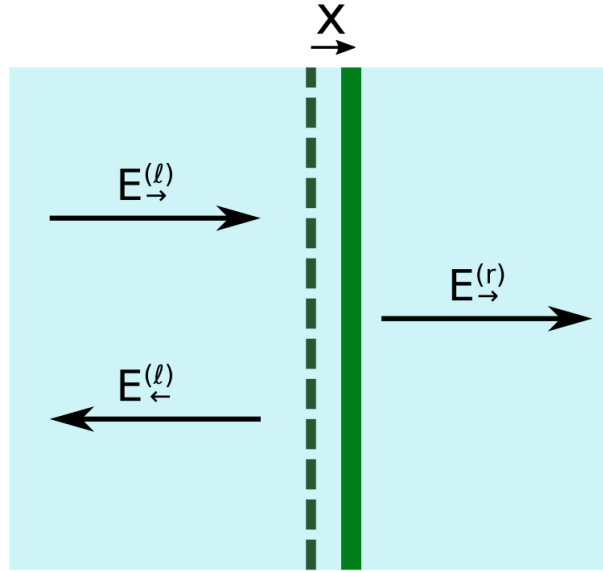


Figure B.3: Schematic an acoustic wave reflecting off a movable boundary.

Now let us consider a different kind of boundary, which can potentially be moving (e.g., a suspended plate inside a liquid). We will assume it to be thin enough compared to the sound wavelength (inside the boundary material), so we can approximate it as an infinitely thin layer. We will denote its displacement from the equilibrium position as  $x$ .

The boundary conditions can be written in the same way as in subsection B.5.3. First, the wave displacement is still the same on both sides; furthermore, the layer displacement is also the same:

$$\chi^{(\ell)} = \chi^{(r)} = x. \quad (\text{B.116})$$

Second, we need to connect the pressures on the two sides. Since the boundary can exert force, these pressures are no longer equal. However, we will assume that this pressure differential is proportional to the boundary displacement with some proportionality coefficient  $\tilde{K}$ :  $\Delta p = p^{(\ell)} - p^{(r)} = \tilde{K}x$ . For example, if the boundary is a plate on a spring with a spring constant per unit area  $k_S$ , we have simply  $\tilde{K} = k_S$ , and if it is a free mass with a surface mass density  $\sigma$ , we have  $\tilde{K} = -\sigma\omega^2$ . Keeping the proportionality coefficient general, we can write

$$-E \frac{\partial \chi^{(\ell)}}{\partial x} + E \frac{\partial \chi^{(r)}}{\partial x} = p^{(\ell)} - p^{(r)} = \tilde{K}x, \quad (\text{B.117})$$

where we assume that the media is the same on both sides of the boundary, so that  $E^{(\ell)} = E^{(r)} = E$ . In terms of incident and reflected wave amplitudes, boundary conditions (B.116) and (B.117) can be rewritten as

$$\chi_{\rightarrow}^{(\ell)} + \chi_{\leftarrow}^{(\ell)} = \chi_{\rightarrow}^{(r)} + \chi_{\leftarrow}^{(r)} \quad (\text{B.118})$$

$$ikE(-\chi_{\rightarrow}^{(\ell)} + \chi_{\leftarrow}^{(\ell)} + \chi_{\rightarrow}^{(r)} - \chi_{\leftarrow}^{(r)}) = \tilde{K}(\chi_{\rightarrow}^{(\ell)} + \chi_{\leftarrow}^{(\ell)}). \quad (\text{B.119})$$

This results in a transfer matrix

$$M^{(\text{mb})}(\tilde{K}) = \begin{pmatrix} 1 + i\xi & i\xi \\ -i\xi & 1 - i\xi \end{pmatrix}, \quad (\text{B.120})$$

where  $\xi = -\tilde{K}/(2kE) = -\tilde{K}/(2\omega\mathcal{Z})$  is the “strength” of the barrier. Note the similarity to the transfer matrix of a dielectric layer (equation (B.44)). It allows us to easily calculate the power transmission coefficient using equation (B.51):

$$T^{(\text{mb})} = \frac{1}{1 + \xi^2} = \frac{1}{1 + \left(\tilde{K}/(2\omega\mathcal{Z})\right)^2}. \quad (\text{B.121})$$

# Appendix C

## General optics derivations

### C.1 Optical detection description

In this section I discuss basics of the photocurrent statistic and the heterodyne measurements. These derivations are used in calculation of the sideband signatures in the photocurrent power spectral density (PSD) in section 7.2, and in the laser noise measurement analysis (section C.2).

I start by quickly introducing the normal ordering approach to the photocurrent correlators, and then I use it to derive general equations for the power spectral density (PSD) and the correlator of the photocurrent.

#### C.1.1 General photocurrent expression

Standard photodetection theory [179] states that, given an optical field  $\hat{a}_{\text{det}}$  landing on the photodetector, the (time-dependent) autocorrelator of the photocurrent  $i(t)$  can be calculated as

$$\begin{aligned} C_{ii}(t, \tau) &\equiv \langle i(t + \tau/2)i(t - \tau/2) \rangle \\ &= G^2 \left\langle : \hat{a}_{\text{det}}^\dagger(t + \tau/2) \hat{a}_{\text{det}}(t + \tau/2) \hat{a}_{\text{det}}^\dagger(t - \tau/2) \hat{a}_{\text{det}}(t - \tau/2) : \right\rangle \\ &\quad + G^2 \left\langle \hat{a}_{\text{det}}^\dagger(t) \hat{a}_{\text{det}}(t) \right\rangle \delta(\tau), \end{aligned} \tag{C.1}$$

where  $G$  is the photodetector gain (for an ideal unamplified photodiode this gain is equal to  $e$ , the electron charge) and  $::$  denotes normal and time ordering. The first term in the expression (C.1) corresponds to the “classical” part of the autocorrelator, arising from the time-varying field amplitude. The second term arises from the autocorrelator of the individual photon pulses (which are described by the  $\delta$ -function in the assumption of infinite photodetector bandwidth), and thus represents the shot noise. Note that since  $i(t)$  is simply a photocurrent, we take it to be classical and real, so  $C_{ii}(t, \tau)$  is real and symmetric in  $\tau$  (see appendix A.2.3).

In the same description the mean photocurrent is simply proportional to the average photon flux:

$$\langle i \rangle(t) = G \left\langle \hat{a}_{\text{det}}^\dagger(t) \hat{a}_{\text{det}}(t) \right\rangle. \tag{C.2}$$

#### C.1.2 Heterodyne measurements and photocurrent PSD

Now we consider heterodyne detection. Let us denote the signal optical field as  $\hat{a}_{\text{sig}}(t)$  and the optical local oscillator (OLO) as  $a_{\text{OLO}} e^{-i\omega_{\text{OLO}} t}$ , where  $a_{\text{OLO}}$  is its amplitude and  $\omega_{\text{OLO}}$  is its frequency. This makes the field incident on the photodiode (after combining with the OLO)  $\hat{a}_{\text{det}} = a_{\text{OLO}} e^{-i\omega_{\text{OLO}} t} + \hat{a}_{\text{sig}}(t)$ . One should keep in mind that in the frame of the signal field we might have  $\omega_{\text{OLO}} < 0$ , since this results in an intuitive picture of the photocurrent spectrum being just a shifted copy of the optical spectrum; the opposite case where the OLO frequency is higher than the sidebands frequency is less convenient, since it leads to the photocurrent spectrum being flipped compared to the optical one.

If we substitute this expression for  $\hat{a}_{\text{det}}$  into equation (C.1) and expand up to second order in  $\hat{a}_{\text{sig}}$  (keeping in mind that the first order terms average to zero), we get

$$\begin{aligned}
C_{ii}(t, \tau) \approx & G^2 |a_{\text{OLO}}|^4 + G^2 |a_{\text{OLO}}|^2 \left( \left\langle \hat{a}_{\text{sig}}^\dagger(t + \tau/2) \hat{a}_{\text{sig}}(t + \tau/2) \right\rangle + \left\langle \hat{a}_{\text{sig}}^\dagger(t - \tau/2) \hat{a}_{\text{sig}}(t - \tau/2) \right\rangle \right) \\
& + G^2 |a_{\text{OLO}}|^2 \left( e^{-i\omega_{\text{OLO}}\tau} \left\langle \hat{a}_{\text{sig}}^\dagger(t + \tau/2) \hat{a}_{\text{sig}}(t - \tau/2) \right\rangle + e^{i\omega_{\text{OLO}}\tau} \left\langle \hat{a}_{\text{sig}}^\dagger(t - \tau/2) \hat{a}_{\text{sig}}(t + \tau/2) \right\rangle \right) \\
& + G^2 (a_{\text{OLO}})^2 e^{-2i\omega_{\text{OLO}}t} \left\langle : \hat{a}_{\text{sig}}^\dagger(t + \tau/2) \hat{a}_{\text{sig}}^\dagger(t - \tau/2) : \right\rangle \\
& + G^2 (a_{\text{OLO}}^*)^2 e^{2i\omega_{\text{OLO}}t} \left\langle : \hat{a}_{\text{sig}}(t + \tau/2) \hat{a}_{\text{sig}}(t - \tau/2) : \right\rangle \\
& + G^2 |a_{\text{OLO}}|^2 \delta(\tau).
\end{aligned} \tag{C.3}$$

The first line in equation (C.3) is the DC component of the correlator, which is not relevant to the optical spectrum, and can be ignored. The next three lines reflect beating of the outgoing cavity field with the LO. Finally, the last line represents the unavoidable detector shot noise.

First, let us consider the time-averaged PSD of the photocurrent, which is defined using the generic PSD expression (A.3) from appendix A.1:

$$S_{ii}[\omega] \equiv \overline{S_{ii}(t, \omega)} = \int_{-\infty}^{+\infty} \overline{C_{ii}(t, \tau)} e^{i\omega\tau} d\tau, \tag{C.4}$$

where  $\overline{S_{ii}(t, \omega)}$  and  $\overline{C_{ii}(t, \tau)}$  denote that these quantities are averaged over the central time  $t$ . We assume that the correlators of the input field are stationary (or at least do not have components at  $2\omega_{\text{OLO}}$ ), and that the integration time is long enough that we can set  $e^{2i\omega_{\text{OLO}}t} = 0$ . In this case, only the second and the last line in the correlator contribute to the PSD above, which can be re-expressed as

$$S_{ii}[\omega] = G^2 |a_{\text{OLO}}|^2 \left( S_{\hat{a}_{\text{sig}}^\dagger, \hat{a}_{\text{sig}}}[\omega - \omega_{\text{OLO}}] + S_{\hat{a}_{\text{sig}}^\dagger, \hat{a}_{\text{sig}}}[-\omega - \omega_{\text{OLO}}] + 1 \right), \tag{C.5}$$

where the spectrum of the outgoing field is calculated in the usual way:

$$S_{\hat{a}_{\text{sig}}^\dagger, \hat{a}_{\text{sig}}}[\omega] = \left\langle \hat{a}_{\text{sig}}^\dagger[\omega] \hat{a}_{\text{sig}}[-\omega] \right\rangle. \tag{C.6}$$

## C.2 Laser noise

In this section I will consider a general description of classical laser noise, its behavior under linear transformations (such as cavity filtering, delay, or self-interference) and the way to measure it using quadratic detectors such as photodiodes. These results are later used in the description of the laser noise measurement procedure appendix D.4.

### C.2.1 Definitions

We start with a generic expression for a single laser tone with amplitude  $a_L$  and frequency  $\omega_L$ :  $a(t) = a_L e^{-i\omega_L t}$ . Next, we add classical noise which in the frame rotating at  $\omega_L$  is represented by a complex random variable  $\zeta(t)$ :

$$a(t) = (a_L + \zeta(t)) e^{-i\omega_L t}. \tag{C.7}$$

Many sources produce noise which is proportional to the total power, and any subsequent attenuation affects the main tone and the classical noise in the same way. Thus, it is more convenient to describe the noise by its amplitude relative to the main tone  $\zeta_{\text{rel}}(t) = \zeta(t)/a_L$ . Such description also allows us to easily separate the noise into an amplitude quadrature  $\zeta_x$  and a phase quadrature  $\zeta_y$  by setting  $\zeta_{\text{rel}}(t) = \zeta_x(t) + i\zeta_y(t)$ , which produces the expression for the light amplitude

$$a(t) = a_L (1 + \zeta_x(t) + i\zeta_y(t)) e^{-i\omega_L t}. \tag{C.8}$$

Each of the noise variables  $\zeta_x$ ,  $\zeta_y$  represents only one noise quadrature, so both of them are real.

Now we need to make some simplifying assumption about the noise. First, let us assume that both amplitude and phase noises are random, stationary, Gaussian and have zero mean. This means that they are fully characterized by their second-order correlation functions

$$\langle \zeta_x(t)\zeta_x(t') \rangle \equiv C_{xx}(t-t') \quad (\text{C.9})$$

$$\langle \zeta_x(t)\zeta_y(t') \rangle \equiv C_{xy}(t-t') \quad (\text{C.10})$$

$$\langle \zeta_y(t)\zeta_y(t') \rangle \equiv C_{yy}(t-t'). \quad (\text{C.11})$$

Since  $\zeta_x$  and  $\zeta_y$  are real variables, all of those correlators also end up being real; additionally,  $C_{xx}$  and  $C_{yy}$  are symmetric in time. Being classical variables,  $\zeta_x$  and  $\zeta_y$  also obey Cauchy-Schwartz inequality:  $|C_{xy}(\tau)|^2 \leq C_{xx}(\tau)C_{yy}(\tau)$ .

Second, we assume that the total noise power is small compared to the signal power:  $C_{xx}(0) \equiv \langle \zeta_x^2 \rangle \ll 1$  and  $C_{yy}(0) \equiv \langle \zeta_y^2 \rangle \ll 1$ . This will later let us drop quartic terms when calculating power spectral density of a quadratic detector output.<sup>a)</sup>

Finally, we can move into the Fourier domain (see appendix A.2) by defining (noise) Fourier transforms  $\zeta_x[\omega]$  and  $\zeta_y[\omega]$ , and corresponding power spectral densities and cross-correlators

$$\langle \zeta_x[\omega]\zeta_x[-\omega] \rangle = S_{xx}[\omega] \quad (\text{C.12})$$

$$\langle \zeta_x[\omega]\zeta_y[-\omega] \rangle = S_{xy}[\omega] \quad (\text{C.13})$$

$$\langle \zeta_y[\omega]\zeta_y[-\omega] \rangle = S_{yy}[\omega]. \quad (\text{C.14})$$

Since  $C_{xx}$  and  $C_{yy}$  are real and symmetric, so are the power spectral densities  $S_{xx}$  and  $S_{yy}$ . The cross-correlator  $S_{xy}$  obeys a weaker relation  $S_{xy}[-\omega] = (S_{xy}[\omega])^*$ , and the flipped-order correlator can be expressed as

$$S_{yx}[\omega] \equiv \langle \zeta_y[\omega]\zeta_x[-\omega] \rangle = S_{xy}[-\omega] = (S_{xy}[\omega])^*. \quad (\text{C.15})$$

## C.2.2 Quadratic detection

Now, let us consider detection of such a noisy laser by an ideal photodiode, for which we start by applying expressions (C.1) and (C.2) to a classical field with an amplitude  $a(t)$ . This results in a mean photocurrent which is simply proportional to a square of the amplitude:

$$\langle i \rangle = G \langle |a(t)|^2 \rangle, \quad (\text{C.16})$$

and a photocurrent correlator expressed as

$$C_{ii}(t-t') \equiv \langle i(t)i(t') \rangle = G^2 \langle |a(t)|^2 |a(t')|^2 \rangle + G^2 \langle |a(t)|^2 \rangle \delta(t-t'), \quad (\text{C.17})$$

where the second  $\delta$ -correlated term describes the shot noise of the photodetector. Both of the expressions above (barring the shot noise term) can also be obtained by simply postulating that the photocurrent is proportional to the photon flux  $i(t) = G|a(t)|^2$ .

We can simplify expressions (C.16) and (C.17) if the laser amplitude can be expressed as  $a(t) = a_L(1 + \zeta_{\text{rel}}(t))e^{-i\omega_L t}$  (where  $a_L$  and  $\zeta_{\text{rel}}(t)$  are not necessarily equal to the non-transformed laser amplitude and noise in the expression (C.7)) and if we assume small laser noise:

$$\langle i \rangle = G \langle |a_L(1 + \zeta(t))|^2 \rangle = G|a_L|^2 + G|a_L|^2 \langle \zeta^*(t)\zeta(t) \rangle \approx G|a_L|^2 \quad (\text{C.18})$$

$$\begin{aligned} C_{ii}(t-t') &= G^2 \langle |a_L(1 + \zeta(t))|^2 |a_L(1 + \zeta(t'))|^2 \rangle + G^2 \langle |a_L(t)|^2 \rangle \delta(t-t') \\ &\approx G^2 |a_L|^4 + G^2 |a_L|^4 (\langle \zeta^*(t)\zeta(t') \rangle + \text{c.c.}) + G^2 |a_L|^4 (\langle \zeta^*(t)\zeta^*(t') \rangle + \text{c.c.}) \\ &\quad + G^2 |a_L|^2 \delta(t-t') \end{aligned} \quad (\text{C.19})$$

<sup>a)</sup>There is an additional assumption required to justify writing the laser field as a perfect wave in equation (C.7): the laser linewidth should be small compared to other frequency scales. This implies that, e.g., the propagation delay difference  $\tau_d$  in subsection C.2.6 is much smaller than the laser coherence time, or that the cavity linewidth in C.2.7 is much larger than the intrinsic laser linewidth.

Since the second expression is at most quadratic in  $\zeta$ , it can be easily recast into the corresponding expression for the power spectral density of the photocurrent:

$$S_{ii}[\omega] = G^2|a_L|^4 (\langle \zeta^*[\omega]\zeta[-\omega] \rangle + \langle \zeta[\omega]\zeta^*[-\omega] \rangle + \langle \zeta[\omega]\zeta[-\omega] \rangle + \langle \zeta^*[\omega]\zeta^*[-\omega] \rangle) + G^2|a_L|^2. \quad (\text{C.20})$$

### C.2.3 Direct detection of a noisy laser

For the non-transformed laser field (C.8) the mean photocurrent is

$$\langle i \rangle = G|a_L|^2, \quad (\text{C.21})$$

and the noise correlators are

$$\begin{aligned} \langle \zeta^*[\omega]\zeta[-\omega] \rangle &= \langle (\zeta_x[\omega] - i\zeta_y[\omega])(\zeta_x[-\omega] + i\zeta_y[-\omega]) \rangle \\ &= S_{xx}[\omega] + S_{yy}[\omega] - 2\text{Im}\{S_{xy}[\omega]\} \end{aligned} \quad (\text{C.22})$$

$$\langle \zeta[\omega]\zeta^*[-\omega] \rangle = S_{xx}[\omega] + S_{yy}[\omega] + 2\text{Im}\{S_{xy}[\omega]\} \quad (\text{C.23})$$

$$\begin{aligned} \langle \zeta[\omega]\zeta[-\omega] \rangle &= \langle (\zeta_x[\omega] + i\zeta_y[\omega])(\zeta_x[-\omega] + i\zeta_y[-\omega]) \rangle \\ &= S_{xx}[\omega] - S_{yy}[\omega] + 2i\text{Re}\{S_{xy}[\omega]\} \end{aligned} \quad (\text{C.24})$$

$$\langle \zeta^*[\omega]\zeta^*[-\omega] \rangle = S_{xx}[\omega] - S_{yy}[\omega] - 2i\text{Re}\{S_{xy}[\omega]\}, \quad (\text{C.25})$$

which results in the photocurrent PSD

$$\begin{aligned} S_{ii}[\omega] &= G^2|a_L|^4 (2S_{xx}[\omega] + 2S_{yy}[\omega]) + G^2|a_L|^4 (2S_{xx}[\omega] - 2S_{yy}[\omega]) + G^2|a_L|^2 \\ &= G^2|a_L|^2 (4|a_L|^2 S_{xx}[\omega] + 1). \end{aligned} \quad (\text{C.26})$$

As one could expect, only the amplitude noise correlator shows up in the photocurrent power spectral density.

Given expression (C.26), we define the laser to be “amplitude shot noise limited” at a frequency  $\omega$  if the classical noise is equal to the shot noise in the photocurrent, i.e., when  $|a_L|^2 S_{xx}[\omega] = 1/4$ . Similarly, the laser is said to be “phase shot noise limited” if  $|a_L|^2 S_{yy}[\omega] = 1/4$ . Both of these criteria can also be described in terms of a “shot noise limited power”  $P_{L,SN}^{(xx)} = \hbar\omega_L/(4S_{xx}[\omega])$  (and the same for  $P_{L,SN}^{(yy)}$ ), which is the power for which the classical laser noise equals the shot noise. The higher the relative classical noise  $S_{xx}$ ,  $S_{yy}$ , the lower the shot noise limited power, i.e., the more attenuated the laser has to be in order for the classical noise to be equal to the shot noise.

### C.2.4 Effects of linear transformations

Now we consider how a linear transformation of the laser field affects the results (C.21), (C.26). We characterize the linear transformation by its Fourier transfer function  $K[\omega]$ , which multiplies both the main laser tone and the noise. This changes the laser amplitude to  $a_L K[0]$  and transforms the noise into

$$\zeta_K[\omega] = K[\omega]\zeta[\omega] \quad (\text{C.27})$$

$$\zeta_K^*[\omega] = (K[-\omega])^* \zeta^*[\omega] \quad (\text{C.28})$$

(note the minus sign in the second line, which comes from our convention for the Fourier transform conjugating), which turns the noise correlators (C.22)-(C.25) into

$$\begin{aligned}\langle \zeta_K^*[\omega] \zeta_K[-\omega] \rangle &= |K[-\omega]|^2 \langle \zeta^*[\omega] \zeta[-\omega] \rangle \\ &= |K[-\omega]|^2 (S_{xx}[\omega] + S_{yy}[\omega] - 2\text{Im} \{S_{xy}[\omega]\})\end{aligned}\quad (\text{C.29})$$

$$\begin{aligned}\langle \zeta_K[\omega] \zeta_K^*[-\omega] \rangle &= |K[\omega]|^2 \langle \zeta[\omega] \zeta^*[-\omega] \rangle \\ &= |K[\omega]|^2 (S_{xx}[\omega] + S_{yy}[\omega] + 2\text{Im} \{S_{xy}[\omega]\})\end{aligned}\quad (\text{C.30})$$

$$\begin{aligned}\langle \zeta_K[\omega] \zeta_K[-\omega] \rangle &= (K[\omega]K[-\omega]) \langle \zeta[\omega] \zeta[-\omega] \rangle \\ &= (K[\omega]K[-\omega]) (S_{xx}[\omega] - S_{yy}[\omega] + 2i\text{Re} \{S_{xy}[\omega]\})\end{aligned}\quad (\text{C.31})$$

$$\begin{aligned}\langle \zeta_K^*[\omega] \zeta_K^*[-\omega] \rangle &= (K[\omega]K[-\omega])^* \langle \zeta^*[\omega] \zeta^*[-\omega] \rangle \\ &= (K[\omega]K[-\omega])^* (S_{xx}[\omega] - S_{yy}[\omega] - 2i\text{Re} \{S_{xy}[\omega]\}).\end{aligned}\quad (\text{C.32})$$

These transformations, in turn, lead to new expressions for the mean photocurrent

$$\langle i \rangle = G|K[0]|^2|a_L|^2 \quad (\text{C.33})$$

and for its power spectral density

$$\begin{aligned}S_{ii}[\omega] &= G^2|a_L|^4 \{ |K[0]|^2 (|K[\omega]|^2 + |K[-\omega]|^2) (S_{xx}[\omega] + S_{yy}[\omega]) \\ &\quad - 2|K[0]|^2 (|K[\omega]|^2 - |K[-\omega]|^2) \text{Im} \{S_{xy}[\omega]\} \\ &\quad + ((K[0])^2 (K[\omega]K[-\omega])^* + \text{c.c.}) (S_{xx}[\omega] - S_{yy}[\omega]) \\ &\quad - 2i ((K[0])^2 (K[\omega]K[-\omega])^* - \text{c.c.}) \text{Re} \{S_{xy}[\omega]\} \} \\ &\quad + G^2|a_L|^2|K[0]|^2.\end{aligned}\quad (\text{C.34})$$

By introducing a “beatnote” transfer function  $\tilde{K}[\omega] = K[\omega](K[0])^*$  we can simplify the power spectral density:

$$\begin{aligned}S_{ii}[\omega] &= G^2|a_L|^4 \left\{ \left| \tilde{K}[\omega] + (\tilde{K}[-\omega])^* \right|^2 S_{xx}[\omega] \right. \\ &\quad \left. + \left| \tilde{K}[\omega] - (\tilde{K}[-\omega])^* \right|^2 S_{yy}[\omega] \right. \\ &\quad \left. + \left( (\tilde{K}[\omega] + (\tilde{K}[-\omega])^*) \left( (\tilde{K}[\omega])^* - \tilde{K}[-\omega] \right) S_{xy}[\omega] + \text{c.c.} \right) \right\} \\ &\quad + G^2|a_L|^2|K[0]|^2.\end{aligned}\quad (\text{C.35})$$

It can be seen that, in general, all the noise correlators contribute to the photocurrent PSD, so it can be used to measure all the noise properties (given an appropriate transformation  $K[\omega]$ ).

One special case is the transformations whose “beatnote” transfer function is real in the time domain:  $\text{Im} \{ \tilde{K}(\tau) \} = 0$ . Examples of such transformation are: constant phase shift ( $\tilde{K}(\tau) = \delta(\tau)$ ), time delay ( $\tilde{K}(\tau) = \delta(\tau - \tau_0)$ ) or attenuation ( $\tilde{K}(\tau) = \alpha^2$ , where  $\alpha$  is the real attenuation factor). In that case the Fourier transfer function satisfies the condition  $\tilde{K}[-\omega] = (\tilde{K}[\omega])^*$ , and the expression (C.35) is greatly simplified:

$$S_{ii}[\omega] = G^2|a_L|^2|K[0]|^2 (4|a_L|^2|K[\omega]|^2 S_{xx}[\omega] + 1). \quad (\text{C.36})$$

As in the direct detection case (C.26), the photocurrent PSD reveals only the properties of the amplitude noise.

### C.2.5 Power dependence

It is useful to inspect how the photocurrent power spectral density changes if the laser is attenuated, for which we consider a simple case of frequency-independent transformation  $K[\omega] = \alpha$ . Since this transformation clearly satisfies the criterion  $K[-\omega] = (K[\omega])^*$ , the resulting PSD can be found using expression (C.36):

$$S_{ii}[\omega] = G^2\alpha^2|a_L|^2 (4\alpha^2|a_L|^2 S_{xx}[\omega] + 1). \quad (\text{C.37})$$

At the same time, the mean photocurrent (C.35) is simply proportional to  $\alpha^2$ :  $\langle i \rangle = G\alpha^2|a_L|^2$ . Thus, the shot noise contribution to the PSD is proportional to the mean current ( $\alpha^2$ ), while the classical noise contribution is proportional to the square of the current (i.e.,  $\alpha^4$ ). This provides a simple practical way to separate the two noise contributions by varying the power landing on the photodetector, as described in appendix D.4.1.

### C.2.6 Delay line phase noise measurement

Now we can consider the laser noise measurements using an optical delay line. The core of the measurement setup is a Mach-Zehnder interferometer with an optical delay line in one arm, as shown in Figure D.8. To describe the interferometer, let us denote the first beam-splitter ratio as  $\alpha_1 : \beta_1$ , the second beam-splitter ratio as  $\alpha_2 : \beta_2$ , the time delay as  $\tau_d$  and the phase difference between the two arms (at the main tone frequency) as  $\delta\phi$ .

The light traveling in the first arm of the interferometer acquires a total attenuation  $\alpha = \alpha_1\alpha_2$ . The light in the second arm similarly experiences attenuation by a factor of  $\beta = \beta_1\beta_2$ , but in addition it acquires a phase difference factor  $e^{-i\delta\phi}$  and a time delay, which manifests as a frequency-dependent phase shift  $e^{-i\omega\tau_d}$ . After recombining, the total transfer function of the interferometer can be expressed as

$$K_d[\omega] = \alpha + \beta e^{-i\delta\phi} e^{-i\omega\tau_d}, \quad (\text{C.38})$$

which leads to the beatnote transfer function

$$\tilde{K}_d[\omega] = \alpha^2 + \beta^2 e^{-i\omega\tau_d} + \alpha\beta(e^{-i\delta\phi - i\omega\tau_d} + e^{i\delta\phi}). \quad (\text{C.39})$$

The output of the interferometer then lands on a photodiode, producing a mean photocurrent

$$\langle i \rangle = G^2|a_L|^2|\alpha + \beta e^{-i\delta\phi}|^2 = G^2|a_L|^2(\alpha^2 + 2\alpha\beta \cos \delta\phi + \beta^2). \quad (\text{C.40})$$

The power spectral density can be found from expression (C.35):

$$\begin{aligned} S_{ii}[\omega] &= G^2|a_L|^4 \{ 4(\alpha^2(\alpha + \beta \cos \delta\phi)^2 + \beta^2(\beta + \alpha \cos \delta\phi)^2) S_{xx}[\omega] \\ &\quad + 8\alpha\beta(\alpha + \beta \cos \delta\phi)(\beta + \alpha \cos \delta\phi) \cos(\omega\tau_d) S_{xx}[\omega] \\ &\quad + 8(\alpha\beta \sin \delta\phi)^2(1 - \cos(\omega\tau_d)) S_{yy}[\omega] \\ &\quad + 4\text{Re} \{ i\alpha\beta \sin \delta\phi(\alpha(\alpha + \beta \cos \delta\phi) + \beta(\beta + \alpha \cos \delta\phi)) e^{-i\omega\tau_d}(1 - e^{-i\omega\tau_d}) S_{xy}[\omega] \} \\ &\quad + G^2|a_L|^2(\alpha^2 + 2\alpha\beta \cos \delta\phi + \beta^2). \end{aligned} \quad (\text{C.41})$$

If the interferometer is balanced ( $\alpha = \beta = 1/2$ ), this expression simplifies to

$$\begin{aligned} S_{ii}[\omega] &= G^2|a_L|^4 \{ 4 \cos^4(\delta\phi/2) \cos^2(\omega\tau_d/2) S_{xx}[\omega] \\ &\quad + 4 \cos^2(\delta\phi/2) \sin^2(\delta\phi/2) \sin^2(\omega\tau_d/2) S_{yy}[\omega] \\ &\quad + 4 \cos^3(\delta\phi/2) \sin(\delta\phi/2) \cos(\omega\tau_d/2) \sin(\omega\tau_d/2) \text{Re} \{ S_{xy}[\omega] \} \\ &\quad + G^2|a_L|^2 \cos^2(\delta\phi/2). \end{aligned} \quad (\text{C.42})$$

There are two complementary approaches that we can take regarding  $\delta\phi$ . In one, we can assume that the the interferometer is stable (or is actively stabilized), so that  $\delta\phi$  has some fixed value. In the other approach, which we chose to implement in the measurements described in appendix D.4, the phase difference is fluctuating by a magnitude much greater than  $2\pi$ . This effectively averages the expressions above over all  $\delta\phi$ , leading to the average photocurrent

$$\langle i \rangle = G^2|a_L|^2(\alpha^2 + \beta^2) \quad (\text{C.43})$$

and reduces equation (C.41) to

$$\begin{aligned} S_{ii}[\omega] &= G^2|a_L|^4 \{ 4(\alpha^4 + \alpha^2\beta^2(1 + 3\cos(\omega\tau_d)) + \beta^4) S_{xx}[\omega] \\ &\quad + 4\alpha^2\beta^2(1 - \cos(\omega\tau_d)) S_{yy}[\omega] \} \\ &\quad + G^2|a_L|^2(\alpha^2 + \beta^2), \end{aligned} \quad (\text{C.44})$$

and equation (C.42) to

$$S_{ii}[\omega] = G^2 |a_L|^4 \left\{ \frac{3}{2} \cos^2(\omega\tau_d/2) S_{xx}[\omega] + \frac{1}{2} \sin^2(\omega\tau_d/2) S_{yy}[\omega] \right\} + \frac{1}{2} G^2 |a_L|^2. \quad (\text{C.45})$$

This expression shows that the sensitivity of the delay line measurement to different kinds of noise depends on the noise frequency: for  $\omega = 2\pi n/\tau_d$  the setup only measures amplitude noise (as  $\sin^2(\pi n) = 0$ ), while for  $\omega = 2\pi(n + 1/2)/\tau_d$  it only measures phase noise (as  $\cos^2(\pi n + \pi/2) = 0$ ), and for other frequencies it measures some linear combination of the two. Note that neither the balanced interferometer expression (C.42) nor the averaged phase expression (C.44) are sensitive to the noise cross-correlation  $S_{xy}$ ; nevertheless, the Cauchy-Schwartz inequality  $|S_{xy}[\omega]|^2 \leq S_{xx}[\omega] S_{yy}[\omega]$  provides us with the upper bound.

### C.2.7 Cavity reflection

Another way of estimating laser noise is by reflecting it off an optical cavity. Consider a cavity of linewidth  $\kappa$ , external coupling efficiency  $\eta_\kappa \equiv \kappa_{\text{ext}}/\kappa$  (where  $\kappa_{\text{ext}}$  is the coupling rate through the input port), and detuning  $\Delta$  from the main laser tone. The reflection transfer function of such cavity is (from equation (2.31) in section 2.1)

$$K_{\text{cav}}[\omega] = 1 - 2\eta_\kappa \chi_{\text{c,rel}}[\omega + \Delta] \quad (\text{C.46})$$

$$\chi_{\text{c,rel}}[\omega] = \frac{1}{1 - 2i\omega/\kappa}. \quad (\text{C.47})$$

For simplicity, we will only consider a far-detuned case  $|\Delta| \gg \kappa$ , where we can approximate  $K_{\text{cav}}[0] = 1 + i\eta_\kappa \kappa/\Delta \approx 1$  and, consequently,  $\tilde{K}_{\text{cav}}[\omega] = K_{\text{cav}}[\omega](K_{\text{cav}}[0])^* \approx K_{\text{cav}}[\omega]$ . Furthermore, we assume a negative detuning:  $\Delta = -\Delta_0 < 0$ , so similarly  $\tilde{K}_{\text{cav}}[-\omega] \approx 1$  for all  $\omega > 0$ . With these simplifications, the photocurrent PSD becomes

$$\begin{aligned} S_{ii}[\omega] &= G^2 |a_L|^4 \left\{ |2 - 2\eta_\kappa \chi_{\text{c,rel}}[\omega - \Delta_0]|^2 S_{xx}[\omega] + |2\eta_\kappa \chi_{\text{c,rel}}[\omega - \Delta_0]|^2 S_{yy}[\omega] \right. \\ &\quad \left. + ((2 - 2\eta_\kappa \chi_{\text{c,rel}}[\omega - \Delta_0]) (2\eta_\kappa \chi_{\text{c,rel}}[\omega - \Delta_0])^* S_{xy}[\omega] + \text{c.c.}) \right\} + G^2 |a_L|^2 \\ &= G^2 |a_L|^4 \left\{ 4 (1 - (2\eta_\kappa - \eta_\kappa^2) |\chi_{\text{c,rel}}[\omega - \Delta_0]|^2) S_{xx}[\omega] \right. \\ &\quad + 4\eta_\kappa^2 |\chi_{\text{c,rel}}[\omega - \Delta_0]|^2 S_{yy}[\omega] \\ &\quad + 8(\eta_\kappa - \eta_\kappa^2) |\chi_{\text{c,rel}}[\omega - \Delta_0]|^2 \text{Re} \{ S_{xy}[\omega] \} \\ &\quad \left. + 8(2(\omega - \Delta_0)/\kappa) |\chi_{\text{c,rel}}[\omega - \Delta_0]|^2 \text{Im} \{ S_{xy}[\omega] \} \right\} + G^2 |a_L|^2. \end{aligned} \quad (\text{C.48})$$

For positive detuning  $\Delta = +\Delta_0$  the expression is essentially the same, but with an additional minus sign in front of the  $\text{Re} \{ S_{xy}[\omega] \}$  term. Thus, these two measurements (positive and negative  $\Delta$ ), together with a simple power detection to determine  $S_{xx}$ , are enough to fully characterize the classical noise.

## C.3 Phase modulation

In this section I present a brief treatment of the phase modulation. I start with a general description (subsection C.3.1), and then discuss the influence of the phase modulation on the heterodyne measurements (subsection C.3.2), which is useful in understanding the way we perform driven response measurements (both the optical cavity response, and mechanical mode response via OMIT/A). Then I describe how the intrinsic non-linearity of the phase modulation influences the OMIT/A and the undriven mechanical motion measurements, and how we account for it in the data analysis (subsection C.3.3). I conclude by describing how the phase modulation is used to produce a more generic kind of modulation (subsection C.3.4), which is important in understanding of our method of adjusting the laser frequency for locking it to the experimental cavity (appendix D.2).

### C.3.1 General representation

We denote the incident optical tone by  $a_L e^{-i\omega_L t}$ , and a set of microwave tones by  $V_n \cos(\nu_n t)$ , where  $V_n$  are the microwave amplitudes and  $\nu_n$  are the corresponding microwave frequencies. The output of the modulator is then expressed as

$$\begin{aligned} a_\phi &= a_L e^{-i\omega_L t} e^{i \sum_n (\pi V_n / V_\pi(\nu_n)) \cos(\nu_n t)} \\ &= a_L e^{-i\omega_L t} \prod_n e^{i (\pi V_n / V_\pi(\nu_n)) \cos(\nu_n t)} \equiv a_L e^{-i\omega_L t} \prod_n e^{i \psi_n \cos(\nu_n t)}, \end{aligned} \quad (\text{C.49})$$

where  $V_\pi(\nu_n)$  is the (frequency-dependent) voltage at which the phase inside the modulator changes by  $\pi$ , and  $\psi_n \equiv \pi V_n / V_\pi(\nu_n)$  is the microwave tone voltage normalized by  $V_\pi$ .

Next, we use the Jacobi-Anger expansion for the exponents

$$e^{i \psi_n \cos(\nu_n t)} = \sum_{n=-\infty}^{+\infty} (-i)^n J_n(\psi_n) e^{-in\nu_n t}, \quad (\text{C.50})$$

where  $J_n(z)$  is  $n^{\text{th}}$  Bessel function of the first kind. With this, the output laser becomes

$$a_\phi = a_L e^{-i\omega_L t} \prod_n \left[ \sum_{n=-\infty}^{+\infty} (-i)^n J_n(\psi_n) e^{-in\nu_n t} \right] \equiv e^{-i\omega_L t} \sum_k a_k e^{-i\nu_k t}, \quad (\text{C.51})$$

where  $\nu_k$  are all possible intermodulation frequencies resulting from the  $\nu_n$ , and  $a_k$  are the corresponding amplitudes which should be calculated using equation (C.51).

If the microwave drive has only one tone with the amplitude  $V_0$  and the frequency  $\nu_0$ , the output becomes

$$a_\phi = \sum_{n=-\infty}^{+\infty} (-i)^n a_L J_n(\psi_0) e^{-i(\omega_L + n\nu_0)t}, \quad (\text{C.52})$$

where  $\psi_0 = \pi V_0 / V_\pi(\nu_0)$ .

### C.3.2 Heterodyne detection

The fact that the phase modulation can not be observed directly has interesting consequences for heterodyne detection. Imagine performing heterodyne cavity response measurement by using a phase modulator, as shown in Figure C.1. There the light from the laser goes through a phase modulator driven by the output of a VNA (the drive amplitude is assumed to be small compared to  $V_\pi$ ). One of the sidebands acquired in the modulator (the upper sideband in Figure C.1b) serves as a probe, while the carrier acts an OLO. The light is then incident on the cavity, reflected, and detected using the photodiode. Finally, the output of the photodiode is sent back into the VNA.

If the amplitude of the drive is small, we can assume that there are only two sidebands generated in the modulator, that is,  $|J_n(\psi_0)|^2 \approx 0$  for  $|n| > 1$ . Then the amplitude of the light leaving the modulator and incident on the cavity can be expressed as

$$\begin{aligned} a_{\text{inc}} &= a_L J_0(\psi_0) e^{-i\omega_L t} - i a_L J_1(\psi_0) \left( e^{-i(\omega_L + \nu_0)t} + e^{-i(\omega_L - \nu_0)t} \right) \\ &= a_{L,0} e^{-i\omega_L t} + a_{L,1} e^{-i(\omega_L + \nu_0)t} + a_{L,1} e^{-i(\omega_L - \nu_0)t}, \end{aligned} \quad (\text{C.53})$$

where  $a_{L,0} = a_L J_0(\psi_0)$  is the carrier amplitude and  $a_{L,1} = -i a_L J_1(\psi_0)$  is the sidebands amplitude

The reflection off the cavity can be decomposed into two parts. First is the prompt reflection, which is simply equal to the incident field. The second is the light which interacts with the cavity and then leaves it through the input mirror. Now, consider the case where the carrier (i.e., OLO) is far detuned from the cavity, and only the upper sideband is ever close to the resonance (as shown in Figure C.1b). Since only this upper sideband

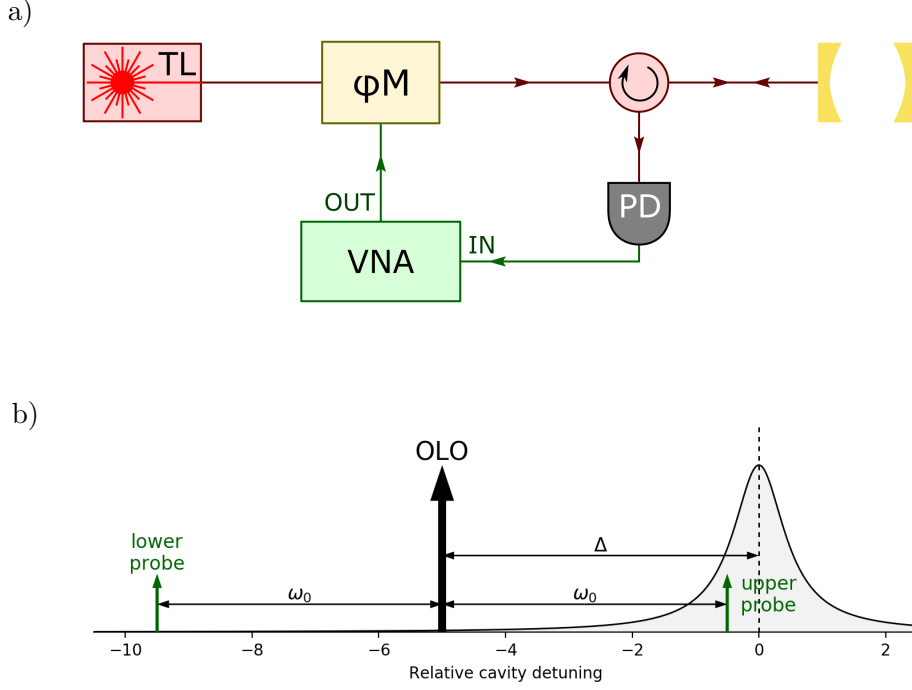


Figure C.1: a) Setup schematic for a heterodyne measurement using a phase modulator. b) Optical tone configuration for the measurement shown in (a).

interacts with the cavity, we can assume that the other two beams are simply reflected, and approximate the reflected light amplitude as

$$\begin{aligned}
a_{\text{refl}} &= a_{L,0}K_{\text{cav}}[\Delta]e^{-i\omega_L t} + a_{L,1}K_{\text{cav}}[\Delta + \nu_0]e^{-i(\omega_L + \nu_0)t} + a_{L,1}K_{\text{cav}}[\Delta - \nu_0]e^{-i(\omega_L - \nu_0)t} \\
&\approx a_{L,0}e^{-i\omega_L t} + a_{L,1}(1 - 2\eta_\kappa\chi_{c,\text{rel}}[\Delta + \nu_0])e^{-i(\omega_L + \nu_0)t} + a_{L,1}e^{-i(\omega_L - \nu_0)t} \\
&= a_{\text{inc}} - 2a_{L,1}\eta_\kappa\chi_{c,\text{rel}}[\Delta + \nu_0]e^{-i(\omega_L + \nu_0)t} \equiv a_{\text{inc}} + a_{\text{refl,cav}},
\end{aligned} \tag{C.54}$$

where  $\Delta$  is the carrier detuning from the cavity and  $K_{\text{cav}}$  is defined in (C.46). Thus, the reflected light is the same as the incident light, with the addition of  $a_{\text{refl,cav}} = -2a_{L,1}\eta_\kappa\chi_{c,\text{rel}}[\Delta + \nu_0]e^{-i(\omega_L + \nu_0)t}$  coming from the interaction of the upper sideband with the cavity.

Upon landing on the photodiode, this field produces a photocurrent

$$\langle i \rangle = G^2|a_{\text{refl}}|^2 = G^2|a_{\text{inc}}|^2 + G^2(a_{\text{inc}}^*a_{\text{refl,cav}} + a_{\text{inc}}a_{\text{refl,cav}}^*) + G^2|a_{\text{refl,cav}}|^2, \tag{C.55}$$

where  $G$  is the photodetector gain, as described in subsection C.2.2. Assuming the ideal heterodyne detection (OLO power much higher than the signal power), we can neglect the last term which is quadratic in  $a_{L,1}$ . The first term is simply a constant  $|a_{\text{inc}}|^2 = |a_L|^2$ , since the phase modulation does not manifest in the intensity. Thus, the only beatnote contribution comes from the middle term. If we are interested in the photocurrent at frequencies close to  $\nu_0$ , we only need to consider the beatnote between the carrier and the sideband (thus neglecting the beatnote of the two sidebands), which leads to the oscillating part of the photocurrent:

$$\langle i \rangle \approx G^2a_{\text{inc}}^*a_{\text{refl,cav}} + \text{c.c.} = -2G^2a_{L,0}^*a_{L,1}\eta_\kappa\chi_{c,\text{rel}}[\Delta + \nu_0]e^{-i\nu_0 t} + \text{c.c.} \tag{C.56}$$

Therefore, the response measured by the network analyzer, which is the complex amplitude of the  $e^{-i\nu_0 t}$  term in the photocurrent, is simply proportional to the cavity susceptibility. This is in contrast with the standard heterodyne detection (which can be achieved by, e.g., replacing the phase modulator with a single-sideband modulator), where this response would have had an additional constant background  $a_{L,0}^*a_{L,1}$  coming from the beating of the promptly reflected sideband with the LO. In the phase modulator heterodyne scheme this

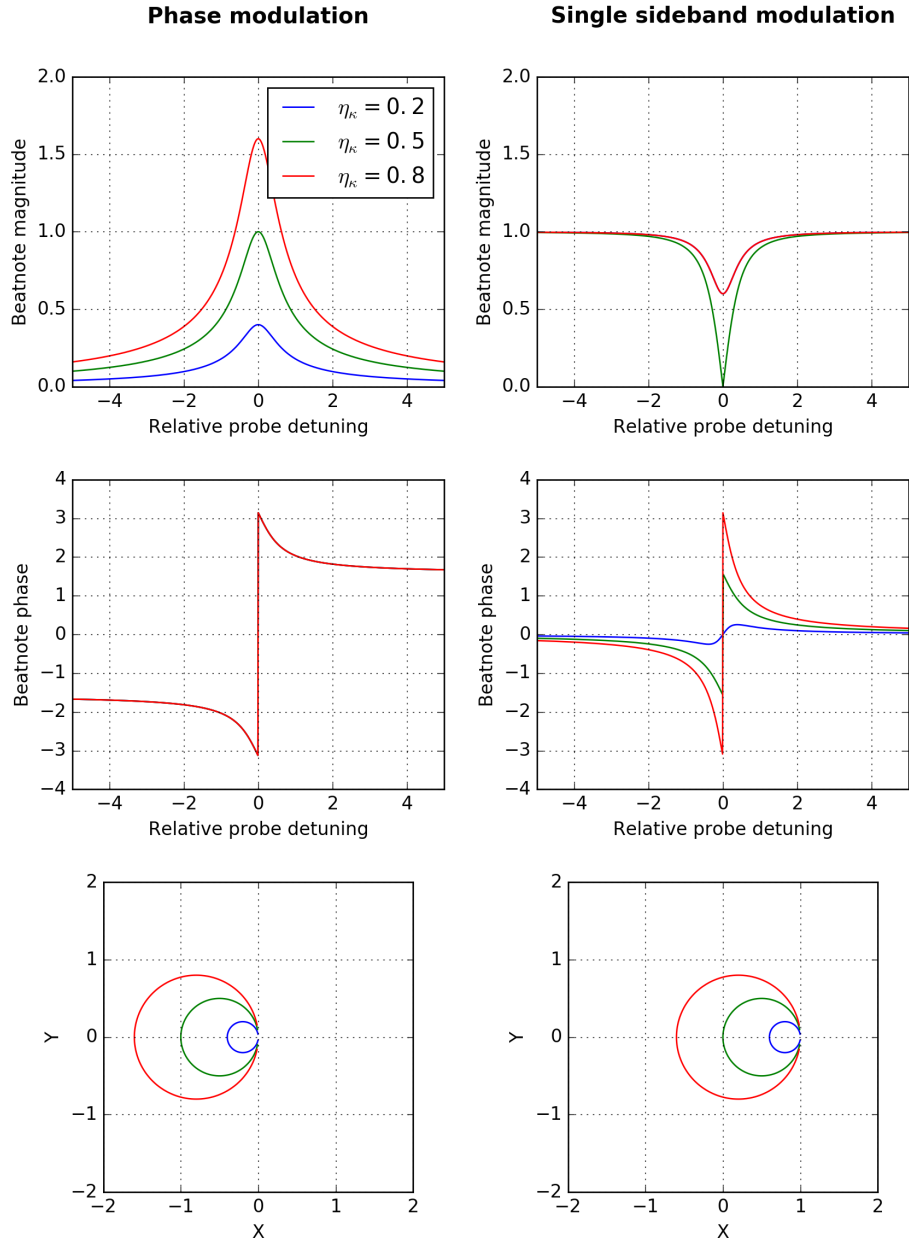


Figure C.2: Comparison of the phase modulation (left) and the single-sideband modulation (right) for the heterodyne detection of the optical cavity response. The top row shows the magnitude of the heterodyne beatnote, the middle row shows its phase, and the bottom row plots the heterodyne signal in a complex plane.

background is effectively canceled by an equal and opposite beatnote of the other promptly reflected sideband with the same LO. Figure C.2 compares the two heterodyne schemes.

The treatment above can be extended to an arbitrary cavity output field  $a_{\text{refl,cav}} = \sqrt{\kappa_{\text{ext}}}a$ , where  $\kappa_{\text{ext}}$  is the external cavity coupling and  $a$  is the intracavity field. In this case, the beatnote part of the photocurrent is

$$\langle i \rangle \approx G^2 a_{L,0}^* (\sqrt{\kappa_{\text{ext}}} a e^{+i\omega_L t}) + \text{c.c.} \quad (\text{C.57})$$

Hence, the phase modulator heterodyne scheme cancels all of the promptly reflected light effects and provides a signal which is directly proportional to the intracavity field.

### C.3.3 Non-linearity effects

#### General treatment

Another effect coming from the use of a phase modulator stems from its intrinsic non-linearity. It manifests in, e.g., equation (C.51), where the output of the modulator contains all possible intermodulation frequencies, i.e., all linear combinations of drive frequencies with integer coefficients. Normally, the drives are weak enough that it is sufficient to only consider first-order sidebands (as in subsection C.3.2). However, in some of the OMIT/A and undriven motion measurements described in Chapters 6 and 8 (generally, the ones with the highest control beam power or circulating photon number) the amplitudes of the control MW tones were large enough ( $V_0 \approx 0.2V_\pi$ ) that the non-linearity could not be ignored.

To describe its effects in a most generic way, we start with equation (C.51) and assume an arbitrary set of MW tones with frequencies  $\nu_n$  and normalized amplitudes  $\psi_n$ . Next, we consider all of these beams (including the carrier) landing on the cavity. To describe the optomechanical system dynamics, we use equations of motion (2.49) and (2.50):

$$\dot{\hat{a}} = -\frac{\kappa}{2}\hat{a} - ig^{(0)}\hat{a}(\hat{b} + \hat{b}^\dagger) + \sqrt{\kappa_{\text{int}}}\hat{\xi}_{\text{int}} + \sqrt{\kappa_{\text{ext}}}\hat{\xi}_{\text{ext}} + \sqrt{\kappa_{\text{ext}}}a_{\text{in}}e^{+i\omega_c t} \quad (\text{C.58})$$

$$\dot{\hat{b}} = -\left(\frac{\gamma_m}{2} + i\omega_m\right)\hat{b} - ig^{(0)}\hat{a}^\dagger\hat{a} + \sqrt{\gamma_m}\hat{\eta}, \quad (\text{C.59})$$

with the incident optical drive  $a_{\text{in}}$  given by equation (C.51).

In the frame rotating at the cavity frequency  $\omega_c$  the incident optical field becomes  $a_{\text{in}} = \sum_k a_k e^{-i\Delta_k t}$ , where  $\Delta_k = \omega_L + \nu_k - \omega_c$  is the detuning of the  $k^{\text{th}}$  phase modulator tone with amplitude  $a_k$  and frequency (relative to the carrier)  $\nu_k$ .

As in subsection 2.3.2, next we linearize these equations. The steady state amplitude of the intracavity field is<sup>b)</sup>

$$\bar{a} = \sum_k \bar{a}_k e^{-i\Delta_k t} \quad (\text{C.60})$$

$$\bar{a}_k = \sqrt{\kappa_{\text{ext}}}a_k\chi_c[\Delta_k], \quad (\text{C.61})$$

where  $\chi_c[\omega] = (\kappa/2 - i\omega)^{-1}$  is the cavity susceptibility. This amplitude results in a force on the mechanical oscillator given by

$$\bar{F}_{\text{RP}} = g^{(0)}\bar{a}^*\bar{a} = g^{(0)}\sum_k \sum_n \bar{a}_k \bar{a}_n^* e^{-i(\Delta_k - \Delta_n)t}. \quad (\text{C.62})$$

Next, we consider the linearized optical equation

$$\begin{aligned} \dot{\hat{d}} &= -\frac{\kappa}{2}\hat{d} - ig^{(0)}\bar{a}(\hat{b} + \hat{b}^\dagger) + \sqrt{\kappa_{\text{int}}}\hat{\xi}_{\text{int}} + \sqrt{\kappa_{\text{ext}}}\hat{\xi}_{\text{ext}} \\ &= -\frac{\kappa}{2}\hat{d} - ig^{(0)}\sum_k \bar{a}_k e^{-i\Delta_k t}(\hat{b} + \hat{b}^\dagger) + \sqrt{\kappa_{\text{int}}}\hat{\xi}_{\text{int}} + \sqrt{\kappa_{\text{ext}}}\hat{\xi}_{\text{ext}}. \end{aligned} \quad (\text{C.63})$$

Its solution in the Fourier domain can be separated into a motional part  $\hat{d}_{\hat{z}}$  (which is found using Fourier transform properties described in appendix A.2.3) and a vacuum noise part  $\hat{d}_{\hat{\xi}}$ :

$$\hat{d}[\omega] = \hat{d}_{\hat{z}}[\omega] + \hat{d}_{\hat{\xi}}[\omega] \quad (\text{C.64})$$

$$\hat{d}_{\hat{z}}[\omega] = -ig^{(0)}\chi_c[\omega]\sum_k \bar{a}_k \left(\hat{b}[\omega - \Delta_k] + \hat{b}^\dagger[\omega - \Delta_k]\right) \quad (\text{C.65})$$

$$\hat{d}_{\hat{\xi}}[\omega] = \chi_c[\omega]\sqrt{\kappa}\hat{\xi}[\omega] \quad (\text{C.66})$$

<sup>b)</sup>As in subsection 7.1.2, we neglect the static mechanical displacement due to a static radiation pressure force.

The contribution of the mechanical motion part  $\hat{d}_z$  to the mechanical force is

$$\begin{aligned}\hat{F}_z &= -ig^{(0)}(\bar{a}^*\hat{d}_z + \bar{a}\hat{d}_z^\dagger) \\ &= \left(g^{(0)}\right)^2 \sum_k \sum_n \bar{a}_k \bar{a}_n^* (\chi_c[\omega - \Delta_k] - \chi_c[\omega + \Delta_n]) \times \\ &\quad \times \left(\hat{b}[\omega + \Delta_n - \Delta_k] + \hat{b}^\dagger[\omega + \Delta_n - \Delta_k]\right).\end{aligned}\tag{C.67}$$

Now we can make a couple of simplifying assumptions. First, we note that  $\hat{b}[\omega]$  is centered around  $\omega = +\omega_{\text{m,eff}}$ , while  $\hat{b}^\dagger[\omega]$  is located around  $\omega = -\omega_{\text{m,eff}}$ . This means that they will be coupled only by terms rotating at  $\sim 2\omega_{\text{m,eff}}$ , i.e., for  $|\Delta_k - \Delta_n| \approx 2\omega_{\text{m,eff}}$  (satisfied with a precision  $\sim \gamma_{\text{m,eff}}$ ). In our case, these terms should be very small, since none of the microwave tones driving the cavity obey that relation (see subsection 7.1.1), and the higher order sidebands need to be at least fourth order in control drive amplitudes, which are still fairly small for the control drives used in the experiment. Thus, we can neglect the  $\hat{b}^\dagger$  terms and get

$$\hat{F}_z \approx \left(g^{(0)}\right)^2 \sum_k \sum_n \bar{a}_k \bar{a}_n^* (\chi_c[\omega - \Delta_k] - \chi_c[\omega + \Delta_n]) \hat{b}[\omega + \Delta_n - \Delta_k].\tag{C.68}$$

Second, the frequency differences between the optical tones are typically much larger than the mechanical linewidth:  $|\Delta_n - \Delta_k| \gg \gamma_{\text{m,eff}}$  for  $n \neq k$  (again, this is true for all the first-order optical beams which directly correspond to the MW drives, and even higher order terms would need to be very well-matched in order to satisfy  $|\Delta_n - \Delta_k| \lesssim \gamma_{\text{m,eff}}$ ). As a result, we disregard all the terms in equation (C.68) for which  $n \neq k$ , which lets us rewrite the optical force as

$$\hat{F}_z = -i\Sigma[\omega]\hat{b}[\omega]\tag{C.69}$$

$$\Sigma[\omega] = i\left(g^{(0)}\right)^2 \sum_k |\bar{a}_k|^2 (\chi_c[\omega - \Delta_k] - \chi_c[\omega + \Delta_k]).\tag{C.70}$$

The RPSN part of the optical force can be written as (similar to equation (7.20))

$$\hat{F}_{\text{RPSN}}[\omega] = g^{(0)} \sum_k \left(\bar{a}_k^* \hat{d}_\xi[\omega + \Delta_k] + \bar{a}_k \hat{d}_\xi^\dagger[\omega - \Delta_k]\right).\tag{C.71}$$

With that, the acoustic equation of motion in the Fourier domain becomes

$$\hat{b}[\omega] = \chi_{\text{m,eff}}[\omega] \left(-i\bar{F}_{\text{RP}}[\omega] - i\hat{F}_{\text{RPSN}}[\omega] + \hat{F}_{\text{th}}[\omega]\right)\tag{C.72}$$

$$\chi_{\text{m,eff}}[\omega] = \left(\frac{\gamma_{\text{m}}}{2} - i(\omega - \omega_{\text{m}}) + i\Sigma[\omega]\right)^{-1},\tag{C.73}$$

where  $\chi_{\text{m,eff}}[\omega]$  is the effective mechanical susceptibility, whose expression (C.73) is identical to equation (2.89), but with the different definition of the optomechanical self-energy  $\Sigma[\omega]$  (equation (C.70)). The thermal force is defined in the same way as before:  $\hat{F}_{\text{th}}[\omega] = \sqrt{\gamma_{\text{m}}}\hat{\eta}[\omega]$ .

Finally, we can calculate the intracavity field:

$$\hat{a}[\omega] = \bar{a}[\omega] + \hat{d}[\omega] = \bar{a}[\omega] + \hat{d}_z[\omega] + \hat{d}_\xi[\omega].\tag{C.74}$$

The mechanical sidebands term  $\hat{d}_z$  can be separated into two parts: one comes from the mechanical motion induced by the drive beatnotes (which corresponds to the force  $\bar{F}_{\text{RP}}$ ), while the other corresponds to the RPSN and thermal force driven motion (containing, respectively,  $\hat{F}_{\text{RPSN}}$  and  $\hat{F}_{\text{th}}$ ). The first part can be phase-coherent with the zeroth order field  $\bar{a}$ , since all of the induced mechanical motion terms correspond to beatnotes of the tones contained in  $\bar{a}$ . This situation describes, for example, the OMIT/A experiment (section 2.7), where one of the mechanical sidebands of the control beam interferes with the probe beam, and vice versa. The second part of the mechanical motion sidebands is not coherent, so it will not interfere with  $\bar{a}$ ; however it might interfere

with the optical vacuum noise  $\hat{d}_{\xi}$ , which contributes to, e.g., sideband cross-correlator measurements (subsection 7.2.2).

Equation (C.74), together with the usual input-output relations (equation (2.8)) lets us express the field reflected off the cavity as

$$\hat{a}_{\text{out,ext}}[\omega] = a_{\text{in}}[\omega] + \hat{\xi}_{\text{ext}}[\omega] - \sqrt{\kappa_{\text{ext}}} \left( \bar{a}[\omega] + \hat{d}_{\bar{z}}[\omega] + \hat{d}_{\xi}[\omega] \right). \quad (\text{C.75})$$

### Driven response measurements

First, let us consider the OMIT/A experiment, for which we neglect all the noise terms and focus on the external coherent drive (like in section 2.7). That transform equation (C.72) into

$$\hat{b}[\omega] = -i\chi_{\text{m,eff}}[\omega]\bar{F}_{\text{RP}}[\omega], \quad (\text{C.76})$$

and equation (C.75) into

$$\hat{a}_{\text{out,ext}}[\omega] = a_{\text{in}}[\omega] - \sqrt{\kappa_{\text{ext}}}\chi_{\text{c}}[\omega] \left( \bar{a}[\omega] + \hat{d}_{\bar{z}}[\omega] \right). \quad (\text{C.77})$$

These two equations are, in principle, sufficient to calculate the reflection off the cavity. For the analysis presented in Chapters 6 and 8, we implement this procedure as follows

- First, knowing the microwave drives and phase modulator response (appendix D.7), calculate tones on the output of the phase modulator using equation (C.51) (for practical reasons, we limit expansion to the third order in the control beams amplitudes and to the first order in the probe beam amplitude);
- Next, from equations (C.60) and (C.61) determine the steady-state (zeroth order) intracavity field;
- Use this to calculate the optical force  $\bar{F}_{\text{RP}}$  (equation (C.62)) and the self-energy  $\Sigma$  (equation (C.70));
- From these, determine the mechanical response (equations (C.76) and (C.73));
- Use this calculated response to get the resulting field  $\hat{a} = \bar{a} + \hat{d}_{\bar{z}}$  inside the cavity and find the cavity reflection  $\hat{a}_{\text{out,ext}}$  (equation (C.77))
- Finally, to relate this field to measured quantities, we calculate the electrical response of the photodiode  $I \propto \hat{a}_{\text{out,ext}}^* \hat{a}_{\text{out,ext}}$ , which will consist of all possible beat notes of the reflected optical tones. The amplitude of the electrical tone oscillating at  $\nu_{\text{p}}$  (the frequency of the probe MW drive) is the relevant OMIT signal. This tone mainly comes of the beating of the probe beam with the OLO, but higher-order intermodulation tones can also play some role.

All of these calculation are performed numerically.

### Undriven motion measurements

When considering the measurement of the undriven motion and the effects of the RPSN, full calculations similar to the ones described above quickly become intractable (as it needs to take into account optical quantum noise taken at  $\pm\omega_{\text{m,eff}}$  away from all of the incident optical beams, which results in many contributions from different parts of the spectrum). Therefore, we make one more simplifying assumption: when we consider the system dynamics, we do not take any higher-order intermodulation tones into account, which means that the treatment presented in Chapter 7 still applies. This is justified by the fact that no immediate higher-order tones lie close the cavity resonance or close to  $\pm\omega_{\text{m,eff}}$  detuned from the cavity, so they do not appreciably contribute to the self-energy, and they do not generate any noticeable mechanical sidebands. It is worth noting, though, that we still use the exact expression for the control beam amplitudes  $a_{L,1} \propto J_1(\pi V_0/V_{\pi})$ , rather than the weak drive approximation  $a_{L,1} \propto (\pi/2)V_0/V_{\pi}$ .

With that assumption, all of the non-linear effects are contained in the description of the photodetection. The most immediate consequence, which is also mentioned in subsection 8.3.2, is the “OLO depletion”: as only a fraction of the total optical power is contained in the OLO, the SNR is reduced (the shot noise background corresponds to the full optical power, but the detection efficiency is proportional to the OLO power). The other consequence is the “sideband mixing”, where the mechanical sidebands in the MW spectrum do not correspond exactly to the same sidebands in the optical spectrum, but instead are some linear combination of these sidebands.

To understand this effect, let us consider the standard double-beam scheme with two control tones with frequencies  $\nu_{\text{con},\ell}$  and  $\nu_{\text{con},\text{u}}$  relative to the OLO. Inside the cavity these beams acquire mechanical sidebands at frequencies  $\nu_{\text{con},\ell} + \omega_{\text{m,eff}}$  and  $\nu_{\text{con},\text{u}} - \omega_{\text{m,eff}}$  respectively, and after mixing with the OLO at the photodetector, these sidebands produce corresponding mechanical motion peaks in the photocurrents. However, there is another process producing similar signals in the photocurrent. Because of the phase modulator non-linearity, there is an extra second-order tone at a frequency  $\nu_{\text{con},\ell} + \nu_{\text{con},\text{u}}$ . When this tone mixes with the lower mechanical sideband frequency  $\nu_{\text{con},\ell} + \omega_{\text{m,eff}}$ , the photocurrent signal occurs at a frequency  $(\nu_{\text{con},\ell} + \nu_{\text{con},\text{u}}) - (\nu_{\text{con},\ell} + \omega_{\text{m,eff}}) = \nu_{\text{con},\text{u}} - \omega_{\text{m,eff}}$ , which is exactly the frequency of the upper mechanical sideband. As a consequence, the two sidebands now interfere with each other in the photocurrent, meaning that the detected MW sidebands are some linear combinations of the optical sidebands.

To account for these effects, we perform numerical calculations similar to the ones we do for the OMIT/A measurements. The procedure is outlined below.

- First, as before, we use the known microwave drives to calculate the optical cavity drive (equation (C.51)) and the corresponding steady-state intracavity field (equations (C.60) and (C.61)). Two of the intracavity tones at frequencies  $\nu_{\text{con},\ell}$  and  $\nu_{\text{con},\text{u}}$  (relative to the OLO) correspond respectively to the lower and to the upper control beam.
- Using the two control beam amplitudes, we perform the theoretical calculations to determine the “unmixed” (i.e., without taking phase modulator and detection process non-linearities into account) sideband PSDs (equations (7.47) and (7.48)) and the sideband cross-correlator (equation (7.55)).
- Next, we determine the “mixing coefficients”, which are the contributions of the optical Stokes and anti-Stokes sidebands in the photocurrent sidebands. To find them, we assume a simple (and unphysical) “calibration” situation where either  $\hat{b}[\omega] = \delta(\omega - \omega_{\text{m,eff}})$  and  $\hat{b}^\dagger[\omega] = 0$  (i.e., only anti-Stokes sidebands exist), or  $\hat{b}^\dagger[\omega] = \delta(\omega + \omega_{\text{m,eff}})$  and  $\hat{b}[\omega] = 0$  (only Stokes sidebands exist). For both of these cases we use equations (C.64) and (C.65) together with the full set of optical tones incident on the cavity (including higher-order phase modulator tones) to find all of the mechanical sidebands inside the cavity. Then we use equation (C.75) to find the reflected light amplitude, and after that calculate the photocurrent using the same expression  $I \propto \hat{a}_{\text{out,ext}}^* \hat{a}_{\text{out,ext}}$  as in the OMIT/A case.

In general, the photocurrent has both the “upper” and the “lower” sidebands due to the higher-order control beam (and, possibly, other higher-order processes). For both of the sidebands we can determine the ratio of the sideband amplitude (which is, in general, complex) to the idealized case where only mixing with the OLO is considered in the photocurrent (which is the case described in section 7.2). This procedure yields a total of four coefficients: two coefficients (for the “upper” and the “lower” sideband) for each of the two calibration cases ( $\hat{b} = 0$  or  $\hat{b}^\dagger = 0$ ). We can denote these coefficients as  $c_{i,j}$ , where  $i$  denotes the photocurrent sideband (“u” for “upper” and “l” for “lower”), and  $j$  denotes the calibration case (“r” for  $\hat{b} = 0$  and “b” for  $\hat{b}^\dagger = 0$ ). Thus,  $c_{i,j}$  is the contribution of  $j^{\text{th}}$  optical sideband to  $i^{\text{th}}$  photocurrent sideband, which can be expressed as

$$i_\ell[\omega] = c_{\ell,\text{b}} i_\text{b}[\omega] + c_{\ell,\text{r}} i_\text{r}^*[\omega] \quad (\text{C.78})$$

$$i_\text{u}[\omega] = c_{\text{u},\text{b}} i_\text{b}^*[\omega] + c_{\text{u},\text{r}} i_\text{r}[\omega]. \quad (\text{C.79})$$

Here we  $i_\ell$  and  $i_\text{u}$  denote the actual photocurrent sidebands, while  $i_\text{r}$  and  $i_\text{b}$  stand for the “unmixed” sidebands defined in equation (7.28). In the ideal case without higher-order tones  $i_\ell = i_\text{b}$  and  $i_\text{u} = i_\text{r}$ , so

$c_{u,r} = c_{\ell,b} = 1$  and  $c_{u,b} = c_{\ell,r} = 0$ . Note the complex conjugates for  $i_r$  in the first equation and  $i_b$  in the second equation. They come about because  $i_b$  (together with  $i_\ell$ ) is proportional to  $\hat{b}$ , while  $i_r$  (and  $i_u$ ) is proportional to  $\hat{b}^\dagger$ , meaning that they need to be conjugated to be related to each other.

- Finally, from  $c_{i,j}$  and equations (C.78) and (C.79) we can express the measured sidebands PSDs and cross-correlator in terms of the unmixed ones. Consider, for example, the “lower” (i.e., anti-Stokes) sideband PSD:

$$\begin{aligned}
S_{ii}^{(\ell\ell)}[\omega] &\equiv \langle i_\ell[\omega](i_\ell[\omega])^* \rangle \\
&= \langle (c_{\ell,b}i_b[\omega] + c_{\ell,r}i_r^*[\omega])(c_{\ell,b}i_b[\omega] + c_{\ell,r}i_r^*[\omega])^* \rangle \\
&= |c_{\ell,b}|^2 \langle i_b[\omega](i_b[\omega])^* \rangle + 2\text{Re} \{ c_{\ell,b}c_{\ell,r}^* \langle i_b[\omega]i_r[-\omega] \rangle \} + |c_{\ell,r}|^2 \langle i_r^*[\omega](i_r^*[\omega])^* \rangle \\
&= |c_{\ell,b}|^2 S_{ii}^{(\text{bb})}[\omega] + 2\text{Re} \left\{ c_{\ell,b}c_{\ell,r}^* S_{ii}^{(\text{rb})}[\omega] \right\} + |c_{\ell,r}|^2 S_{ii}^{(\text{rr})}[-\omega].
\end{aligned} \tag{C.80}$$

In a similar manner, we can derive expressions for the other quantities:

$$\begin{aligned}
S_{ii}^{(\text{uu})}[\omega] &\equiv \langle i_u[\omega](i_u[\omega])^* \rangle \\
&= |c_{u,r}|^2 S_{ii}^{(\text{rr})}[\omega] + 2\text{Re} \left\{ c_{u,r}c_{u,b}^* S_{ii}^{(\text{rb})}[-\omega] \right\} + |c_{u,b}|^2 S_{ii}^{(\text{bb})}[-\omega]
\end{aligned} \tag{C.81}$$

$$\begin{aligned}
S_{ii}^{(\text{u}\ell)}[\omega] &\equiv \langle i_\ell[\omega]i_u[-\omega] \rangle \\
&= c_{\ell,b}c_{u,b} S_{ii}^{(\text{bb})}[\omega] + c_{\ell,b}c_{u,r} S_{ii}^{(\text{rb})}[\omega] \\
&\quad + c_{\ell,r}c_{u,b} (S_{ii}^{(\text{rb})}[\omega])^* + c_{\ell,r}c_{u,r} S_{ii}^{(\text{rr})}[-\omega].
\end{aligned} \tag{C.82}$$

- Alternatively, one can invert equations (C.78), (C.79) (or equations (C.80)-(C.82)) and get expressions for the unmixed PSDs and correlator in terms of the measured ones. This is the route we take in the experiment.

Similar to the OMIT/A experiments, these calculation are performed numerically to the third order in the control MW drive amplitudes.

When analyzing the undriven motion, we need to consistently account for non-linear effects both when “unmixing” the undriven motion sidebands, and when interpreting OMIT/A data for the undriven motion normalization (subsection 8.3.2). For the latter, we calculate the OMIT/A signal amplitude using two methods: the complete one, which is described in this section, and a simplified one, which corresponds to the standard OMIT/A theory (section 2.7). We then find the ratio of the two amplitudes and use it as a scaling factor in determining the measurement rate  $\Gamma_{\text{meas}}$  from the OMIT/A response amplitude (described in subsection 8.3.2). Since the OMIT/A amplitude is linear in  $\Gamma_{\text{meas}}$  and in the total optical power (which is the main factor that the calibration scheme is designed to address), this scaling factor is sufficient to account for the non-linearity in the undriven motion calibration.

### C.3.4 IQ optical modulation

Phase modulation can serve as a basis for different kinds of modulation. One of the most generic kinds is IQ modulation, which allows independent control of the phase and the amplitude of the output field. Such modulator takes a single optical input  $a(t) = a_L e^{-i\omega_L t}$  and two control electrical (usually MW) inputs  $I(t)$  and  $Q(t)$  encoding two quadratures of the output field ( $I(t)$  stands for “in-phase”, i.e., amplitude modulation, and  $Q(t)$  stands for “in-quadrature”, meaning that it is shifted by  $90^\circ$  and corresponds to a phase modulation). The output of the modulator is described as

$$a_{\text{IQ}}(t) = a_L e^{-i\omega_L t} (I(t) + iQ(t)), \tag{C.83}$$

where for simplicity we assume  $I(t)$  and  $Q(t)$  to be normalized.

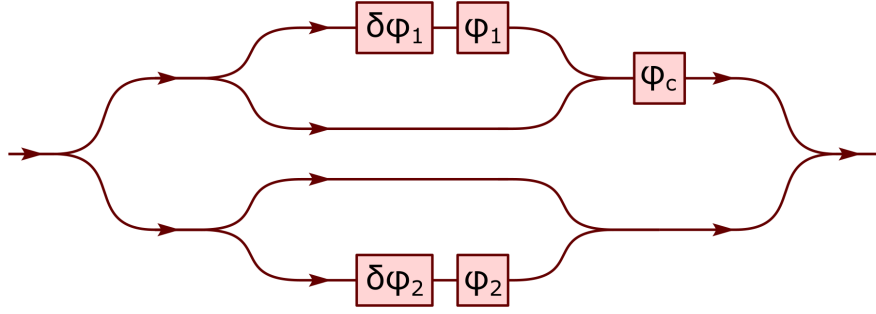


Figure C.3: Schematic of a DP-MZM. Each splitting/joining point stands for a 50:50 splitter/combiner, and rectangles denote phase modulators.

The implementation of the IQM used in our setup is a so-called dual-parallel Mach-Zehnder modulator (DP-MZM), whose schematic is shown in Figure C.3. It consists of two Mach-Zehnder interferometers whose outputs are combined together with an adjustable phase shift  $\phi_c$ . Each of the interferometers in turn has a phase modulator in one of its arms. For clarity of the derivation, and to be more faithful to the hardware implementation, we divide the phase modulators in two groups: slow, large-span control signals  $\phi_1$ ,  $\phi_2$  and  $\phi_c$ ; and fast, small-span modulation signals  $\delta\phi_1$ ,  $\delta\phi_2$ . The control signals are used to adjust the operation mode of the modulator (as demonstrated below, IQ modulation corresponds to a particular combination of these voltages), while the modulation signals directly correspond to the quadrature signals  $I(t)$  and  $Q(t)$ .

Let us start by considering a single interferometer, for example, the top one. Assuming perfect 50:50 splitters, the amplitude of light entering each interferometer is  $a_L/\sqrt{2}$ , and the amplitude in each the interferometer arms is  $a_L/2$ . The top arm of the interferometer acquires a phase  $\phi_1 + \delta\phi_1$  relative to the bottom arm of the same interferometer, so before the arms are recombined, its amplitude is  $a_L e^{i(\phi_1 + \delta\phi_1)}$ . This turns the output of the top interferometer into

$$a_{IQ,1} = \frac{a_L e^{-i\omega_L t}}{2} \frac{(1 + e^{i(\phi_1 + \delta\phi_1)})}{\sqrt{2}}. \quad (\text{C.84})$$

Similarly, the bottom interferometer's output is

$$a_{IQ,2} = \frac{a_L e^{-i\omega_L t}}{2} \frac{(1 + e^{i(\phi_2 + \delta\phi_2)})}{\sqrt{2}}. \quad (\text{C.85})$$

The final output is a combination of these two outputs with an additional phase shift  $\phi_c$ :

$$a_{IQ} = \frac{a_{IQ,1} e^{i\phi_c} + a_{IQ,2}}{\sqrt{2}} = \frac{a_L e^{-i\omega_L t}}{4} \left( (1 + e^{i(\phi_1 + \delta\phi_1)}) e^{i\phi_c} + (1 + e^{i(\phi_2 + \delta\phi_2)}) \right). \quad (\text{C.86})$$

Now we have to figure out control phases  $\phi_1$ ,  $\phi_2$  and  $\phi_c$  corresponding to the IQ modulation. First, we need to suppress the carrier, which is the signal at the original frequency  $\omega_L$ ; this implies having zero output amplitude when  $\delta\phi_1 = \delta\phi_2 = 0$ :

$$a_{IQ}|_{\delta\phi_1=\delta\phi_2=0} \propto (1 + e^{i\phi_1}) e^{i\phi_c} + (1 - e^{i\phi_2}) = 0. \quad (\text{C.87})$$

To satisfy this requirement independently of  $\phi_c$ , we set  $\phi_1 = \phi_2 = \pi$ . This simplifies expression (C.86) to

$$a_{IQ} = \frac{a_L e^{-i\omega_L t}}{4} \left( (1 - e^{i\delta\phi_1}) e^{i\phi_c} + (1 + e^{i\delta\phi_2}) \right). \quad (\text{C.88})$$

Next, as is often the case, we take the limit of small modulation amplitudes  $|\delta\phi_{1,2}| \ll 1$  and expand the exponents:

$$\begin{aligned} a_{\text{IQ}} &\approx \frac{a_{\text{L}}e^{-i\omega_{\text{L}}t}}{4} \left( (1 - 1 - i\delta\phi_1) e^{i\phi_c} + (1 - 1 - i\delta\phi_2) \right) \\ &= \frac{-ia_{\text{L}}e^{-i\omega_{\text{L}}t}}{4} \left( \delta\phi_2 + \delta\phi_1 e^{i\phi_c} \right). \end{aligned} \quad (\text{C.89})$$

If we compare this expression to equation (C.83), we see that we can match them up to a factor of  $-i/4$  (which is just a combination of attenuation and an unimportant phase shift) if we set  $\phi_c = \pi/2$ , and associate  $\delta\phi_2 = I(t)$  and  $\delta\phi_1 = Q(t)$ :

$$a_{\text{IQ}} = \frac{-i}{4} a_{\text{L}} e^{-i\omega_{\text{L}}t} (\delta\phi_2 + i\delta\phi_1) = \frac{-i}{4} a_{\text{L}} e^{-i\omega_{\text{L}}t} (I(t) + iQ(t)). \quad (\text{C.90})$$

Hence, by setting  $\phi_1 = \phi_2 = \pi$ ,  $\phi_c = \pi/2$  we can operate DP-MZM as an IQM. It is important to note that the control phases must be precisely maintained. Otherwise, the modulator output can transmit a non-suppressed carrier (if  $\phi_1$  or  $\phi_2$  are off), or the modulation quadratures can deviate from the ideal  $I$  and  $Q$  quadratures (if  $\phi_c$  is off). The latter can lead to, e.g., non-vanishing second sideband when attempting to perform a single-sideband suppressed carrier modulation (see appendix D.2.2).

# Appendix D

## Measurement setup details

In this Appendix I will describe details, auxiliary calibration and characterization methods required for the measurements of the superfluid helium device.

### D.1 Tunable filter cavity setup

Here I describe the tunable filter cavity setup, which is used to get rid of the classical laser phase noise at  $\omega_m \approx 2\pi \cdot 320$  MHz detuning from the main tone. As mentioned later in section D.4, it allows us to increase the shot noise limited power of our laser from  $\sim 30 \mu\text{W}$  to  $< 200 \mu\text{W}$ .

#### D.1.1 Setup schematic

The tunable filter cavity setup (TFCS in Figure 5.2) schematic is shown in Figure D.1. The light enters through the circulator and into the polarization controller (PCnt), where its polarization is adjusted to one of the polarization eigenstates of the tunable filter cavity (TFC). The TFC is highly birefringent (the splitting of the two polarization modes is about half of the free spectral range), so the polarization adjustment is necessary. The reflected light goes back through the circulator and onto the photodetector (PD), while the transmitted light passes through a second PCnt to adjust its polarization to the correct axis of the polarization-maintaining fiber on the output of the setup.

The TFC has a tuning input connected to an internal piezo which controls the cavity length. This input is driven by two signals combined with a bias tee. The DC signal is used to adjust the cavity resonance and keep it locked to the laser. The RF signal is driven with a sine wave from an arbitrary waveform generator (AWG); this drive is used to generate the error signal for the lock. Similarly, the reflection signal gets split with another bias tee into a DC and an RF component. The DC component provides the average reflection power, and the RF component is mixed with the same AWG signal to produce the error beatnote (BN) signal. Both DC and BN signal are sent into the micro-controller ( $\mu\text{C}$ ), which uses this information to generate the feedback signal (FB OUT) controlling the cavity resonance frequency.

#### D.1.2 Error signal

To understand the error signal, let us examine the PD output (a similar derivation is also given in Ref. [180]). As mentioned in appendix C.2.7, reflection off the cavity is described by the susceptibility function (C.46)

$$K_{\text{cav}}[\Delta] = 1 - \frac{2\eta_\kappa}{1 - 2i\Delta/\kappa}, \quad (\text{D.1})$$

where  $\kappa$  is the cavity linewidth,  $\Delta$  is the drive detuning and  $\eta_\kappa \equiv \kappa_{\text{ext}}/\kappa$  is the input coupling efficiency, with  $\kappa_{\text{ext}}$  being the input coupling of the cavity. Given the laser amplitude  $a_L$ , laser frequency  $\omega_L$  and cavity resonance

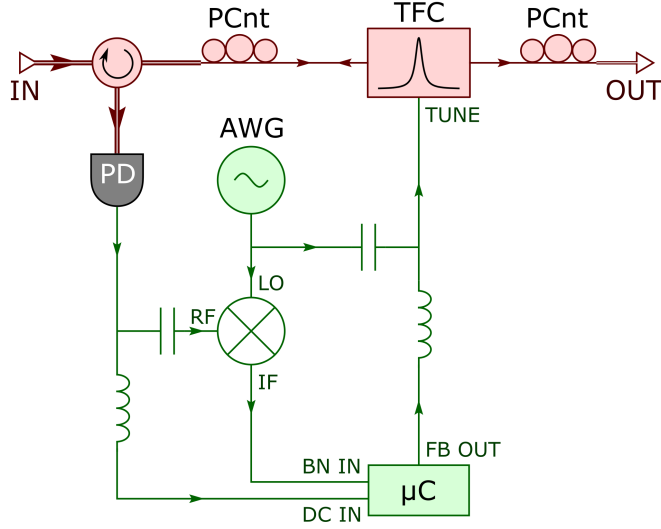


Figure D.1: Schematic of the tunable filter cavity setup. Red symbols denote optical components, with red lines corresponding to the interconnecting optical fibers; double lines denote polarization-maintaining fibers, while single lines denote regular fibers. Green symbols denote electrical components, with green lines showing electrical connections.

frequency  $\omega_c$ , the amplitude of the reflected light is

$$a_{\text{refl}} = a_L K_{\text{cav}}[\omega_L - \omega_c] = a_L \left( 1 - \frac{2\eta\kappa}{1 - 2i(\omega_L - \omega_c)/\kappa} \right), \quad (\text{D.2})$$

and the corresponding power is

$$P_{\text{refl}} = |a_{\text{refl}}|^2 = |a_L|^2 \left( 1 - \frac{4\eta\kappa(1 - \eta\kappa)}{1 + 4(\omega_L - \omega_c)^2/\kappa^2} \right). \quad (\text{D.3})$$

Now let us consider a small sinusoidal perturbation in  $\omega_c$  with frequency  $\omega$  and amplitude  $a \ll \kappa$ :  $\omega_c = \omega_{c0} + a \sin(\nu t)$ . Given that the cavity bandwidth is much larger than the perturbation frequency (in our setup  $\kappa \approx 30$  MHz and  $\nu = 37$  kHz), the reflection power  $P_{\text{refl}}$  can be assumed to be an instantaneous function of the cavity resonance frequency. Since the perturbation is small, we can expand the reflection power to the first order in  $a$ :

$$P_{\text{refl}}(t) \approx P_{\text{refl}}|_{\omega_c=\omega_{c0}} + \left. \frac{\partial P_{\text{refl}}}{\partial \omega_c} \right|_{\omega_c=\omega_{c0}} a \sin(\nu t). \quad (\text{D.4})$$

The PD signal is proportional to this reflection power. After mixing it with the original drive  $\sin(\nu t)$  and low-pass filtering, the result is the error signal which is proportional to the coefficient in front of  $\sin(\nu t)$ :

$$V_e = \left. \frac{\partial P_{\text{refl}}}{\partial \omega_c} \right|_{\omega_c=\omega_{c0}} \propto \frac{(\omega_L - \omega_{c0})/\kappa}{(1 + 4(\omega_L - \omega_{c0})^2/\kappa^2)^2}. \quad (\text{D.5})$$

Examples of the DC reflection (D.4) and the error signal (D.5) are shown in Figure D.2. The error signal, being essentially the derivative of the DC reflection, is equal to zero and has a linear slope when the laser is resonant with the cavity. This makes it a convenient error signal for locking the cavity on resonance with the laser. In contrast, the DC reflection signal is quadratic at zero detuning, which means that it does not provide information on the deviation of the cavity frequency from the laser frequency (deviation in either side produces the same response), and therefore cannot serve as an error signal.

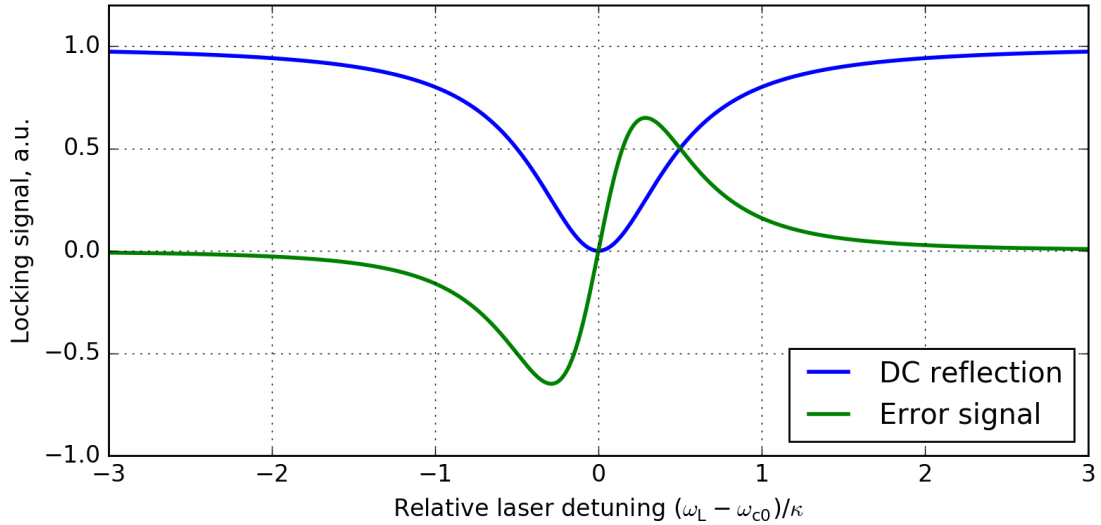


Figure D.2: The DC reflection signal  $P_{\text{ref}}$  (blue) and the error signal  $V_e$  (green) as a function of the laser detuning from the cavity.

## D.2 Locking and IQ modulator details

In this section I describe parts of the measurement setup that are related to locking of the laser to the cavity: obtaining the error signal, using it to generate the feedback signal, and turning it into a change in the laser frequency.

### D.2.1 Obtaining error signal

As described in subsection 5.2.4, the error signal for cavity locking is obtained by analyzing the reflection of the weak locking beam. In the limit of far red-detuned OLO (which is the case in our measurements), the corresponding photocurrent beatnote was derived in the appendix C.3.2, equation (C.56):

$$\langle i \rangle \propto a_{L,0}^* a_{L,1} \chi_{c,\text{rel}}[\Delta + \nu_{\text{lock}}] e^{-i\nu_{\text{lock}} t}. \quad (\text{D.6})$$

Here  $a_{L,0}$  and  $a_{L,1}$  are the amplitudes of the carrier (OLO) and the sideband (locking beam) respectively,  $\Delta$  is the OLO detuning from the cavity resonance,  $\chi_{c,\text{rel}}[\omega] = (1 - 2i\omega/\kappa)^{-1}$  is the normalized optical cavity susceptibility, and  $\nu_{\text{lock}}$  is the carrier-sideband frequency difference, i.e., the frequency of the locking beam drive in the setup (2100 MHz in our case). Mixing this current with the MWLO and demodulating it inside the ZILI yields two quadratures  $X$  and  $Y$ , which correspond to the complex amplitude of the photocurrent beatnote:

$$X + iY \propto a_{L,0}^* a_{L,1} \chi_{c,\text{rel}}[\Delta + \nu_{\text{lock}}]. \quad (\text{D.7})$$

Thus, up to some prefactor the quadratures directly correspond to the cavity susceptibility function.

The top left part of Figure D.3 shows an example of the signal (D.7) plotted in the  $XY$ -plane for varying locking beam detuning  $\Delta_{\text{lock}} = \Delta + \nu_{\text{lock}}$ . After the quadratures are calculated, the data is internally shifted and rotated inside the ZILI, as shown in the top right part of Figure D.3. These transformed  $XY$  quadratures are subsequently converted into voltage signals and sent into an FPGA, where the error signal  $\phi_e$  is calculated as the angle of the quadrature signal:  $\phi_e = \arg(X + iY)/\pi$ .

The bottom plot in Figure D.3 shows the error signal  $\phi_e$  (black) as a function of lock beam detuning; for comparison, it also demonstrates the standard Pound-Drever-Hall[180, 181] (PDH) lock signal (gray), which is simply the  $Y$  quadrature of the beatnote. The advantage of the angle error signal is that it is a monotonous function of the detuning  $\Delta_{\text{lock}}$ . This means that it is possible to change the lock set-point by simply applying a shift to the error signal, while maintaining a large (potentially, infinite) capture and lock range. This is in

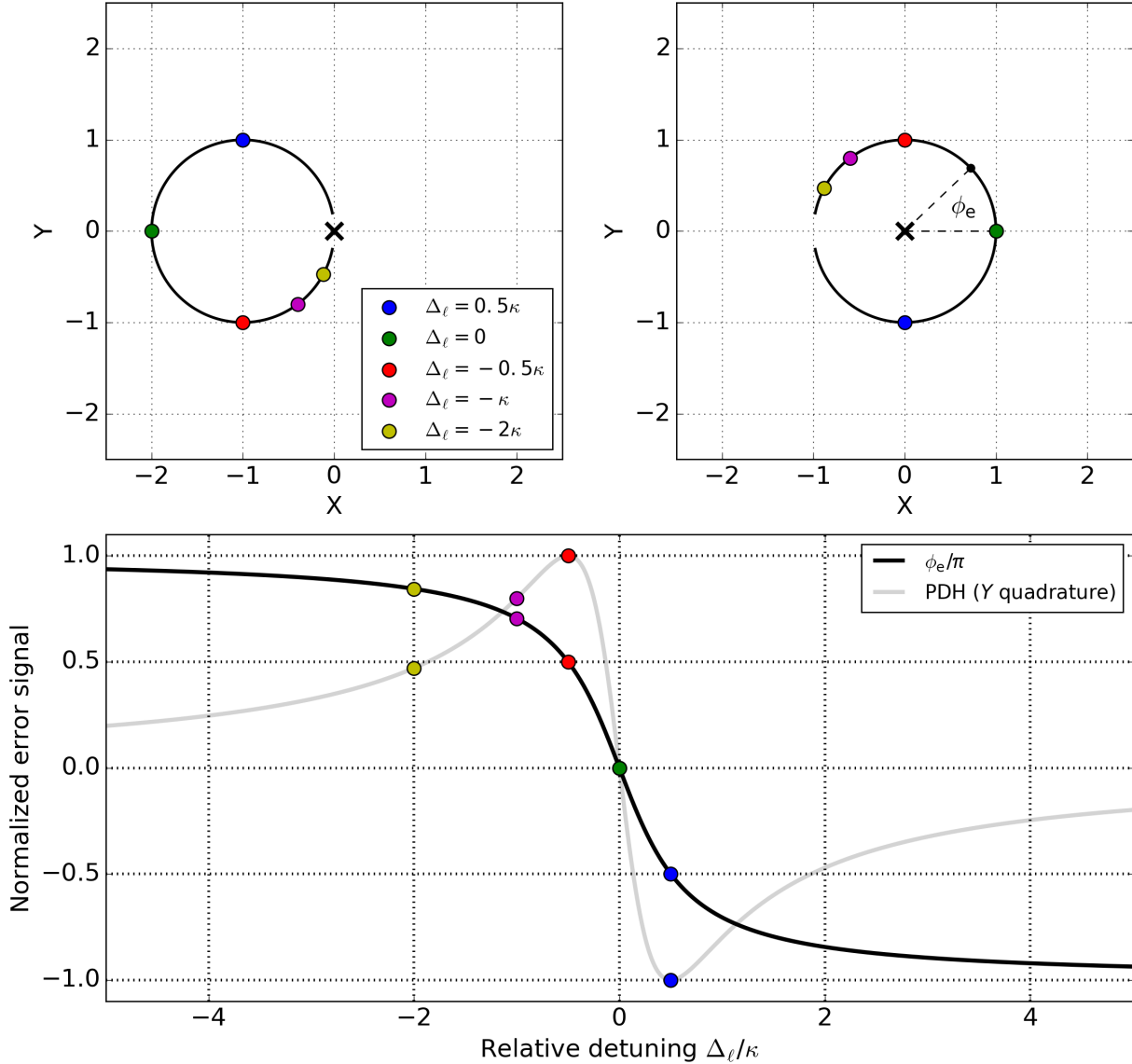


Figure D.3: Top left: demodulated quadratures of the locking beam beatnote. Top right: same data, but rotated by  $180^\circ$  and shifted by  $-1$  to make the resonance circle centered at zero. Bottom: comparison of the angle-derived error signal  $\phi_e$  (black) to the Pound-Drever-Hall (PDH) error signal (gray). In the top plots the black line shows the quadratures for the detuning range  $-5\kappa \leq \Delta_{\text{lock}} \leq 5\kappa$ . The colored markers show the quadratures (top plots) or error signals (bottom plots) for specific values of  $\Delta_{\text{lock}}$ . The angle  $\phi_e$  on the top right plot is the error signal for the beatnote denoted by the black dot, assuming that the lock point is  $\Delta_{\text{lock}} = 0$ .

contrast with the standard PDH locking technique, where only locking to the cavity resonance has an unlimited range, and locking at  $\Delta_{\text{lock}} = \pm\kappa/2$  (turning points of the signal) is impossible.

## D.2.2 Adjusting laser frequency

The modulator used for the frequency adjustment has a dual-parallel Mach-Zehnder modulator (DP-MZM) realization, which can be set up to work as an IQM by adjusting its internal bias DC voltages (not shown in

the schematic), as described in appendix C.3.4. By injecting the same MW signal shifted by  $90^\circ$  in the I and Q ports, one can obtain the modulator output which is a frequency-shifted copy of its input, with the shift equal to the frequency of the MW signal.

To demonstrate this, let us assume the incident optical beam to have amplitude  $a_L$  and frequency  $\omega_L$ , and the MW modulation having frequency  $\nu_0$  and depth  $b$  (the same for both quadratures). Furthermore, we will ignore the carrier, because the modulator works in the suppressed carrier regime. This turns the output of the modulator (starting from equation (C.83)) into

$$\begin{aligned} a_{\text{out}}(t) &= a_L e^{-i\omega_L t} (I(t) - iQ(t)) \\ &= a_L e^{-i\omega_L t} (b \cos(\nu_0 t) - ib \sin(\nu_0 t)) = a_L b e^{-i(\omega_L + \nu_0)t}, \end{aligned} \quad (\text{D.8})$$

where  $I(t) = b \cos(\nu_0 t)$  and  $Q(t) = b \sin(\nu_0 t)$  are the microwave signals controlling respectively I and Q quadratures of the optical field. It can be seen, that the output signal is shifted in frequency by  $\nu_0$  and scaled down by a factor of  $b$ . The shift direction can be reversed by flipping sign of one of the microwave signals, or by exchanging them.

### D.2.3 Calibrating and stabilizing IQM control voltages

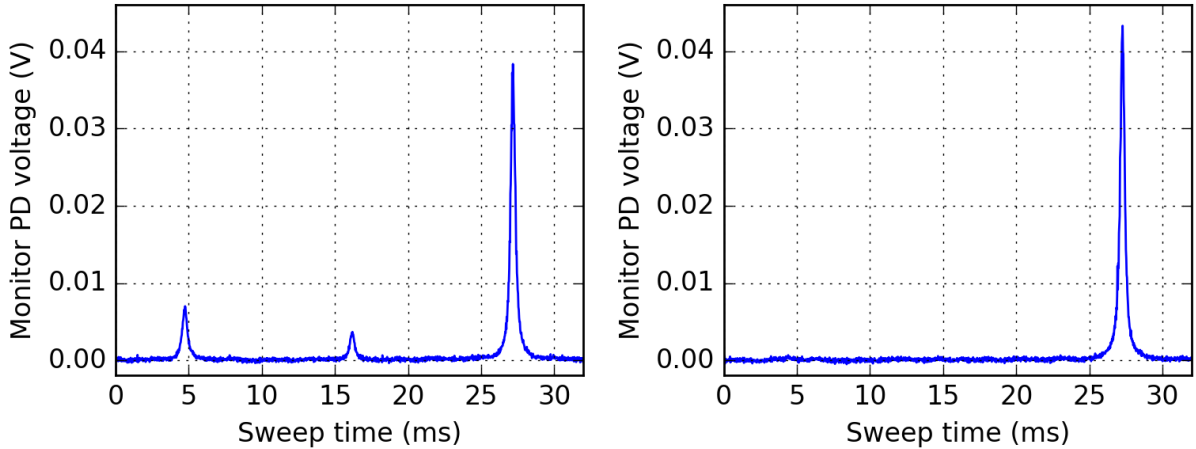


Figure D.4: Typical TFPC sweep for the DP-MZM output with unadjusted control voltages (left) and with adjusted control voltages (right). The width of the peaks corresponds to the TFPC linewidth, which is about 200 MHz. The distance between the peaks corresponds to the IQM drive frequency, which is typically around 3 GHz.

As mentioned in appendix C.3.4, operating the DP-MZM in the IQM mode requires careful adjustment of the control voltages (denoted as  $\text{DC}_1 \dots \text{DC}_3$  in Figure D.5). To perform the initial voltage calibration, we use the TFPC as a spectrum analyzer, which allows us to measure the power in the carrier and both sidebands transmitted through the IQM. Examples of such spectra are shown in Figure D.4. Using this data, we adjust the control voltages until only one sideband is visible in the IQM transmission; from the estimated SNR of the spectrum measurements, this corresponds to at least 99% of the transmitted power contained in the sideband.

To perform subsequent fine tuning and stabilization during the experiment, we make use of the high-frequency beatnotes in the monitor FPD. The schematic of the corresponding part of the setup is shown in the top part of Figure D.5. The high-frequency part of the monitor FPD photocurrent is separated from the DC part in the bias tee, and then amplified by a chain of broadband ( $0.05 \div 6$  GHz frequency range) MW amplifiers. This amplified signal can contain two beatnotes: one at a VCO frequency ( $2.8 \div 3.5$  GHz), which comes from the sidebands beating with the carrier, and another at twice the VCO frequency ( $5.6 \div 7.0$  GHz), coming from the two sidebands beating with each other. If the DP-MZM operates as a perfect IQM, then neither carrier nor the other sideband are present, and both beatnotes should be zero. Thus, we need to tune the control voltages

in a way that minimizes the beatnotes. To detect their powers separately, the amplified beatnote is sent into a 2-way splitter, one arm of which is low-pass filtered (to keep only the beatnote at the VCO frequency), and the other arm is high-pass filtered (to keep the other beatnote). After that, both arms are sent into MW power detectors (MWPDP), which transform the beatnote powers into DC voltages. These voltages are then digitized and sent into a PC, which generates the three control voltages  $DC_1 \dots DC_3$  that minimize the beatnote powers.

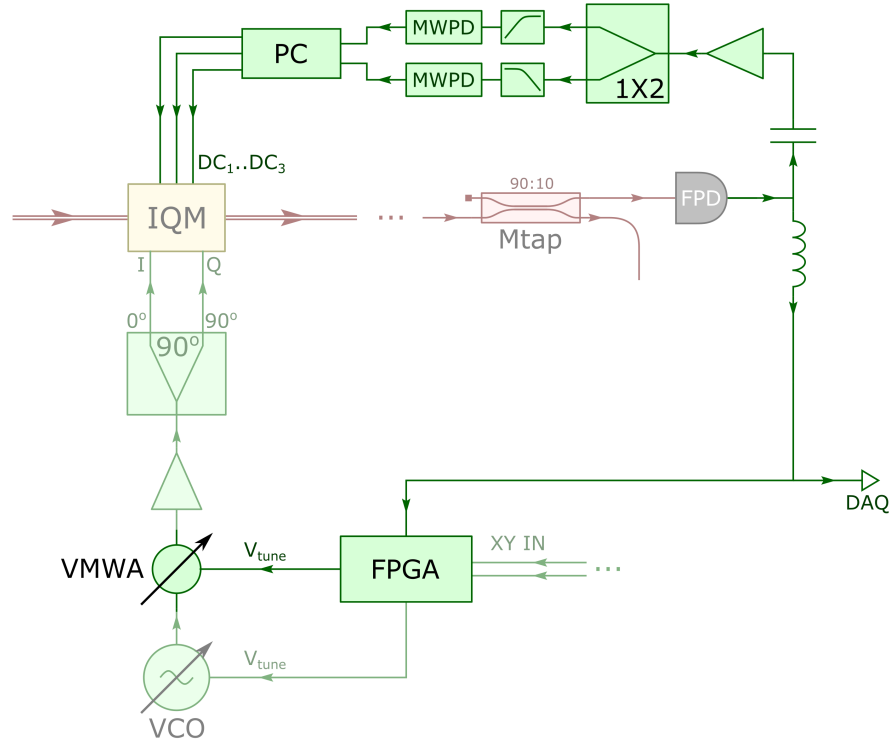


Figure D.5: Schematic of the IQM control voltage stabilization. Red symbols denote optical components, with red lines corresponding to the interconnecting optical fibers; double lines denote polarization-maintaining fibers, while single lines denote regular fibers. Green symbols denote electrical components, with green lines showing either MW or low frequency connections. The parts present in the main schematic (Figure 5.2) are faded out. The optical switch and the TFPC in the monitor part of the setup are omitted for clarity.

One more source of potential uncertainty is the frequency dependence of the IQ modulation efficiency, which arises due to all of the MW components (VCO, amplifier,  $90^\circ$  hybrid and IQM) having their parameters vary with the VCO output frequency. To account for that, the output of the VCO is passed through the variable MW attenuator (VMWA), whose tuning voltage (which determines the attenuation) is controlled to keep the total optical power on the output of the IQM constant. The optical power is obtained from the DC port of the bias-tee (which contain information about the optical power landing on the monitor photodiode), and the feedback parameters are controlled with the FPGA, which is the same one that controls the VCO tuning voltage.

### D.3 Image rejection mixer circuit

The main Lock-in/Spectrum Analyzer used in the measurement system (ZILI) has frequency range of 600 MHz, while the locking MW tone and the motional sidebands in the MW domain are both around 2 GHz. In order to bridge this frequency gap, we employ single-sideband (SSB) mixers (which we call “up-mixers”) to increase the frequency of the ZILI outputs, and an image rejection mixer (which we call “down-mixer”) for shifting the

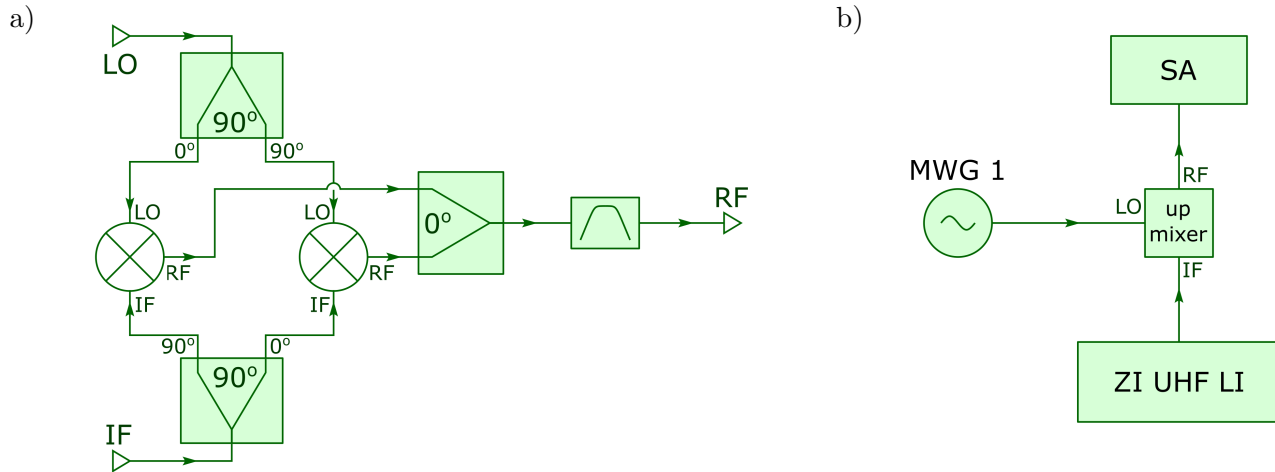


Figure D.6: a) Schematic of the SSB mixer (“up-mixer”) circuit. b) Schematic of the setup used for calibration of the mixer circuit.

frequency of the photocurrent back into the lock-in range.

Figure D.6a shows the schematic of the SSB up-mixer, which is a relatively standard design. Here both microwave local oscillator (LO) and the intermediate frequency signal (IF) from ZILI are split via  $90^\circ$  hybrids, and then get mixed in two separate mixers. The outputs of the mixers are recombined on an in-phase combiner, and then sent through a band-pass filter to improve the rejection of the unwanted sideband. The device operation is based on  $90^\circ$  hybrids providing different phase shifts for the two sidebands. The upper sideband acquires a  $+90^\circ$  phase shift in both mixers (due to the  $+90^\circ$  IF shift in the left mixer, and due to the  $+90^\circ$  LO shift in the right one), so it interferes constructively at the in-phase combiners. The lower sideband, however, gets the same  $+90^\circ$  shift in the right mixer, but a  $-90^\circ$  shift in the left mixer, since it involves the conjugate of the IF tone. As a result, it is  $180^\circ$  out of phase at the two mixer outputs, so it cancels at the final combiner. If the direction of either of the hybrids is flipped, the sideband roles are reversed, so only the lower sideband is present at the output. The down-mixer scheme is essentially the same, just with one of the  $90^\circ$  hybrids flipped and run in reverse (i.e., so that the signal enters the RF port and exits from the IF port).

The important mixer figure of merit is the full rejection ratio, which is the ratio of the up-mixed tone to all other undesirable signals on the output (lower sideband, LO leaked through, higher mixer harmonics, etc.). In the tone generation part of the setup this ratio determines the strength of the additional unwanted optical tones (generated in the phase modulator from these undesirable MW signals) landing on the cavity. In the detection part it characterizes the amount of the image noise mixed down to the IF band, which leads to SNR reduction.

To characterize the performance of the mixer circuit, we use the simple scheme shown in Figure D.6b. The up-mixer is operating in the usual regime with a fixed LO power ( $\sim 12$  dBm) and frequency (1900 MHz), while the IF signal frequency is varied over the full operation range (0 to 600 MHz). The output of the mixer is directed to the SA, which is used to measure power in all of the output tones and determine the full rejection ratio. A typical result of this kind of measurement is shown in Figure D.7. At the optimal LO power this ratio is above 20 dB in the working IF frequency band (150 MHz to 400 MHz), so in the data analysis we assume the mixer to be ideal (i.e., adding no extra tones in the generation part, and no extra noise in the detection part).

## D.4 Laser noise measurements

Here I present the procedure for measuring the classical laser noise in our setup. Since this noise can mimic quantum signatures in our undriven motion measurements[182, 13], it is important to make sure that its magnitude is low enough. Our scheme for the laser noise measurement relies on the theoretical description presented in appendix C.2.

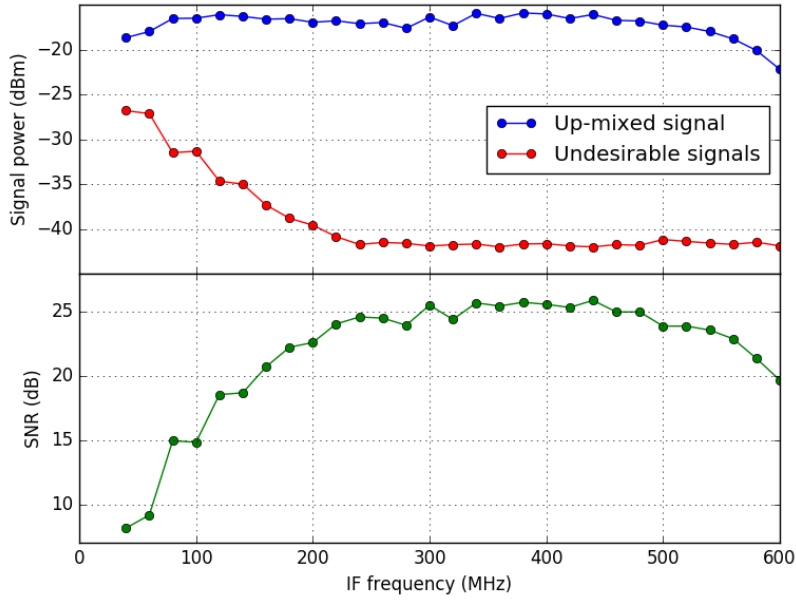


Figure D.7: Result of the mixer circuit characterization. The top figure shows the power in the up-mixed tone (blue circles) and the combined power in all other tones (red crosses) at the up-mixer output. The bottom figure plots SNR, which is the ratio of the two powers. The presented data is taken at the LO frequency of 1.9 GHz and the LO power of 12 dBm. In the experiment the typical IF frequency is  $200 \pm 20$  MHz, which implies SNR of about 22 dB.

#### D.4.1 Direct detection

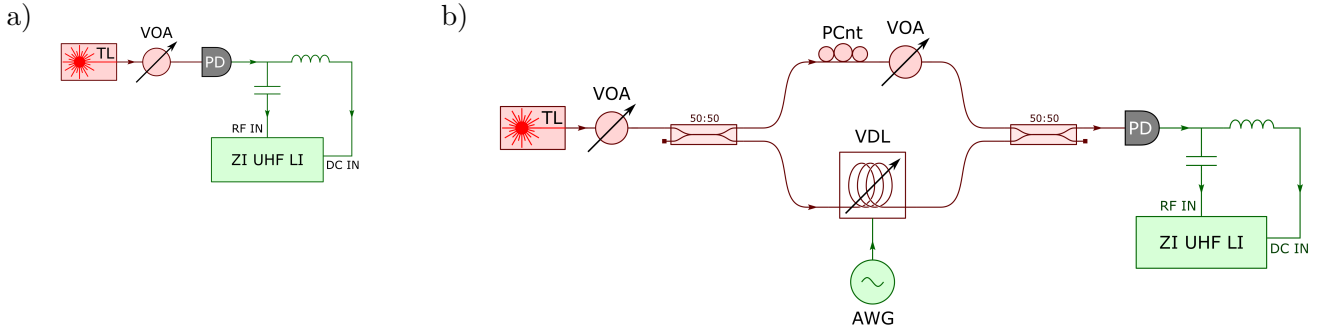


Figure D.8: a) Schematic of the setup used to measure the amplitude laser noise. b) Schematic of the delay line setup used to measure the phase laser noise.

Let us start with direct detection of the laser, which allows one to measure the laser amplitude noise. The schematic of this measurement is shown in Figure D.8a. There the output of the laser simply passes through a VOA and lands on the photodetector. The output of this detector passes through a diplexer, whose outputs are sent into the ZILI inputs. The low-frequency (DC) port of the diplexer is used to monitor the mean laser power, and the high-frequency (RF) port is routed to the spectrum analyzer inside ZILI to measure the voltage noise of the photodetector output.

We can represent the photodetector as a biased photodiode with quantum efficiency  $\sigma$ , whose output is sent into a transimpedance amplifier with a frequency-dependent gain  $G_I[\omega]$  (V/A). The representation of the photodiode can be further subdivided as an optical attenuator with the amplitude attenuation coefficient  $\sqrt{\sigma}$  (i.e., a power attenuation coefficient  $\sigma$ ) followed by an ideal photodiode. Given an optical tone of power  $P_L$

and frequency  $\omega_L$ , the amplitude incident on the photodetector is  $a_L = \sqrt{\frac{P_L}{\hbar\omega_L}}$  and the amplitude after the attenuator is  $\sqrt{\sigma}a_L$ , which generates the mean photocurrent  $\langle i \rangle = e|\sqrt{\sigma}a_L|^2 = e\sigma\frac{P_L}{\hbar\omega_L}$ . Finally, the voltage on the photodiode output is

$$V = G_I[0]\langle i \rangle = \sigma\frac{e}{\hbar\omega_L}G_I[0]P_L = G_P[0]P_L \quad (\text{D.9})$$

$$G_P[\omega] = \sigma\frac{e}{\hbar\omega_L}G_I[\omega], \quad (\text{D.10})$$

where we have defined the frequency-dependent power gain of the photodiode  $G_P[\omega]$ , which is the proportionality coefficient between the optical power modulation at a frequency  $\omega$  and the corresponding voltage response.

Next, we consider the photodiode voltage PSD, for which we use the expression (C.37) with the attenuation coefficient  $\alpha = \sqrt{\sigma}$ :

$$\begin{aligned} S_{VV}[\omega] &= (G_I[\omega])^2 S_{ii}[\omega] = (G_I[\omega])^2 e^2 \sigma |a_L|^2 (4\sigma |a_L|^2 S_{xx}[\omega] + 1) \\ &= (G_P[\omega])^2 \left( 4P_L^2 S_{xx}[\omega] + P_L \frac{\hbar\omega_L}{\sigma} \right). \end{aligned} \quad (\text{D.11})$$

One can see that non-ideal quantum efficiency ( $\sigma < 1$ ) can lead to overestimation of the shot noise level.

From equation (D.11) the classical and the quantum noise produce equal contributions to the photocurrent PSD when the laser power is  $P_L = \hbar\omega_L/(4\sigma S_{xx}[\omega])$ . For an ideal photodiode ( $\sigma = 1$ ) we recover the shot noise limited power  $P_{L,\text{SN}}^{(\text{xx})} = \hbar\omega_L/(4S_{xx}[\omega])$  defined in appendix C.2.3. For a realistic photodiode this power is higher, since the light experiences additional attenuation  $\sigma$  (see also equation (C.37)).

Different dependence of the classical noise and shot noise on  $P_L$  in equation (D.11) provides a way to separate the two contributions in the noise PSD by varying the total laser power. In order to do that reliably, one needs to know the frequency dependence of the photocurrent amplifier gain  $G_I[\omega]$  (in the simplest case, the amplifier bandwidth is large enough that  $G_I$  can be assumed frequency-independent) and the quantum efficiency of the photodetector (which is usually specified, or can be extracted from the power gain  $G_P$  if the photocurrent amplifier gain  $G_I$  is known). The procedure goes as follows:

- (a) Establish the power gain  $G_P[\omega]$  of the photodetector. One can either use a value specified in the manufacturer's datasheet, or determine  $G_P[0]$  using an independent optical power meter and then use known dependence  $G_I[\omega]$  to find  $G_P[\omega] = (G_I[\omega]/G_I[0])G_P[0]$ .
- (b) Using the VOA, vary the power  $P_L$  incident on the photodetector, and for each power determine  $S_{VV}(P_L)$  at the frequency of interest using a spectrum analyzer.
- (c) Fit this dependence  $S_{VV}(P_L)$  to a second-degree polynomial:  $S_{VV}(P_L) = a_2 P_L^2 + a_1 P_L + a_0$ . By comparing this expression to (D.11) we obtain

$$a_2 = 4(G_P[\omega])^2 S_{xx} \quad (\text{D.12})$$

$$a_1 = (G_P[\omega])^2 \frac{\hbar\omega_L}{\sigma}. \quad (\text{D.13})$$

The coefficient  $a_2$  yields the classical noise magnitude  $S_{xx}$ , while  $a_1$  (which should be known given  $G_P[\omega]$  and  $\sigma$ ) provides a self-consistent check of the calibration procedure. The zeroth-order coefficient  $a_0$  is simply the combined dark noises of the photodetector and the spectrum analyzer.

## D.4.2 Phase noise measurements

As shown in equation (C.37), the phase laser noise can not be measured via direct detection. In order to convert it into an amplitude noise and observe it, we employ the delay line measurement technique described in appendix C.2.6.

The setup schematic is shown in Figure D.8b. Like in the direct detection method, the laser first goes through the VOA to vary the total power. After that it is sent into a Mach-Zehnder interferometer, one arm of which contains a variable delay line (VDL), while the other has a VOA and a PCnt. Both the VOA and the PCnt ensure that the light in the two arms of the interferometer have equal amplitude ( $\alpha = \beta$  in terms of appendix C.2.6) and polarization, which simplifies interpretation of the experimental results. After recombining, the light is sent to the photodiode (PD), and the resulting signal is treated in the same way as for direct detection. The delay line is driven by a sine wave from an arbitrary wave generator with amplitude on the order of laser wavelength. This leads to averaging over all possible values of the phase shift  $\delta\phi$  between the two arms, as described in C.2.6.

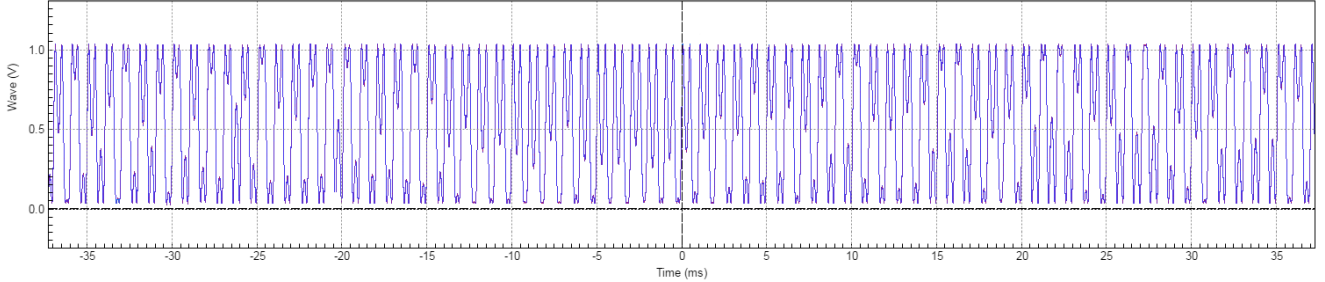


Figure D.9: Typical time dependence of the DC photodetector signal in the delay line measurement setup. The fast (on the scale of  $\sim 1$  ms) oscillations are created by the VDL drive generated by AWG, which for the shown data has a span of about one optical wavelength. The slower ( $\sim 10$  ms) variations correspond to the drift in the path length difference between the two arms coming from external acoustic vibrations and temperature fluctuations.

Figure D.9 shows a typical time trace of the DC voltage on the output of the photodetector. It oscillates between about zero when the light from the two arms interferes destructively and maximum of  $\sim 1$  V when the light interferes constructively. The phase modulator and the variable optical attenuator are adjusted to minimize the lower voltage bound. This ensures that the destructive interference of the light in two arms is complete, which guarantees that they are matched in power and polarization.

Since the interferometer is designed to average over all phase differences  $\delta\phi$ , and it is adjusted to have equal arms ratio, the average photocurrent is given by equation (C.43) with  $\alpha = \beta = 1/2$ , and its PSD is described by equation (C.45). After introducing the power photodetector gain similarly to equation (D.9) from the previous subsection, equation (C.45) gives rise to the following voltage PSD:

$$S_{VV}[\omega] = (G_P[\omega])^2 \times \left( 6P_L^2 S_{xx}[\omega] \cos^2(\omega\tau_d/2) + 2P_L^2 S_{yy}[\omega] \sin^2(\omega\tau_d/2) + P_L \frac{\hbar\omega_L}{\sigma} \right). \quad (\text{D.14})$$

Note that in this expression  $P_L$  denotes the average power landing on the photodiode, which is only half of the power emitted by the laser. This produces the difference (by a factor of two) compared to equation (C.45).

In the majority of cases the phase noise of the laser is significantly larger than the amplitude noise. This means that the PSD described by the equation (D.14) will have noticeable modulations with a period of  $\Delta\omega = 2\pi/\tau_d$ . These come from the oscillation (in  $\omega$ ) between the points where the PSD contains strictly amplitude noise, and the point where it contains strictly phase noise. An example of such oscillations is shown in figure D.10; their period is about 13.7 MHz, which means that the time delay between the two arms is about  $\tau_d = 73$  ns, corresponding to the path length difference of 21.9 m. This is consistent with the specified VDL length of 19 m, which corresponds to  $\sim 27$  m of the effective path length difference.

By choosing the appropriate noise measurement frequency, it is possible to perform measurements sensitive only to the amplitude noise or only to the phase noise. Since we are mostly interested in phase noise (as it is usually much larger than the amplitude noise in a typical laser), we can choose the frequency to be

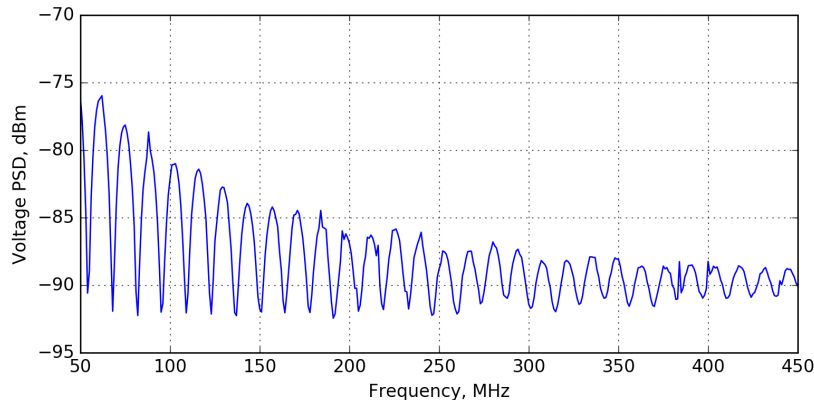


Figure D.10: Typical PSD of the photodetector voltage in the delay line measurement. The minima are located at frequencies  $\omega_n = 2\pi n/\tau_d$  where the measurement is only sensitive to the amplitude noise; the maxima correspond to frequencies  $\omega_n = 2\pi(n + 1/2)/\tau_d$ , where the measurement is only sensitive to the phase noise.

$\omega_n = 2\pi(n + 1/2)/\tau_d$ , where the expression (D.14) gets simplified to

$$S_{VV}[\omega_n] = (G_P[\omega_n])^2 \left( 2P_L^2 S_{yy}[\omega_n] + P_L \frac{\hbar\omega_L}{\sigma} \right). \quad (\text{D.15})$$

This expression is almost exactly identical to equation (D.11) obtained for the direct detection. Hence, the rest of the measurement proceeds as described in the previous section.

In the end, we measured the phase shot noise limited power for our laser around 300 MHz away from the main tone to be  $30 \pm 5 \mu\text{W}$  without the filter cavity, and  $> 200 \mu\text{W}$  with the filter cavity (the classical noise was too small to detect it definitively).

The scheme for the phase noise measurements described here is fairly simple and versatile, as it only requires a single laser and can in principle be implemented with minimal number of optical components: the variable delay line, the only non-trivial component, can be substituted for a long enough optical fiber, provided that the ambient temperature and acoustic fluctuations lead to sufficient averaging over  $\delta\phi$ . The main limitation is that its sensitivity is frequency dependent. In the simple case described above it measures phase noise only at specific frequencies  $\omega_n$ ; in principle, it is possible to measure the amplitude noise separately and subtract it in the equation (D.14), yielding decent sensitivity to the phase noise at most frequencies.

Another way to estimate the laser phase noise using the reflection off of the experimental cavity is mentioned in appendix D.10.

## D.5 EDFA noise calibration

As the mechanical motion calibration scheme relies on knowledge of the total quantum efficiency of the measurement setup, it is important to determine the added noise of the EDFA. The scheme that we use to calibrate it relies on adding a small amplitude-modulation signal to the laser, and using the shot noise background as a reference for the added noise. This way, the added noise is determined directly in the units of shot noise, which is the amplifier noise figure (NF).

Figure D.11 shows the schematic of the noise measurement setup. The light out of the laser first enters the amplitude modulator (AM) driven by a sine wave from the arbitrary wave generator (AWG), where it acquires small amplitude sidebands serving as a calibration signal. After that it passes through a VOA and into a 90:10 optical splitter. The light out of the 10% port lands on the power meter (PM) and serves to monitor the power leaving at the other (90%) port of the splitter. After that the light out of the 90% port either lands directly on the PD, or passes through the EDFA and a wide-bandwidth (0.5 nm) TF which filters out amplified spontaneous emission (ASE) on the output of the EDFA. The output of the photodetector then passes through a diplexer, and then both arms are sent into the ZILI.

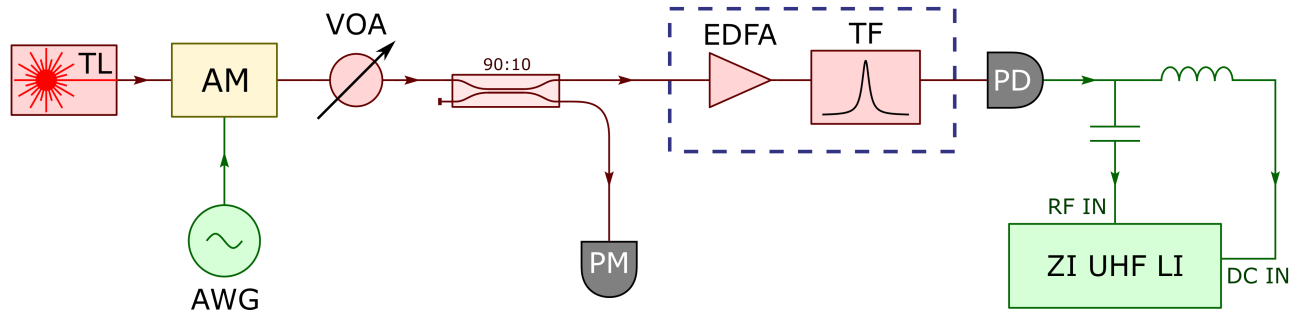


Figure D.11: Schematic of the setup used for the EDFA calibration.

The noise figure calibration proceeds in two stages. First, the measurement is done without the EDFA and the TF. The total laser power is varied using the VOA, and for each laser power the tap PM reading, the DC voltage, the noise PSD (in  $V^2/\text{Hz}$ ) and the power in the signal (in  $V^2$ ) are recorded. The noise PSD is analyzed in the same way as the classical amplitude noise (subsection D.4.1), yielding the magnitude of the classical noise and the RF power gain  $G_P[\omega]$  extracted from the shot noise power (assuming we know the quantum efficiency of the PD). A typical result of this analysis is shown in Figure D.12a. The signal power is fit to the quadratic function of the incident optical power, which lets us extract the signal tone magnitude relative to the optical carrier. An example of such a fit is demonstrated in Figure D.12b.

After that, the EDFA and the filter are inserted in the setup, and the measurement described above is repeated. While doing that, it is important to keep the AM drive constant, as the calibration scheme relies on it being the same in both stages. The analysis then proceeds as follows:

- (a) Using the tap power and the signal power dependence extracted earlier, calculate the expected signal power in the absence of the amplifier. Comparing it to the measured signal power allows us to extract the small-signal gain of the EDFA.
- (b) Subtract the electronic noise background and the photodiode shot noise (calculated for the actual power landing on the photodiode, as measured by its output DC voltage) from the background PSD. The resulting noise is solely the output noise the EDFA.
- (c) Using the small-signal gain, calculate the expected amplified classical and shot noise background PSDs. After subtracting the classical noise contribution from the experimental noise PSD we are left with only amplified shot noise and intrinsic EDFA noise.
- (d) Divide the residual by the expected amplified shot noise. This ratio characterizes the noise figure of the amplifier, i.e., the added input noise of the amplifier relative to the vacuum (shot) noise.

This procedure is repeated for different powers incident on the EDFA, producing the dependence of the noise figure on the EDFA input power. Figure D.12c shows the measurement result. At low powers the noise figure reaches about 4 dB; for comparison, the quantum limit for an ideal phase-preserving amplifier is 3 dB. This plot also compares the NF with and without the TF, which clearly demonstrates the effect of the filtering: adding the TF reduces the NF by about 1 dB over the whole range, and also prevents it from going up at low powers. This rise without the TF happens because at low incident optical power most of the output EDFA power is contained in ASE<sup>a)</sup>, and if unfiltered it contributes a lot of noise (see also footnote in subsection 5.2.3).

After the calibration is done, it is important to preserve the connection between the 90:10 splitter and the EDFA if possible, as remaking it will likely alter the losses in the connector. This can lead to systematic errors in determining the power landing on the EDFA and, consequently, invalidate the EDFA calibration. This

<sup>a)</sup>Generally, the total EDFA output power changes by less than 20% when the input power is varied (including having no incident light at all). The main effect of changing the incident power is changing the ratio between the ASE and the amplified signal.

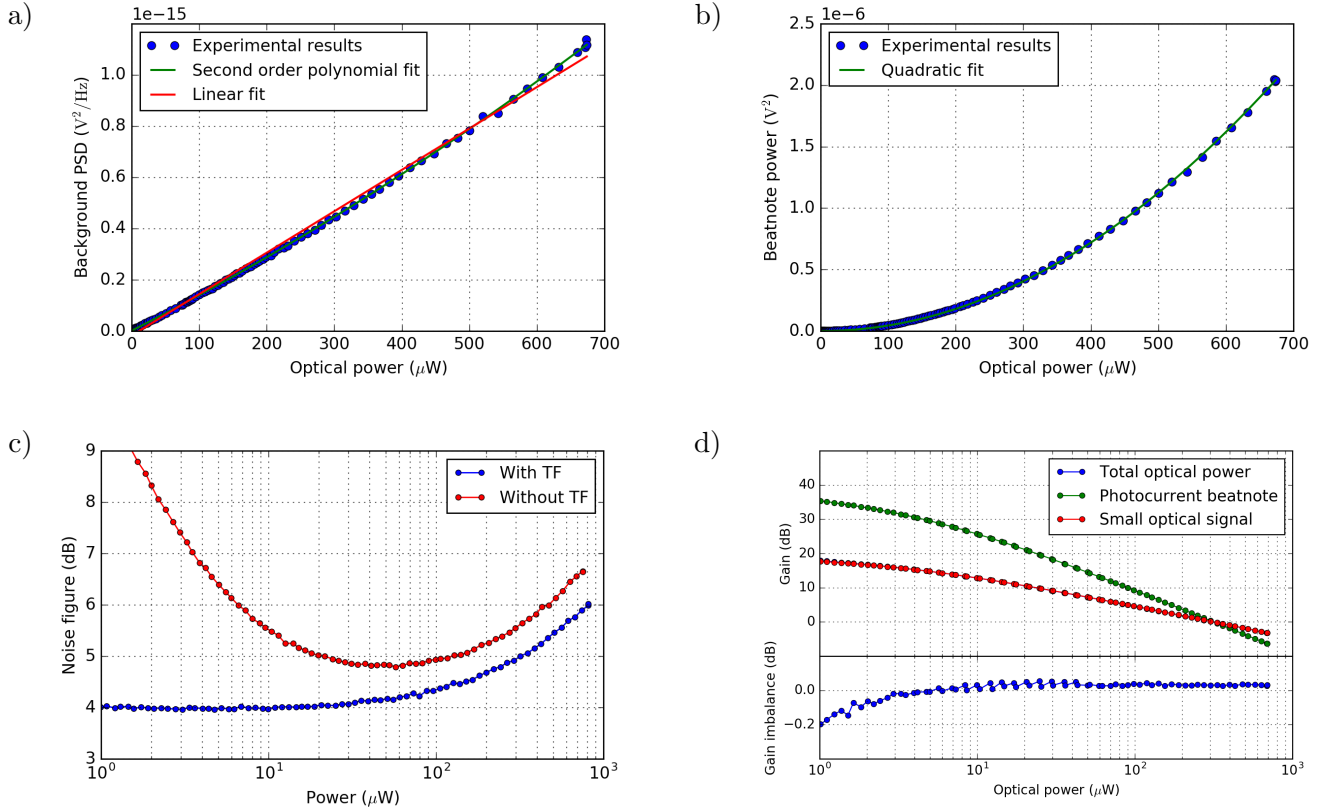


Figure D.12: Results of the EDFA noise figure calibrations.

- The background noise PSD as a function of the incident laser power (without the EDFA in the circuit). The green line is a fit to a second order polynomial with zero intercept, while the red line shows a fit to a linear function (used only for comparison). The dark noise has been subtracted, so the PSD is expected to be zero at zero optical power.
- The power in the signal peak as a function of the laser power (without the EDFA in the circuit). The green line is a fit to a quadratic function.
- The dependence of the EDFA noise figure on the incident power. The blue and the red lines show the NF with and without the TF respectively.
- The comparison of the small-signal gain and the output power gain of the amplifier. The top plot shows the output power gain (blue, almost invisible behind red), the beatnote gain (green) and the small-signal optical gain (red). The bottom plot shows the ratio of the small-signal optical gain and the output power gain.

All the measurements shown in this Figure were performed for the laser wavelength of 1539 nm (which is the optical resonance frequency in the first generation device) and the signal frequency of 32 MHz. The signal frequency is chosen as a compromise between having low laser noise (which gets lower for higher frequencies) and being well within the PD bandwidth ( $\sim 150$  MHz).

connection is still present in the main measurement setup (figure 5.2 in section 5.2), where the 90:10 splitter is denoted as Rtap.

To simplify the measurement setup, one could imagine using the ratio of the input and the output powers of the EDFA to measure gain, as opposed to adding a small AM signal as described above. However, since the EDFA output contains both the amplified signal and the ASE, the output power is not a good measure of the signal gain for low input powers. Figure D.12d illustrates this point: by taking the square root of the

small-signal beatnote gain (green) we can obtain the small-signal optical gain (red). While it looks almost identical to the optical power gain (blue, hidden behind red), the bottom plot reveals that for  $1 \mu\text{W}$  of laser power incident on the EDFA there is 0.2 dB difference in the gains. The difference comes from the fact that the output power has some ASE fraction, so the power ratio overestimates the actual optical gain.

## D.6 VNA loop gain calibration

The measurements performed by the VNA (such as OMIT/A sweeps or cavity response sweeps) can have frequency span of several hundreds of MHz (e.g., cavity sweep in the first generation device, which has optical linewidth of  $\sim 70$  MHz), and on those scales many of the employed microwave components have varying gains and phase shifts. This means that in order to extract the purely optical part of the response (which is the part occurring between the output of the phase modulator ( $\phi\text{M}$ ) and the input of the main reflection photodiode), we need to measure and cancel those frequency-dependent effects.

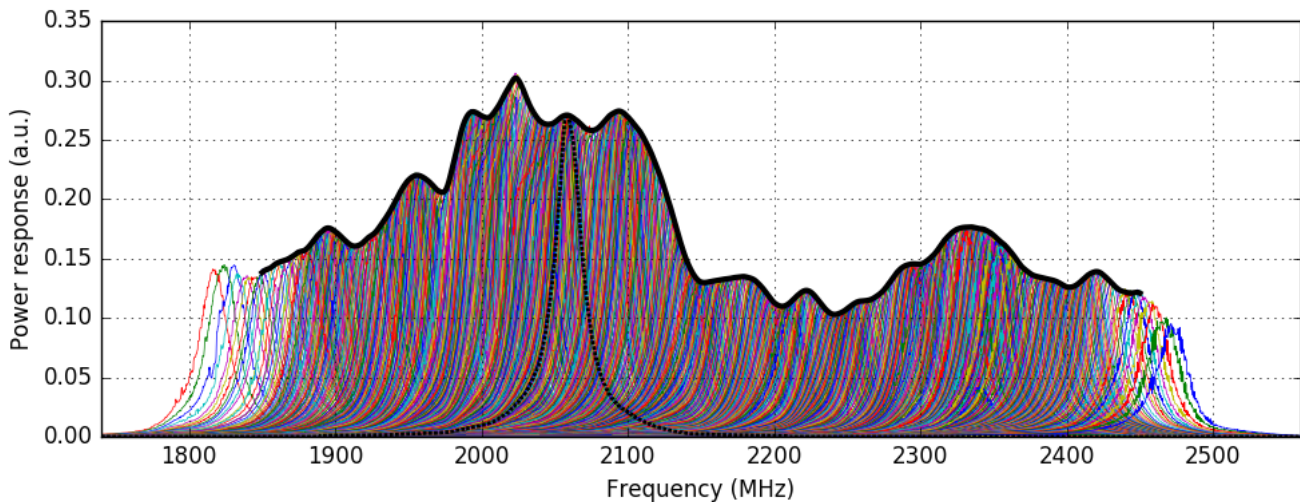


Figure D.13: Amplitude of multiple cavity response sweeps obtained with the VNA. The solid black line shows a smoothed envelope (i.e., the line passing through the maxima) of the sweeps, which is interpreted as a frequency-dependent gain. The dashed black line highlights one of the sweeps.

To do that, we need to have some controlled, consistent and detectable optical response between the phase modulator and the photodetector, which can be used as a reference to calculate the rest of the measurement loop gain (coming from the MW components). The easiest way to obtain such response is to use the experimental optical cavity itself.<sup>b)</sup> The calibration is done in the same setup as is used in the main experiments, and it essentially repeats some of the same steps. It proceeds in the following way:

- (a) In the standard experimental setup, lock the laser to the cavity. Do not send any other microwave tones (i.e., in addition to the locking tone) into the phase modulator.
- (b) Perform a standard sweep over the cavity resonance using the VNA (the basics of this measurement are described in subsection C.3.2). The sweep result is a complex Lorentzian as given by equation (C.56), but distorted by a frequency-dependent gain of the rest of the setup. The distortion includes the microwave components in the tone generation arm, frequency response of the phase modulator, frequency response of the photodetector and the microwave components in the detection arm. The central frequency of this Lorentzian is the detuning of the OLO from the cavity resonance, which is determined by the frequency

<sup>b)</sup>Since it is impossible to detect the phase modulation by direct detection, we need some non-trivial optical element to make it visible. If instead of the phase modulation we used an amplitude or a single sideband modulation, it would be sufficient to simply send the output of a modulator on the photodiode and measure the resulting response.

of the locking tone and the lock settings in the FPGA feedback. One of such sweeps is shown by a dashed black line in Figure D.13.

- (c) Repeat the VNA sweeps for multiple central frequencies of the Lorentzian, covering the whole range of frequencies for which we need to determine the loop gain. Figure D.13 shows a set of 891 such sweeps obtained over a range of cavity detunings between 1850 MHz and 2450 MHz.
- (d) Determine the envelope of the resulting set of Lorentzians. Since the Lorentzian response in the optical domain does not depend on the OLO detuning (at least, as long as that detuning is much greater than the cavity linewidth), the frequency dependence of the Lorentzians magnitude arises solely from the loop gain that we set out to calibrate. Thus, the envelope can be interpreted as the magnitude of the gain. Figure D.13 plots the smoothed envelope with a thick black line.
- (e) The phase part of the response can be determined by examining the phase the Lorentzian which contributes to the envelope (i.e., the tallest Lorentzian) at each frequency.

## D.7 Phase modulator $V_\pi$ calibration

A lot of the optomechanical measurements (such as determining optomechanical coupling from the OMIT/A signals or calibrating the undriven motion measurements) require precise knowledge of individual powers in each optical tone incident on the experimental cavity. The combined power in all the beams can be obtained using the monitor PD (its calibration is described in section D.8). The relative powers of the beams can be found by monitoring the microwave drive of the phase modulator and calibrating how the strengths of the drives at different frequencies translate to the phase sidebands strengths. In this section I describe two different procedures for performing this calibration.

### D.7.1 Optical spectroscopy approach

We start with equation (C.52) expressing the output of the phase modulator. It describes a set of optical tones centered around the optical carrier frequency  $\omega_L$  and spaced by the microwave drive frequency  $\nu_0$ . From that equation we can extract the relative power in the  $m^{\text{th}}$ -order tone (the tone with frequency  $\omega_L + m\nu_0$ ):

$$P_{\text{rel}}(m) = |J_m(\pi V_0/V_\pi)|^2. \quad (\text{D.16})$$

This expression suggests that by determining the relative optical tone powers it is possible to extract the relative drive voltage  $V_0/V_\pi$ . To measure the tone powers, we use the tunable Fabry-Perot cavity (TFPC) in the monitor arm of the setup as an optical spectrum analyzer (see Figure 5.2 and subsection 5.2.5). At the same time, we measure the microwave drive power by sending off some of the phase modulator drive through the directional coupler onto the microwave SA. The same directional coupler and SA are later used to measure the strength of the modulator drive in the experiment, which ensures that the calibration is applied in a consistent manner.

The calibration procedure goes as follows:

- (a) Using one of the available microwave generators, send a single microwave tone into the phase modulator. Configure the OSW to send the analyzed light through the TFPC, and sweep the TFPC resonance frequency over the optical carrier and the phase sidebands. Examples of such sweeps are shown in Figure D.14a.
- (b) Fit the sweep to a sum of three Lorentzians (black line in Figure D.14a), and from the fit extract  $r_{s/c}$ , the ratio of the first-order sideband power to the carrier power. Simultaneously, measure the microwave drive power  $P_0$  on the input of the spectrum analyzer.
- (c) Repeat this procedure while varying  $P_0$  to obtain the power dependence of  $r_{s/c}$ . Fit this dependence to the expected expression

$$r_{s/c}(P_0) = (J_1(\pi\sqrt{P_0/P_\pi}))^2 / (J_0(\pi\sqrt{P_0/P_\pi}))^2 \quad (\text{D.17})$$

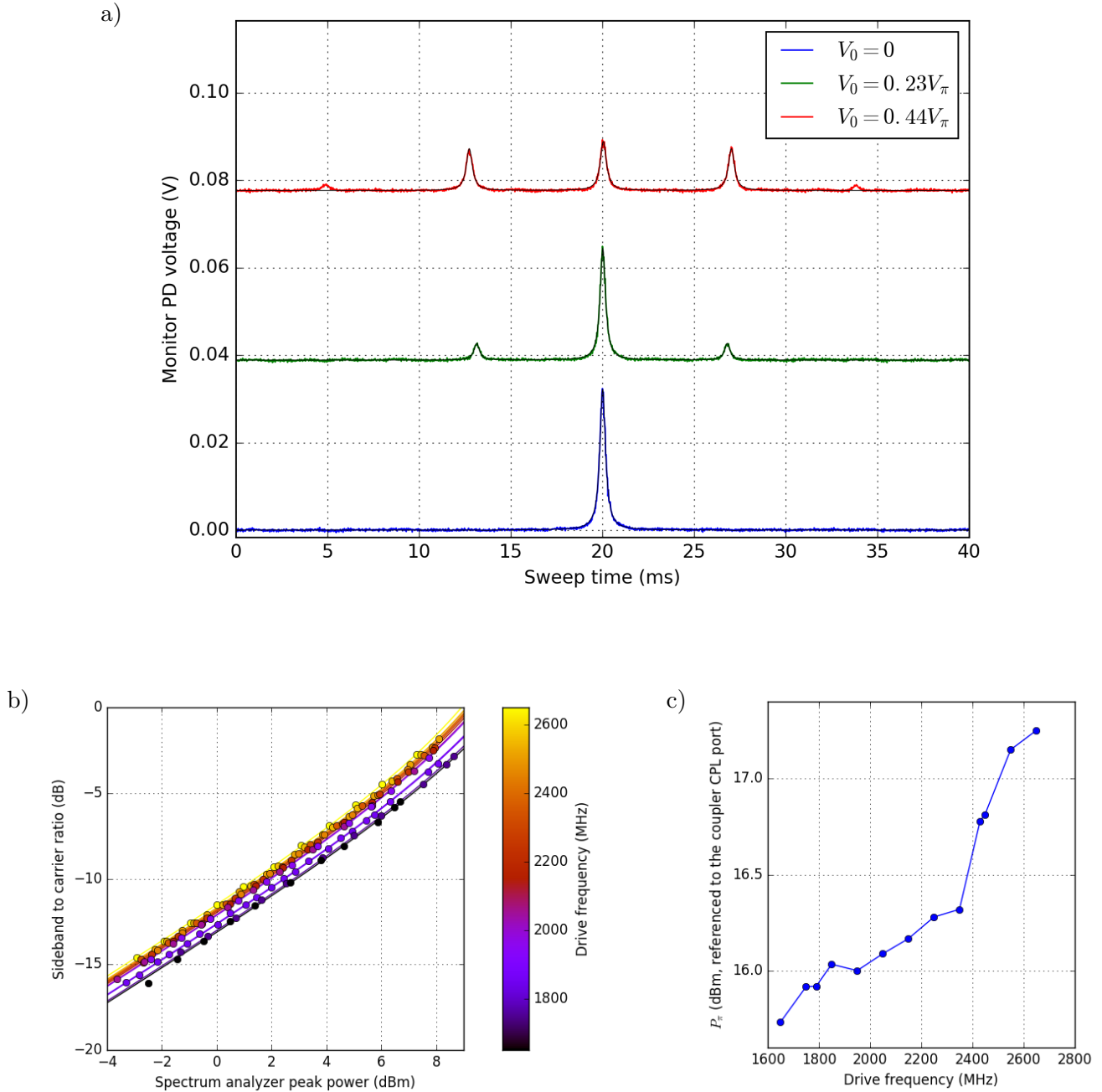


Figure D.14: Results of the  $V_\pi$  calibration using the optical spectroscopy approach.

- Examples of TFPC sweeps for different amplitudes of the microwave drive  $V_0$ . Thin black lines show fits to a sum of three Lorentzian peaks as discussed in the text. The sweeps are offset vertically for clarity.
- Dependence of the sideband-to-carrier ratio at the phase modulator output on the phase modulator drive power, as measured by the SA. Markers show experimental results, solid lines are fits to the expected dependence (D.17). Marker and line colors encode MW drive frequency.
- Resulting  $P_\pi$  (referenced to the SA input) for different drive frequencies  $\nu_0$ .

to obtain  $P_\pi$ , which is the power corresponding to  $V_\pi$  referenced to the SA. Typical experimental results for  $r_{s/c}(P_0)$  along with fits to the expression (D.17) are shown in Figure D.14b.

- (d) Repeat these steps for different drive frequencies  $\nu_0$  to get the frequency dependence of  $P_\pi$ . Figure D.14c shows this dependence for our experimental setup.

## D.7.2 Carrier depletion approach

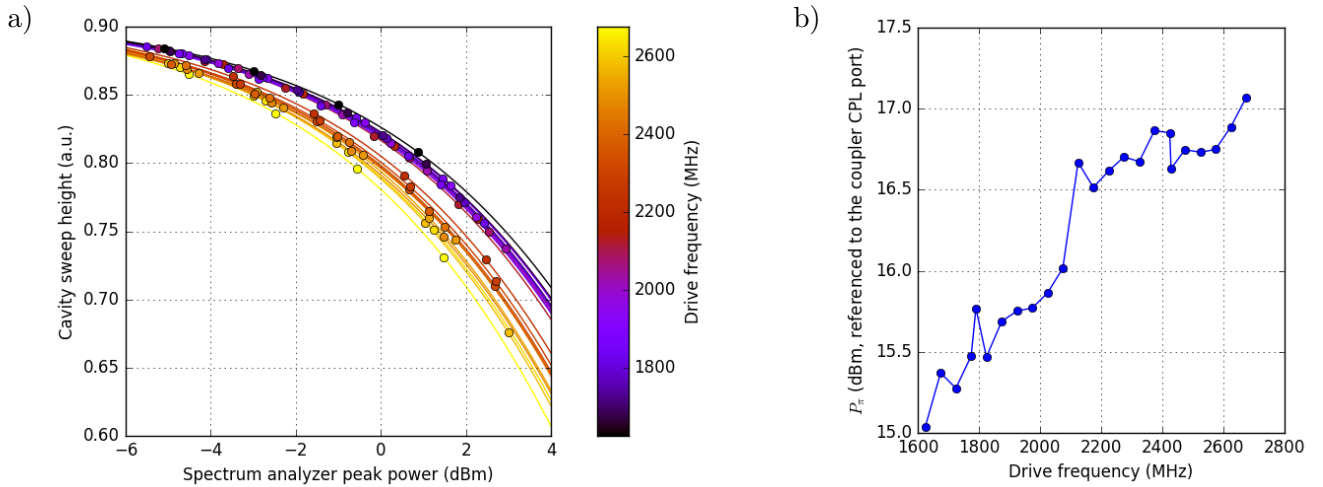


Figure D.15: Results of the  $V_\pi$  calibration using the carrier depletion approach.

- a) Dependence of the amplitude of the experimental cavity sweep on the phase modulator drive power, as measured by the SA. Markers show experimental results, solid lines are fits to the expected dependence (D.19). Marker and line colors encode MW drive frequency.
- b) Resulting  $P_\pi$  (referenced to the SA input) for different drive frequencies  $\nu_0$ .

Another way to determine the sideband magnitude is by using the fact that the sidebands draw their power from the carrier, so the carrier becomes weaker for strong MW drives. If the power in the carrier (relative to the undriven case) is detected, it can be used to extract the power in the phase sidebands and determine the microwave drive strength relative to  $V_\pi$ .

Let us consider the full expansion (C.51) for the phase modulator output in the presence of two microwave drives: a strong control tone with frequency  $\nu_0$  and relative amplitude  $\psi_0$ , and a weak probe tone with frequency  $\nu_p$  and amplitude  $\psi_p$ . If we only leave the terms up to first order in  $\psi_p$ , the output of the phase modulator can be expressed as

$$a_\phi = a_L e^{-i\omega_L t} \sum_{m=-\infty}^{+\infty} (-i)^m J_m(\psi_0) (J_0(\psi_p) - iJ_1(\psi_p)e^{-i\nu_p t} - iJ_1(\psi_p)e^{+i\nu_p t}) e^{-im\nu_0 t}. \quad (\text{D.18})$$

To extract the carrier depletion due to the control tone  $J_0(\psi_0)$ , we perform the cavity response sweep, as described in section D.6 and appendix C.3.2. We assume that only the upper probe sideband is close to the cavity resonance, and all other tones (including the ones generated by the presence control drive) are far off resonance, and therefore are simply reflected off the input cavity mirror. As shown in appendix C.3.2, the photocurrent beatnote at the frequency  $\nu_p$  comes from the beating of the carrier and the probe sideband which interacted with the cavity, and the magnitude of this beatnote is proportional to the product of the two amplitudes. In our case the carrier amplitude is  $a_{L,0} = a_L J_0(\psi_0) J_0(\psi_p)$ , and the probe sideband amplitude is  $a_{L,1} = -i a_L J_0(\psi_0) J_1(\psi_p)$ . This leads to the beatnote (c.f. (C.56)

$$\begin{aligned} \langle i \rangle &\propto (a_L J_0(\psi_0) J_0(\psi_p))^* (a_L J_0(\psi_0) J_1(\psi_p)) \chi_{c,\text{rel}}[\Delta + \nu_p] e^{-i\omega_p t} \\ &= (J_0(\psi_0))^2 (|a_L|^2 J_0(\psi_p) J_1(\psi_p)) \chi_{c,\text{rel}}[\Delta + \nu_p] e^{-i\omega_p t}. \end{aligned} \quad (\text{D.19})$$

Since its magnitude is proportional to  $(J_0(\psi_0))^2$ , by performing this kind of sweep for multiple control beam amplitudes  $\psi_0 = \pi\sqrt{P_0/P_\pi}$  and fitting their magnitude to the expected dependence  $|\langle i \rangle| \propto (J_0(\psi_0))^2$  it is possible to extract  $P_\pi$  for a given frequency of the control beam. The rest of the calibration procedure is essentially the same as in the previous subsection. Figure D.15a shows the measured beatnote magnitude as a function of the phase modulator drive power  $P_0$  together with the fits to the expected dependence (D.19), and Figure D.15b shows the resulting values of  $P_\pi$  for different drive frequencies.

## D.8 Incident and reflected power calibration

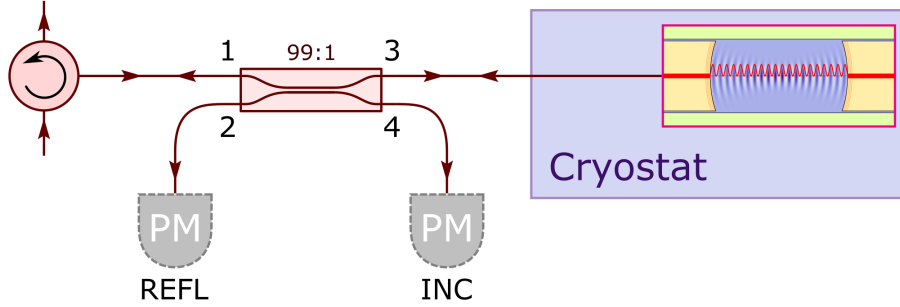


Figure D.16: Schematic of the power calibration part of the setup.

As mentioned in section D.7, to determine powers in individual laser tones we need to determine the total laser power. This power calibration is performed using the 99:1 splitter between the circulator and the experimental cavity. The schematic of this part of the setup is shown in Figure D.16. The splitter has been pre-calibrated to precisely determine the ratio between the power incident on the device (port 3) and power in the INC tap (port 4) and the ratio between the power reflected from the device (port 3) and the REFL tap (port 2).

During the calibration procedure, a power meter is connected to either port 2 or port 4 of the splitter, and its reading together with the splitter ratios provide respectively reflected or incident laser power. These powers are then related to the DC voltages on the output of the monitor (Mtap splitter in Figure 5.2) or the reflection (Rtap splitter in Figure 5.2) photodiode, providing a way to determine them during the experiment without use of the power meter. In addition, the ratio of the reflected power to the power landing on the reflection photodiode yields  $\eta_{\ell, \text{EDFA}}$ , the magnitude of the loss between the calibration splitter and the EDFA. This value is important in determining the total measurement quantum efficiency for the undriven motion calibrations (see subsection 8.3.2).

In principle, there can be additional losses between port 3 of the splitter and the experimental cavity, which could come from the fiber connector or light absorption inside the refrigerator. We assume that these losses are equal for the incident and for the reflected light, which is true for reciprocal noise sources such as simple absorption or scattering. This lets us calculate one-way loss as a square root of the round-trip loss:  $\eta_{\ell, \text{fridge}} = \sqrt{P_{\text{refl}}/P_{\text{inc}}}$ , where  $P_{\text{inc}}$  and  $P_{\text{refl}}$  are respectively the incident and the reflected power measured at the port 3 of the splitter. Hence, the power incident on the input mirror of the cavity is  $P_{\text{ext}} = P_{\text{inc}}\eta_{\ell, \text{fridge}} = \sqrt{P_{\text{inc}}P_{\text{refl}}}$ , and the total loss between the device and the EDFA is  $\eta_{\ell} = \eta_{\ell, \text{EDFA}}\eta_{\ell, \text{fridge}}$ .

## D.9 Sideband correlator angle calibration

The sideband correlator  $S_{ii}^{(\text{rb})}[\delta\omega]$  is a complex quantity, so it is important to calibrate its complex phase in order to correctly extract its real (Lorentzian) and imaginary (anti-Lorentzian) parts. To understand the way we do it, first recall the procedure for obtaining the sideband spectra  $S_{ii}^{(\text{rr})}$  and  $S_{ii}^{(\text{bb})}$  described in subsection 8.3.2. There the two mechanical sidebands in the photocurrent get eventually mixed down in the ZILI to produce

the two records  $i_\ell(t)$  and  $i_u(t)$ , which correspond to some narrow ( $\sim 100$  kHz) frequency band around the corresponding demodulation frequencies. If the demodulation frequencies are chosen correctly, the two records can be readily identified with the sideband photocurrents  $i_r[\delta\omega]$  and  $i_b[\delta\omega]$  defined in equation (7.28). Given this correspondence, we Fourier transform these photocurrent records, which allows us to calculate their PSDs as  $S_{ii}^{(\text{uu})}[\delta\omega] = \langle |i_u[\delta\omega]|^2 \rangle$  and  $S_{ii}^{(\ell\ell)}[\delta\omega] = \langle |i_\ell[\delta\omega]|^2 \rangle$  and associate them with the theoretical PSD expressions (equation (7.29) and (7.30)). In calculating  $S_{ii}^{(\text{uu})}$  and  $S_{ii}^{(\ell\ell)}$  the ensemble averaging is usually replaced by time averaging or data binning.

In the same manner, we can calculate the cross-correlator  $S_{ii}^{(\text{u}\ell)}[\delta\omega] = \langle i_u[\omega]i_\ell[-\omega] \rangle$ , which is an analogue of the theoretical cross-correlator  $S_{ii}^{(\text{rb})}[\delta\omega]$ . However, unlike the PSDs which only depend on a single photocurrent record, the cross-correlator includes both of the records, so it is crucially dependent on the frequencies and phases of the records being precisely defined and locked to each other. If their relative phase is poorly defined, the cross-correlator will also acquire a random phase, and if their frequencies are slightly shifted (e.g., if the frequencies of the two control tones are not locked), the phase of  $S_{ii}^{(\text{u}\ell)}[\omega]$  will change in time, and it will converge to zero instead of some finite value.

Let us examine these effects quantitatively. We start by establishing a theoretical expression for the photocurrent  $i(t)$  right at the photodetector output, i.e., before mixing down and demodulating. Even though the exact cross-correlator value (7.55) depends on quantum effects and inclusion of the optical vacuum noise, here for simplicity we will consider a classical system by setting  $\hat{\xi} = 0$  and treating the mechanical amplitude  $\hat{c} = c$  as a classical random variable. As far as the control beam frequencies and phases are concerned, this treatment should capture all of the important issues. In this classical treatment we can simply say that the photocurrent is (up to a gain coefficient  $G$ ) square of the incident optical field:  $i(t) = G|a_{\text{det}}(t)|^2$ . If we assume the same heterodyne measurement scheme as in appendix C.1.2, we can represent  $a_{\text{det}}$  as

$$a_{\text{det}}(t) = a_{\text{OLO}}e^{-i\omega_{\text{OLO}}t} + d_{\text{out}}(t). \quad (\text{D.20})$$

Up to first order in  $d_{\text{out}}$  the photocurrent is

$$i(t) \approx |a_{\text{OLO}}|^2 + (a_{\text{OLO}}^*d_{\text{out}}(t)e^{+i\omega_{\text{OLO}}t} + \text{c.c.}). \quad (\text{D.21})$$

Here we only focus on the interesting part of the reflected light (the one containing the mechanical sidebands), and not on, e.g., the reflected control beams. To express  $d_{\text{out}}$  in the time domain, we are going to use equation (7.23) and assume the fast (compared to the mechanical lifetime) cavity limit  $\gamma_{\text{m,eff}} \ll \kappa$  (in our systems  $\gamma_{\text{m,eff}} < 2\pi \cdot 10$  kHz and  $\kappa > 2\pi \cdot 20$  MHz), i.e., set  $\chi_c[\omega] \approx \chi_c[\omega_r]$  for the Stokes sideband and  $\chi_c[\omega] \approx \chi_c[\omega_b]$  for the anti-Stokes sideband:

$$d_{\text{out}}[\omega] \approx i\sqrt{\kappa_{\text{ext}}}g^{(0)}\chi_c[\omega_b]\bar{a}_\ell c[\omega - \Delta_\ell] - i\sqrt{\kappa_{\text{ext}}}g^{(0)}\chi_c[\omega_r]\bar{a}_u c^*[\omega - \Delta_u] \quad (\text{D.22})$$

$$d_{\text{out}}(t) \approx i\sqrt{\kappa_{\text{ext}}}g^{(0)}\chi_c[\omega_b]c(t)\bar{a}_\ell e^{-i\Delta_\ell t} - i\sqrt{\kappa_{\text{ext}}}g^{(0)}\chi_c[\omega_r]c^*(t)\bar{a}_u e^{-i\Delta_u t}. \quad (\text{D.23})$$

We have to keep in mind that this expression for  $d_{\text{out}}$  is derived in the cavity frame, which means that  $\omega_{\text{OLO}}$  is specified in the same frame, i.e., it is the OLO detuning from the cavity resonance.

Given the expression (D.22) for  $d_{\text{out}}$ , we obtain the photocurrent

$$i(t) = |a_{\text{OLO}}|^2 + \left( i\sqrt{\kappa_{\text{ext}}}g^{(0)}\chi_c[\omega_b]c(t)(a_{\text{OLO}}^*\bar{a}_\ell e^{-i(\Delta_\ell - \omega_{\text{OLO}})t}) \right. \\ \left. - i\sqrt{\kappa_{\text{ext}}}g^{(0)}\chi_c[\omega_r]c^*(t)(a_{\text{OLO}}^*\bar{a}_u e^{-i(\Delta_u - \omega_{\text{OLO}})t}) + \text{c.c.} \right). \quad (\text{D.24})$$

Since  $\Delta_\ell$ ,  $\Delta_u$  and  $\omega_{\text{OLO}}$  are in the same frame, the terms  $\Delta_\ell - \omega_{\text{OLO}}$  and  $\Delta_u - \omega_{\text{OLO}}$  are the absolute frequency differences between the control beams and the OLO, i.e.,  $\Delta_\ell - \omega_{\text{OLO}} = \nu_{\text{con},\ell}$ ,  $\Delta_u - \omega_{\text{OLO}} = \nu_{\text{con},u}$ .

Finally, we can separate the photocurrent into two different parts corresponding to the two sidebands:

$$i(t) = |a_{\text{OLO}}|^2 + (i_\ell(t) + i_u(t) + \text{c.c.}) \quad (\text{D.25})$$

$$i_\ell(t) = i\sqrt{\kappa_{\text{ext}}}g^{(0)}\chi_c[\omega_b]\alpha_\ell c(t)e^{-i\nu_{\text{con},\ell}t} \equiv G_\ell\alpha_\ell c(t)e^{-i\nu_{\text{con},\ell}t} \quad (\text{D.26})$$

$$i_u(t) = -i\sqrt{\kappa_{\text{ext}}}g^{(0)}\chi_c[\omega_r]\alpha_u c^*(t)e^{-i\nu_{\text{con},u}t} \equiv G_u\alpha_u c^*(t)e^{-i\nu_{\text{con},u}t}, \quad (\text{D.27})$$

where  $G_{\ell,u} = \pm i\sqrt{\kappa_{\text{ext}}}g^{(0)}\chi_c[\omega_{b,r}]|a_{\text{OLO}}|^2$  are the proportionality coefficients, and  $\alpha_{\ell,u} = \bar{a}_{\ell,u}/a_{\text{OLO}}$  is the ratio of the control beams to the OLO (as shown in section C.3, it is proportional to the corresponding MW drive amplitude, including the phase). Since  $c(t)$  peaks around  $\omega_{m,\text{eff}}$ , we get the maximum of  $i_\ell$  at  $(\Delta_\ell - \omega_{\text{OLO}}) + \omega_{m,\text{eff}} = \omega_b - \omega_{\text{OLO}}$  and, similarly, maximum if  $i_u$  at  $(\Delta_u - \omega_{\text{OLO}}) - \omega_{m,\text{eff}} = \omega_r - \omega_{\text{OLO}}$ .

Up to a frequency shift, these photocurrents can be associated with  $i_r$  and  $i_b$  defined in (7.28):

$$i_\ell(t) = e^{-i(\omega_b - \omega_{\text{OLO}})t} i_b(t) \quad (\text{D.28})$$

$$i_u(t) = e^{-i(\omega_r - \omega_{\text{OLO}})t} i_r(t). \quad (\text{D.29})$$

However, to obtain the required frequency shifts, we still need to demodulate the signal at some frequencies  $\nu_{\text{dem},\ell}$  and  $\nu_{\text{dem},u}$  generated internally in the ZILI. This operation can be represented as multiplying the photocurrent by a corresponding demodulating signal  $a_{\text{dem},\ell}^* e^{+i\nu_{\text{dem},\ell}t}$  or  $a_{\text{dem},u}^* e^{+i\nu_{\text{dem},u}t}$ ;  $\nu_{\text{dem},\ell}$  and  $\nu_{\text{dem},u}$  are the demodulation frequencies, while  $a_{\text{dem},\ell}$  and  $a_{\text{dem},u}$  are the amplitudes of the corresponding local oscillators, which encode their respective phases.<sup>c)</sup> With that, the actual measured demodulated photocurrents are

$$i_{d,\ell} = a_{\text{dem},\ell}^* e^{+i(\nu_{\text{dem},\ell})t} i_\ell = G_\ell \left( \alpha_\ell a_{\text{dem},\ell}^* e^{-i(\nu_{\text{con},\ell} - \nu_{\text{dem},\ell})t} \right) c(t) \quad (\text{D.30})$$

$$i_{d,u} = a_{\text{dem},u}^* e^{+i(\nu_{\text{dem},u})t} i_u = G_u \left( \alpha_u a_{\text{dem},u}^* e^{-i(\nu_{\text{con},u} - \nu_{\text{dem},u})t} \right) c^*(t). \quad (\text{D.31})$$

Finally, the cross-correlator calculated from these photocurrents is

$$\begin{aligned} C_{ii}^{(u\ell)}(t, \tau) &= \langle i_{d,\ell}(t - \tau/2) i_{d,u}(t + \tau/2) \rangle \\ &= G_u G_\ell \langle c(t - \tau/2) c^*(t + \tau/2) \rangle e^{-i(\nu_{\text{con},u} - \nu_{\text{con},\ell} - \nu_{\text{dem},u} + \nu_{\text{dem},\ell})\tau/2} \times \\ &\quad \times \langle \alpha_\ell a_{\text{dem},\ell}^* \alpha_u a_{\text{dem},u}^* \rangle e^{-i(\nu_{\text{con},\ell} + \nu_{\text{con},u} - \nu_{\text{dem},\ell} - \nu_{\text{dem},u})t}. \end{aligned} \quad (\text{D.32})$$

(in this expression we made a reasonable assumption that the mechanical mode dynamics is uncorrelated from the various microwave signal phases, so their ensemble averages can be separated).

We can compare this expression to an idealized classical cross-correlator  $S_{ii}^{(\text{rb})}[\delta\omega]$ , which can be obtained by using equations (7.35) and (7.49) and neglecting all vacuum noise:

$$\begin{aligned} S_{ii}^{(\text{rb})}[\delta\omega] &= -G^2 (a_{\text{OLO}}^*)^2 \kappa_{\text{ext}} (\chi_c[\omega_r] \chi_c[\omega_b]) (g^{(0)})^2 \bar{a}_\ell \bar{a}_u S_{\hat{c}, \hat{c}^\dagger}[\omega_{m,\text{eff}} + \delta\omega] \\ &= -G_\ell G_u \alpha_\ell \alpha_u S_{\hat{c}, \hat{c}^\dagger}[\omega_{m,\text{eff}} + \delta\omega], \end{aligned} \quad (\text{D.33})$$

or in the time domain

$$\begin{aligned} C_{ii}^{(\text{rb})}(\tau) &\equiv \langle i_r(t + \tau/2) i_b(t - \tau/2) \rangle \\ &= -G_\ell G_u \alpha_\ell \alpha_u \langle c(t - \tau/2) c^*(t + \tau/2) \rangle e^{i\omega_{m,\text{eff}}\tau}. \end{aligned} \quad (\text{D.34})$$

While the control beam beatnotes  $\alpha_\ell$  and  $\alpha_u$  are still present, the rest of the microwave drive does not show up in this expression, and it also does not depend on the common time  $t$ . This comes from an implicit assumption of “ideal” frequency shifts of  $i_{r,b}$  given by equation (7.28).

Let us consider the requirements for equation (D.32) needed to produce a stable predictable result:

- First, all dependence on the common time  $t$  needs to be eliminated, otherwise, the time average of the correlator will become zero. This requires precise cancellation of the microwave drive frequencies  $\nu_{\text{con},\ell} + \nu_{\text{con},u} - \nu_{\text{dem},\ell} - \nu_{\text{dem},u} = 0$ , which is achieved by locking all the microwave generators and the ZILI to the same 10 MHz synchronization signal and choosing appropriate numerical values for their output frequencies.

<sup>c)</sup>For simplicity, we omit the fact that the photocurrent has an extra stage of mix-down before entering the ZILI. It does not affect the generality of the derivation, as the phase and the frequency of this mix-down signal can be absorbed into the demodulation signals.

- Second, to relate  $C_{ii}^{(u\ell)}$  to  $C_{ii}^{(rb)}$  we need to match the mechanical motion correlator frequency shift (the frequency in the exponent containing  $\tau$ ):  $\nu_{\text{con,u}} - \nu_{\text{con,\ell}} - \nu_{\text{dem,u}} + \nu_{\text{dem,\ell}} = 2\omega_{\text{m,eff}}$ . Since the mismatch in this equation simply shifts the perceived mechanical frequency, it does not need to be satisfied exactly; nevertheless, we need it to be approximately correct to be able to extract the mechanical frequency from the cross-correlator. In practice, we satisfy it by separately setting  $\nu_{\text{dem,\ell}} - \nu_{\text{con,\ell}} = \nu_{\text{con,u}} - \nu_{\text{dem,u}} \approx \omega_{\text{m,eff}}$ , which means that the mechanical motion is centered independently in both photocurrent records  $i_\ell$  and  $i_u$ .
- Finally, we need to know the phase factor  $\langle \alpha_\ell a_{\text{dem,\ell}}^* \alpha_u a_{\text{dem,u}}^* \rangle$ . This is required both to correctly extract the phase of the cross-correlator, and to make sure that averaging of separate measurements is done properly (if each measurement has an independent random phase, then their average will end up being zero).

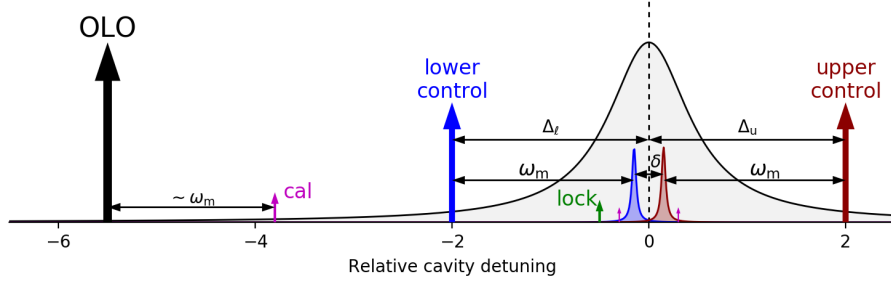


Figure D.17: Optical tone configuration for simultaneous measurements of both mechanical sidebands. The horizontal axis is scaled in units of optical cavity linewidths. Tones detunings and the mechanical motion linewidth are not to scale (except for the locking beam).

In order to determine this phase factor, we use an additional microwave drive of the phase modulator, which we call a “calibration” tone. In the schematic tone configuration shown in Figure D.17 the sidebands arising due to this drive are denoted with purple arrows. This microwave tone is generated at a frequency  $\nu_{\text{cal}}$  close (but not exactly equal) to the mechanical frequency  $\omega_{\text{m,eff}}$ . Due to the non-linearity of the phase modulator (discussed in appendix C.3), it results in second order sidebands on both control beams; their frequencies are  $\nu_{\text{con,u}} \pm \nu_{\text{cal}}$  and  $\nu_{\text{con,\ell}} \pm \nu_{\text{cal}}$  relative to the OLO, or  $\Delta_u \pm \nu_{\text{cal}}$  and  $\Delta_\ell \pm \nu_{\text{cal}}$  relative to the cavity. We are interested in the sidebands closest to the optical cavity resonance, which are at frequencies  $\Delta_u - \nu_{\text{cal}}$  and  $\Delta_\ell + \nu_{\text{cal}}$  (denoted by small purple arrows in Figure D.17); the other two sidebands are far from the optical resonance, and therefore can not be detected, as described in appendix C.3.2. We want these sidebands to be close enough to the mechanical frequency that they fall within the demodulation window ZILI (i.e., less than 100 kHz away from the mechanical motion sidebands), but far enough that they do not experience any OMIT effects:  $|\nu_{\text{cal}} - \omega_{\text{m,eff}}| \gg \gamma_{\text{m,eff}}$ . Typically, we choose  $\omega_{\text{m,eff}} - \nu_{\text{cal}} \approx 2\pi \cdot 50$  kHz, which satisfies both criteria. After reflection off the cavity and detection, these sidebands (similarly to the mechanical motion sidebands) produce beatnotes in the photocurrent at frequencies  $\nu_{\text{con,u}} - \nu_{\text{cal}}$  and  $\nu_{\text{con,\ell}} + \nu_{\text{cal}}$ . It is these beatnotes which we use to calibrate the phase factor.

Let us denote the normalized amplitude of the MW calibration tone as  $\alpha_{\text{cal}}$ , so that the tone itself is expressed as  $\alpha_{\text{cal}} e^{-i\nu_{\text{cal}} t}$ . As per appendix section C.3, the second order optical sidebands due to this tone will have amplitudes (neglecting the uninteresting  $\pi/2$  phases)  $a_{\text{cal,\ell}} = a_{\text{OLO}} \alpha_\ell \alpha_{\text{cal}}$  for the sideband at a frequency  $\nu_{\text{con,\ell}} + \nu_{\text{cal}}$  and  $a_{\text{cal,u}} = a_{\text{OLO}} \alpha_u \alpha_{\text{cal}}^*$  for the sideband at a frequency  $\nu_{\text{con,u}} - \nu_{\text{cal}}$ . After reflection and detection, these sidebands produce beatnotes in the photocurrent with respective amplitudes (excluding real factors which do not change the complex signal phase)

$$a_{\text{bn,\ell}} \propto a_{\text{OLO}} a_{\text{cal,\ell}} \chi_c[\omega_b] = |a_{\text{OLO}}|^2 \alpha_\ell \alpha_{\text{cal}} \chi_c[\omega_r] \quad (\text{D.35})$$

$$a_{\text{bn,u}} \propto a_{\text{OLO}} a_{\text{cal,u}} \chi_c[\omega_b] = |a_{\text{OLO}}|^2 \alpha_u \alpha_{\text{cal}}^* \chi_c[\omega_r]. \quad (\text{D.36})$$

After exactly the same demodulation step as for the mechanical sidebands, these end up producing demodulated signals (similar to equations (D.30) and (D.31))

$$\begin{aligned} i_{\text{cal},\ell}(t) &\propto a_{\text{dem},\ell}^* e^{-i\nu_{\text{dem},\ell}t} a_{\text{bn},\ell} e^{-i(\nu_{\text{con},\ell} + \nu_{\text{cal}})t} \\ &= |a_{\text{OLO}}|^2 \alpha_{\ell} \alpha_{\text{cal}}^* a_{\text{dem},\ell}^* \chi_c[\omega_{\text{b}}] e^{-i(\nu_{\text{con},\ell} + \nu_{\text{cal}} - \nu_{\text{dem},\ell})t} \end{aligned} \quad (\text{D.37})$$

$$\begin{aligned} i_{\text{cal},\text{u}}(t) &\propto a_{\text{dem},\text{u}}^* e^{-i\nu_{\text{dem},\text{u}}t} a_{\text{bn},\text{u}} e^{-i(\nu_{\text{con},\text{u}} - \nu_{\text{cal}})t} \\ &= |a_{\text{OLO}}|^2 \alpha_{\text{u}} \alpha_{\text{cal}} a_{\text{dem},\text{u}}^* \chi_c[\omega_{\text{r}}] e^{-i(\nu_{\text{con},\text{u}} - \nu_{\text{cal}} - \nu_{\text{dem},\text{u}})t} \end{aligned} \quad (\text{D.38})$$

for the lower and the upper control beam sideband respectively. Note that these signals have all the same microwave amplitudes as the mechanical sideband signals (D.30) and (D.31) (in fact, the expressions become almost identical if we replace the mechanical motion  $c(t)$  by the calibration MW tone  $\alpha_{\text{cal}} e^{-i\nu_{\text{cal}}t}$ ).

If we calculate the product of the two demodulated signals, we obtain

$$\begin{aligned} \langle i_{\text{cal},\ell}(t) i_{\text{cal},\text{u}}(t) \rangle &= |a_{\text{OLO}}|^4 |\alpha_{\text{cal}}|^2 \chi_c[\omega_{\text{b}}] \chi_c[\omega_{\text{r}}] \langle \alpha_{\ell} a_{\text{dem},\ell}^* \alpha_{\text{u}} a_{\text{dem},\text{u}}^* \rangle \times \\ &\quad e^{-i(\nu_{\text{con},\ell} + \nu_{\text{con},\text{u}} - \nu_{\text{dem},\ell} - \nu_{\text{dem},\text{u}})t}, \end{aligned} \quad (\text{D.39})$$

which (up to some real positive prefactors and a known cavity susceptibility) exactly coincides with the phase factor in the expression (D.32). Thus, we can determine the phase factor by adding a calibration tone, detecting the second order phase sidebands it produces in the demodulator record, and calculating the product of these sidebands.

In the experiment we have to be careful to make sure that this procedure does not introduce any additional laser noise. Hence, we choose to alternate the periods when the calibration tone is on (usually 2 seconds long), which are used to calibrate the phase, and the periods when it is off (usually 10-20 seconds long), which are used for the detection of the mechanical motion. Since all of the microwave generators are locked to the same clock reference, the phase does not fluctuate appreciably in between the calibration periods. At the same time, the calibration tone is not present during the sensitive mechanical motion detection, so its extra noise is not an issue.

With all of the phase uncertainty sources taken into account, we are able to reliably measure the microwave phase factor and determine the correct quadratures of the cross-correlator. The residual phase error obtained from the fits (as described in section 8.5) is typically less than 20 mrad.

## D.10 Additional calibrations

In order to detect and exclude some systematic effects, we were performing additional checks during the main measurement routine:

- One possible source of error is the frequency dependence of the MW and optical gains on the scale of the distance between the two motional sidebands  $\delta \approx 2\pi \cdot 200$  kHz (see subsection 7.1.1), which could lead to systematic differences in the estimation of the sidebands' sizes. To account for that, we were periodically (approximately once every couple of hours) swapping the positions of the sidebands by slightly altering the MW frequencies of the control beam drives. As an example, the arrangement shown in Figure D.17b can be flipped via reducing the upper control drive frequency  $\nu_{\text{con},\text{u}}$  by  $\delta$  and increasing the lower control drive frequency by the same amount.
- Another potential source of asymmetry in the measurement scheme is the location of the OLO. So far in all of the discussions we were assuming that it had lower frequency than both of the control beams, as shown in, e.g., Figure D.17. This can affect the measurements through interaction of the OLO with the cavity (which changes its phase differently depending on its position with respect to the cavity), and simply

through the fact the the lower control beam is closer to the OLO, which means that its corresponding MW frequency is lower than for the upper control beam. This difference can result in systematic uncertainty if combined with, e.g., errors in the calibration of the phase modulator drive (appendix D.7). Similarly to the previous effect, we correct for this by occasional (approximately once an hour) flipping of the OLO position with respect to the cavity. This is straightforward to arrange, since the OLO already has copies of all of the necessary beams (lock, upper and lower control, probe) on the other side due to the symmetry of the phase modulation (see appendix C.3). Thus, to change the OLO detuning sign, we simply shift its frequency by  $\approx 2\nu_{\text{lock}} = 4180$  MHz (to move the lock beam on the other side of the OLO closer to the cavity resonance), and change the sign of the lock gain to account for the resulting flipped error signal. The rest of the measurement and the analysis remains the same, with occasional complex conjugates arising due to the switched OLO side.

- Finally, we perform one more check by taking some of the experimental data in the “unlocked” configuration, i.e., with the laser being fairly far ( $\sim 20$  GHz) detuned from the cavity. Since the phase modulation is invisible in this situation (as discussed in appendix C.2.3), we do not expect to see any heterodyne signal. Thus, this measurement lets us ensure that there is no pickup in the MW part of the setup.

Furthermore, this measurement can serve to roughly estimate the amount of the residual laser phase noise. This estimation is done by comparing the background in the undriven motion measurement in the “unlocked” configuration to that of the standard measurement. Since the phase noise does not contribute in the “unlocked” measurement, the background there only contains the EDFA noise (the classical laser amplitude noise is very small, so we ignore it in this discussion). At the same time, as demonstrated in appendix C.2.7, the phase noise does appear in the photocurrent when the laser is reflected off a cavity, which corresponds to the standard measurement situation. Thus, by comparing the two background, we can determine the amount of the classical phase noise, or at least place an upper bound on it. In our case this comparison reveals the amount of classical phase noise corresponding to the shot-noise limited power (reference to the control beams) of  $25 \mu\text{W}$ . The highest control beam power in the measurements shown in Figure 8.9 is  $10 \mu\text{W}$ , which corresponds to the ratio of the classical to the shot noise of 0.4. Most of the measurements were performed at lower powers of  $\leq 3 \mu\text{W}$ , reducing this ratio further to  $\sim 0.1$ . This amount of classical phase noise leads to over-estimation of the sideband asymmetry [182, 13] by about 0.1, which possibly contributes to the deviation of the experimental data from the theory prediction in Figure 8.9.

Name	Description	Model/Part number	Relevant parameters
<b>Main schematic</b>			
TL	Tunable laser	PurePhotonics PPCL200	Output power: $< 60$ mW; wavelength range: $1550 \pm 20$ nm
IQM	Optical IQ modulator	EOspace IQ-0DKS-25	Bandwidth: 25 GHz
$\phi$ M	Optical phase modulator	EOspace PM-0K5-10	Bandwidth: 10 GHz
PCnt	Polarization controller	Oz Optics EPC-400	
VOA	Variable optical attenuator	Oz Optics DD-100-MC	Attenuation range: $0 \div 60$ dB
EDFA	Optical amplifier	NuPhoton NP2000	Noise figure: 4 dB; output power: 20 mW
TF	Tunable optical filter	Oz Optics TF100	Bandwidth: 0.6 nm
TFPC	Tunable Fabry-Perot cavity	Made in-house	Linewidth: 200 MHz, FSR: 1.5 THz
OSW	Optical $2 \times 2$ switch	JDSU SW22-Z348	
Mtap, Rtap	Optical 90:10 splitter	Thorlabs TW1550R2A2	
Ctap	Optical 99:1 splitter	Thorlabs TW1550R1A2	
Circulator	Optical circulator	Oplink MIOC1550	Polarization insensitive
FPD	Fast photodiode	Thorlabs DET08CFC	Bandwidth: 8 GHz (diode capacitance of 0.3 pF)
PM	Optical power meter	Thorlabs PM100D + S144C	
<b>Filter cavity setup schematic</b>			
TFC	Tunable filter cavity	Micron Optics FFP-TF	Bandwidth: 30 MHz; FSR: 15 GHz
PCnt	Polarization controller	Newport F-POL-IL	
Circulator	Optical circulator	Thorlabs CIR1550PM-APC	Polarization maintaining
PD	Photodiode	Thorlabs PDA10CF	Bandwidth: 150 MHz

Table 9.1: List of optical components in the main setup schematic (Figure 5.2) and the filter cavity subsystem (Figure D.1).

Name/Location	Description	Model/Part number	Relevant parameters
<b>Main schematic</b>			
ZILI	Lock-In + DAQ system	Zurich Instrument UHF LI	Frequency range: 0 ÷ 600 MHz
VNA	Vector network analyzer	HP 8722D	
MWG1, MWG2	Microwave generator	Vaunix LabBrick LMS-232D	Frequency range: 0.7 ÷ 2.2 GHz
MWG3	Microwave generator	Agilent N9310A	Frequency range: < 3 GHz
SA	Spectrum analyzer	Rigol DSA1030A	Frequency range: < 3 GHz
FPGA	DSP module	NI PXI-7854R	
Reflection FPD amplifier	Low-noise MW amplifier chain	Minicircuits (ZX60-P105LN+) + 2× (ZX60-V62+)	First amplifier NF: 2 dB; total gain: ~ 45 dB
4 × 1 combiner, 1 × 3 splitter	Power splitter/combiner	Minicircuits ZB4PD-462W-S+	Frequency range: 0.38 ÷ 4.6 GHz
ϕM drive amplifier	Low-noise MW amplifier	Minicircuits ZX60-H242+	NF: 2.5 dB; output power: 23 dBm
ϕcal tone combiner	MW directional coupler	ZNDC-18-2G-S+	Coupling: 18 dB; frequency range: 0.8 ÷ 2.0 GHz
ϕM drive SA tap	MW directional coupler	ZFDC-10-182-S+	Coupling: 10 dB; frequency range: 0.1 ÷ 1.8 GHz
MWSW	MW switch	Minicircuits MSP2TA-18-12+	
VCO	Voltage-controlled oscillator	Minicircuits ZX95-3555+	Frequency range: 2.8 ÷ 3.5 GHz
VCO amplifier	High-power MW amplifier	Minicircuits ZHL-42W+	Output power: 30 dBm
IQM 0° – 90° splitter	MW 90° hybrid	Minicircuits ZAPDQ-4-S	Frequency range: 2 ÷ 4.2 GHz
MWG1 splitter	Power splitter	Two 2-way MW splitters (Minicircuits ZAPD-20-S+)	Frequency range: 700 ÷ 2000 MHz
<b>Filter cavity setup schematic</b>			
AWG	Function generator	Agilent 33220A	
Mixer	Low-frequency mixer	Minicircuits ZP-3+	LO frequency range: 0.15 ÷ 400 MHz
Bias tee	Low-frequency MW bias tee	Minicircuits ZFBT-4R2GW+	Cutoff frequency: 0.1 MHz
μC	Micro-controller	Arduino Uno + in-house ADC/DAC board	Feedback delay: ~ 1 ms

Table 9.2: List of electronic components in the main setup schematic (Figure 5.2) and the filter cavity subsystem (Figure D.1).

Name/Location	Description	Model/Part number	Relevant parameters
<b>Mixer circuit</b>			
LO 90° splitter	High-frequency 90° hybrid	Minicircuits ZX10Q-2-27-S+	Frequency range: 1700 ÷ 2700 MHz
IF 90° splitter	Low-frequency 90° hybrid	Minicircuits ZX10Q-2-3-S+	Frequency range: 220 ÷ 470 MHz
RF combiner	Power splitter/combiner	Minicircuits ZAPD-20-S+	Frequency range: 700 ÷ 2000 MHz
Mixers	MW mixer	Minicircuits ZEM-M2TMH+	Frequency range: 10 ÷ 2400 MHz
RF output filter	Bandpass filter	Minicircuits (VHF-2000+) + (VLF-2250+)	Frequency range: 2000 ÷ 2600 MHz
<b>IQM circuit</b>			
VMWA	Variable MW attenuator	Minicircuits ZX73-2500M-S+	Frequency range: 0 ÷ 2500 MHz
Bias tee	Low-frequency MW bias tee	Minicircuits ZFBT-4R2GW+	Cutoff frequency: 0.1 MHz
Amplifier	Low-noise MW amplifier chain	Minicircuits (ZX60-6013E-S+) + (ZX60-V63+) + 2 × (ZX60-V62+)	Frequency range: 50 ÷ 6000 MHz; first amplifier NF: 3.5 dB; total gain: 60 dB
Splitter	Power splitter	Minicircuits ZN2PD2-63-N+	Frequency range: 350 ÷ 6000 MHz
High-pass filter	High-pass filter	Minicircuits VHF-4600+	Cutoff frequency: 4600 MHz
Low-pass filter	Low-pass filter	Minicircuits VLF-3000+	Cutoff frequency: 3600 MHz
Top MWPD	MW power detector	Minicircuits ZX47-55LN-S+	Frequency range: 10 ÷ 8000 MHz
Bottom MWPD	MW power detector	Minicircuits ZX47-40LN-S+	Frequency range: 10 ÷ 8000 MHz

Table 9.3: List of electronic components in the mixer circuit (Figure D.6a) and the IQM stabilization circuit (Figure D.5).

# Bibliography

- [1] M. Aspelmeyer, T. J. Kippenberg, and F. Marquardt, *Cavity optomechanics*, Reviews of Modern Physics **86**, 1391 (2014), URL <https://dx.doi.org/10.1103/RevModPhys.86.1391>.
- [2] M. J. Collett and C. W. Gardiner, *Squeezing of intracavity and traveling-wave light fields produced in parametric amplification*, Physical Review A **30**, 1386 (1984), URL <https://dx.doi.org/10.1103/PhysRevA.30.1386>.
- [3] C. W. Gardiner, *Handbook of Stochastic Methods*, Springer-Verlag, Berlin Heidelberg (2004), ISBN 9783540208828.
- [4] H. B. G. Casimir, *On the attraction between two perfectly conducting plates*, Koninkl. Ned. Adak. Wetenschap. Proc **51**, 793 (1948), URL <http://www.dwc.knaw.nl/toegangen/digital-library-knaw/?pagetype=publDetail&pId=PU00018547>.
- [5] M. Bordag, U. Mohideen, and V. M. Mostepanenko, *New developments in the Casimir effect*, Physics Reports **353**, 1 (2001), URL [https://dx.doi.org/10.1016/S0370-1573\(01\)00015-1](https://dx.doi.org/10.1016/S0370-1573(01)00015-1).
- [6] M. Eichenfield, J. Chan, R. M. Camacho, K. J. Vahala, and O. Painter, *Optomechanical crystals.*, Nature **462**, 78 (2009), URL <https://dx.doi.org/10.1038/nature08524>.
- [7] T. Carmon, H. Rokhsari, L. Yang, T. J. Kippenberg, and K. J. Vahala, *Temporal Behavior of Radiation-Pressure-Induced Vibrations of an Optical Microcavity Phonon Mode*, Physical Review Letters **94**, 223902 (2005), URL <https://dx.doi.org/10.1103/PhysRevLett.94.223902>.
- [8] F. Marquardt, J. G. E. Harris, and S. M. Girvin, *Dynamical Multistability Induced by Radiation Pressure in High-Finesse Micromechanical Optical Cavities*, Physical Review Letters **96**, 103901 (2006), URL <https://dx.doi.org/10.1103/PhysRevLett.96.103901>.
- [9] A. Dorsel, J. D. McCullen, P. Meystre, E. Vignes, and H. Walther, *Optical Bistability and Mirror Confinement Induced by Radiation Pressure*, Physical Review Letters **51**, 1550 (1983), URL <https://dx.doi.org/10.1103/PhysRevLett.51.1550>.
- [10] A. A. Clerk, S. M. Girvin, F. Marquardt, R. J. Schoelkopf, and M. H. Devoret, *Introduction to quantum noise, measurement, and amplification*, Reviews of Modern Physics **82**, 1155 (2010), URL <https://dx.doi.org/10.1103/RevModPhys.82.1155>.
- [11] F. Y. Khalili, H. Miao, H. Yang, A. H. Safavi-Naeini, O. Painter, and Y. Chen, *Quantum back-action in measurements of zero-point mechanical oscillations*, Physical Review A **86**, 033840 (2012), URL <https://dx.doi.org/10.1103/PhysRevA.86.033840>.
- [12] A. J. Weinstein *et al.*, *Observation and Interpretation of Motional Sideband Asymmetry in a Quantum Electromechanical Device*, Physical Review X **4**, 041003 (2014), URL <https://dx.doi.org/10.1103/PhysRevX.4.041003>.

- [13] K. Børkje, *Heterodyne photodetection measurements on cavity optomechanical systems: Interpretation of sideband asymmetry and limits to a classical explanation*, Physical Review A **94**, 043816 (2016), URL <https://dx.doi.org/10.1103/PhysRevA.94.043816>.
- [14] S. Weis *et al.*, *Optomechanically induced transparency*, Science **330**, 1520 (2010), URL <https://dx.doi.org/10.1126/science.1195596>.
- [15] A. H. Safavi-Naeini *et al.*, *Electromagnetically induced transparency and slow light with optomechanics.*, Nature **472**, 69 (2011), URL <https://dx.doi.org/10.1038/nature09933>.
- [16] F. Massel *et al.*, *Microwave amplification with nanomechanical resonators*, Nature **480**, 351 (2011), URL <https://dx.doi.org/10.1038/nature10628>.
- [17] V. B. Braginsky and A. B. Manukhin, *Ponderomotive effects of electromagnetic radiation*, Soviet Physics JETP **25**, 653 (1967), URL <http://jetp.ac.ru/cgi-bin/e/index/e/25/4/p653?a=list>.
- [18] V. B. Braginsky, A. B. Manukhin, and M. Y. Tikhonov, *Investigation of Dissipative Ponderomotive Effects of Electromagnetic Radiation*, Soviet Physics JETP **31**, 829 (1970), URL <http://jetp.ac.ru/cgi-bin/e/index/e/31/5/p829?a=list>.
- [19] A. Gozzini, I. Longo, S. Barbarino, F. Maccarrone, and F. Mango, *Light-pressure bistability at microwave frequencies*, Journal of the Optical Society of America B **2**, 1841 (1985), URL <https://dx.doi.org/10.1364/JOSAB.2.001841>.
- [20] B. Abbott *et al.*, *Observation of a kilogram-scale oscillator near its quantum ground state*, New Journal of Physics **11**, 073032 (2009), URL <https://dx.doi.org/10.1088/1367-2630/11/7/073032>.
- [21] B. Abbott *et al.*, *Observation of Gravitational Waves from a Binary Black Hole Merger*, Physical Review Letters **116**, 061102 (2016), URL <https://dx.doi.org/10.1103/PhysRevLett.116.061102>.
- [22] T. Corbitt *et al.*, *An All-Optical Trap for a Gram-Scale Mirror*, Physical Review Letters **98**, 150802 (2007), URL <https://dx.doi.org/10.1103/PhysRevLett.98.150802>.
- [23] T. Corbitt *et al.*, *Optical Dilution and Feedback Cooling of a Gram-Scale Oscillator to 6.9 mK*, Physical Review Letters **99**, 160801 (2007), URL <https://dx.doi.org/10.1103/PhysRevLett.99.160801>.
- [24] D. Kleckner *et al.*, *High Finesse Opto-Mechanical Cavity with a Movable Thirty-Micron-Size Mirror*, Physical Review Letters **96**, 173901 (2006), URL <https://dx.doi.org/10.1103/PhysRevLett.96.173901>.
- [25] I. Favero *et al.*, *Optical cooling of a micromirror of wavelength size*, Applied Physics Letters **90**, 104101 (2007), URL <https://dx.doi.org/10.1063/1.2711181>.
- [26] D. Kleckner, B. Pepper, E. Jeffrey, P. Sonin, S. M. Thon, and D. Bouwmeester, *Optomechanical trampoline resonators.*, Optics Express **19**, 19708 (2011), URL <https://dx.doi.org/10.1364/OE.19.019708>.
- [27] P. F. Cohadon, A. Heidmann, and M. Pinard, *Cooling of a mirror by radiation pressure*, Physical Review Letters **83**, 4 (1999), URL <https://dx.doi.org/10.1103/PhysRevLett.83.3174>.
- [28] M. Evans *et al.*, *Observation of parametric instability in advanced LIGO*, Physical Review Letters **114**, 6 (2015), URL <https://dx.doi.org/10.1103/PhysRevLett.114.161102>.
- [29] D. K. Armani, T. J. Kippenberg, S. M. Spillane, and K. J. Vahala, *Ultra-high-Q toroid microcavity on a chip*, Nature **421**, 925 (2003), URL <https://dx.doi.org/10.1038/nature01371>.
- [30] T. J. Kippenberg, H. Rokhsari, T. Carmon, A. Scherer, and K. J. Vahala, *Analysis of Radiation-Pressure Induced Mechanical Oscillation of an Optical Microcavity*, Physical Review Letters **95**, 033901 (2005), URL <https://dx.doi.org/10.1103/PhysRevLett.95.033901>.

- [31] A. Schliesser, P. Del’Haye, N. Nooshi, K. J. Vahala, and T. J. Kippenberg, *Radiation Pressure Cooling of a Micromechanical Oscillator Using Dynamical Backaction*, Physical Review Letters **97**, 243905 (2006), URL <https://dx.doi.org/10.1103/PhysRevLett.97.243905>.
- [32] R. Ma, A. Schliesser, P. Del’Haye, A. Dabirian, G. Anetsberger, and T. J. Kippenberg, *Radiation-pressure-driven vibrational modes in ultrahigh-Q silica microspheres.*, Optics letters **32**, 2200 (2007), URL <https://dx.doi.org/10.1364/ol.32.002200>.
- [33] Q. Lin, J. Rosenberg, X. Jiang, K. J. Vahala, and O. Painter, *Mechanical Oscillation and Cooling Actuated by the Optical Gradient Force*, Physical Review Letters **103**, 103601 (2009), URL <https://dx.doi.org/10.1103/PhysRevLett.103.103601>.
- [34] J. D. Thompson, B. M. Zwickl, A. M. Jayich, F. Marquardt, S. M. Girvin, and J. G. E. Harris, *Strong dispersive coupling of a high-finesse cavity to a micromechanical membrane.*, Nature **452**, 72 (2008), URL <https://dx.doi.org/10.1038/nature06715>.
- [35] A. M. Jayich *et al.*, *Dispersive optomechanics: a membrane inside a cavity*, New Journal of Physics **10**, 095008 (2008), URL <https://dx.doi.org/10.1088/1367-2630/10/9/095008>.
- [36] J. C. Sankey, C. Yang, B. M. Zwickl, A. M. Jayich, and J. G. E. Harris, *Strong and tunable nonlinear optomechanical coupling in a low-loss system*, Nature Physics **6**, 707 (2010), URL <https://dx.doi.org/10.1038/nphys1707>.
- [37] D. Lee, M. Underwood, D. Mason, A. B. Shkarin, S. W. Hoch, and J. G. E. Harris, *Multimode optomechanical dynamics in a cavity with avoided crossings*, Nature Communications **6**, 6232 (2015), URL <https://dx.doi.org/10.1038/ncomms7232>.
- [38] A. B. Shkarin *et al.*, *Optically Mediated Hybridization between Two Mechanical Modes*, Physical Review Letters **112**, 013602 (2014), URL <https://dx.doi.org/10.1103/PhysRevLett.112.013602>.
- [39] H. Xu, D. Mason, L. Jiang, and J. G. E. Harris, *Topological energy transfer in an optomechanical system with exceptional points*, Nature **537**, 80 (2016), URL <https://dx.doi.org/10.1038/nature18604>.
- [40] P.-L. Yu, T. P. Purdy, and C. A. Regal, *Control of Material Damping in High-Q Membrane Microresonators*, Physical Review Letters **108**, 083603 (2012), URL <https://dx.doi.org/10.1103/PhysRevLett.108.083603>.
- [41] M. Yuan, V. Singh, Y. M. Blanter, and G. A. Steele, *Large cooperativity and microkelvin cooling with a three-dimensional optomechanical cavity*, Nature Communications **6**, 8491 (2015), URL <https://dx.doi.org/10.1038/ncomms9491>.
- [42] R. W. Andrews *et al.*, *Bidirectional and efficient conversion between microwave and optical light*, Nature Physics **10**, 321 (2014), URL <https://dx.doi.org/10.1038/nphys2911>.
- [43] C. Reinhardt, T. Müller, A. Bourassa, and J. C. Sankey, *Ultralow-Noise SiN Trampoline Resonators for Sensing and Optomechanics*, Physical Review X **6**, 021001 (2016), URL <https://dx.doi.org/10.1103/PhysRevX.6.021001>.
- [44] M. Yuan, M. A. Cohen, and G. A. Steele, *Silicon nitride membrane resonators at millikelvin temperatures with quality factors exceeding  $10^8$* , Applied Physics Letters **107** (2015), URL <https://dx.doi.org/10.1063/1.4938747>.
- [45] Y. Tsaturyan, A. Barg, E. S. Polzik, and A. Schliesser, *Ultraslow nanomechanical resonators via soft clamping and dissipation dilution*, Nature Nanotechnology **12**, 776 (2017), URL <https://dx.doi.org/10.1038/nnano.2017.101>.

- [46] I. Favero *et al.*, *Fluctuating nanomechanical system in a high finesse optical microcavity*, Optics Express **17**, 12813 (2009), URL <https://dx.doi.org/10.1364/oe.17.012813>.
- [47] N. Kiesel, F. Blaser, U. Delic, D. Grass, R. Kaltenbaek, and M. Aspelmeyer, *Cavity cooling of an optically levitated submicron particle*, Proceedings of the National Academy of Sciences **110**, 14180 (2013), URL <https://dx.doi.org/10.1073/pnas.1309167110>.
- [48] K. W. Murch, K. L. Moore, S. Gupta, and D. M. Stamper-Kurn, *Observation of quantum-measurement backaction with an ultracold atomic gas*, Nature Physics **4**, 561 (2008), URL <https://dx.doi.org/10.1038/nphys965>.
- [49] G. Anetsberger *et al.*, *Near-field cavity optomechanics with nanomechanical oscillators*, Nature Physics **5**, 909 (2009), URL <https://dx.doi.org/10.1038/nphys1425>.
- [50] J. D. Teufel *et al.*, *Circuit cavity electromechanics in the strong-coupling regime*, Nature **471**, 204 (2011), URL <https://dx.doi.org/10.1038/nature09898>.
- [51] J.-M. Pirkkalainen, S. U. Cho, J. Li, G. S. Paraoanu, P. J. Hakonen, and M. A. Sillanpää, *Hybrid circuit cavity quantum electrodynamics with a micromechanical resonator.*, Nature **494**, 211 (2013), URL <https://dx.doi.org/10.1038/nature11821>.
- [52] J.-M. Pirkkalainen *et al.*, *Cavity optomechanics mediated by a quantum two-level system*, Nature Communications **6**, 6981 (2015), URL <https://dx.doi.org/10.1038/ncomms7981>.
- [53] R. Y. Chiao, C. H. Townes, and B. P. Stoicheff, *Stimulated Brillouin Scattering and Coherent Generation of Intense Hypersonic Waves*, Physical Review Letters **12**, 592 (1964), URL <https://dx.doi.org/10.1103/PhysRevLett.12.592>.
- [54] B. J. Eggleton, C. G. Poulton, and R. Pant, *Inducing and harnessing stimulated Brillouin scattering in photonic integrated circuits*, Advances in Optics and Photonics **5**, 536 (2013), URL <https://dx.doi.org/10.1364/AOP.5.000536>.
- [55] M. Tomes and T. Carmon, *Photonic Micro-Electromechanical Systems Vibrating at X-band (11-GHz) Rates*, Physical Review Letters **102**, 113601 (2009), URL <https://dx.doi.org/10.1103/PhysRevLett.102.113601>.
- [56] I. S. Grudinin, A. B. Matsko, and L. Maleki, *Brillouin Lasing with a CaF<sub>2</sub> Whispering Gallery Mode Resonator*, Physical Review Letters **102**, 043902 (2009), URL <https://dx.doi.org/10.1103/PhysRevLett.102.043902>.
- [57] G. Bahl, J. Zehnpfennig, M. Tomes, and T. Carmon, *Stimulated optomechanical excitation of surface acoustic waves in a microdevice*, Nature Communications **2**, 403 (2011), URL <https://dx.doi.org/10.1038/ncomms1412>.
- [58] G. Bahl, M. Tomes, F. Marquardt, and T. Carmon, *Observation of Spontaneous Brillouin Cooling*, Nature Physics **8**, 203 (2011), URL <https://dx.doi.org/10.1038/nphys2206>.
- [59] J. Kim, M. C. Kuzyk, K. Han, H. Wang, and G. Bahl, *Non-reciprocal Brillouin scattering induced transparency*, Nature Physics **11**, 275 (2015), URL <https://dx.doi.org/10.1038/nphys3236>.
- [60] X. Xu and J. M. Taylor, *Optomechanically-induced chiral transport of phonons in one dimension*, arXiv pp. 1–20 (2017), URL <https://arxiv.org/abs/1701.02699>.
- [61] G. Bahl, K. H. Kim, W. Lee, J. Liu, X. Fan, and T. Carmon, *Brillouin cavity optomechanics with microfluidic devices*, Nature Communications **4**, 1994 (2013), URL <https://dx.doi.org/10.1038/ncomms2994>.

- [62] J. Zhang, K. Peng, and S. L. Braunstein, *Quantum-state transfer from light to macroscopic oscillators*, Physical Review A **68**, 013808 (2003), URL <https://dx.doi.org/10.1103/PhysRevA.68.013808>.
- [63] A. D. O'Connell *et al.*, *Quantum ground state and single-phonon control of a mechanical resonator.*, Nature **464**, 697 (2010), URL <https://dx.doi.org/10.1038/nature08967>.
- [64] R. Riedinger *et al.*, *Non-classical correlations between single photons and phonons from a mechanical oscillator*, Nature **530**, 313 (2016), URL <https://dx.doi.org/10.1038/nature16536>.
- [65] A. Einstein, *Entwicklung unserer Anschauungen ber das Wesen und die Konstitution der Strahlung*, Physikalische Zeitschrift **10**, 817 (1909), URL <https://dx.doi.org/10.1002/phbl.19690250902>.
- [66] C. Caves, *Quantum-Mechanical Radiation-Pressure Fluctuations in an Interferometer*, Physical Review Letters **45**, 75 (1980), URL <https://dx.doi.org/10.1103/PhysRevLett.45.75>.
- [67] V. B. Braginsky and Y. I. Vorontsov, *Quantum-mechanical limitations in macroscopic experiments and modern experimental technique*, Uspekhi Fizicheskikh Nauk **114**, 41 (1974), URL <https://dx.doi.org/10.3367/UFNr.0114.197409b.0041>.
- [68] V. B. Braginsky and A. B. Manukhin, *Measurement of Weak Forces in Physics Experiments*, University of Chicago Press (1977), ISBN 9780226070704.
- [69] S. Schreppler, N. Spethmann, N. Brahms, T. Botter, M. Barrios, and D. M. Stamper-Kurn, *Optically measuring force near the standard quantum limit*, Science **344**, 1486 (2014), URL <https://dx.doi.org/10.1126/science.1249850>.
- [70] T. P. Purdy, R. W. Peterson, and C. A. Regal, *Observation of radiation pressure shot noise on a macroscopic object.*, Science **339**, 801 (2013), URL <https://dx.doi.org/10.1126/science.1231282>.
- [71] C. Fabre, M. Pinard, S. Bourzeix, A. Heidmann, E. Giacobino, and S. Reynaud, *Quantum-noise reduction using a cavity with a movable mirror*, Physical Review A **49**, 1337 (1994), URL <https://dx.doi.org/10.1103/PhysRevA.49.1337>.
- [72] S. Mancini and P. Tombesi, *Quantum noise reduction by radiation pressure*, Physical Review A **49**, 4055 (1994), URL <https://dx.doi.org/10.1103/PhysRevA.49.4055>.
- [73] S. Vyatchanin and E. Zubova, *Quantum variation measurement of a force*, Physics Letters A **201**, 269 (1995), URL [https://dx.doi.org/10.1016/0375-9601\(95\)00280-G](https://dx.doi.org/10.1016/0375-9601(95)00280-G).
- [74] K. Jacobs, P. Tombesi, M. J. Collett, and D. F. Walls, *Quantum-nondemolition measurement of photon number using radiation pressure*, Physical Review A **49**, 1961 (1994), URL <https://dx.doi.org/10.1103/PhysRevA.49.1961>.
- [75] M. Pinard, C. Fabre, and A. Heidmann, *Quantum-nondemolition measurement of light by a piezoelectric crystal*, Physical Review A **51**, 2443 (1995), URL <https://dx.doi.org/10.1103/PhysRevA.51.2443>.
- [76] D. W. C. Brooks, T. Botter, S. Schreppler, T. P. Purdy, N. Brahms, and D. M. Stamper-Kurn, *Non-classical light generated by quantum-noise-driven cavity optomechanics*, Nature **488**, 476 (2012), URL <https://dx.doi.org/10.1038/nature11325>.
- [77] A. H. Safavi-Naeini, S. Gröblacher, J. T. Hill, J. Chan, M. Aspelmeyer, and O. Painter, *Squeezed light from a silicon micromechanical resonator.*, Nature **500**, 185 (2013), URL <https://dx.doi.org/10.1038/nature12307>.
- [78] T. P. Purdy, P.-L. Yu, R. W. Peterson, N. S. Kampel, and C. A. Regal, *Strong Optomechanical Squeezing of Light*, Physical Review X **3**, 031012 (2013), URL <https://dx.doi.org/10.1103/PhysRevX.3.031012>.

- [79] N. S. Kampel *et al.*, *Improving Broadband Displacement Detection with Quantum Correlations*, Physical Review X **7**, 021008 (2017), URL <https://dx.doi.org/10.1103/PhysRevX.7.021008>.
- [80] A. H. Safavi-Naeini, J. Chan, J. T. Hill, T. P. M. Alegre, A. G. Krause, and O. Painter, *Observation of Quantum Motion of a Nanomechanical Resonator*, Physical Review Letters **108**, 033602 (2012), URL <https://dx.doi.org/10.1103/PhysRevLett.108.033602>.
- [81] N. Brahms, T. Botter, S. Schreppler, D. W. C. Brooks, and D. M. Stamper-Kurn, *Optical Detection of the Quantization of Collective Atomic Motion*, Physical Review Letters **108**, 133601 (2012), URL <https://dx.doi.org/10.1103/PhysRevLett.108.133601>.
- [82] M. Underwood *et al.*, *Measurement of the motional sidebands of a nanogram-scale oscillator in the quantum regime*, Physical Review A **92**, 061801 (2015), URL <https://dx.doi.org/10.1103/PhysRevA.92.061801>.
- [83] T. P. Purdy *et al.*, *Optomechanical Raman-ratio thermometry*, Physical Review A **92**, 031802 (2015), URL <https://dx.doi.org/10.1103/PhysRevA.92.031802>.
- [84] T. A. Palomaki, J. W. Harlow, J. D. Teufel, R. W. Simmonds, and K. W. Lehnert, *Coherent state transfer between itinerant microwave fields and a mechanical oscillator.*, Nature **495**, 210 (2013), URL <https://dx.doi.org/10.1038/nature11915>.
- [85] R. W. Andrews, A. P. Reed, K. Cicak, J. D. Teufel, and K. W. Lehnert, *Quantum-enabled temporal and spectral mode conversion of microwave signals.*, Nature Communications **6**, 10021 (2015), URL <https://dx.doi.org/10.1038/ncomms10021>.
- [86] J. T. Hill, A. H. Safavi-Naeini, J. Chan, and O. Painter, *Coherent optical wavelength conversion via cavity optomechanics*, Nature Communications **3**, 1196 (2012), URL <https://dx.doi.org/10.1038/ncomms2201>.
- [87] F. Lecocq, J. B. Clark, R. W. Simmonds, J. Aumentado, and J. D. Teufel, *Mechanically Mediated Microwave Frequency Conversion in the Quantum Regime*, Physical Review Letters **116**, 043601 (2016), URL <https://dx.doi.org/10.1103/PhysRevLett.116.043601>.
- [88] M. Paternostro *et al.*, *Creating and Probing Multipartite Macroscopic Entanglement with Light*, Physical Review Letters **99**, 250401 (2007), URL <https://dx.doi.org/10.1103/PhysRevLett.99.250401>.
- [89] D. Vitali *et al.*, *Optomechanical Entanglement between a Movable Mirror and a Cavity Field*, Physical Review Letters **98**, 030405 (2007), URL <https://dx.doi.org/10.1103/PhysRevLett.98.030405>.
- [90] C. Genes, A. Mari, P. Tombesi, and D. Vitali, *Robust entanglement of a micromechanical resonator with output optical fields*, Physical Review A **78**, 032316 (2008), URL <https://dx.doi.org/10.1103/PhysRevA.78.032316>.
- [91] K. Børkje, A. Nunnenkamp, and S. M. Girvin, *Proposal for Entangling Remote Micromechanical Oscillators via Optical Measurements*, Physical Review Letters **107**, 123601 (2011), URL <https://dx.doi.org/10.1103/PhysRevLett.107.123601>.
- [92] S. G. Hofer, W. Wieczorek, M. Aspelmeyer, and K. Hammerer, *Quantum entanglement and teleportation in pulsed cavity optomechanics*, Physical Review A **84**, 052327 (2011), URL <https://dx.doi.org/10.1103/PhysRevA.84.052327>.
- [93] T. A. Palomaki, J. D. Teufel, R. W. Simmonds, and K. W. Lehnert, *Entangling mechanical motion with microwave fields.*, Science **342**, 710 (2013), URL <https://dx.doi.org/10.1126/science.1244563>.

- [94] R. J. Donnelly and C. F. Barenghi, *The Observed Properties of Liquid Helium at the Saturated Vapor Pressure*, Journal of Physical and Chemical Reference Data **27**, 1217 (1998), URL <https://dx.doi.org/10.1063/1.556028>.
- [95] R. J. Donnelly, *Quantized vortices in helium II*, Cambridge University Press (1991), ISBN 9780521324007.
- [96] D. R. Tilley and J. Tilley, *Superfluidity and superconductivity*, CRC Press (1990), ISBN 9780750300339.
- [97] W. F. Vinen and J. J. Niemela, *Quantum Turbulence*, Journal of Low Temperature Physics **129**, 213 (2002), URL <https://dx.doi.org/10.1023/A:1020890811263>.
- [98] K. R. Atkins, *Third and Fourth Sound in Liquid Helium II*, Physical Review **113**, 962 (1959), URL <https://dx.doi.org/10.1103/PhysRev.113.962>.
- [99] C. C. Grimes and G. Adams, *Evidence for a liquid-to-crystal phase transition in a classical, two-dimensional sheet of electrons*, Physical Review Letters **42**, 795 (1979), URL <https://dx.doi.org/10.1103/PhysRevLett.42.795>.
- [100] G. Papageorgiou *et al.*, *Counting Individual Trapped Electrons on Liquid Helium*, Applied Physics Letters **86**, 153106 (2005), URL <https://dx.doi.org/10.1063/1.1900301>.
- [101] G. Yang *et al.*, *Coupling an Ensemble of Electrons on Superfluid Helium to a Superconducting Circuit*, Physical Review X **6**, 011031 (2016), URL <https://dx.doi.org/10.1103/PhysRevX.6.011031>.
- [102] W. B. Fowler and D. L. Dexter, *Electronic Bubble States in Liquid Helium*, Physical Review **176**, 337 (1968), URL <https://dx.doi.org/10.1103/PhysRev.176.337>.
- [103] C. C. Grimes and G. Adams, *Infrared-absorption spectrum of the electron bubble in liquid helium*, Physical Review B **45**, 2305 (1992), URL <https://dx.doi.org/10.1103/PhysRevB.45.2305>.
- [104] J. C. Hill, O. Heybey, and G. K. Walters, *Evidence of Metastable Atomic and Molecular Bubble States in Electron-Bombarded Superfluid Liquid Helium*, Physical Review Letters **26**, 1213 (1971), URL <https://dx.doi.org/10.1103/PhysRevLett.26.1213>.
- [105] A. V. Benderskii, R. Zadoyan, N. Schwentner, and V. A. Apkarian, *Photodynamics in superfluid helium: Femtosecond laser-induced ionization, charge recombination, and preparation of molecular Rydberg states*, Journal of Chemical Physics **110**, 1542 (1999), URL <https://dx.doi.org/10.1063/1.477796>.
- [106] B. Tabbert, H. Günther, and G. zu Putlitz, *Optical Investigation of Impurities in Superfluid  $^4\text{He}$* , Journal of Low Temperature Physics **109**, 653 (1997), URL <https://dx.doi.org/10.1023/A:1022245700833>.
- [107] J. P. Toennies and A. F. Vilesov, *Spectroscopy of Atoms and Molecules in Liquid Helium*, Annual Review of Physical Chemistry **49**, 1 (1998), URL <https://dx.doi.org/10.1146/annurev.physchem.49.1.1>.
- [108] J. P. Toennies and A. F. Vilesov, *Superfluid helium droplets: A uniquely cold nanomatrix for molecules and molecular complexes*, Angewandte Chemie - International Edition **43**, 2622 (2004), URL <https://dx.doi.org/10.1002/anie.200300611>.
- [109] P. C. Hendry and P. V. E. McClintock, *Continuous flow apparatus for preparing isotopically pure  $^4\text{He}$* , Cryogenics **27**, 131 (1987), URL [https://dx.doi.org/10.1016/0011-2275\(87\)90069-5](https://dx.doi.org/10.1016/0011-2275(87)90069-5).
- [110] C. M. Surko, G. J. Dick, F. Reif, and W. C. Walker, *Spectroscopic Study of Liquid Helium in the Vacuum Ultraviolet*, Physical Review Letters **23**, 842 (1969), URL <https://dx.doi.org/10.1103/PhysRevLett.23.842>.
- [111] M. Joppien, R. Karnbach, and T. Möller, *Electronic excitations in liquid helium: The evolution from small clusters to large droplets*, Physical Review Letters **71**, 2654 (1993), URL <https://dx.doi.org/10.1103/PhysRevLett.71.2654>.

- [112] L. A. De Lorenzo and K. C. Schwab, *Ultra-High Q Acoustic Resonance in Superfluid  $^4\text{He}$* , Journal of Low Temperature Physics **186**, 233 (2017), URL <https://dx.doi.org/10.1007/s10909-016-1674-x>.
- [113] F. Pobell, *Matter and Methods at Low Temperatures*, Springer-Verlag, Berlin Heidelberg (2007), ISBN 9783540463603.
- [114] B. Rollin and F. Simon, *On the film phenomenon of liquid helium II*, Physica **6**, 219 (1939), URL [https://dx.doi.org/10.1016/S0031-8914\(39\)80013-1](https://dx.doi.org/10.1016/S0031-8914(39)80013-1).
- [115] A. D. Kashkanova *et al.*, *Superfluid Brillouin optomechanics*, Nature Physics **13**, 74 (2016), URL <https://dx.doi.org/10.1038/nphys3900>.
- [116] A. D. Kashkanova *et al.*, *Optomechanics in superfluid helium coupled to a fiber-based cavity*, Journal of Optics **19**, 034001 (2017), URL <https://dx.doi.org/10.1088/2040-8986/aa551e>.
- [117] E. R. Pike, J. M. Vaughan, and W. F. Vinen, *Brillouin scattering from superfluid  $^4\text{He}$* , Journal of Physics C: Solid State Physics **3**, L40 (1970), URL <https://dx.doi.org/10.1088/0022-3719/3/2/001>.
- [118] D. A. Rockwell, R. F. Benjamin, and T. J. Greytak, *Brillouin scattering from superfluid  $^3\text{He}$ - $^4\text{He}$  solutions*, Journal of Low Temperature Physics **18**, 389 (1975), URL <https://dx.doi.org/10.1007/BF00116133>.
- [119] E. A. Lazarus, N. C. Ford, R. B. Hallock, and K. H. Langley, *Rayleigh linewidth measurements in liquid helium*, Journal of Low Temperature Physics **29**, 431 (1977), URL <https://dx.doi.org/10.1007/BF00661538>.
- [120] G. Winterling, F. S. Holmes, and T. J. Greytak, *Light Scattering from First and Second Sound near the  $\lambda$  Transition in Liquid He*, Physical Review Letters **30**, 427 (1973), URL <https://dx.doi.org/10.1103/PhysRevLett.30.427>.
- [121] T. J. Greytak and J. Yan, *Light Scattering from Rotons in Liquid Helium*, Physical Review Letters **22**, 987 (1969), URL <https://dx.doi.org/10.1103/PhysRevLett.22.987>.
- [122] T. J. Greytak, R. Woerner, J. Yan, and R. F. Benjamin, *Experimental evidence for a two-roton bound state in superfluid helium*, Physical Review Letters **25**, 1547 (1970), URL <https://dx.doi.org/10.1103/PhysRevLett.25.1547>.
- [123] E. R. Pike, J. M. Vaughan, and W. F. Vinen, *Brillouin scattering from superfluid  $^4\text{He}$* , Journal of Physics C: Solid State Physics **3**, L40 (1970), URL <https://dx.doi.org/10.1088/0022-3719/3/2/001>.
- [124] G. Winterling, J. Miller, and T. J. Greytak, *Light scattering from thermal second sound in liquid  $^4\text{He}$  near the  $\lambda$ -transition and at 1.9 atmospheres*, Physics Letters A **48**, 343 (1974), URL [https://dx.doi.org/10.1016/0375-9601\(74\)90458-7](https://dx.doi.org/10.1016/0375-9601(74)90458-7).
- [125] F. Wagner, *Scattering of light by thermal ripplons on superfluid helium*, Journal of Low Temperature Physics **13**, 317 (1973), URL <https://dx.doi.org/10.1007/BF00654070>.
- [126] L. A. De Lorenzo and K. C. Schwab, *Superfluid optomechanics: Coupling of a superfluid to a superconducting condensate*, New Journal of Physics **16** (2014), URL <https://dx.doi.org/10.1088/1367-2630/16/11/113020>.
- [127] G. I. Harris, D. L. McAuslan, E. Sheridan, Y. Sachkou, C. Baker, and W. P. Bowen, *Laser cooling and control of excitations in superfluid helium*, Nature Physics **12**, 788 (2016), URL <https://dx.doi.org/10.1038/nphys3714>.
- [128] P. J. Shirron and J. M. Mochel, *Atomically thin superfluid helium films on solid hydrogen*, Physical Review Letters **67**, 1118 (1991), URL <https://dx.doi.org/10.1103/PhysRevLett.67.1118>.

- [129] J. F. Allen and H. Jones, *New Phenomena Connected with Heat Flow in Helium II*, Nature **141**, 243 (1938), URL <https://dx.doi.org/10.1038/141243a0>.
- [130] D. L. McAuslan *et al.*, *Microphotonic Forces from Superfluid Flow*, Physical Review X **6**, 021012 (2016), URL <https://dx.doi.org/10.1103/PhysRevX.6.021012>.
- [131] X. Rojas and J. P. Davis, *Superfluid nanomechanical resonator for quantum nanofluidics*, Physical Review B **91**, 024503 (2015), URL <https://dx.doi.org/10.1103/PhysRevB.91.024503>.
- [132] F. Souris, X. Rojas, P. H. Kim, and J. P. Davis, *Ultralow-Dissipation Superfluid Micromechanical Resonator*, Physical Review Applied **7**, 044008 (2017), URL <https://dx.doi.org/10.1103/PhysRevApplied.7.044008>.
- [133] M. Kriss and I. Rudnick, *Superfluid Helmholtz Resonators*, Physical Review **174**, 326 (1968), URL <https://dx.doi.org/10.1103/PhysRev.174.326>.
- [134] G. S. Agarwal and S. S. Jha, *Theory of optomechanical interactions in superfluid He*, Physical Review A **90**, 023812 (2014), URL <https://dx.doi.org/10.1103/PhysRevA.90.023812>.
- [135] C. J. Pethick and D. ter Haar, *On the attenuation of sound in liquid helium*, Physica **32**, 1905 (1966), URL [https://dx.doi.org/10.1016/0031-8914\(66\)90157-1](https://dx.doi.org/10.1016/0031-8914(66)90157-1).
- [136] B. M. Abraham, Y. Eckstein, J. B. Ketterson, M. Kuchnir, and J. Vignos, *Sound Propagation in Liquid  $^4\text{He}$* , Physical Review **181**, 347 (1969), URL <https://dx.doi.org/10.1103/PhysRev.181.347>.
- [137] H. J. Maris and W. E. Massey, *Phonon Dispersion and the Propagation of Sound in Liquid Helium-4 below 0.6K*, Physical Review Letters **25**, 220 (1970), URL <https://dx.doi.org/10.1103/PhysRevLett.25.220>.
- [138] H. J. Maris, *Attenuation and velocity of sound in superfluid helium*, Physical Review Letters **28**, 277 (1972), URL <https://dx.doi.org/10.1103/PhysRevLett.28.277>.
- [139] J. Jäckle and K. W. Kehr, *Note on phonon lifetimes in He II*, Physics Letters A **37**, 205 (1971), URL [https://dx.doi.org/10.1016/0375-9601\(71\)90463-4](https://dx.doi.org/10.1016/0375-9601(71)90463-4).
- [140] J. Capilla, J. Olivares, M. Clement, J. Sangrador, E. Iborra, and A. Devos, *Characterization of amorphous tantalum oxide for insulating acoustic mirrors*, Proceedings of the IEEE International Frequency Control Symposium and Exposition (2011), URL <https://dx.doi.org/10.1109/FCS.2011.5977833>.
- [141] A. D. Kashkanova, *Optomechanics with Superfluid Helium*, Ph.D. thesis, Yale University (2017).
- [142] I. M. Khalatnikov, *An Introduction to the Theory of Superfluidity*, CRC Press (2000), ISBN 9780738203003.
- [143] L. Tisza, *Transport Phenomena in Helium II*, Nature **141**, 913 (1938), URL <https://dx.doi.org/10.1038/141913a0>.
- [144] L. Landau, *Theory of the Superfluidity of Helium II*, Phys. Rev. **60**, 356 (1941), URL <https://dx.doi.org/10.1103/PhysRev.60.356>.
- [145] D. D. Awschalom and K. W. Schwarz, *Observation of a remanent vortex-line density in superfluid helium*, Physical Review Letters **52**, 49 (1984), URL <https://dx.doi.org/10.1103/PhysRevLett.52.49>.
- [146] D. E. Zmeev *et al.*, *Excimers  $^4\text{He}_2$  as Tracers of Quantum Turbulence in  $^4\text{He}$  in the* Physical Review Letters **110**, 175303 (2013), URL <https://dx.doi.org/10.1103/PhysRevLett.110.175303>.

- [147] J. W. Keto, F. J. Soley, M. Stockton, and W. A. Fitzsimmons, *Dynamic properties of neutral excitations produced in electron-bombarded superfluid helium. I. The He(2 S<sub>3</sub>) and He2(a 3) atomic and molecular metastable states*, Physical Review A **10**, 872 (1974), URL <https://dx.doi.org/10.1103/PhysRevA.10.872>.
- [148] R. W. Whitworth, *Experiments on the Flow of Heat in Liquid Helium below 0.5 degrees K*, Proceedings of the Royal Society A: Mathematical, Physical and Engineering Sciences **246**, 390 (1958), URL <https://dx.doi.org/10.1098/rspa.1958.0146>.
- [149] J. D. Jackson, *Classical Electrodynamics*, Wiley (1998), ISBN 9780471309321.
- [150] N. W. Ashcroft and N. D. Mermin, *Solid State Physics*, Saunders College Publishing (1976), ISBN 9780030839931.
- [151] D. Hunger, T. Steinmetz, Y. Colombe, C. Deutsch, T. W. Hänsch, and J. Reichel, *A fiber Fabry-Perot cavity with high finesse*, New Journal of Physics **12**, 065038 (2010), URL <https://dx.doi.org/10.1088/1367-2630/12/6/065038>.
- [152] A. E. Siegman, *Lasers*, University Science Books (1986), ISBN 9780935702118.
- [153] G. Seidel, R. Lanou, and W. Yao, *Rayleigh scattering in rare-gas liquids*, Nuclear Instruments and Methods in Physics Research Section A: Accelerators, Spectrometers, Detectors and Associated Equipment **489**, 189 (2002), URL [https://dx.doi.org/10.1016/S0168-9002\(02\)00890-2](https://dx.doi.org/10.1016/S0168-9002(02)00890-2).
- [154] C. Kittel and H. Kroemer, *Thermal Physics*, W. H. Freeman (1980), ISBN 9780716710882.
- [155] B. Bertman and T. A. Kitchens, *Heat transport in superfluid filled capillaries*, Cryogenics **8**, 36 (1968), URL [https://dx.doi.org/10.1016/S0011-2275\(68\)80051-7](https://dx.doi.org/10.1016/S0011-2275(68)80051-7).
- [156] R. W. Peterson *et al.*, *Laser Cooling of a Micromechanical Membrane to the Quantum Backaction Limit*, Physical Review Letters **116**, 063601 (2016), URL <https://dx.doi.org/10.1103/PhysRevLett.116.063601>.
- [157] J. D. Teufel, F. Lecocq, and R. W. Simmonds, *Overwhelming Thermomechanical Motion with Microwave Radiation Pressure Shot Noise*, Physical Review Letters **116**, 013602 (2016), URL <https://dx.doi.org/10.1103/PhysRevLett.116.013602>.
- [158] K. Børkje, A. Nunnenkamp, B. M. Zwickl, C. Yang, J. G. E. Harris, and S. M. Girvin, *Observability of radiation-pressure shot noise in optomechanical systems*, Physical Review A **82**, 013818 (2010), URL <https://dx.doi.org/10.1103/PhysRevA.82.013818>.
- [159] T. P. Purdy, K. E. Grutter, K. Srinivasan, and J. M. Taylor, *Quantum correlations from a room-temperature optomechanical cavity*, Science **356**, 1265 (2017), URL <https://dx.doi.org/10.1126/science.aag1407>.
- [160] A. Kronwald, F. Marquardt, and A. A. Clerk, *Arbitrarily large steady-state bosonic squeezing via dissipation*, Physical Review A **88**, 063833 (2013), URL <https://dx.doi.org/10.1103/PhysRevA.88.063833>.
- [161] E. E. Wollman *et al.*, *Quantum squeezing of motion in a mechanical resonator*, Science **349**, 952 (2015), URL <https://dx.doi.org/10.1126/science.aac5138>.
- [162] F. Lecocq, J. B. Clark, R. W. Simmonds, J. Aumentado, and J. D. Teufel, *Quantum Nondemolition Measurement of a Nonclassical State of a Massive Object*, Physical Review X **5**, 041037 (2015), URL <https://dx.doi.org/10.1103/PhysRevX.5.041037>.

- [163] J.-M. Pirkkalainen, E. Damskäg, M. Brandt, F. Massel, and M. A. Sillanpää, *Squeezing of Quantum Noise of Motion in a Micromechanical Resonator*, Physical Review Letters **115**, 243601 (2015), URL <https://dx.doi.org/10.1103/PhysRevLett.115.243601>.
- [164] J. Restrepo, J. Gabelli, C. Ciuti, and I. Favero, *Classical and quantum theory of photothermal cavity cooling of a mechanical oscillator*, Comptes Rendus Physique **12**, 860 (2011), URL <https://dx.doi.org/10.1016/j.crhy.2011.02.005>.
- [165] *Correspondence with LaserOptik mirror coating company* (2012).
- [166] V. Arp, *Heat transport through helium II*, Cryogenics **10**, 96 (1970), URL [https://dx.doi.org/10.1016/0011-2275\(70\)90078-0](https://dx.doi.org/10.1016/0011-2275(70)90078-0).
- [167] M. Sciacca, A. Sellitto, and D. Jou, *Transition to ballistic regime for heat transport in helium II*, Physics Letters A **378**, 2471 (2014), URL <https://dx.doi.org/10.1016/j.physleta.2014.06.041>.
- [168] G. I. Harris, private communication (2017).
- [169] B. M. Zwickl *et al.*, *High quality mechanical and optical properties of commercial silicon nitride membranes*, Applied Physics Letters **92**, 103125 (2008), URL <https://dx.doi.org/10.1063/1.2884191>.
- [170] F. Massel, S. U. Cho, J.-M. Pirkkalainen, P. J. Hakonen, T. T. Heikkilä, and M. A. Sillanpää, *Multimode circuit optomechanics near the quantum limit.*, Nature communications **3**, 987 (2012), URL <https://dx.doi.org/10.1038/ncomms1993>.
- [171] H. Seok, L. F. Buchmann, S. Singh, and P. Meystre, *Optically mediated nonlinear quantum optomechanics*, Physical Review A **86**, 063829 (2012), URL <https://dx.doi.org/10.1103/PhysRevA.86.063829>.
- [172] C. F. Ockeloen-Korppi, E. Damskäg, J.-M. Pirkkalainen, A. A. Clerk, M. Woolley, and M. A. Sillanpää, *Quantum Backaction Evading Measurement of Collective Mechanical Modes*, Physical Review Letters **117**, 140401 (2016), URL <https://dx.doi.org/10.1103/PhysRevLett.117.140401>.
- [173] A. Xuereb, C. Genes, and A. Dantan, *Strong Coupling and Long-Range Collective Interactions in Optomechanical Arrays*, Physical Review Letters **109**, 223601 (2012), URL <https://dx.doi.org/10.1103/PhysRevLett.109.223601>.
- [174] L. Childress *et al.*, *Cavity Optomechanics in a Levitated Helium Drop*, arXiv pp. 1–13 (2017), URL <http://arxiv.org/abs/1708.01803>.
- [175] H. Kerscher, M. Niemetz, and W. Schoepe, *Viscosity and Mean Free Path of Very Diluted Solutions of  $^3\text{He}$  in  $^4\text{He}$* , Journal of Low Temperature Physics **124**, 163 (2001), URL <https://dx.doi.org/10.1023/A:1017525901859>.
- [176] S. V. Pereverzev, A. Loshak, S. Backhaus, J. C. Davis, and R. E. Packard, *Quantum oscillations between two weakly coupled reservoirs of superfluid He-3*, Nature **388**, 449 (1997), URL <https://dx.doi.org/10.1038/41277>.
- [177] K. Sukhatme, Y. Mukharsky, T. Chui, and D. Pearson, *Observation of the ideal Josephson effect in superfluid  $^4\text{He}$* , Nature **411**, 280 (2001), URL <https://dx.doi.org/10.1038/35077024>.
- [178] E. Hoskinson, Y. Sato, and R. E. Packard, *Superfluid  $\text{He}_4$  interferometer operating near 2 K*, Physical Review B - Condensed Matter and Materials Physics **74**, 2 (2006), URL <https://dx.doi.org/10.1103/PhysRevB.74.100509>.
- [179] H. J. Carmichael, *Spectrum of squeezing and photocurrent shot noise: a normally ordered treatment*, Journal of the Optical Society of America B **4**, 1588 (1987), URL <https://dx.doi.org/10.1364/JOSAB.4.001588>.

- [180] E. D. Black, *An introduction to Pound-Drever-Hall laser frequency stabilization*, American Journal of Physics **69**, 79 (2001), URL <https://dx.doi.org/10.1119/1.1286663>.
- [181] R. W. P. Drever *et al.*, *Laser phase and frequency stabilization using an optical resonator*, Applied Physics B **31**, 97 (1983), URL <https://dx.doi.org/10.1007/BF00702605>.
- [182] A. M. Jayich *et al.*, *Cryogenic optomechanics with a  $Si_3N_4$  membrane and classical laser noise*, New Journal of Physics **14** (2012), URL <https://dx.doi.org/10.1088/1367-2630/14/11/115018>.